Site BA1[1]

Kelemen, P.B., Matter, J.M., Teagle, D.A.H., Coggon, J.A., and the Oman Drilling Project Science Team[2]

Keywords: Oman Drilling Project, OmanDP, Samail ophiolite, Site BA1, Hole BA1A, Hole BA1B, Hole BA1C, Hole BA1D, rotary coring, Tayin Massif, Wadi Lawayni, Batin alteration, multiborehole observatory

Chapter contents

[1]Kelemen, P.B., Matter, J.M., Teagle, D.A.H., Coggon, J.A., and the Oman Drilling Project Science Team, 2021. Site BA1. *In* Kelemen, P.B., Matter, J.M., Teagle, D.A.H, Coggon, J.A., and the Oman Drilling Project Science Team, *Proceedings of the Oman Drilling Project*: College Station, TX (International Ocean Discovery Program). https://doi.org/10.14379/OmanDP.proc.2020
[2]OmanDP Science Team affiliations.

MS OmanDP-115
Published 10 May 2021

Introduction

Site BA1 is located in Wadi Lawayni at the eastern margin of the Tayin Massif (Fig. F1 in the **Introduction to Science Theme 3** chapter). Site BA1 is a multiborehole site that forms the core of the BA (Batin alteration) multiborehole observatory in Wadi Lawayni, along with Sites BA3 to the south and BA4 to the north (Fig. F2 in the **Introduction to Science Theme 3** chapter). The boreholes at Site BA1 were designed to facilitate detailed study and sampling of the partially serpentinized dunite and peridotite in this section of the ophiolite (Hole BA1B) as well as hydrogeological and microbiological sampling (of the actively altering peridotite) in wider diameter rotary boreholes (Holes BA1A, BA1C, and BA1D) using a SolExperts packer system. The holes are spaced to allow interborehole tracer testing at different length scales and in different directions.

Geological setting

Site BA1 is in the center of the ~350 m wide wadi, with a ~25 m thick cover of wadi gravels. The bedrock in this part of the wadi is dunite underlain by harzburgite. The geology of the wider area is described in the **Introduction to Science Theme 3** chapter. An overview of all holes drilled is given in Table T3 in the **Methods** chapter.

Operations: Hole BA1A

Rotary Hole BA1A (drilled in January 2017) is located 120 m from cored Hole BA1B (drilled in January 2018). Detailed petrological observations were made on core from Hole BA1B during summer 2018 onboard DV *Chikyu*.

Here we summarize results from the lithology logs of Hole BA1A drill cuttings (originally logged on site in March 2017 and relogged in Southampton in October 2020), a series of X-ray diffraction (XRD) measurements on powdered cuttings, 3 X-ray fluorescence (XRF) measurements on powdered cuttings, and a petrographic study undertaken by Alexis Templeton's group at the University of Colorado.

All times are reported as local time in Oman (UTC + 4 h).

Drilling summary

- Spud in: 20 Feb 2017, 09:25 h
- Surface casing (SW) installed: 22 Feb 2017, 16:00 h
- Surface casing type: MS; 13-3/8 inch

- Surface casing depth: 0.30–21 m below ground level (mbgl)
- Hole diameter: 6 inches, 21–400 mbgl
- Total depth (TD) of borehole: 400.00 mbgl
- Completion type: open hole
- Discharge by air lift: 2.97 LPS
- Static water level: 15.67 mbgl

Geology summary

Partially serpentinized harzburgite and dunite.

Technical issues

Drilling started with a 12-1/4 inch bottom-hole assembly (BHA) from ground level to 15 mbgl; drilling stopped at 15 mbgl to install 10 m of 9-5/8 inch surface casing. Cementing of the 9-5/8 inch surface casing failed, and surface casing was pulled out of hole (POOH), resulting in collapse of the borehole. The borehole design was changed and drilling resumed using a 17-1/2 inch BHA. Drilling stopped at 21 mbgl, and 13-3/8 inch MS surface casing was installed. After cement grouting the annulus (SG = 1.74), the hole was left to settle. Drilling continued with a 6 inch diameter tricone bit from 21 to 400 mbgl.

Operations summary

- 15–19 Feb 2017: mobilize rig, equipment, and drilling crew from Muscat to Ibra; prepare drill pad.
- 20 Feb 2017: start drilling Hole BA1A with a 12-1/4 inch BHA, 0–15 mbgl. The target was to drill through the alluvium into the partially serpentinized peridotite to install surface casing.
  - Stop drilling at 15 mbgl to install 9-5/8 inch MS surface casing.
  - Rudimentary cementing failed to successfully install the surface casing.
  - Drillers pull out surface casing and discuss redesign of the borehole with J. Matter.
- 21 Feb 2017: transport 17-1/2 inch bit and 13-3/8 and 9-5/8 inch MS surface casing from Muscat to drill site.
- 22 Feb 2017: resume drilling with 17-1/2 inch bit, 0–21 mbgl; install 13-3/8 inch surface casing, 0.3–21 mbgl. Cement annulus (SG = 1.74), leave to dry and settle.
- 23 Feb 2017: start drilling 6 inch diameter hole, 21–40 mbgl. Collect and describe drill cuttings every meter; collect subsamples for later analysis. First seepage of groundwater at 26 mbgl (flow [Q] = not measurable, electrical conductivity [EC] = 552 µS/cm, pH = 9.2, temperature [T] = 30°C).
- 24 Feb 2017: Friday, no work
- 25 Feb 2017: standing water level (SWL) in borehole = 14.70 mbtoc (meters below top of casing). Continue drilling 40–123 mbgl; collect and describe drill cuttings every meter; collect subsamples for later analysis. Flow increase at 42 mbgl (Q = 1.00 L/s, EC = 508 µS/cm, pH = 9.1, T = 29.6°C) and again at 52 mbgl (Q = 1.83 L/s, EC = 742 µS/cm, pH = 9.3, T = 32.6°C) and 77 mbgl (Q = 2.18 L/s, EC = 710 µS/cm, pH = 9.1, T = 32.7°C).
- 26 Feb 2017: SWL = 15.08 mbgl. Continue drilling 123–205 mbgl; collect and describe drill cuttings every meter; collect subsamples for later analysis. No increase in flow (Q = 2.18 L/s, EC = 718 µS/cm, pH = 8.8, T = 32.4°C).
- 27 Feb 2017: SWL = 15.28 mbgl. Continue drilling 205–267 mbgl; collect and describe drill cuttings every meter; collect subsamples for later analysis. No increase in flow (Q = 2.18 L/s, EC = 728 µS/cm, pH = 8.9, T = 31.9°C).
- 28 Feb 2017: SWL = 15.37 mbgl. Continue drilling 267–351 mbgl; collect and describe drill cuttings every meter; collect subsamples for later analysis. No increase in flow (Q = 2.18 L/s, EC = 755 µS/cm, pH = 8.8, T = 32.5°C).
- 01 Mar 2017: SWL = 15.10 mbgl; no circulation in drill string. Pull out 11 drill rods until circulation resumes at 250.57 mbgl. Continue drilling 351–396 mblg. Collect and describe drill cuttings every meter; collect subsamples for later analysis. No increase in flow (Q = 2.18 L/s, EC = 620 µS/cm, pH = 8.8, T = 31.6°C). Add new drill rod for drilling next 4 m, but drilling mud circulation stopped. Pull out 16 drill rods until drilling mud circulation resumes at 249.92 mbgl. Continue drilling 396–400 m mbgl. No change in groundwater flow (Q = 2.18 L/s, EC = 747 µS/cm, pH = 8.7, T = 31.0°C).
- 02–03 Mar 2017: SWL = 15.06 mbgl. Conduct lift test for 5 h (see **Supplementary material** > **N_Drill site reports**). (At 400 mbgl: Q = 2.97 L/s, EC = 663 µS/cm, pH = 8.3, T = 32.8°C). Construct wellhead and demobilize equipment; transport equipment to Site BA2 location.

Petrology from drill cuttings: Hole BA1A

Shipboard core description of core from Hole BA1B revealed a dunite-rich interval extending to ~160 m depth underlain by a harzburgite-rich interval from ~160 m to the bottom of the hole at ~400 m. Similarly, the cuttings log for Hole BA1A is dominated by dunite to 157 m depth, underlain by harzburgite. Additional dunite layers are present at 250–270, 319, and 349 m, and gabbro is present at 65, 67, 77, 103, 141, and 335 m (Fig. **F1**). Cuttings log data are presented in Table **T1**.

Hydrothermal alteration/veins: Hole BA1A

Thin section petrography and Raman spectroscopy

The University of Colorado group conducted microscopic and spectroscopic analyses of well chips recovered during rotary drilling in Hole BA1 to determine how changes in Fe- and S-bearing primary and secondary phases vary as a function of depth. Thin sections were prepared from drill cuttings material from Hole BA1 sampled every 20 m in the interval 10–390 m depth. Across all depths, the majority of grains are dominated by mesh-textured serpentine replacing olivine, sometimes with variable amounts of brucite, olivine, pyroxene, and chromite. Bastite textures (serpentine replacing orthopyroxene) are also frequently observed in association with mesh-textured serpentine. Other rock fragments are also common. Many are mostly colorless in thin section, often with a fibrous texture. The colorless fragments contain a mixture of some subset of the minerals diopside, talc, amphibole, clinochlore, garnet, and xonotlite. Still other chips contain mottling of different textures, including mesh-textured serpentine, large pyroxene crystals, and colorless regions with fibrous texture. Examples of these three types of chips are shown in Figure F2.

Samples collected very near the surface have clear differences from deeper samples. The sample from 10 m, which represents alluvium, is dominated by oxidized orange serpentine; some relict olivine and pyroxene are also present. Based on Raman spectroscopy, the orange staining results from the presence of hematite and goethite intermixed with serpentine. The sample from 30 m depth, from bedrock, appears very heterogeneous; some chips have orange-colored serpentine and others have notable opaque overprinting associated with mesh texture rims as well as cores.

Samples from 50–250 m contain variable amounts of the same opaque overprinting observed in some grains of the 30 m sample. The opaques peak in abundance at ~70 m and then decrease at greater depths. The opaque phases are often limited to mesh cores but were also observed in mesh rims. Raman spectra collected from the opaque material were consistent with a sulfide mineral in many cases, although magnetite is present as well. Sulfide minerals are generally characterized by several bands at low Raman shifts (100–400 cm^{-1}), but uniquely identifying specific sulfide minerals based only on the Raman spectrum is often difficult. Wavelength dispersive spectrometry (WDS) mapping of these areas shows that sulfur is present with the opaque material, corroborating that these are sulfide minerals. Brucite was also identified in many of the mesh cores containing sulfides. The extensive formation of sulfide is of great interest to studies of biologically mediated processes such as sulfate reduction coupled to the oxidation of hydrogen, formate, or methane, resulting in formation of secondary Fe and Ni sulfides.

Other observations

Serpentine and/or the rock type serpentinite are noted in various intervals in the cuttings log. Because there are no primary mantle minerals in most of the core from Hole BA1B, it is likely that all of the cuttings for Hole BA1A are dominated by serpentine ± brucite alteration assemblages.

Carbonate is noted in the Hole BA1A cuttings log at depths of 44, 53, 55, 87, 125, and 140 m. Magnesite is noted at 264 and 285 m. These notations indicate the presence of white vein fragments. Because the shipboard core description for Holes BA1B, BA3A, and BA4A did not include any carbonate veins below a depth of 100 m and very few below 50 m, it is likely that some of the carbonate and magnesite noted in the cuttings log for Hole BA1A is actually derived from white serpentine veins.

X-ray diffraction

XRD data indicate that samples from 199, 209, and 329 m depths contain orthopyroxene, in keeping with shipboard observations of Hole BA1B core, indicating that minor relict primary mantle minerals are present in the lower half of the hole (see Table T1 in the **Introduction to Science Theme 3** chapter).

XRD data were gathered for powders from drill cuttings at 10 m intervals in Hole BA1A. The resulting spectra were qualitatively analyzed by James Bird at University of Southampton. All intervals contained serpentine, interpreted as lizardite. Two depths (29 and 379 m) contained talc. "Amphibole" was detected at 199 m, and "eckermannite" was interpreted to be present at 169, 259, 269, 299, 309, 319, 329, 339, 359, 369, and 399 m. If these identifications are approximately correct, the amphiboles may be part of alteration assemblages in gabbroic or pyroxenite dikes. Intervals at 249, 269, 319, and 369 m contain detectable brucite. XRD peaks at low 2θ angles in most intervals of Hole BA1A were interpreted to indicate the presence of "clinochlore," "eastonite," "stevensite," "biotite," and/or "muscovite." We think this indicates the ubiquitous presence of low-Al, high-Mg sheet silicates in the alteration assemblage, possibly with some K. It is likely that all incorporate Cr in their octahedral sites. This information is useful because such phases were not well characterized during core description of Holes BA1B, BA3A, and BA4A onboard *Chikyu*.

Identification of "bementite" and "hedenbergite" based on XRD data is probably in error.

Geochemistry: Hole BA1A

XRF samples from 99, 199, and 289 m have molar (Mg + Fe)/Si ratios of 1.3–1.7 and Mg# (molar Mg/[Mg + Fe] ratios) of 0.878–0.905, and so these three intervals are probably dominated by residual mantle harzburgite (see Table T2 in the **Introduction to Science Theme 3** chapter).

XRF analyses of cuttings from the three 1 m intervals indicate that all are harzburgites: Mg# = 0.878–0.905, Ni = 1600–1800 ppm, and Cr = 1900–3500 ppm. The presence of 1–4 wt% CaO probably indicates variable amounts of gabbroic and/or pyroxenite dikes in the analyzed intervals.

Downhole measurements: Hole BA1A

Wireline logs were recorded by the University of Montpellier group using a slimline logging system in May 2017 and March 2018 (see Tables T56, T57 in the **Methods** chapter). The full set of logs are available in **Supplementary material** > **L_Wireline logging**. The dual laterolog resistivity log coincides with the cuttings log, indicating low-resistivity (<2000 Ω·m) dunite layers at 70–160, 250, 270, 349, and 394 m. Some layers with resistivities >10,000 Ω·m occur at 201–203 and 244 m, most likely representing gabbroic dikes. Preliminary optical and acoustic televiewer log analyses reveal mostly steep fractures with the majority striking northwest–southeast and decreasing fracture and vein frequency with increasing depth. Most of the fractures are closed with the exception of clearly visible open fractures in the optical televiewer log at 27, 32, 62, 64, and 133 m. Fluid column logs indicate stratification in the hole regarding pH, electrical conductivity, and oxidation-reduction (redox) potential. At 200 m, electrical conductivity increases from ~500 to >1500 µS/cm and pH increases from ~8 to 10, followed by a slight decrease to pH 9.7 at 250–400 m. This clear stratification between lower pH and electrical conductivity water in the upper 200 m and higher pH and electrical conductivity water deeper than 200 m also coincides with a change from highly oxidized (+200 mV) to highly reduced (approximately –600 mV) water at 200 m, as indicated by the Eh log (**Supplementary material** > **L_Wireline logging**). Cross-borehole multilevel hydraulic tests were conducted in Holes BA1A and BA1D in 2018 and 2019. Results of these tests are published in Lods et al. (2020).

Microbiology: Hole BA1A

Microbiology results are given in the **Microbiology** chapter.

Operations: Hole BA1B

Drilling operations and core curation information are reported in Table T2. All times are reported as local time in Oman (UTC + 4 h).

Drilling summary

- Spud-in: 24 Jan 2018, 14:02 h
- First core on deck: 24 Jan 2018, 14:30 h
- Surface casing (HW) installed: 24 Jan 2018, 2.70 mbgl
- HW casing extended:
  - 25 Jan 2018, 11.70 mbgl
  - 27 Jan 2018, 20.80 mbgl
  - 11 Feb 2018, 31.00 mbgl
- NW casing installed: 12 Feb 2018, 32.8 mbgl
- Final core on deck: 12 Feb 2018, 13:00 h
- TD of borehole: 401.70 mbgl

Geology summary

Mostly serpentinized dunite at 0–162 m, followed by serpentinized harzburgite with thin gabbroic dikes.

Technical issues

HW surface casing had to be extended several times because of loss of fluid circulation and slipping casing. Vibration combined with drilling fluid circulation might have caused the top of the hole to widen, resulting in falldown of the shoe bit and casing. Drillers used bentonite to pack and stabilize casing on 10 Feb 2018.

Operations summary

- 23 Jan 2018: mobilize rig, drilling equipment, and other accessories from Hole BA3A to Hole BA1B. Rehabilitate Hole BA3A and transport core boxes to Muscat.
- 24 Jan 2018: start drilling Hole BA1B after setup of HQ drill bit assembly from 0 to 11.70 mbgl.
- 25 Jan 2018: complete circulation fluid loss at 19.20 mbgl; no return of flow. Extend surface casing to 11.70 mbgl. Fluid circulation resumed after extension. Core to 21.00 mbgl.
- 27 Jan 2018: extend surface casing to 20.80 mbgl and redrill 20.70–32.70 mbgl.
- 28 Jan–10 Feb 2018: core to 236.70 mbgl.
- 29 Jan: SolExperts arrive for packer test training in Hole BA1A.
- 3 Feb: epic day—3 operations simultaneously going on (Hole BA1B coring, Hole BA1C rotary drilling, and packer test training in Hole BA1A).
- 11 Feb 2018: extend casing to 31 mbgl due to falling shoe bit and casing. Core to 386.70 mbgl.

- 12 Feb 2018: continue coring with HQ drill bit to TD 401.70 mbgl. Install HW casing to final depth of 32.80 mbgl. POOH and demobilize Hole BA1B.

Background description: Hole BA1B

The main lithologies logged in Hole BA1B are dunite and harzburgite with minor abundances of gabbro, olivine gabbro, clinopyroxenite, wehrlite, and leucocratic bodies injected as dikes. A summary of the lithologic column with mineral proportions and grain size variations in depth is given in Figure F3. Table T3 lists the abundance of the principal rock types in unit count percentages and cumulative thickness, and Figure F4 shows the graphical representation.

Rocks from Hole BA1B record a high degree of alteration. Visual estimates of alteration vary from 100% to 85%, with the lowest values toward the bottom of the column. Alteration is generally pervasive but occurs rarely as isolated patches. Alteration is also identified at the contact between dikes and peridotite or along veins in the form of halos or associated with deformation zones. Veins occur in close association with massive alteration and with a variety of compositions and multiple generations. These veins are described in **Veins: Hole BA1B**. In most cases, alteration minerals could not be identified in hand sample because of the very fine grained nature of these serpentinized rocks. Thin section observation and XRD results provided supporting information used to describe the altered rocks (see **Supplementary material** > **B_Thin section description**).

Lithologic units and subunits are defined by changes in lithology, mineral assemblage, modal abundance, and structural and textural variations, as well as changes in alteration, veining, and fracturing. Summaries of all units and subunits, their depths, and descriptions are provided **Supplementary material** > **E_Tabulated VCD data**.

Note that leucocratic bodies were described visually as anorthosite and troctolite. Figures and tables extracted from the macroscopic observation of the cores still use the anorthosite and troctolite terminology, but these units were sufficiently altered that the protolith could not be identified with confidence, so the term "leucocratic dike" is used in this text.

Lithologic sequences

Apart from 0.7 m of alluvium at the top (Unit 1 in Section BA1B-1Z-1), Hole BA1B can be divided into two major sequences, the Dunite with Gabbro Sequence and the Harzburgite with Gabbro Sequence, both of which are crosscut by a similar set of dike lithologies. The evolution of lithologies with depth, including their mineral modal composition, shows a clear change around 160 m depth (Fig. F5 [peridotites], Fig. F6 [dikes]), marking the limit between the two sequences.

Table T4 lists the abundance of the rock types within each sequence, both in terms of the number of units (percent) and cumulative thickness (percent). Figure F7 presents a graphical illustration. The depths and properties of the sequences are summarized in Table T5. The two sequences are separated by a major fault zone.

Dunite with Gabbro Sequence

Depth: 0.7–161.87 m
Interval: Sections BA1B-1Z-1 through 62Z-1
Units: 2a–41a

The major lithology in the Dunite with Gabbro Sequence is dunite (79.8%, 136.2 m thick), sometimes orthopyroxene bearing, with gabbro, olivine gabbro, and pyroxenite as intrusive dikes of centimeter to decimeter dimensions. Some leucocratic intrusions are present toward the top of the sequence. Harzburgite intervals or patches make up 18.1 m (10.5%) of this sequence.

Alteration is massive and almost completely replaces the ultramafic rocks. Almost all the original peridotitic textures have been obliterated, and almost no plutonic mineralogy is macroscopically observable. An exception is provided by orthopyroxenes that were pseudomorphed by bastite and other alteration minerals. Color in the upper 23 m is often yellowish to brownish orange, attributed to a high degree of oxidation (e.g., Fig. F8A). From 23 m to the bottom of this sequence at 161.87 m, dark brown to black dunite predominates (e.g., Fig. F8B). Dikes are commonly associated with visible greenish to yellowish halos up to several centimeters thick.

The contact between the Dunite with Gabbro Sequence and the subsequent sequence moving downhole, the Harzburgite with Gabbro Sequence, is marked by the prevailing occurrence of harzburgite from 161.87 m and deeper.

Harzburgite with Gabbro Sequence

Depth: 161.87–401.94 m (end of hole)
Interval: Sections BA1B-62A-1 through 142A-4
Units: 41b–77

The 239 m thick Harzburgite with Gabbro Sequence includes harzburgite (82.3%, 193.8 m thick) and, commonly, orthopyroxene-bearing dunite (8.7%, 20.4 m). Toward the bottom of the hole, dunite and harzburgite start to exhibit characteristic mantle banding and weak foliation. The remaining 9% of lithologies described consist of gabbro, olivine gabbro, clinopyroxenite, wehrlite, and leucocratic intrusions mostly occurring as thin sills or dikes (millimeter to centimeter thick). Wehrlitic dikes are characteristic of this sequence. Below ~300 m, pyroxenite dikes are more olivine rich with sometimes irregular borders and without clear-cut contacts with the harzburgite.

The background alteration is pervasive but less complete than in the upper sequence. It varies from 100% to ~90% and locally to 85%. Colors of the ultramafic rocks vary from dark blue and green tones to brownish tones. The latter appear to be very spatially associated with dunitic layers and patches. A lower content of orthopyroxene in harzburgites and their transition to dunite is easily recognizable by the appearance of brown serpentinization and oxidation together with an increased number of fine white veins. However, less common brownish alteration also occurs in harzburgite.

Principal rock types

In this section, descriptions of the principal rock types and corresponding core images are presented in order of abundance (according to the accumulated thickness; Table T3; Fig. F4).

Harzburgite

Harzburgite is the most abundant lithology in the Harzburgite with Gabbro Sequence, comprising 82.3% (193.75 m) of the total recovery from Hole BA1B (Fig. F7; Table T4). The harzburgites are medium to coarse grained and have equigranular grain size distributions (e.g., Fig. F10C). Textures are typically porphyroclastic to granular. In the Harzburgite with Gabbro Sequence, harzburgites are often foliated with the foliation plane defined by shape-preferred orientation (SPO) of the orthopyroxenes. Locally, they exhibit bands of high orthopyroxene concentration (Fig. F10D). Orthopyroxene abundances vary between 15% and 35% with typically lower abundances than in the harzburgite observed in the Dunite with Gabbro Sequence. Grain sizes are 1–10 mm, and grains are subequant to equant and subhedral. Up to 3% spinel is present (grain size typically = 0.5–2 mm) and can be interstitial to subhedral. Spinel is sometimes aligned in horizontal to inclined bands. Trace sulfides were observed infrequently in hand specimen, but small grains were revealed to be common using examination by petrographic microscope. Contacts between harzburgite and the dunite layers are typically sharp and irregular, whereas contacts between harzburgite and intrusive gabbro, olivine gabbro, clinopyroxenite, and leucocratic dikes are usually sharp and planar (see below).

Variations in the downhole modal and textural characteristics of the harzburgites of Hole BA1B were observed in thin section. Harzburgites in the Dunite with Gabbro Sequence are finer grained than those in the Harzburgite with Gabbro Sequence and exhibit porphyroclastic texture, with larger orthopyroxene grains surrounded by undeformed olivine neoblasts (Fig. F9A). Some of these olivine grains are partially or surrounded by larger orthopyroxene grains (Fig. F9B). The harzburgites from this sequence are almost completely devoid of clinopyroxene aside from those that occur as exsolution lamellae in orthopyroxenes (Fig. F9C). Thin section (TS) observation indicates that some small discrete clinopyroxene grains are preserved in TS Samples 5Z-1, 26–29 cm (12 m depth), and 35Z-3, 11–14 cm (82.2 m), consistently occurring with exsolved vermicular reddish brown spinel (Fig. F9D). Large clinopyroxene grains interstitial to serpentinized olivine are also observed in some harzburgite samples, and these are best illustrated in thin section (e.g., Sample 55Z-3, 33–37 cm; Fig. F9E).

Harzburgites from the Harzburgite with Gabbro Sequence preserve protogranular texture (Fig. F10A, F10B). Olivine and orthopyroxenes are coarse in size and exhibit kink banding and/or undulose extinction (Fig. F10A). Exsolution lamellae of clinopyroxenes in the orthopyroxenes are observed (Fig. F10C). Discrete clinopyroxenes are more common and coarser in size (3–4 mm) in these harzburgites than in harzburgites from the Harzburgite with Dunite Sequence and are typically subhedral in shape (Fig. F10D). Spinel is granular with anhedral shape and is more translucent and reddish brown in color in these harzburgites than in harzburgites from the Harzburgite with Dunite Sequence (Fig. F10E). Vermicular spinel associated with pyroxenes is observed in TS Sample 76Z-4, 42–45 cm. Large clinopyroxene clusters were observed at 287.2 m depth (Fig. F10F; Section 103Z-3, Subunit 55w). Only a curvilinear and irregular boundary separates the clinopyroxene from the surrounding grains; no reaction rim was observed. This texture is observed in both harzburgites and dunites.

Dunite

Dunites are the second most abundant lithology recovered from Hole BA1B (Fig. F4; Table T3). Dunite prevails in the Dunite with Gabbro Sequence and occurs in patches and layers in the Harzburgite with Gabbro Sequence.

Dunites in the Dunite with Gabbro Sequence begin at 0.7 m and reach 161.87 m depth. They make up 136.72 m (79.8%) of this sequence. The dunites are fine to medium grained, equigranular, and are typically completely altered (e.g., Fig. F11A, F11B). The original olivine-rich mineralogy is completely overprinted by serpentinization, and in the upper 20 m of the sequence the dunites are very strongly oxidized (e.g., Fig. F11A). The only clearly recognizable mineral is spinel, which tends to be equant and subhedral. Spinel has diameter up to 4 mm and occurs at up to ~3% modal fraction.

Dunite in the Harzburgite with Gabbro Sequence begins at Unit 63 (165.89 m, Section 62Z-2) as layers and patches within host harzburgites. Dunite totals about 20.4 m of this sequence (8.7%) with thicknesses of 4–70 cm. A few percent of subequant and subhedral orthopyroxene grains of ~3 mm size are common in the dunites of this lower sequence. Equant and subhedral spinels with a mode of ~1 mm size are commonly present in the dunites and represent 1%–5% of the mode. The dunite in this sequence is macroscopically indistinguishable from that in the upper sequence.

Under the microscope, the dunites from the Dunite with Gabbro and from the Harzburgite with Gabbro Sequences exhibit similar characteristics. They comprise subhedral olivine extensively replaced by low-temperature phases such as serpentine and chlorite, forming a dense network of polymineralic pseudomorphs of the original subequant phases with fine to medium grain size. The texture is granular with equigranular grain size distribution. A typical example of this mesh texture is seen in TS Sample 24Z-3, 14–19 cm (Fig. F11A). The original modal abundance of olivine ranges 92%–100% and decreases slightly with depth with increasing amounts of orthopyroxene, which have a modal abundance from <5% and average grain size of 0.4–1.6 mm. The general grain size of olivine ranges 0.2–3.5 mm. In most of the observed samples, even the centers of former olivine crystals are completely serpentinized with colors ranging from orange to black in plane-polarized light (Fig. F11A, F11B). However, some olivine close to the boundary between the Dunite with Gabbro and the Harzburgite with Gabbro Sequences still display relict olivine cores (Fig. F11C, F11D).

Orthopyroxenes are subhedral in shape with concentrations <3%. They range 0.2–1.6 mm in size. Spinels, representing 1%–3% of the total composition, are often subhedral and polygonal with average grain sizes of 0.4–1.8 mm (Fig. F11E). Partial alteration of Cr-spinel to magnetite is rarely observed. Sulfides are accessory with a general size <0.8 mm (Fig. F11F). The contact between dunite and gabbroic dikes is sometimes filled with low-temperature chlorite (e.g., TS Sample 58Z-2, 45–48 cm; Fig. F12).

Massive dunites in the Harzburgite with Gabbro Sequence bear textural relics of pyroxene porphyroclasts. Clinopyroxene is accessory in some investigated samples (Fig. F13A, F13B), and replacement of chromite by magnetite is more common (Fig. F13C). Close to the contact to gabbroic dikes, serpentine grades toward colorless from a green color elsewhere, and a thin layer of colorless serpentine forms at the limit between the dunite and the dike (Fig. F13D–F13F).

Dikes

Many dikes crosscut the main dunitic and harzburgitic sequences. Although the mineralogical composition of dikes varies from plagioclase-rich gabbro to wehrlite and clinopyroxenite, these variations are transitional and occur in a similar way in the upper and the lower sequence. The number of dikes in the harzburgitic sequence is significantly larger than in the dunitic sequence (Fig. F6). However, the thickness varies to compensate for the change in number; the proportion is 10% of the rock in the upper sequence and only slightly less (9%) in the lower sequence (Fig. F7). It is noteworthy that despite the consistency in many parameters downhole for Hole BA1B, mafic compositions are more frequent in the lower sequence (Fig. F6). For example, wehrlites occur only in the lower sequence (Fig. F6). Further, composite dikes are commonly observed in the Harzburgite sequence.

The number of dikes declines in each of the two sequences with depth. Because of the overwhelming similarities between the dikes in the two sequences, we describe in the following paragraphs the dikes according to their composition without distinction by host sequences or depth.

Dike alteration is highly variable throughout the core with a tendency for clinopyroxenite to look fresher than gabbroic dikes. The estimated degree of alteration ranges 5%–100%. However, even apparently fresh dikes may be completely altered, and only thin section observations and XRD results are reliable indicators of the extent of conservation of the original mineralogy.

In Figure F14 the apparent thicknesses of dikes in Hole BA1B is plotted as a function of measured halo apparent thicknesses. The limited number of points in the uppermost 30 m is because dike and halo thicknesses were not measured on the first description day. Dike and halo thickness are not statistically correlated, but halo thickness decreases somewhat with depth. A notable feature is an increase in the occurrence of halos below ~180 m, where the Harzburgite with Gabbro Sequence starts. This is likely the consequence of a higher number of dikes in this lower sequence.

Gabbro and olivine gabbro dikes

Gabbroic dikes represent the main dike type in the Dunite with Gabbro and the Harzburgite with Gabbro Sequences. Their olivine content is highly variable (0%–70%) throughout the section. Dikes with >5% olivine have been described as olivine gabbros. Gabbros make up 3.7% of the core in its upper part and 0.5% in its lower part. Olivine gabbro in Hole

BA1B cores comprises 2.7% of the recovered core in the upper sequence and 4.6% of the lower sequence (Fig. F7). Gabbros and olivine gabbros tend to show sharp planar intrusive contacts with the host dunite or harzburgite. Their grain size varies from fine to coarse grained but is most commonly medium grained (Fig. F15A–F15C). Some of the gabbroic dikes in the Harzburgite with Gabbro Sequence show moderate to weak layering features. The layering intensity varies from strong to weak with modal, sharp, and planar contacts between layers such as in Section 124Z-3 (349.9 m) (Fig. F15D). The majority of gabbros with variable composition are varitextured.

Olivine in the gabbros occurs as interstitial anhedral to subhedral subequant grains. Plagioclase constitutes up to 90% of some gabbroic dikes. Plagioclase grain size is difficult to measure because of the high degree of alteration. Clinopyroxenes represent up to 70% of the dikes' composition with grain sizes of 0.5–15 mm. Their habit is subhedral with subequant dimensions. Neither orthopyroxenes nor sulfides were identified in any of the gabbroic intrusives in hand specimen.

In both sequences the most obvious alteration is the transformation of gabbroic and leucocratic dikes into rodingitized rocks (Fig. F16A, F16B). Rodingitization is typically associated with shearing, cataclastic features, and low-grade metamorphic selvages. Most of the gabbroic dikes are characterized by a high degree of preservation of plutonic textures, whereas the original mineralogy is transformed to serpentine and other hydrous phases. The variance of preservation is not consistent with depth or host lithology but seems to be related to local tectonic and fluid overprinting as exemplified by the rodingitized material. Common minerals identified by XRD are hydrogrossular garnet, xonotlite, phlogopite, and amphibole (see **Supplementary material** > **F3_XRD data**).

Under the microscope, only fine- to medium-grained gabbros have preserved magmatic textures (e.g., Fig. F17). The coarser grained gabbros are extensively altered. For example, TS Sample 30Z-2, 10–13 cm, is fine grained and comprises equigranular and subhedral clinopyroxenes as the main cumulus phases (Fig. F17B). They do not exhibit deformation and do not contain exsolution lamellae of orthopyroxenes. Serpentinized olivine grains are also sometimes partially to completely included in clinopyroxenes. TS Sample 33Z-1, 32–35 cm, is fine to medium grained and contains some coarser clinopyroxenes that exhibit deformation structures (Fig. F17C). Plagioclase in both samples is completely altered to clay and chlorite but is inferred to have been interstitial based on relict structures and the distribution of its associated alteration minerals (Fig. F17D).

Olivine gabbro samples are mostly well preserved compared to the gabbroic dikes under the microscope (e.g., Fig. F18). Olivine grains are subhedral in shape and have irregular grain boundaries (e.g., Fig. F18A). Partial to complete replacement of olivine by lizardite is observed in most samples. Similar to the gabbro samples, olivine gabbro–hosted clinopyroxenes do not exhibit exsolution lamellae or record deformation. They sometimes include euhedral plagioclase and olivine grains (Fig. F18A, F18B). Subhedral grains of orthopyroxene were also observed on most olivine gabbro samples (Fig. F18C). Plagioclase is preserved only in TS Sample 142Z-4, 41–43 cm, where it is observed as an interstitial phase with subhedral clinopyroxenes and olivine as the main cumulus phase (Fig. F18C). In most samples (e.g., TS 47Z-1, 63–66 cm; 75Z-3, 18–22 cm), plagioclase is altered to fine clay minerals and/or chlorite, which preserves its interstitial form (Fig. F18D).

Clinopyroxenite and olivine clinopyroxenite dikes

Clinopyroxenite dikes are present throughout both sequences of Hole BA1B (2.4%, 17.4 m in the Dunite with Gabbro Sequence; 2.1%, 5 m in the Harzburgite with Gabbro Sequence) (Fig. F19). Their thickness varies within a small range of 0.5–15 cm, with the majority 1–3 cm thick. The dikes often show a chainlike clustering of clinopyroxene such as seen in Figure F19A, F19B. Neither spinel nor sulfide were observed. Clinopyroxenites generally comprise 60%–90% clinopyroxene with subequant and subhedral habit and size up to 10 mm. Olivine in these dikes has similar habit but is sometimes elongated and interstitial and is more common toward the bottom of the hole (Fig. F19C). Plagioclase and other constituents are very rare in these dikes.

A remarkable alteration feature is the appearance in the Harzburgite with Gabbro Sequence of red clinopyroxenites (Fig. F19C). These pyroxenites are in most cases completely pseudomorphically replaced by magnesium-rich amphiboles and serpentine (XRD analysis 78Z-3, 14 cm). In thin section, some dikes were observed to host well-preserved subhedral prismatic clinopyroxenes with an average grain size of 3 mm (Fig. F20A, F20B).

Clinopyroxenites in the Dunite with Gabbro Sequence are in general altered and in some cases replaced by talc (Fig. F20C) and in some cases host minor carbonate (Fig. F20D). In contrast, pyroxenites from the lower sequence are less altered and contain minor amounts of interstitial orthopyroxene (Fig. F21A, F21B). Clinopyroxenites in some thin sections form prismatic subhedral crystals with an average grain size up to 5.5 mm (e.g., Fig. F21C, F21D), typical of clinopyroxenites in this lower sequence. Contacts between clinopyroxenite and serpentinized harzburgite are often irregular, and in one case phlogopite was observed (Fig. F21E).

Wehrlite dikes

Wehrlite dikes and sills are present in the Harzburgite with Gabbro Sequence from 172 m depth in 0.5–25 cm thick intrusions (Fig. F22A) (Section 77Z-1; 207.1 m; Subunit 49b). This dike is a composite dike associated with gabbro seams a few millimeters thick at both contacts. The wehrlites are the only major dike lithology that does not occur in the upper sequence. They make up 1.6% (3.7 m) of the total section. Wehrlites consist of 50%–90% subequant and subhedral olivine with grain sizes <1 mm. Subequant and subhedral clinopyroxenes make up 10%–50% of these rocks, whereas plagioclase or spinel are rarely found. Orthopyroxene and sulfide are absent.

A thin section of the wehrlitic sill in the Harzburgite with Gabbro Sequence (Sample 134Z-4, 69–71 cm) is typical. The rock is mostly altered to secondary phases and shows a granular medium-grained texture with equigranular grain size distribution (Fig. F23A, F23B). Clinopyroxene crystals range from anhedral to subhedral with interstitial habit and a mode of 40%. The average grain size ranges 0.8–4.5 mm. Subhedral olivine has a mode of 58%, subequant shape, and average grain size of 1.2–5 mm. Spinel has a mode of 2%, subhedral and subequant habit, average grain size of 0.1–0.4 mm, and consists mainly of chromite and magnetite. Spinel is replaced locally by various accessory sulfides (Fig. F23C).

Leucocratic dikes

A few leucocratic dikes and patches with maximum thicknesses of 70 cm are present in the Dunite with Gabbro and the Harzburgite with Gabbro Sequences (Fig. F22B, F22C). They make <1% of the upper part of Hole BA1B and 0.2% of its lower part and together measure 2.0 m thickness. Their contact with the host rocks is sharp and intrusive, usually associated with shearing and cataclastic deformation. Rodingitization, with similar characteristics to rodingitization of the gabbros, affects almost all of the leucocratic dikes.

Inferred plagioclase modes are 95%–100%, and pseudomorphed plagioclase grains are subequant to equant and subhedral to anhedral with grain sizes up to 50 mm. Olivines are present in some units with modes 1%–5% and grain sizes 1–5 mm. A thin section of an anorthosite dike from the Dunite with Gabbro Sequence (TS Sample 7Z-1, 48–53 cm) is totally altered rock, so evaluation of primary igneous features must be undertaken with caution. Olivine is completely replaced by serpentine and plagioclase by clay and hydrogrossular (Fig. F24). The anorthosite shows relict granular medium-grained texture with equigranular grain size distribution. Plagioclase is subhedral with an inferred tabular shape and a modal abundance of 90%. Olivine is anhedral and clinopyroxene is subhedral. Both precursor minerals are inferred to have had a subequant shape and a modal abundance of 5%.

Basalt dikes

Three basaltic dikes of 2–5 cm thicknesses with microcrystalline appearance were recorded in the upper 25 m of Hole BA1B. They were observed at Sections 5Z-2 (12.6 m) and 14Z-2 (23.95 and 24.9 m).

Summary

Hole BA1B lithology is composed of two main sequences: the Dunite with Gabbro Sequence and the Harzburgite with Gabbro Sequence. Both sequences are crosscut by a large number of dikes of similar types, the most common being gabbroic dikes and to a lesser extent clinopyroxenites. The upper sequence is crosscut by a lesser number of thicker dikes, whereas the lower is crosscut by a higher number of thinner dikes. Harzburgitic patches are common in the dunitic sequence, and dunitic patches are common in the harzburgitic sequence.

The whole section has undergone intense low-temperature alteration. The main alteration is the almost complete serpentinization of the peridotite with a slight decrease of alteration degree toward the bottom of the core. The uppermost 25 m is also intensely oxidized due to surface weathering. Alteration in dikes is variable but homogeneous along the section. Rodingitization is in dikes throughout the core, most commonly associated with gabbroic and leucocratic intrusive rocks.

A log summarizing the lithostratigraphy of Hole BA1B can be found in Figure F25.

Veins: Hole BA1B

Veins in core from Hole BA1B formed within fractures that provide a fast path for fluids migrating through mantle peridotite of the Samail ophiolite, starting in the Late Cretaceous and continuing today. Analysis of veins in core from Hole BA1B offers the opportunity to link observations of matrix alteration with those from downhole logging, water sampling, and microbiological studies. The veins record a variety of time-integrated water/rock ratios ranging from fluid-dominated to rock-dominated mineral compositions, reflecting mass transfer across the extreme chemical potential gap between fresh mantle peridotite and surface water, particularly in terms of oxygen, carbon, and—of course—water fugacity.

In the following sections, we describe the vein assemblages and their variation as a function of depth below the surface. A secondary consideration is the transition from dunite-dominated core in the upper 160 m of Hole BA1B to harzburgite-dominated core in the lower 240 m. And, significant local control on vein assemblages is imposed by the numerous dikes of gabbro and pyroxenite that cut both dunite and harzburgite.

Overviews of the overall downhole variation in vein mineralogy and area% of veins, together with a summary of crosscutting relationships between different vein types, are shown in Figures F26, F28, and F30.

The vein description team defined an open-ended list of vein types, discussed below. We used these in describing the veins encountered in the core. In doing so, we departed somewhat from the common practice of defining a series of vein generations. We reasoned that different types of veins record variable fluid composition and interaction with rocks with variable, time-integrated reaction histories. Thus, a carbon-bearing, oxygen-rich surface fluid might form carbonate and/or hematite veins early in the history of a given rock volume, after which they might be cut by later veins. Alternatively, the same type of fluid might access the rock much later, when a fault provides a new permeable pathway into the subsurface. Thus, we expected that there could be mutually crosscutting relationships between vein types rather than a specific sequence from v1, v2 … vn, and indeed this is borne out by the quantitative crosscutting statistics in Figure F26. For example, though calcite-bearing veins generally crosscut all other vein types, Figure F26 shows that they are, in a few instances, cut by white (vein type Sf, 1 observation), black and composite (Sa and Se, 2 observations each), and waxy green (Sb, 3 observations) serpentine veins.

Before we discuss vein frequency and proportion in the core, a caveat is necessary. Estimates of vein frequency in the peridotites are complicated by the pervasive development of a microscopic serpentine mesh texture, with mesh veins surrounding polygonal to rounded mesh cores and typical vein spacing as small as tens of micrometers. The smallest through-going veins arise via coarsening of linear zones of mesh veins (Figure F27), sometimes associated with oxide veins that may represent small fractures that transported fluids conducive to coarsening the serpentine mesh veins. To varying degrees, depending on the color of microscopic mesh veins and the host rock matrix, the smallest veins emerging from the mesh vein network are more or less visible. As a result, these were not logged consistently. Moreover, depending on the size cutoff that is chosen for logging veins, the mesh veins and the tiniest veins emerging from the mesh are far more numerous and occupy a larger area than all of the other vein types combined, and data on these would tend to obscure area and frequency data for the larger, younger, and more easily observed vein types. Thus, in what follows, we have filtered out frequency and area data for mesh veins and for the generally oldest vein type we identified and logged (black serpentine veins, type Sa). In doing so, we do not mean to imply that these oldest, smallest veins are not important. They are, and an adequate quantification of the full size-frequency relationships in core from the BA drill sites is likely to be an important and rewarding research topic.

Other than the mesh veins and black type Sa serpentine veins, veins are most numerous and comprise the largest proportion of the core in the upper 200 m of Hole BA1B (Figure F28; also see Note below). This figure summarizes observations for the younger, and more obvious, through-going veins: carbonate-bearing veins (types Ca and Cb), all serpentine veins except vein type Sa (black; see Note, below), and Sg (blue-green patches around and within highly deformed magmatic blocks). The estimated area of these veins per meter downhole is about one order of magnitude lower in the lower half of the core. The decrease in vein proportion at midcore does not correspond closely to the contact between dunite and harzburgite.

Note. The values of vein area, in percent of the core face area per meter of core, should be viewed as a quantitative estimate of relative vein area. They are not accurate estimates of the actual area of veins on the core face. We found it difficult to use our adopted method—logging vein "density" and apparent width of veins—to convert our observations into fully quantitative estimates of total vein frequency and area. Problems arose mainly because (1) it is impossible to make a significant estimate of the width of macroscopically evident veins whose apparent width is <500 µm, (2) the vein density estimates do not differentiate between numerous veins <1 cm long that terminate within the core face on the one hand, and veins that extend across the core face or along the core for tens of centimeters on the other, and (3) our method of identifying the location of individual veins (the top and lower intersections of vein contacts with the centerline of the core) did not allow quantitative estimation of the apparent vein dip on the core face. In logging subsequent Holes during ChikyuOman Leg 4, we added observations of vein area on the core face within the logged interval for each vein, vein set, or vein network.

Based on crosscutting relationships, most of the youngest veins are calcite bearing (composite with serpentine and others—somewhat more common—that are ~100% calcite). In the upper 50 m of the hole, carbonate-bearing veins comprise 39% of the veins logged and perhaps ~3 vol% of the core in this interval. Since most or all geochemical samples were taken from vein-free core intervals and contain just a few weight percent $CaCO_3$ (assuming almost all of the C is incorporated in calcite/aragonite), the veins probably constitute a significant reservoir for carbon in the core, comparable to the matrix.

Carbonate veins decrease in frequency and proportion downhole (Figs. F29, F30). In contrast, the core is dominantly composed of serpentinized dunite to a depth of ~160 m. Thus, the decreasing frequency of carbonate-bearing veins is not strongly related to the change in host lithology. Similarly, there is a high proportion of waxy green veins in the upper half of the hole, reaching a maximum at ~100 m depth, within the dunite interval in the core.

"Waxy green serpentine" veins in the upper 200 m and "white serpentine" veins in the lower 200 m are also relatively young and are the most numerous of the younger veins below ~40 m depth. Some uncertainty exists in the identification of "waxy" vs. "white" veins in the lower 200 m because they are texturally and morphologically similar, "waxy white" and "waxy gray," concentrated near magmatic dikes where they cut dike/peridotite contacts. Moreover, they are joined by white xonotlite-bearing veins in gabbro dikes that cross contacts into peridotite. Nevertheless, where both can be distinguished, waxy green veins cut white serpentine veins, and it is clear that the frequency of waxy veins declines whereas that of white veins increases below 200 m.

The occurrence of the waxy green veins is of particular interest since they commonly contain zones of microcrystalline to nanocrystalline (optically isotropic) serpentine (Figs. F31, F34C–F34D), which probably formed at low temperature, as discussed below.

The presence of xonotlite-bearing veins extending from gabbroic dikes into peridotite is also notable because it attests to the mobility of Ca during parts of the water-rock interaction history of the core.

Macroscopic identification of vein types

In this section we describe each of the vein types used in logging the core, classified into 10 groups, as well as a set of undefined vein types (Fig. F31A).

Carbonate-bearing veins

Ca veins

Ca veins are layered composite veins composed of green to black serpentine and carbonate minerals. They are pervasive in the uppermost cores. Ca veins are divided into three subgroups based on their appearance:

- Ca1 veins have dark-colored serpentine cores with carbonate rims (Fig. F31B);
- Ca2 veins have carbonate cores with serpentine rims (Fig. F31C), and
- Ca3 veins (few) include waxy green serpentine and carbonate minerals.

Cb veins

Cb veins are white monomineralic granular veins of carbonate minerals, commonly with vuggy texture (Fig. F31D). They occur in the uppermost cores together with Ca veins. The abundance of both Ca and Cb veins decreases systematically with depth, and they were not observed in the core below 100 m (Figs. F29, F30).

Serpentine veins

Serpentine vein types were classified based on color and texture. "Ideal" examples of each vein type were clearly distinct in the core and dominated the veins we described, although of course ambiguous instances also occur. In some cases, the underlying reasons for the varying color of serpentine veins—and the serpentine within them—were not identified. The various colors may be due to varying amounts, types, and distributions of Fe oxides and oxyhydroxides and/or the presence of minor components (Al, Cr, Fe^{2+}, Fe^{3+}, Ni) within the serpentine minerals themselves. Tentative identification of serpentine polytypes in XRD samples include Al-, Cr-, and/or Ni-rich minerals such as amesite and népouite. Because serpentine colors are much less distinct in thin section, in many cases it was not evident which vein types were present in specific thin sections.

Sa veins

Sa veins are black network or branched veins of serpentine with cryptocrystalline magnetite (Fig. F31E). Sa veins occur throughout the core, irrespective of depth. In most cases, Sa veins are cut by other types of veins. In the lower part of Hole BA1B, Sa veins are difficult to see against the background of dark, partially serpentinized harzburgite. Also, they arise more or less gradationally from the black microscopic mesh vein network in these rocks (Fig. F27), and it is difficult to discern where they rise to the level of through-going veins worthy of recording. As a result, they were not logged consistently. However, some observers recorded the presence of conjugate sets of steeply dipping Sa veins when they were particularly obvious.

Some black veins classified as Sa may be composed entirely of Fe oxides and oxyhydroxides with no serpentine. Such veins are observed in thin section, particularly in samples from the upper 100 m of the core. These, too, may arise via lengthening and coarsening of initially microscopic mesh veins.

Sb veins

Sb veins are waxy green to waxy white serpentine veins (Fig. F31F). Sb veins occur throughout the core, but their frequency increases from 0 to ~120 m and then decreases with increasing depth below (Fig. F30). Sb veins have variable texture, connectivity, morphology, and so on. In most cases, Sb veins cut other types of veins. They are particularly abundant in and around magmatic intrusions, where they commonly cut across dike/peridotite boundaries. They also sometimes exhibit “Frankenstein” connectivity.

Sb veins are clearly distinguishable in thin section and are commonly microcrystalline to optically isotropic, with “devitrification” textures such as microcrystalline cross-fiber rims growing into amorphous vein cores and spherulites with interference crosses, as discussed further in **Thin section observation of veins**.

Sc veins

Sc veins are thin (typically < 0.5 mm) brown to brownish white serpentine veins (Fig. **F31G**). They are common in the upper levels of the cores. Like the black Sa veins, the brown veins are generally crosscut by all other vein types and are gradational with mesh veins. Some could be oxidized black veins; more specifically (and speculatively), near the top of the core, some could be hematite veins and/or serpentine relatively rich in Fe^{3+}, which is translucent brown to yellow in thin section. Downhole, we have the impression that brown veins grade into thin white veins with brown halos. These are distinct from the more common, relatively young white serpentine veins (Sf), but some of each type could be misclassified in the vein logs.

Sd veins

Sd veins are dark green serpentine veins (Fig. **F31H**). Serpentine veins in shear zones are usually classified as type Sd.

Se veins

Se veins are composite serpentine veins composed of more than one distinctly different color of serpentine (Fig. **F32A, F32B**).

Sf veins

Sf veins are thin (typically < 0.5 mm) white serpentine veins (Fig. **F32C**). They typically occur in the middle to lower levels of the cores, where they are among the youngest veins present. Below ~200 m depth, waxy veins grade from mainly light green (above) to mainly white (below) and lose some of their waxy luster. In many cases it becomes difficult to distinguish Sb and Sf veins in the lower third of the core. Thin Sf veins become abundant near magmatic dikes and cross dike contacts as the Sb veins commonly do higher in the hole. Adding an additional complication, white veins containing xonotlite (± serpentine) are present in (at least) the lower third of the core, and these two concentrate in and around gabbroic dikes. We did not become aware of this until we were logging the lower 100 m of the core. As a result, it’s quite possible that many of the white veins classified as “other” by some observers and some of the white serpentine veins contained xonotlite. As a practical matter, these potential uncertainties are not particularly significant because white waxy veins (Sb), white serpentine veins (Sf), and xonotlite-bearing veins (X) are all relatively young—crosscutting the earlier Sa, Sc, Sd, and Se veins—and are common near the margins of gabbroic dikes.

Sg veins

Sg veins are bluish green (horrible green) (Fig. **F32D**), generally >5 mm thick, and restricted to the lowermost level of the cores, where they replace and surround highly deformed blocks of magmatic rocks.

X veins

X veins contain xonotlite, which is a translucent white mineral (Fig. **F32E**) with and without serpentine. They often cut contacts between gabbroic dikes and peridotite. As discussed in the section on Sf veins above, they are similar in relative age and occurrence to Sf veins and white waxy veins (Sb), but the xonotlite veins are much harder than the Sf and Sb veins.

Other veins

Veins other than carbonate(-bearing) veins and serpentine veins were defined as “other.” As noted in **Sf veins**, white “other” veins may be xonotlite-bearing veins that were logged prior to our recognition of the xonotlite-bearing vein type.

Thin section observation of veins

The crosscutting relations of veins in Hole BA1B dunites, harzburgites, and magmatic dikes are complex and not unambiguous for several reasons: (1) not all vein types are present in every part of the core, (2) the formation of distinct textures such as crosscutting networks is continued, producing mutually crosscutting relations, and (3) earlier stages of serpentinization can be overprinted by reopening of fractures.

Upon serpentinization, olivine and orthopyroxene in dunites and harzburgites form 10 µm scale mesh and bastite textures that pervasively penetrate the rocks. With ongoing serpentinization, several other vein types form.

Examples of typical veins are shown in Figures **F33**, **F34**, and **F35**. The pervasive mesh network comprises serpentine and magnetite (Fig. **F33A**). In light-colored oxidized dunites and harzburgite, these veins may be detected in macroscopic observations of the core, whereas they largely remain undetected in darker, reduced parts of the dunite sequence.

From the mesh network, subparallel serpentine veins (Fig. F33B) emerge that form in close relation to the prevalent mesh texture. Because of their small size and distribution, many of these remain undetected during macroscopic core description. However, they may initialize formation of long-range serpentine networks, which were logged as vein sets or networks of banded or composite serpentine veins (Fig. F33C, logged as vein type Sf; Fig. F31D, logged as vein type Se), penetrating large sections of the core. In some intervals such veins form subparallel sets, through-going orthogonal, crosscutting networks, or "Frankenstein" structure. In crosscutting "Frankenstein" texture, a large central vein is orthogonally cut by numerous smaller veins. In branching "Frankenstein" texture, the central vein has orthogonal terminated branches of the same serpentine type with no crosscutting features in both macroscopic and thin section observations. Carbonate is present in two distinct, relatively late vein types. Calcite-bearing zones are present within banded or composite serpentine veins (Fig. F33E, logged as vein type Ca) or in monomineralic carbonate veins, commonly just one or two crystals wide (Fig. F33F, logged as vein type Cb).

Microcrystalline (in places amorphous) serpentine (tentatively identified as lizardite by XRD) comprises a relatively late stage generation of veins that occurs as "Frankenstein" crosscut over earlier tabular serpentine veins, as "turtle" networks in both gabbroic and peridotite host rocks (Fig. F34A, F34B shows microcrystalline lizardite in rodingitized gabbro), and as veins cutting dike/peridotite contacts, generally at a high angle. Veins related to rodingitized gabbro and pyroxenite dikes exhibit single, branched, or network connectivity and generally extend a few millimeters into host peridotite. On occasion, they form isolated patches within highly deformed blocks of meta-igneous material. Predominant vein fillings in these settings are microcrystalline or amorphous serpentine (Fig. F34A–F34D, all logged as vein type Sb). In gabbroic rocks, xonotlite-bearing (Fig. F34E) and prehnite-bearing veins are also found in the lower third of the core (Fig. F34F).

Opaque minerals

Based on reflected light microscopy, a few sporadic sulfides (predominantly pentlandite and heazlewoodite) were found in the upper level of Hole BA1B (Fig. F35A). In rare cases, Ni-Fe alloy (e.g. awaruite) was recognized in serpentine veins of the mesh texture (Fig. F35B). Generally, in the lower third of Hole BA1B, several highly reduced assemblages including native copper, Ni-Fe alloy, and undefined ore minerals shielded by magnetite were distinguished. It is highly recommended to measure the composition of these phases to better understand of redox conditions during the formation of these assemblages throughout the core from Hole BA1B.

XRD results for vein samples

About 99 XRD analyses of material from Hole BA1B were performed using a PANalytical CubiX^3 X-ray diffractometer. A total of 28 of these were related to veins and are discussed in this section. An overview of the vein mineral spectra and sample locations within the core is given in Table T6. Results of XRD analyses of altered peridotites and magmatic rocks are provided in Background description: Hole BA1B. Background and bulk rock analysis are presented in Geochemistry: Hole BA1B.

The main target of the XRD analyses of vein samples was to identify minerals in different vein types, especially when this was uncertain based on macroscopic core description alone. Thus, many XRD samples may be "pathological" rather than exemplary cases.

XRD analyses confirm the presence of magnetite along with serpentine in the black Sa type veins (Fig. F36A, F36B). Veins identified as Sb, with a waxy green color, contain serpentine as the main phase (Table T6). Some include other mineral phases such as xonotlite (hydrous Ca silicate), chlorite, and kaolinite. One dark green vein classified as Sd contained serpentine as the only phase (TS Sample 102Z-2, 15 cm). Brown serpentine veins classified as Sc are rich in serpentine, with magnetite, garnet, phlogopite, and zeolite as other present phases. White serpentine veins classified as Sf contained serpentine as either the only phase (TS Sample 78Z-4, 30 cm) or as the most abundant phase, accompanied by clinochlore (TS Sample 4Z-2, 60.5 cm).

Vein type X—commonly crosscutting magmatic features (except for Sample 70Z-3, 38 cm)—can easily be confused with type Sf. Type X samples analyzed by XRD are rich in xonotlite, a hydrous Ca silicate (Fig. F36C, F36D).

Comparison with veins in Hole CM2B

Veins in peridotite

Several generations of serpentine veins—many containing carbonate—were recognized in dunite from Hole CM2B:

- v1: mesh veins,
- v2: relatively old serpentine-magnetite veins that may correspond to black serpentine veins (Sa) in Hole BT1B,
- v3: massive, uniform networks of irregular yellowish white serpentine veins ~0.5 mm wide, and
- v4: steeply dipping, banded cross-fiber serpentine veins.

In addition, several generations of serpentine veins, many locally or commonly containing calcite, were identified in harzburgite from Hole CM2B:

- v1: mesh veins,
- v2: poorly developed 0.5–3 mm serpentine veins with dark green and black colors that render them macroscopically unrecognizable,
- v3: massive, black magnetite-rich serpentine 1–100 mm veins,
- v4: green or orange-green banded slip-fiber serpentine veins in their centers or at the margins,
- v5: blue-green serpentine veins in zones of high fracture intensity,
- v6: white, fibrous serpentine veins with a "distinct wavy appearance similar to ribbons," commonly forming "swarms" of parallel, isolated, or connected and curved veinlets and frequently containing calcite, and
- v7: late, massive calcite veins.

We may speculatively associate the black type Sa veins in Hole BA1B with the v2 and v3 generations in Hole CM2B harzburgites; the blue-green type Sg veins with v5 in Hole CM2B; the late, white serpentine veins (type Sf, ± xonotlite) with v6; and of course the late, monomineralic calcite veins with v7 in Hole CM2B. The presence of several types of composite serpentine-calcite veins extending to 300 m in Hole CM2B is distinct from the observation that calcite-bearing veins are restricted to the upper 100 m in Hole BA1B. The talc-carbonate serpentinites at the bottom of Hole CM2B also have no analog in Hole BA1B.

Veins in gabbroic rocks

Prehnite ± chlorite ± clinozoisite veins are commonly present in altered gabbroic rocks in Hole CM2B, whereas prehnite is rare and clinozoisite was not detected in similar lithologies in Hole BA1B. Though xonotlite was observed in XRD spectra from Hole CM2B, it appears that it was much less common than the xonotlite veins in Hole BA1B. Hydrogrossular and various other garnet-hydroxides plus diopside were detected by XRD in altered gabbroic rocks at both sites.

Discussion

Near-surface gradients in fO_2 and $CaCO_3$ solubility

The waxy green serpentine veins that are abundant in core from Hole BA1B are typical of low-temperature serpentinization in other localities. Their fine-grained to amorphous materials are indicative of slow crystallization and crystal growth kinetics at low temperature. It is striking that vein intensity, the abundance of carbonate veins and amorphous serpentine, and the abundance of waxy green serpentine veins all decline with depth in Hole BA1B (Figs. F28, F29, F30). In addition, hematite (and perhaps Fe oxyhydroxide) minerals are present in oxide veins and the surrounding serpentinized host rock in the upper part of the core, whereas highly reduced phases including awaruite and native copper are present near the bottom of the hole (Figs. F35, F36, F37), as previously reported in serpentinized Samail ophiolite peridotites by Lorand (1978). Low-temperature oxygen fugacities during formation of these reduced phases must have been $<10^{-80}$ bars, whereas the near-surface hematite veins are probably close to equilibrium with atmospheric fO_2 (~0.2 bars) and/or typical groundwater fO_2 (10^{-25} to 10^{-35} bars). Although this vertical zonation in carbon content, low-temperature serpentine may be a coincidence or may be related in some way to the change in host rock lithology from dunite to harzburgite at 160 m depth, we hypothesize that these trends indicate substantial alteration occurred in a low-temperature, near-surface weathering environment.

We can use the results of prior work and the downhole data on water composition collected in Hole BT1B during March 2018 (Figs. F37, F38; Pezard et al., pers. comm.) to further evaluate this hypothesis. Oxygen fugacity in borehole waters, determined from Eh and pH data, declines from values at 10 m depth that are almost as high as in typical surface waters to values ~10^{-85} bars deeper than 30 m, as predicted from thermodynamic calculations for reaction of water with peridotite (e.g., Frost, 1985; Bruni et al., 2002). Metal and sulfide occurrences in serpentinites worldwide also correspond to oxygen fugacities less than ~10^{-60} bars (e.g., de Obeso et al., 2020, and references therein).

pH increases from ~6 to 9 in the upper 30 m of Hole BA1B and then the gradient shallows, increasing to 10.8 at ~140 m depth. As a result of the well-known negative dependence of $CaCO_3$ (calcite, aragonite) solubility with pH, groundwater descending through subsurface pore space near Hole BA1B would crystallize virtually all dissolved $CaCO_3$ along this pH gradient. Figure F39 illustrates that the frequency of calcite veins shows a strong negative correlation with pH in present-day borehole waters in Hole BA1B.

Temperature in borehole waters in Hole BA1B increases downhole by ~10°C over 400 m. $CaCO_3$ solubility in water has a negative temperature dependence, so increasing temperature could have played a role in precipitation of calcite from downward migrating fluids in the area. However, the temperature increase of ~2.5°C in the upper 100 m of the hole would only cause a ~5% decrease in solubility, which is small compared to the ~75% decrease in solubility between pH 9.2 and 10.6 over the same depth range.

It remains to be seen whether these observations are indicative of ongoing carbonate precipitation and oxidative weathering in the upper 100 m of serpentinized peridotite near Site BA1 or are, instead, the result of buffering of fluids in the peridotite aquifer to compositions in equilibrium with older alteration assemblages.

Calcium mobility

The widespread occurrence of xonotlite-bearing veins extending into peridotite from gabbroic dikes is also noteworthy. It suggests that buffering of fluid compositions occurred on the scale of typical dikes in Hole BA1B during formation of these veins. Gabbroic dikes are much more abundant in Hole BA1B than in most of the Oman mantle section. Mobility of readily available Ca^{2+} from these dikes may explain why the carbonate minerals in core from Hole BA1B are dominated by calcite, whereas dolomite and magnesite are typical of carbonate veins in Samail ophiolite peridotite (e.g., Kelemen et al., 2011).

Structural geology: Hole BA1B

A vertical section drilled in Hole BA1B in the midst of the mantle sequence of the Wadi Tayin Massif (Samail ophiolite) yielded 401.07 m of core. We present the results from core descriptions and thin section observations performed on the *Chikyu* and based on a structural scheme defined and detailed in **Structural geology** in the **Methods** chapter. Following, we report macro- and microstructural observations and measurements of magmatic structures and brittle and plastic deformation. All dips are measured relative to the core reference frame (CRF); consequently, the measurements are reported in a reference frame that is rotated ~30° compared to the mantle reference frame of the Oman ophiolite (the Mohorovicic Discontinuity [Moho] dips 30° south-southeast at this locality; see Figure **F3** in the **Introduction to Science Theme 3** chapter. All the apparent dips of magmatic contacts, peridotite foliation, veins (magmatic and alteration), fractures, and faults were measured when possible and plotted.

Lithologic contacts

Hole BA1B is mainly composed of harzburgite and dunite crosscut by numerous dikes or magmatic veins of pyroxenite, gabbro and olivine gabbro, anorthosite, wehrlite (mainly occurring in the harzburgite), and partially to completely rodingitized gabbroic rock. We recovered a large number of primary magmatic contacts between gabbroic dikes and the host peridotite (see also **Background description: Hole BA1B**; Fig. **F40**); we measured these where possible (i.e., 761 orientations of the contact surface and 685 thicknesses between the top and the bottom of the contacts). We also measured 28 magmatic contacts between the harzburgite and dunite. The contact between the main dunite section and the harzburgite section occurs at ~161.85 m, just at the top of a major fault zone (Sections 61Z-4 through 62Z-2; see **Brittle structures**). Other logged lithologic contacts are mainly minor patches and/or lenses in the harzburgite. Magmatic boundaries vary from sharp to transitional type and from straight to irregular; the true dip angle of the contacts is variable downhole, mostly discordant to the porphyroclastic fabric in the harzburgite (Fig. **F40**). Magmatic contacts are often characterized by alteration halos and are crosscut by veins or reworked as tectonic contacts. In places the halos hinder the primary contact and make it difficult to distinguish between the magmatic and the metasomatic contact with the host rock. Throughout the core the dikes and veins are typically partially to completely serpentinized or rodingitized.

Harzburgite/dunite contacts

The main contact between the dunite section and the harzburgite section occurs at 161.85 m (Section 61Z-4) in correspondence with a fault zone (see **Brittle structures**). A gabbro dike occurs at the bottom of the fault zone within the harzburgite, and the number of gabbroic dikes increases downhole within the harzburgite (almost 300 dikes were recovered at 163–250 m depth). Other contacts between harzburgite intervals in the upper dunite section and dunite intercalations in the harzburgitic section are mostly irregular and gradational, with the gradation occurring over ~1–4 cm. These irregular and gradational contacts are often curved and are typically difficult to measure. The 28 measured contacts between the dunite and the harzburgite show variable dips from nearly horizontal to highly inclined (Figs. **F41**, **F42**). The dunite bodies in the harzburgite show contacts with dip angles that range from 3°–6° to 70° (maximum = 40°–50°).

Gabbroic dikes and contacts with the host peridotite

In the Hole BA1B cores, 929 magmatic dikes were recovered by the background team and 761 of them were measured by the structural team (dips and thickness; see **Supplementary material** > **E_Tabulated VCD data**; Figs. **F40**, **F41**, **F42**). These include gabbro (270) and rodingitized gabbro (5), olivine gabbro (120), pyroxenite (298), anorthosite (8), and wehrlite (60) (even if their mineralogical composition is remarkably variable and not always easy to check on the cores). Figures **F41**, **F42**, and **F43** show the calculated dip angles and thicknesses of the dikes that are distinguished according to the classification discussed in **Background description: Hole BA1B**.

Magmatic layering in wider dikes is compositional or defined by variations of mineral grain size. In places the layering is discordant to the contact of the gabbro with the host rock (Section 43Z-1) or the gabbroic body seems discontinuous or patchy (e.g., interval 58Z-3, 20–30 cm); this could be interpreted as impregnation of gabbroic melts rather than an injection-like vein or dike but could be also affected by secondary mineral alteration. These features need more detailed investigation in thin section.

Pyroxenite dikes

Pyroxenite dikes or dikelets (including ortho- and clinopyroxenite) occur throughout the hole and are more frequent in the harzburgite section (161.8–401.7 m), mostly concentrated at the top of the unit (161.8–228.2 m). The uppermost recovered dike is located at 0.99 m top depth in Section 1Z-2, and the deepest occurs at 399 m in Section 142Z-1. The thickness of the dikes in the harzburgite ranges 0.4–12 cm, but the majority are 1–3 cm; the thicknesses apparently increase downhole from ~160 to 200 m and then decrease. In the dunite sequence (0–161.8 m), pyroxenite dikes are less frequent and thinner (>1–5 cm), with the exception of one 6.7 cm dike at 144.3 m top depth (Section 56Z-2). The dikes show sharp and straight contacts when their grain size is <1 mm; however, when coarse grained, they have mostly irregular contacts. Dip angle of pyroxenite dikes ranges from 0° to steeply dipping (maximum = 20°–30°) (Figs. **F41**, **F42**); nearly horizontal pyroxenite dikes occur mostly at 200–270 m depth. The orientation of pyroxenite in the core is usually discordant with respect to the peridotite foliation. One folded pyroxenite dike was recovered from interval 66Z-2, 43–83 cm (Fig. **F44**).

Gabbro dikes

The intrusive contacts of gabbro dikes and dikelets (including rodingitized gabbro) are mostly sharp and planar; occasionally they have an irregular top contact and a sharper bottom contact (Fig. **F40**). Gabbroic dikes occur throughout the recovered cores with the uppermost occurrence at 0.77 m (Section 1Z-1); thicknesses range 0.4–3.1 cm (Fig. **F43**). The widest logged dike (45 cm) is at 50 m (Section 24Z-4; Fig. **F43**). In the dunite sequence (0–161.8 m), the gabbroic dikes are generally thinner (>1–5 cm) except for the shallower part of the section (5.9–12.9 m) and near the contact with the harzburgite lens (74–77 m) (Sections 32Z-4 through 33Z-4), where thicknesses are up to 20 cm (Fig. **F43**). The harzburgite sequence (161.8–401.7 m; Fig. **F43**) has more dikes, most concentrated at the top of the sequence (161.8–233.4 m). The dikes at the top of the sequence are also generally larger (0–12 cm, with two big dikes of 27 and 22.5 cm) than those in the bottom part (0–7 cm, with two big dikes of 16.5 and 16.3 cm) (Fig. **F43**).

The dip angle ranges 0°–70° (maximum = 30°–50°) (Figs. **F41**, **F42**). The dip distribution with depth downhole is relatively homogeneous.

Olivine gabbro dikes

Olivine gabbroic dikes or dikelets occur frequently throughout the core (Fig. **F43**), and thicknesses range 0.4–40 cm, the majority 0.5–10 cm; the thicknesses increase with depth between ~200 and 250 m and then decrease to the bottom of the hole. The uppermost reported dike is 5 cm thick and is located at 36 m top depth. The largest reported dike at 297 m top depth measures 14 cm in thickness (Fig. **F43**). The frequency of olivine gabbro apparently slightly increases with depth from the top of the harzburgitic section. Similarly, the dip angle of the contacts increases from 200 to ~300 m and ranges 10°–60° (maximum = 30°–40°) (Figs. **F41**, **F42**). In the dunite sequence (0–161.8 m) the olivine gabbro dikes are concentrated in 3 intervals (~50, 100, and 130 m depth) with variable dip angles.

In the harzburgite sequence (161.8–401.7 m), more dikes are situated mostly throughout the upper and middle parts of the unit (161.8–359 m) with 6 particularly large dikes (Fig. **F43**). Olivine gabbro dikes again occur in 3 main depth intervals (171–185, 208–356, and 378–400 m). In the uppermost interval (171–185 m) the olivine gabbro dikes are mostly thin (0.8–3.4 cm) and have a dip angle of 10°–49° (Figs. **F41**, **F42**). In the second interval (208–356 m) the olivine gabbroic dikes vary in thickness, with a maximum of 14 cm at 297 m (Fig. **F43**) and dip angles ranging 5°–61° except for two steeply dipping dikes at 309 m (70°) and 318 m (83°) (Figs. **F41**, **F42**). In the lowest interval (378–400 m) the olivine gabbroic dikes are again typically very small (1–1.9 cm) with dip angles 25°–38° and one at 83° at 318 m (Section 114Z-1) (Figs. **F41**, **F42**).

Wehrlitic and anorthositic dikes

Orientation and thickness of 60 wehrlitic dikes were measured; all of them occur in the harzburgite section. Their distribution downhole is homogeneous throughout the sequence. Dip angles range 10°–79° (maximum = 30°–40°) (Figs. **F41**, **F42**). Few anorthositic dikes were recovered, and only 8 dips were measured because of the irregular form of the contacts. Dips vary from subhorizontal to subvertical.

Peridotite fabric

In Hole BA1B the relatively high degree of alteration of the harzburgite and dunite makes recognition of crystal-plastic deformation difficult at the macroscopic scale. Deformation recorded in the harzburgite is easier to characterize than in the dunite because of the elongation of orthopyroxene and the preferred orientation of spinel grains. Crystal-plastic fabric was defined by the geometry of pyroxene porphyroclasts. However, in some intervals orthopyroxene pseudomorphs show subrounded shape or form aggregates affected by the intense serpentinization, making it difficult to discern their original fabric. Most harzburgites in the shallower part of the hole (e.g., 170.7–260.7 m; Sections 65Z-1 through 94Z-4) (Fig. **F44**) show porphyroclastic texture with slightly elongated orthopyroxene. The degree of deformation increases in the deeper part of the harzburgite sequence (e.g., 260.7–353.8 m; Sections 95Z-1 through 125Z-4) (Fig. **F45**). Harzburgites gradually exhibit strongly foliated to protomylonitic texture. In the interval 126.6–170.7 m (Sections 50Z-1 through 64Z-4) harzburgites are undeformed to moderately foliated and show dominantly porphyroclastic texture. Harzburgites in the interval 170.7–215.6 m (Sections 65Z-1 through 79Z-4) show slightly to moderately foliated, partly protomylonitic texture. Figure **F44E** (TS Sample 65Z-1, 46–48 cm) shows slightly elongated porphyroclastic pyroxene. In the interval between Sections 80Z-1 and 94Z-4 (215.7–260.7 m), porphyroclastic to protomylonitic textures are exhibited by moderately elongated orthopyroxene. In the interval 260.7–305.8 m (Sections 95Z-1 through 109Z-4), harzburgites contain moderately to strongly elongated orthopyroxene grains defining foliation and showing strongly foliated to protomylonitic fabric (Fig. **F44**; TS Sample 102Z-2, 39–41 cm). The interval 305.8–401.2 m (Sections 110Z-1 through 142Z-4) shows a tendency of decreasing degree of deformation with harzburgites mostly exhibiting a strongly foliated texture. Dip angles of measured foliations range from nearly horizontal to 30°–40° (maximum = 1°–10°). Figure **F44** shows one folded pyroxenite dike at interval 66Z-2, 43–83 cm, with a shallowly dipping axial plane lined by peridotite foliation.

Crystal-plastic/semibrittle deformation and microstructures

In Hole BA1B, a few subsolidus examples of crystal-plastic fabrics were observed in cores at the macroscopic scale. Ubiquitous serpentinization and alteration of the deformed zones hinders recognition of higher temperature deformation in the cores. That being said, inspection of thin sections revealed that in general deformation is dominantly semibrittle to brittle in nature (see TS Sample 35Z-4, 76–79 cm). Throughout the hole are several generally narrow (millimeter to centimeter scale) domains with incipient crystal-plastic deformation and/or low-temperature (i.e., subgreenschist to low-greenschist facies conditions) semibrittle deformation mainly located at the boundary of gabbroic dikes or serpentine veins. Gabbroic dikes in the whole mantle sequence seem to have localized the brittle-plastic and brittle deformation, and consequently they were the loci for intense fluid circulation (see Fig. **F46**). Gabbroic dikes are often characterized by sheared or fractured/veined contacts and rimmed by altered halos.

In thin section, crystal-plastic fabric and dynamic recrystallization were observed mainly at the boundary of the dikes but also within a single dike; see intervals 35Z-3, 19–36 cm (Fig. **F47**), 45Z-2, 52–55 cm, 70Z-1, 9–12 cm, and 73Z-2, 36–50 cm (Fig. **F48**).

In interval 35Z-3, 19–36 cm, a shear zone affects a ~5 cm wide whitish to light green rodingitized gabbroic dike (Fig. **F47**). The shear zone shows nicely how strain is partitioned within the dike. The internal fabric of the dike is characterized by millimeter-scale levels of low-grade mylonite, cataclasite, and ultramylonite/ultracataclasite (the ultrafine grain size of the minerals makes the distinction uncertain at the scale of the optical microscope) mainly composed of diopside; the intensity of deformation increases moving from the contact to the center of the dike. Larger diopside grains show strong shape-preferred orientation (SPO) and crystal-preferred orientation with evidence of syntectonic crystallization and plastic plus brittle deformation. These observations point to evolution from fluid-assisted mylonitization to deformation dominated by cataclastic and granular flow.

In interval 78Z-3, 4–16 cm, a 1–2 cm thick gabbroic dike is mostly completely replaced by secondary minerals (such as amphibole and chlorite) and intensely sheared; it shows mylonitic to cataclastic texture cut by veinlets of serpentine and very low grade secondary minerals (Fig. **F49**); its contacts with the host peridotite show evidence of repeated crack and seal episodes (Fig. **F49D**) associated with alteration of the wall rock minerals (Fig. **F49F**).

At the core scale, partially to completely rodingitized gabbroic dikelets (1–2 cm wide) show irregular contacts and shapes associated with complex flow structures. At the microscopic scale, these dikes are characterized by cataclastic flow with associated plastic deformation in secondary minerals (i.e., chlorite, likely prehnite, and phlogopite) (e.g., intervals 73Z-2, 36–50 cm [Fig. **F49**], and 78Z-3, 4–16 cm [Fig. **F48**]).

In thin sections from coarser grained gabbroic dikes, primary magmatic pyroxenes (e.g., TS Samples 34Z-4, 14–17 cm, and 133Z-1, 23–26 cm) show evidence of incipient crystal-plastic deformation and/or semibrittle deformation (e.g., deformation bands, kinking, bending, and subgrain rotation). However, crystal-plastic deformation and dynamic recrystallization affect mostly secondary minerals such as diopside, amphiboles, Na plagioclase, chlorite, and serpentine. TS Sample 73Z-2, 37–41 cm, shows large plagioclase grains with undulose extinction, deformation lamellae and bands, subgrain rotation, and formation of new grains along their boundaries. In Figure F48 large plagioclase grains show trails of new small grains associated with an amphibole-bearing veinlet (Fig. F48E, F48F) and to phlogopite (Fig. F48G, F48H) blastesis, testifying to fluid-assisted deformation.

Thin section Sample 133Z-1, 23–26 cm, from a centimeter vein in the harzburgite, shows relics of primary pyroxene and olivine with evidence of high-temperature dynamic recrystallization and deformation (new grains, subgrain rotation, symplectitic coronas, sygma-porphyroclasts) partially masked by recrystallization of secondary lower grade minerals (amphiboles, chlorite, prehnite).

Deformation in serpentine minerals seems to be strictly related to the different types of serpentine and to their habit (e.g., fibrous vs. platy habit) or grain size. In places, serpentine minerals show bending and undulatory extinction. Mesh textures after harzburgite show SPO often following the elongated shape of the pyroxenes.

A strongly foliated cohesive serpentinitic cataclasite was recorded at the dunite/harzburgite main boundary at 160–163 m (Section 62Z-1). The foliation is characterized by millimeter-scale levels of serpentine interlayered with minor amphibole-rich levels (probably derived from strongly deformed gabbroic veins). Serpentine minerals show mostly brittle deformation but also relics with plastic deformation.

Brittle deformation

Brittle structures

Deformation zones and features occur throughout Hole BA1B but vary in terms of form, abundance, and intensity. The majority of deformation is brittle in character and is mostly accommodated by cataclastic zones, shear veins, and several fault zones (Fig. F50). Semibrittle deformation is observed in places, particularly in intervals in fault zones where fine-grained cataclastic rock has deformed by granular flow (e.g., interval 45Z-1, 10–19 cm). In addition, crystal-plastic shear zones were observed especially throughout the lower part of the hole, predominantly localized within and at the boundaries of gabbroic dikes. The orientations (in the CRF), damage zone thickness, intensity, and downhole distribution of deformation structures in Hole BA1B were logged, and the fracture and vein density was assessed in 10 cm intervals throughout the core. In total, 527 brittle features or zones were logged, not including veins and vein sets that were not interpreted to have accommodated shear. These data are summarized in Figure F51, which shows the damage zone thickness of each structure (Fig. F51B) along with intensity (Fig. F51C), multiplication of these two parameters to give an estimate of relative importance (Fig. F51D), and a plot of the fracture/vein density against depth (Fig. F51E). A lithologic log of the hole is also given for correlation with fault zones indicated (Fig. F51A). In Figure F51D, the widest highly deformed zones form large peaks, whereas individual shear veins or joints form the background. The major fault zone at 160 m is clearly defined as the most important deformation feature in the hole and corresponds to the boundary between the upper dunitic sequence and the lower harzburgitic sequence. The upper 30 m of the hole was characterized by surface-related damage in which true brittle features such as faults were difficult to distinguish and true thicknesses or orientations could sometimes not be measured. However, some features within this zone did have the characteristics of fault zones and other deformation structures, and these data are recorded in the log. Dip angle vs. depth of all deformation structures is shown in Figures F52 and F53. In general, little if any correlation was observed between dip angle and the depth of each type of structure.

Fault zones

Fault zones are present in both the dunite and harzburgite sequences of Hole BA1B. Fault zones were logged where significant fracturing or brittle damage was present within a definable zone that also displayed planar fabric or some clear indicator of displacement and/or accommodation of strain. Many similar regions were logged as cataclastic zones where the fracturing did not possess a clear planar fabric or where the presence of significant displacement was uncertain. Most fault zones consisted of multiple types of fractures and grades of cataclasis or brecciation but were logged as single zones unless clear and unequivocal crosscutting relationships were observed.

The key major fault zone in the sequence of Hole BA1B along which a large amount of strain is inferred to have been accommodated is located at the boundary between the dunite and harzburgite at 160–163 m depth (Fig. F54). The fault zone is ~3 m wide, dips at ~53°, and appears to have a normal shear sense, although this inference is tentative and based on only one kinematic indicator located at the base of the fault damage zone. The upper half of the fault zone is composed of a highly fractured, poorly cohesive cataclastic section at ~160–161.5 m (Fig. F54C). Below this the fault becomes more cohesive and may contain an element of semibrittle or even crystal-plastic deformation (Fig. F54D). The base of the fault zone is marked by a gabbroic dike that displays protomylonitic texture (Fig. F54E). Throughout its thickness the fault zone comprises multiple anastomosing and mutually crosscutting shear planes, suggesting significant accommodation of strain.

The distribution of other, smaller fault zones throughout the hole is characterized by three discrete groupings. In the upper 32 m, 15 fault zones were logged; however, much of this region was dominated by surface-related deformation and damage, resulting in a significant amount of incohesive material in which individual fault zones were difficult to distinguish and measurements of orientation or damage zone thickness could not be reliably obtained (Fig. **F54B**). At 50–160 m several fault zones occur in the dunitic sequence. This corresponds with the region of highest fracture and vein density throughout the hole and culminates with the major fault zone already discussed. Immediately below the major fault zone in the upper part of the harzburgite unit is a distinct lack of smaller fault zones and lower intensity of deformation features in general. In contrast, the lower ~60 m of the hole contains 11 fault zones that vary in thickness from 35 to 4 cm and typically display elements of both brittle and plastic deformation (Fig. **F54F**).

Shear veins and slickenlines

Shear veins were the most abundant deformation feature in Hole BA1B, with a total of 252 logged. This reflects the fact that veins are present in large quantities throughout the hole and that many also serve as deformation features. Shear veins could be distinguished from regular veins by the presence of mineral lineations and polishing on exposed surfaces or by the apparent displacement of another vein or dike. Shear veins are also generally straighter with more planar features than other veins that may have a branching or wavy morphology; however, they were sometimes observed to be anastomosing or splayed (Fig. **F55**). While abundant, shear veins typically are low-intensity deformation features with a mean apparent offset of 1.9 cm in the cases where a measurable offset was present. It should be noted however that large displacements are not observable in drill core and that in almost three quarters of the cases no apparent offset could be measured. Despite the apparently small amount of deformation associated with shear veins, they are ubiquitous throughout the hole and as such become an important deformation feature between 163 and ~300 m, where fault zones and other fractures are less common. Shear veins occasionally contain clear lineations or slickenlines on exposed surfaces that were measured to yield information on the shear sense of that plane. The majority of measured lineations had a plunge of <30° suggesting broadly strike-slip motion on the planes concerned (Fig. **F56**).

Shear zones

Shear zones were logged where zones of predominantly crystal-plastic or semibrittle deformation were observed. Microstructural analysis of these zones reveals that most are associated with granular flow of fine-grained material that is mesoscopically plastic but microscopically brittle; however, in some cases true crystal plasticity was observed (Fig. **F47**). Shear zones in Hole BA1B occurred dominantly along the margins of gabbroic dikes (Fig. **F50A**). In most cases, only one margin, either upper or lower, was deformed, while the other retained an igneous character. Although some of this viscous behavior may relate to intrusion of the dikes, microstructural observations suggest that dynamic recrystallization has occurred in many cases, particularly in the plagioclase and pyroxene phases of gabbroic dikes (Fig. **F48**).

Cataclastic zones

Cataclastic zones occur throughout Hole BA1B and vary in character from narrow fracture networks to large sections of highly fractured and damaged material (Fig. **F50D, F50E**). They are ubiquitous throughout the core but are most prevalent in the dunite sequence. The damage zone thickness of cataclastic zones ranges 90–1 cm (mean = 5.2 cm). Complicated zones of cohesive fracture and vein networks were also logged as cataclastic zones (Fig. **F50B, F50C**). These regions were highly altered with few if any straight, planar features and consisted of large clasts (centimeter scale) broken up by extensive veining and alteration. The origin of these zones is unclear, but they appear to be related to in situ cataclasis of the host rock and so were logged in this category.

Joints

Joints were logged in Hole BA1B where fractures were observed with no observable mineral vein fill. They are relatively uncommon in the core for two main reasons: (1) most open fractures within the Hole BA1B sequence occur in the form of veins with precipitation of serpentine, carbonate, or other minerals within fractures, and (2) it is challenging to correctly differentiate true joints from the drilling-induced fractures common in some sections of core. Although these are typically horizontal in orientation, they can also follow preexisting lines of weakness and open fractures that did not exist in the rock before coring. The logged joints were typically 1 or 2 mm wide and show a slight tendency toward an increase in dip angle with depth.

Orientations of alteration veins

In Hole BA1B, orientations of alteration veins were measured in the upper 162 m, 583 veins mostly hosted in dunite and 610 veins in the harzburgite-dominated interval (162–403 m). Individual veins, vein sets, and vein networks were defined, located, and described by the vein alteration team (see **Veins: Hole BA1B**). As defined by the vein alteration team, veins are grouped into carbonate-serpentine veins (type Ca) and carbonate veins (type Cb) (Fig. **F57B**), and different serpentine vein generations are based on their color and texture (types Sa, Sb, Sc, Sd, Se, and Sf) (Fig. F31); see Macroscopic identification of vein types). Crosscutting relationships between the different vein types are often ambiguous, but generally black serpentine veins (Sa) appear to be the oldest and waxy green serpentine (Sb) and carbonate(-bearing) veins (Ca, Cb) the youngest generations (see Veins: Hole BA1B). Orientation measurements are given in the same data set as that used by the vein team as true dip and apparent dip azimuth in the CRF. Because of high vein densities (Fig. F26; see Veins: Hole BA1B), measurements were limited to orientations of single veins and representative orientations in systematic vein sets. For conjugate vein sets of the same vein type (e.g., Fig. F57D), we measured two or three predominant orientations where well defined. Chaotic, strongly branching, or anastomosing vein networks, polygonal (e.g., "turtle-textured"; see Veins: Hole BA1B) networks, and veins that do not crosscut the core surfaces (e.g., ladder crack/"Frankenstein" vein sets of type Sb; see Veins: Hole BA1B) were not measured.

Dips are highly variable for all vein types and generally become slightly steeper with depth (Fig. F57). Between 200 and 300 m depth, serpentine veins with dips <30° are rare (Fig. F57). No major fault zones are recorded in this depth interval (Fig. F54), in contrast to shallower and deeper levels where fault zones and shallow-dipping veins are more common. Dip distributions of carbonate(-bearing) veins and selected well-defined serpentine vein generations are illustrated in rose diagrams (circular histogram plots) for the dunite- and harzburgite-dominated intervals (Fig. F58). Rose diagrams and their mean vectors are calculated using vein density (values 1–5 as defined by the vein alteration team; see Vein structure and petrology in the **Methods** chapter) as a weighting factor to account for different statistical relevance of single veins and high-density vein sets where only a single representative measurement was taken. Carbonate-bearing serpentine veins (Ca) and carbonate veins (Cb) in the upper 100 m predominantly have dips 10°–55° (mean = 38°) (Fig. F58). Their dip angles are slightly shallower than a random normal distribution (mean angle = 45°) and substantially shallower than most serpentine veins. Serpentine veins predominantly dip 50°–60° in the upper 162 m of Hole BA1B and 60°–70° between 162 and 403 m (Fig. F58). Black serpentine veins (type Sa) show generally relatively steep dips in both depth intervals with no obvious differences between dunitic and harzburgitic units (Fig. F58). Below 300 m depth, Sa serpentine veins are occasionally associated with white, antithetic riedel veins indicating a normal sense of shear (Fig. F57C). There are minor differences in dips of serpentine vein types Sb, Sc, Sd, and Sf between the upper dunite and lower harzburgite units (see mean vectors reported in Fig. F58), but these may in part be due to better identification of conjugate sets further downhole. Dip angles of waxy green (Sb) and white (Sf) serpentine vein generations are generally more variable than those of serpentine veins of types Sa, Sd, and Se and show bimodal distributions with one shallower dipping set related to the presence of conjugate vein sets (Figs. F58, F57D). Similar conjugate vein sets of early Sa veins are also occasionally evident (Fig. F57E) but are not obvious in the rose diagrams, possibly due to difficulties in their identification.

Summary

The cores of Hole BA1B are mainly composed of dunite and harzburgite with minor pyroxenite cut by gabbroic dikes or veins. The abundance of gabbroic dikes described (>700) in Hole BA1B is a quite unique feature for the Samail ophiolite peridotite. The peridotites are extensively serpentinized throughout the hole, and alteration is dominated by serpentine and magnetite forming typical serpentine mesh textures. The dikes/veins are mostly affected by hydrothermal alteration with crystallization of secondary Ca-rich silicate and hydrous mineral phases (e.g., hydrogarnet, diopside, amphibole, chlorite, xonotlite). The majority of the observed deformation is brittle in character and is mostly accommodated by shear veins, cataclastic zones, and fault zones. Syntectonic shear veins with fibers and slickenfibers (mostly composed of serpentine) were the most abundant (~252) recovered deformation feature in the Hole BA1B cores. Semibrittle deformation is observed in places, particularly in intervals within fault zones and within or at the boundaries of gabbroic dikes. Below are summarized some of the main outcomes from the structural logging.

- One major fault zone in the Hole BA1B sequence was located at the boundary between the dunite and harzburgite at 160–163 m, along which a large amount of strain is inferred to have been accommodated.
- Other minor discrete fault zones were located and grouped in three major intervals downhole: the upper 32 m, 50–160 m in the dunite, and in the deeper part of the hole (lowermost ~60 m) in the harzburgite. Calculated dip angles for the fault zones show a maximum dip of 50°–60°, the same for the shear veins and slickenfibers. Faults and shear veins record mostly oblique and dip-slip movement. Reverse and normal sense of shear are equally represented (i.e., 57 normal, 44 reverse).
- The gabbroic dikes seem to play an important role in localizing deformation and fluid circulation during the evolution of the peridotites recovered from Hole BA1B. Gabbroic dikes or layers are often characterized by sheared or fractured/veined contacts, protomylonitic texture, intense micro-

fracturing within those that are coarser grained, and they are mostly rimmed by alteration halos. Sheared and veined contacts show repeated episodes of crack and seal and/or slip, testifying to multiple phases of fluid infiltrations and fluid-rock interaction accompanied by episodes of deformation at different temperatures. Moreover, the formation of syntectonic secondary minerals (such as diopside, amphibole, phlogopite, albite, likely prehnite, and garnet) along the margins or within the dike strongly influenced the type of active deformation mechanisms. For the above reasons, the 400 m continuous section of peridotite with gabbro dikes recovered in Hole BA1B represents a rare opportunity to investigate crosscutting relationships between different episodes of deformation and fluid-rock interaction in different temperature ranges.

- In Hole BA1B a wide range of alteration veins was recovered (see **Veins: Hole BA1B**) and grouped into carbonate-serpentine veins, carbonate veins, and a range of serpentine vein generations with different colors and textures. The measured alteration veins (583 veins measured in the upper 162 m, mostly in dunite, and 610 veins in the harzburgite at 162–403 m) show a wide range of dip angles, but generally they become slightly steeper with depth. At 200–300 m, serpentine veins with dips <30° are rare. Carbonate-bearing veins in the upper 100 m predominantly dip 10°–55° (mean = 39°). These dip angles are slightly shallower than a random normal distribution (mean angle = 45°) and substantially shallower than most serpentine veins.
- As concerns plastic deformation, examples of crystal-plastic deformation and dynamic recrystallization were recovered, mostly in orthopyroxene in harzburgite; plagioclase, diopside, amphiboles, and phlogopite in gabbro; and serpentine along damage zones. This testifies to a range of episodes of deformation occurring at different temperatures during the tectonic evolution of the Oman ophiolite peridotite.

The harzburgite, even if serpentinized, exhibits relics of orthopyroxene forming a range of textures from weakly foliated porphyroclastic to protomylonitic. The degree of deformation seems to increase in the deeper part of the hole (e.g., 260.7–353.8 m). Dip angles of measured foliations range from nearly horizontal to 30°–40°. One folded pyroxenite dike with a shallowly dipping axial plane lined by peridotite foliation represents an important record to unravel the mantle deformation history of the harzburgite.

Geochemistry: Hole BA1B

Whole-rock chemical compositions were determined on 82 samples collected from Hole BA1B (Tables **T7**, **T8**). A total of 38 samples were selected by the shipboard science party as representative of the different lithologies recovered from Hole BA1B, and 44 samples were collected on site every 10 m during drilling operations and then powdered and analyzed at the University of Southampton (see **Geochemistry** in the **Methods** chapter). All onsite samples and most shipboard samples have a thin section taken adjacent to the sample. In addition, XRD analyses were made on all the whole-rock powders for detailed mineral characterization.

The shallowest cores (<10 m) of Hole BA1B are highly altered and more fractured than the deeper core (see **Background description: Hole BA1B**, **Veins: Hole BA1B**, and **Structural geology: Hole BA1B**). In the upper 160 m of core, dunite is the dominant lithology with subordinate harzburgite and crosscutting gabbro dikes. At 160–400 m, the base of the core, harzburgite is dominant and is cut by dunite and gabbro dikes. The geochemistry samples are divided by lithology: 38 harzburgites, 22 dunites, 20 gabbros, and 2 pyroxenites. Pyroxenites occur as dikes.

Loss on ignition, H_2O, and CO_2 contents

The recovered samples from Hole BA1B display variable loss on ignition (LOI) values: 3.14–16.03 wt% (average ~ 11.93 wt%) (Fig. **F59**). LOI variability in Hole BA1B is correlated with lithology and depth of the recovered samples. Dunites (principally shallower than 160 m) were quite varied, containing 6.56–16.03 wt% water, but the vast majority were very close to the average of 14.31 wt% (standard deviation = 2.00). The harzburgites (161.87–401.94 m depth) vary over a narrower range: 10.56–14.57 wt%, with the majority remaining near 12.61 wt% (standard deviation = 0.79). The gabbro sampled from dikes throughout the hole have the lowest average value for LOI at 8.27 wt% but a large range (3.14–13.61 wt%). Harzburgites show a general decrease in LOI downhole from ~14 to 12 wt%. Gabbros and dunites show no discernible correlation of LOI with depth. The highest water concentration on average (15.1 wt%) and on a per sample basis was found in dunitic rocks. The LOI range of dunites is similar to that from Wadi Tayin, but in the harzburgites the LOI range is higher than that from Wadi Tayin and Maqsad (Godard et al., 2000; Hanghøy et al., 2010).

Correlation between LOI and H_2O (determined by elemental analysis [EA]) shows that degree of hydration controls LOI values (Fig. **F60A**) with slight but consistent overestimation (~0.5 wt%) of H_2O for a given LOI. This may be due to LOI underestimation associated with oxidation of Fe(II) to Fe(III) during ignition of powders. A correction factor was calculated as follows:

$$Fe_{(III)LOI} = Fe_{(III)}O - Fe_{(III)}O \times 1.11. \qquad (1)$$

The sum of this and LOI plot on a 1:1 line with H_2O with the exception of high-LOI samples (Fig. F60C). All Hole BA1B core samples are highly serpentinized (50%–90%) and have thus been exposed to some degree of hydrous fluid. XRD data clearly show hydrous minerals including serpentine and brucite and other hydroxides are present in the samples with high LOI.

The average CO_2 concentrations for all lithologies are generally <0.5 wt% with some exceptions in the samples from upper part of the hole (<100 m depth) and in 1 gabbro sample (Fig. F59). CO_2 contents are uncorrelated with LOI and depth (Fig. F60B). The CO_2 contents of convecting mantle are estimated to be ~0.03 wt% (Dasgupta and Hirschmann, 2010), suggesting local carbonatization has occurred throughout the core. The high abundance of carbonate veins observed in the upper unit of the core are probably the origin of the higher CO_2 enrichment seen at <100 m depth. One gabbro sample in the deep part of the hole (342 m) shows high CO_2 concentration with relatively low LOI. XRD analysis shows that serpentine and chlorite are the main mineral phases in this sample, with no carbonates. From the geochemical data, this gabbro dike possibly included some carbonate because of relatively high CaO and $CaCO_3$ concentrations.

Whole-rock major and minor elements

Major element compositions reflect the different lithologic units sampled in the core (Figs. F61, F62). Dunite and harzburgites have similar compositions, characterized by higher Mg# (87.5–91.5) and lower CaO (<2.2 wt%), Al_2O_3 (<2.6 wt%), and TiO_2 (<0.06 wt%) contents than those of the gabbros. The Mg# of the thick dunite above 160 m is generally less than those of dunite dikes in the main harzburgite sequence (>160 m) and also less than those in harzburgite. Dunites generally have higher MgO and Fe_2O_3 and lower SiO_2, Al_2O_3, CaO, and Cr than harzburgite (Fig. F61). Lower SiO_2 in the dunites reflects the lack of modal orthopyroxene ($Mg_2Si_2O_6$).

The dunites of the Dunite Sequence are relatively homogeneous with slightly elevated LOI and Fe_2O_3 and low SiO_2. The three dunites analyzed from the Harzburgite Sequence, however, show significant variation in most major element abundances. They have lower Fe_2O_3 and Al_2O_3 compared to the upper dunites with similar range of MgO and TiO_2; however, XRD analysis shows no difference in mineral compositions between upper dunites and lower dunites (**Supplementary material** > **F3_XRD data**). Dunites display high concentrations of Ni and Co: 1572–2752 ppm Ni (average = 2083 ppm) and 91–131 ppm Co (average = 111 ppm). They also contain variable Cr content: 867–4052 ppm (average = 2113 ppm). These data trace a pattern similar to the dunite data from Holes CM1B and CM2A. The upper dunites have relatively constant Ni composition except the samples taken from the uppermost part. In contrast, deeper dunites have variable Ni concentrations. The major and trace element abundances show variation in the dunite in the lower harzburgite-dominated sequence. V and Sr concentrations are low (<57 ppm and <33 ppm, respectively) and are also quite similar in range to the concentrations measured in dunites from OmanDP Holes CM1B and CM2A.

Compared to the dunites, major element abundances in the harzburgites are relatively homogeneous and decrease little with depth. Average Mg# (cationic Mg/[Mg + Fe]; calculated assuming all Fe as FeO) in the harzburgite samples (Mg# = 91.2) is slightly higher than that in the dunites (Mg# = 89.3). The major element distributions of Hole BA1B harzburgites are quite similar to those of the previous data from Oman ophiolite mantle section (Fig. F61, F62). The trace element abundances in harzburgites are relatively homogeneous compared to those of the dunitic and gabbroic samples. Ni, Co, and Cr concentrations range 2047–2411 ppm Ni (average = 2223 ppm), 72–111 ppm Co (average = 88 ppm), and 1635–3854 ppm Cr (average = 2507 ppm). These elements and other trace element abundances are stable from the top to the bottom of the hole, even in the samples with high LOI (>12 wt%), consistent with harzburgites from Holes CM1B and CM2A (Fig. F62). Most of the large ion lithophile elements (LILE), especially Rb and Ba, exist at concentrations below the detection limit of XRF. Sr concentrations in the harzburgites from Hole BA1B range 7–27 ppm; these values are higher than those from Holes CM1B and CM2A (<10 ppm). Holes CM1B and CM2A are defined as a Crust–Mantle Transition Zone from lower crustal gabbro to uppermost mantle section dunite and harzburgite. If Hole BA1B does indeed represent a mantle section, the aforementioned data imply that the mantle transition zone represented by Holes CM1B and CM2A is more depleted (in Mg# and LILE) than Hole BA1B.

Gabbros occur as dikes in both dunitic and harzburgitic sequences. They display high Mg# values (79.5–91.0) (Fig. F64), and CaO, Al_2O_3, and TiO_2 contents range widely: 1–26 wt% CaO, 0.7–15 wt% Al_2O_3, and 0.02–0.40 wt% TiO_2. Trace element compositions in the gabbros display large ranges: 223–2232 ppm Ni (average = 985 ppm), 28–101 ppm Co (average = 28 ppm), and 513–3121 ppm Cr (average = 1923 ppm). Compared to the gabbros from Holes GT1A and GT2A (Fig. F62), the gabbros from Hole BA1B have higher MgO, Ni, and Cr and lower SiO_2 and Al_2O_3. Fe_2O_3, CaO, and TiO_2 abundances are of similar range to the lower crustal gabbros sampled in Holes GT1A and GT2A (OmanDP Leg 2) but are more scattered in Hole BA1B. The gabbros from Hole BA1B plot closer to the peridotites from Hole BA1B than to gabbros from Holes GT1A and GT2A in most major element abundances (Fig. F62), suggesting they have depleted major element abundances.

Hole BA1B gabbros show constant Ca# (96.1–99.9; average = 99.1) with decreasing Mg# (Fig. F63). Most of the Hole BA1B gabbros show higher Mg# than the gabbros from Holes GT1A and GT2A and do not plot on the crystal fractionation line defined by the GT gabbros (e.g., Figs. F62, F64). One possible explanation is that Hole BA1B gabbros originated from more depleted mantle. This would explain the high Mg# and depleted gabbro composition. However, such a depleted source would likely require some addition of water to produce volumetrically significant volumes of melt. Another more probable hypothesis is that melt-rock interaction occurred when the gabbro intruded into mantle rocks similar to what has been proposed for the formation of olivine-rich troctolites in slow-spread lithosphere (e.g., Godard et al., 2009). Wide variations of the major and trace element abundances also support reactions between gabbroic melts and dunite and/or harzburgite. Most of the gabbros from Hole BA1B appeared as thin dikes in the cores, most less than 20 cm thick. The gabbro dikes generally show sharp contact with wall rock lithologies; however, some dikes show mixing textures and reaction rims are observed between some dikes and surrounding ultramafic rocks (see **Background description: Hole BA1B** and **Structural geology: Hole BA1B**). In addition, TiO_2 abundances in the gabbros negatively correlate with Mg# (Fig. F65A), defining an apparent mixing line between the gabbros from Holes GT1A and GT2A and Hole BA1B peridotites and suggesting varying degrees of interaction between melts and their host peridotites.

Summary

A total of 82 samples from Hole BA1B were analyzed for whole-rock geochemistry during OmanDP Phase 2 Leg 4. Three main lithologies were identified: dunite dominates the upper unit (shallower than 160 m), whereas harzburgite is predominant deeper in the core. Both are intruded by numerous gabbro dikes. All samples were highly serpentinized with the exception of some gabbros. LOI values of Hole BA1B samples display good correlation with H_2O contents, whereas CO_2 concentrations are always <1% indicating that water is the main component of LOI of Hole BA1B samples. Harzburgites show similar major and trace element abundances to those of the surface rocks from previous Oman mantle study. Gabbros show clearly different distribution from lower crustal gabbros drilled in Holes GT1 and GT2. Gabbros from Hole BA1B are more refractory than those from holes drilled at Sites GT1 and GT2, which sampled the lower crustal section of the Oman ophiolite. There are two possibilities. One is that Hole BA1B gabbros originated from a slightly different mantle domain than the mantle transition gabbros. Another possibility is that the gabbros are influenced by reaction with surrounding mantle rocks during emplacement.

Microbiology: Hole BA1B

Microbiology results are discussed in the **Microbiology** chapter.

Paleomagnetism: Hole BA1B

Remanent magnetization

Magnetic remanence measurements were made at the University of Iceland in 2019 on discrete sample cubes taken from the working half cores from Hole BA1B. A total of 134 discrete samples were measured, of which approximately one-quarter (34 samples) were thermally demagnetized while all others were subjected to stepwise alternating field (AF) demagnetization in tumbling mode to isolate the characteristic remanent magnetization (ChRM) direction. Some irregularly shaped and broken samples were omitted from measurements.

Natural remanent magnetization (NRM) intensity values range between 3.4×10^{-5} and 4.3 A/m (geometric mean = 0.16 A/m) (Fig. F66; Table T9). There is no distinct trend of NRM strength with depth; however, NRM orientations transition from mostly small negative inclinations in the upper half of the hole to small positive inclinations in the bottom half (Fig. F67). Principal component analysis (PCA) of demagnetization data was used to identify distinct remanence components.

A stable ChRM that trends to the origin at the highest field and temperature steps was identified in approximately 90% of samples. The majority of ChRM orientations have consistently low-angle negative inclinations, although a few outliers with positive inclinations also occur (Fig. F67). The direction of the ChRM vectors determined by thermal demagnetization and AF demagnetization are very similar overall, indicating that both demagnetization methods isolated the same remanence component. Mean inclinations were calculated using the Arason and Levi (2010) maximum likelihood method (Table T10). This results in a mean inclination for the highest temperature/coercivity component of –12.4° (k = 11.7, $\alpha95$ = 3.9°, n = 122).

An additional component with lower coercivity or unblocking temperatures and a distinct orientation from the ChRM was isolated in ~80% of the samples, here termed the “soft” component. A small proportion of samples contained only a single remanence component. The majority of soft components have orientations with positive inclinations that progressively steepen downhole, mirroring the trend of NRM orientations (Fig. F67). A small number of negatively inclined soft components were identified in the uppermost 100 m of the core. The inclinations of soft components isolated by thermal and AF demagnetization methods are not distinguishable. Several samples demagnetized by both AF and thermal demagnetization exhibited curvature in remanence directions on orthogonal vector diagrams (Figs. F68, F69) due to overlapping coercivity distributions between the ChRM and soft components.

AF demagnetization was effective at removing nearly all remanence in Hole BA1B samples (Fig. F68A). A majority of the samples (three-quarters) were demagnetized to <90% of their NRM intensity by 40 mT (Fig. F68B). Median destructive field (MDF) values range 5.7–99 mT (mean = 19 mT) (Table T9). MDF values are slightly lower in the uppermost 50 m of the hole (Fig. F70).

Thermal demagnetization was complete in most samples by 580°C (Fig. F69A). Distinct decreases in remanence intensity were observed around 200°, 400°, and 500° in some samples, which were associated with distinct remanence component orientations. The highest-unblocking-temperature component exhibited a sharp decrease in remanence occurring close to 580° (Fig. F69B), which was interpreted as the ChRM. Changes in magnetic susceptibility were observed after each heating step during thermal demagnetization. Bulk susceptibilities increased with progressive heating, likely reflecting the production of secondary magnetite due to thermal alteration of the rocks. However, this increase was not associated with changes in remanence vector orientations and is not likely to have affected the directional paleomagnetic results. Median destructive temperatures (MDT) range 170°–578° (mean = 493°C). MDT values increase markedly in the uppermost 50 m of Hole BA1B and remain near 515°C thereafter (Fig. F70). Mineralogical and petrographic analysis of samples in the uppermost 50 m is needed to identify the magnetic mineral phases that carry the lower-temperature remanence components in this interval.

Magnetic susceptibility

Bulk magnetic susceptibility

Volume susceptibility values range between 229 × 10^{-6} and 44,995 × 10^{-6} SI (geometric mean = 5,831 × 10^{-6} SI) (Fig. F66; Table T9). The downhole profile of bulk magnetic susceptibility is similar to that of NRM intensity, suggesting that the variation in both properties with depth is controlled by the concentration of magnetic minerals rather than differences in magnetic grain size and mineralogy.

The Königsberger ratio, *Q*, in Hole BA1B ranges 0.004–27 (geometric mean = 8.7). The majority of samples exhibit *Q* values near or <1 (Fig. F66; Table T9), indicating that induced magnetization contributes more to the total in situ magnetization than remanent magnetization for much of Hole BA1B. There is somewhat less variability in *Q* values in the lower half of the hole (Fig. F66), suggesting greater uniformity in magnetic grain size or mineralogy than in the upper portion.

Anisotropy of magnetic susceptibility

Anisotropy of magnetic susceptibility (AMS) determinations were performed on all discrete samples prior to stepwise demagnetization to characterize the shape-preferred orientations of magnetic minerals in the core samples. Magnetic fabric shapes are highly variable throughout the hole, ranging from strongly oblate (T = 0.97) to strongly prolate (T = –0.83) (Fig. F71A); however, more oblate fabrics are present overall. Samples with a relative high degree of anisotropy (P′ > 1.25) are exclusively oblate (Fig. F71C), defining strong magnetic foliation. Fabric intensity indicated by the P′ parameter is consistently low shallower than ~150 m. Deeper than 150 m, magnetic fabrics are overall stronger and more variable. The degree of anisotropy is only weakly correlated with bulk susceptibility (K_{mean}) (Fig. F71B).

Magnetic fabric orientations are generally inconsistent and do not exhibit any observable trend with depth. K_{min} axes (poles to magnetic foliation) generally dip <60° (mean = 34°) (Fig. F71A). However, contoured stereoplots of AMS principal axis orientations reveal a weak girdle of K_{max} and K_{int} axes that outline poorly defined, moderately dipping magnetic foliation (Fig. F72).

Physical properties: Hole BA1B

Physical properties of ultramafic rocks and gabbroic dikes from Hole BA1B were characterized through a series of measurements on whole-round sections, section halves, section-half pieces, and discrete samples (see **Physical properties** in the **Methods** chapter). All whole-round sections were run through the X-ray computed tomography (XCT) scanner and measured for gamma ray attenuation (GRA) density, magnetic susceptibility (MS), noncontact electrical resistivity (NCR), and natural gamma ray radiation (NGR) on the Whole-Round Multisensor Core Logger (MSCL-W). Whole-round *P*-wave velocity was not measured because of a mechanical issue with the transmitter. We then measured point magnetic susceptibility (MSP) and reflectance spectroscopy and colorimetry (RSC) with the Split Half Multisensor Core Logger (MSCL-C) and recorded line scan color images with the Imaging Multisensor Core Logger (MSCL-I) on the split surface of archive halves. Thermal conductivity was measured on section-half pieces. Compressional wave (*P*-wave) velocity (V_P), electrical resistivity (IMP), and density and porosity (MAD) were measured on discrete minicube samples (20 mm × 20 mm × 20 mm). MAD measurements were also conducted on some irregular shaped discrete samples. The rock names reported in data tables correspond to the primary lithologies described in **Background description: Hole BA1B**.

Whole-round and section half measurements

A total of 548 whole-round and archive-half sections were measured from Cores BA1B-1Z to 142Z. The downhole data plot is shown in Figure **F73** for whole-round measurements. All data are shown in supplemental Tables **ST1** and **ST2**).

X-ray computed tomography (XCT)

XCT was continuously logged for all 548 whole-round core sections recovered from Hole BA1B. The XCT number of minerals is essentially a function of the density and chemical composition of the sample. Hence, XCT numbers in the core sections result from a combination of their mineral composition and pore structure in a voxel (0.625 mm × 0.175 mm × 0.175 mm). Figure **F74** shows examples of XCT images from Sections 18Z-1, 57Z-2, 62Z-1, and 97Z-3. The gabbroic layer, veins, and fractures are visible in these images, and the dip angle can be analyzed using the whole-round image. An XCT image of the archive-half split surface with XCT number represented on a color scale was generated for every section. The average and mode of XCT numbers for every scan slice (0.625 mm thick) were also computed and plotted downhole (Fig. **F73**). Average XCT number is susceptible to the effect of cracks in the core section because the XCT number of air is significantly lower than that of minerals (XCT number of air is about –1000; see **Physical properties** in the **Methods** chapter). On the other hand, mode of XCT numbers tends to reflect a representative lithology in a scan slice, although it overlooks some minor but dense minerals (e.g., Cr-spinel).

In Hole BA1B, dunite and harzburgite have average XCT numbers of ~3000. XCT numbers for ultramafic rocks are lower than gabbroic layers. Harzburgite shows higher XCT numbers than dunite. This reflects either the higher abundance of orthopyroxene in harzburgite or a lower degree of serpentinization in harzburgite compared to dunite.

Because XCT number of a core section depends on mineral composition and porosity, the trends of the average and mode of XCT numbers clearly follow those of GRA density in the downhole plot (Fig. **F73**). All lithologies show a relation between XCT number and GRA density. These correlations can be controlled by several factors such as modal abundances of low-density minerals (e.g., serpentine), abundance of high atomic number elements in minerals (e.g., calcium in diopside, iron in magnetite, and chromium in Cr-spinel), and pore structure. Overall, variability in the XCT number downhole trends reflect the lithologic and structural variations observed in Hole BA1B.

Colorimetry

RSC data were obtained for 548 sections of archive halves, from Core 1Z to 142Z. The "specular component included" (SCI) setting was used for measuring the cores; this setting provides data that are closer to the actual color than does the "specular component excluded" (SCE) setting (see **Physical properties** in the **Methods** chapter). Color data acquired from reflectance spectroscopy and high-resolution images can provide insights into the variability of different lithologic units recovered from Hole BA1B. Lightness (L*) and chromaticity (a* and b*) variables were generated from reflected light collected through the spectrophotometer every 2 cm. High L* values indicate lighter colors, with 0 representing black and 100 white. Directions toward more +a* denotes a shift toward red from green, whereas +b* depicts a shift toward yellow from blue. High-resolution (100 pixels/cm) half-section images produced by the MSCL-I provide an alternative source of 2-D color data. Although a* and b* are nearly constant or gradually change with depth in Hole BA1B, harzburgites show markedly higher L* values compared to dunites. This is most likely due to less hydration and relatively low porosity in harzburgite. Gabbroic intrusions show more or less similar a*, b*, and L* to those observed in previous holes.

Gamma ray attenuation density

GRA density measurements were conducted for the 548 sections at a spacing of 4 cm. Data are summarized in Figure **F73**. The GRA values of the harzburgite-dominated sequence are slightly higher than those of the dunite-dominated sequence. The GRA density of talc and carbonate-bearing dunites are highly scattered at shallow depth. The depth profile of the bulk density obtained from discrete sample measurements seems to closely follow the upper bound of the GRA depth profile. Figure **F75** shows correlation between the GRA density and XCT value. The GRA density is correlated to XCT value with density >2.5 g/cm^3, whereas it is highly scattered with low density, possibly due to relatively high porosity in the samples.

Electrical resistivity

NCR data indicate that the cores from Hole BA1B are relatively resistive (Fig. **F73**). Most readings in these sequences are saturated and equal to the maximum measurable value (~85 Ω·m); therefore, actual averages of NCR for these sections should be higher than shown in Figure F73. Although variation of resistivity is large even in the same lithology, resistivity tends to increase with depth. The resistivity of ultramafic rocks is generally related to hydration (serpentinization) due to formation and connection of magnetite, suggesting less hydration in the deeper portion relative to shallow portion. There is a marked difference between dunite- and harzburgite-dominated sequences, also recognized in magnetic susceptibility as a negative jump (in detail, see **Whole-round magnetic susceptibility** and Half-round magnetic susceptibility (supplemental Table ST2). This could be explained by the difference in modal abundances of conductive phase (i.e., magnetite) and unconductive phase (e.g., fresh olivine and orthopyroxene) in each sequence. We note that NCR is systematically about 20 times lower than the electrical resistivity measured from discrete samples (Figs. F73, F76). This can be due to low accuracy of the NCR measurements for high-resistivity samples because the instrument is designed for measuring resistivity in porous and conductive ocean wet sediments, while the overall characteristics of NCR in the depth profile are quite similar to that of the discrete sample data.

Whole-round magnetic susceptibility

Magnetic susceptibility (MS) of whole-round core sections was measured before splitting using the MSCL-W with a 125 mm loop sensor. Whole-round MS (WRMS) values are shown in downhole plots (Fig. F73). Magnetic susceptibility values are >1000 × 10^{-5} SI for dunite and ~1000 × 10^{-5} SI for harzburgite. There is a large change of MS between dunite- and harzburgite-dominated sequences. Figure F75 shows a correlation between MS and the inverse of NCR (i.e., electrical conductivity) measured at the same depth. MS and inverse NCR show a somewhat linear correlation regardless of lithology.

Natural gamma ray radiation

NGR in Hole BA1B is generally low (Fig. F73). There seems to be no or few correlations with other physical property data and structural observations.

Discrete sample measurements

P-wave velocity

P-wave velocity was measured in Hole BA1B on 150 cube samples along the three principal directions *x*, *y*, and *z* in the CRF (see Tables T11, T12; Fig. F76). *P*-wave velocity is 4.77 ± 0.63 km/s on average in the dunite-dominated sequence and 5.02 ± 0.49 km/s on average in the harzburgite-dominated sequence. Gabbroic layers exhibit higher velocities (maximum = 6.47 km/s). *P*-wave velocity of the dunite-dominated sequence is relatively scattered, possibly due to weathering and relatively large variation in porosity, whereas the harzburgite-dominated sequence shows a systematic increase of velocity with depth, suggesting less serpentinization in the deeper portion (Fig. F76).

P-wave velocity is slightly different in the three orthogonal directions. The magnitude of azimuthal anisotropy (A_v) is calculated from

$$A_V = (V_{max} - V_{min})/V_{mean}, \quad (2)$$

where V_{max} and V_{min} are the maximum and minimum velocities and V_{mean} is the average velocity of the three orthogonal directions (Birch, 1961). The azimuthal anisotropy mostly ranges 2%–7% (Fig. F77). In general, velocity along the *z*-axis is slower than other directions. If the microcracks are a major source of V_P anisotropy, cracks should be oriented normal to the *z*-axis. However, anisotropy is relatively weak in the dunite sequence where cracks are ubiquitous, and relatively high porosity was reported. This means that velocity anisotropy might be caused by crystal fabric, such as that of serpentine, where the basal plane is oriented subparallel to the horizontal plane (see **Veins: Hole BA1B** and **Structural geology: Hole BA1B**).

Density and porosity

Bulk density, grain density, and porosity were calculated from measurements on 152 sample cubes (20 mm × 20 mm × 20 mm) taken from the working-half sections of Hole BA1B, approximately one sample per core and reflecting lithologic and alteration variation (Tables T11, T12; Fig. F76). Average bulk densities of cube samples from Hole BA1B are 2.53 ± 0.06 g/cm³ for dunite and 2.65 ± 0.09 g/cm³ for harzburgite. As in previous holes, the cube samples were mostly taken from relatively homogeneous intervals with fewer or no visible cracks or veins, and some were taken from large veins and vein halos. Noncube irregular shape samples and broken cubes in highly altered or deformed intervals were measured only for density and porosity (Table T12). Note that some samples exhibit extremely high porosity (>10%), possibly due to chips lost during MAD measurements. The highly altered or deformed samples have high porosities (up to 16%) and lower bulk densities (down to 2.42 g/cm³) and grain densities (2.53 g/cm³). Gabbro samples show higher bulk and grain densities (2.74 and 2.87 ± 0.21 g/cm³, respectively) than ultramafic rocks. As shown in Figure F76, discrete samples have lower bulk density in the dunite-dominated sequence and show a gradual increase of bulk density through Hole BA1B, nearly consistent with velocity data. The low grain densities of dunites (~2.60 g/cm³) at shallow depths suggest that olivine (density ~ 3.3 g/cm³) in these rocks is nearly 100% serpentinized (density of lizardite serpentine ~ 2.58

g/cm^3; Mellini and Zanazzi, 1987). The grain density in the harzburgite-dominated sequence is higher than in the dunite-dominated sequence and tends to increase with depth (up to 2.72 g/cm^3). This suggests less alteration in the harzburgite-dominated sequences with depth, as low as ~75% serpentinization.

The porosity of discrete cube samples ranges 0.2%–16% (mean = 5.56% for dunite, = 1.60% for harzburgite). Gabbro samples show variable porosity, ranging 0.4%–18%. The dunite-dominated sequence shows the highest porosity in Hole BA1B (up to 16%), reflecting weathering near the surface, whereas the harzburgite-dominated sequence shows relatively constant and low porosity (mostly <2%) (Fig. **F76**).

Relationships between densities, *P*-wave velocity, and porosity in Hole BA1B are shown in Figures **F78** and **F79**, along with comparison to data from other OmanDP holes. Bulk and grain densities and *P*-wave velocity are overall inversely correlated to porosity, but different trends are observed in gabbros in ultramafic rocks. Similar features are seen in the same lithologies (gabbros and ultramafics) from other OmanDP Holes (see **Physical properties** sections in previous site chapters). *P*-wave velocity is linearly correlated with bulk density, whereas the correlation between *P*-wave velocity and grain density is slightly scattered (Fig. **F79**). Downhole plots of *P*-wave velocity with color scale reveals differences between the sequences and between lithologies.

Electrical resistivity

Electrical resistivity was measured in 143 cube samples from Hole BA1B (Tables **T11**, **T12**; Fig. **F76**). Resistivity ranges 13–18,665 Ω·m). The dunite-dominated sequence shows systematically lower resistivity than the harzburgite-dominated sequence. We measured both dry and wet resistivity, and wet resistivity is markedly lower than dry resistivity. The difference between dry and wet resistivity is likely related to the crack density and connectivity in samples. The relatively large difference in dry and wet resistivity is found in the dunite-dominated sequence, which can be related to higher permeability resulting from extensive fracturing.

Dry electrical resistivity has a weak correlation with bulk magnetic susceptibility of the same cube samples using the following relation (Fig. **F80**):

$$R = 1219 \times B^{-0.32} \qquad (R^2 = 0.2). \qquad (3)$$

where R = resistivity of cube sample B = bulk magnetic susceptibility of the cube sample. This correlation infers similar source between electrical conductivity and magnetic susceptibility, most likely caused by the magnetite fraction in ultramafic rocks.

Magnetic susceptibility

Magnetic susceptibility was measured in 147 cube samples from Hole BA1B (Tables **T11**, **T12**; Fig. **F76**). Magnetic susceptibility ranges from 0.0002 to 0.045 × 10^{-5} SI (average = 0.0142 × 10^{-5} SI for dunite and 0.0073 × 10^{-5} SI for harzburgite). Gabbros show a relatively lower magnetic susceptibility than ultramafic rocks (Table **T11**). The anisotropy of magnetic susceptibility (AMS) measurements show a continuous decreasing trend in the bulk and discontinuous decrease for the three orthogonal directions. Such a trend shows consistent correlation to lithology, where the overall level of anisotropy is higher in the dunite-dominated sequence compared to the harzburgite-dominated sequence. This is consistent with the whole-round magnetic susceptibility in Section 37Z-1 (Fig. **F73**), although absolute values are different between the discrete samples and the whole-round measurements.

Thermal conductivity

A total of 112 thermal conductivity measurements were taken on core pieces from the working halves in Hole BA1B (Tables **T11**, **T13**; Fig. **F76**). Thermal conductivity ranges 1.85–4.01 W/m·K. Thermal conductivity increases with depth, and no systematic difference between dunite and harzburgite was observed. This trend is opposite to those observed in Hole CM2B, where thermal conductivities of dunite slightly decreased with increasing depth. Since thermal conductivity changes with the degree of serpentinization, the increase of thermal conductivity in Hole BA1B suggests less alteration of the ultramafic sequence with increasing depth, consistent with grain density and velocity data. The values from the harzburgite-dominated sequence are similar to those reported in the harzburgites from Hole 1274A, Ocean Drilling Program (ODP) Leg 209, Mid-Atlantic Ridge 1520′N Fracture Zone (Kelemen et al., 2004). Troctolite and anorthosite showed markedly high thermal conductivity (up to 4.01 W/m·K). Thermal conductivity is correlated to XCT value as shown in Figure **F81**, suggesting that XCT value can be used as an indicator of alteration of ultramafic rocks.

Imaging spectroscopy: Hole BA1B

All sections of Hole BA1B were imaged onboard the *Chikyu* during Leg 3. The exceptions were the sections and portions of sections removed during drilling for microbiology analyses; these were not available to scan. The ~400 m of Hole BA1B was imaged in seven 12 h shifts over 3.5 days. A total of 542 sets of very near infrared (VNIR) and short-wave infrared (SWIR) images were acquired of core sections. Some scanning of these cores did occur while the ship was at sea during a typhoon and may have some artifacts from the ship movement, as described in **Imaging spectroscopy** in the **Methods** chapter. However, each scan was checked visually for artifacts. Otherwise, an initial check of data quality was good, and the images will be processed and analyzed at Caltech. This core was similar to that from Hole BA3A; for an example of the data set, see Figure **F75** in the **Site BA3** chapter.

Downhole logging/ hydrogeological testing: Hole BA1B

Downhole logging and hydrogeological testing operations and acquisition parameters for each borehole are available in Tables **T55** and **T56** in the **Methods** chapter. Raw and processed data from all downhole logs are available in **Supplementary material** > **L_Wireline logging** and in the ICDP Oman Drilling Project online data repository.

Operations: Hole BA1C

Rotary Hole BA1C (drilled in early 2018) is located 90 m from cored Hole BA1B (also drilled in early 2018). Drilling operations and core curation information are reported in Table **T3** in the **Methods** chapter.

All times are reported as local time in Oman (UTC + 4 h).

Drilling summary

- Spud in: 03 Feb 2018, 10:05 h
- Surface casing (SW) installed: 06 Feb 2018, 11:41
- Surface casing type: MS; 9-5/8 inches
- Depth of surface casing: 0.30–25.5 mbgl
- Hole diameter: 8 inches at 25.5–50.00 mbgl; 6-1/8 inches at 50.00–400 mbgl
- TD of borehole: 400.00 mbgl (collapsed at 60 mbgl on 17 Feb 2018)
- Completion type: open hole
- Discharge by air lift: 3.05 L/s
- Static water level: 18.30 (22 Feb 2018)

Geology summary

Serpentinized dunite and harzburgite.

Technical issues

Geophysical borehole logging indicated that Hole BA1C collapsed at 60 mbgl. J. Matter requested the drill rig to be moved to Hole BA1C location after completion of Hole BA1D. Borehole was cleaned to 75 mbgl by pumping compressed air with subsequent air-lift well development for 90 min while keeping drill bit at 75 m. After air-lift well development, drillers started to POOH drill pipes but the drill pipe line got stuck after pulling out the first one. There was no rotation or up/down movement of the drill string. Drillers unsuccessfully tried to release the stuck drill string from 17 March to 26 March 2018. Finally, they unscrewed the drill string as instructed by the LAVOL office. The drill string unscrewed from the second connection, and they were able to recover 15.20 m of drill pipe. The following material remained in the borehole: 45.6 m of drill pipe and one 6-1/8 inch tricone drill bit.

Operations summary

- 01 Feb 2018: mobilize drill rig, equipment, and drilling crew from CM site.
- 02 Feb 2018: prepare drill site by removing top soil and installing empty barrel.
- 03 Feb 2018: spud drill with 12-1/4 inch tricone bit using air foam.
- 04 Feb 2018: no drilling—waiting for casing supply from Muscat.
- 05 Feb 2018: resume spud drilling to 25.5 mbgl and install 9-5/8 inch MS casing
- 06 Feb 2018: cement grout 12-1/4 and 9-5/8 inch casing annulus.
- 07 Feb 2018: hammer drill 8 inch diameter hole 25.5–50 mbgl using air foam. Collect and describe drill cuttings every meter; collect subsamples for later analysis. Stop drilling at 50 mbgl to flush hole and POOH completely. Change bit to 6-1/8 inch tricone and continue drilling to 66 mbgl.
- 08–16 Feb 2018: continue drilling to 364.8 mbgl using 6-1/8 inch tricone bit and air foam circulation. Collect and describe drill cuttings every meter; collect subsamples for later analysis.
- 17–19 Feb 2018: drill rig under breakdown.
- 20–21 Feb 2018: continue drilling to 400 mbgl using 6-1/8 inch tricone bit and air foam circulation. Collect and describe drill cuttings every meter; collect subsamples for later analysis. Well development was conducted by air lift test for 5 h (see **Supplementary material** > **N_Drill site reports**). (Q = 3.05 L/s, EC = 1151.00 µS/cm, pH = 10.29, T = 33.30°C). SWL = 18.30 mbgl.
- 22 Feb 2018: POOH and rig down. Mobilize drill rig and drilling accessories to Hole BA1D location and construct wellhead for Hole BA1C.
- 16 March 2018: mobilize drill rig and drilling accessories to Hole BA1C from Hole BA1D to start borehole cleaning.
- 17 March 2018: lower drill string with 6-1/8 inch tricone bit to 42 mbgl. Clean collapsed borehole

42–60 mbgl by pumping compressed air; complete POOH. Borehole sounding indicates borehole blockage at 42 m. Run 6-1/8 inch cleaning assembly again and clean hole to 75 mbgl by compressed air; subsequent air-lift test for 90 min while keeping bit at 75 m. During POOH after well development, line got stuck after removing one drill pipe. No rotation or up/down movement of drill string observed.

- 18–25 March 2018: try to release stuck drill string with no success.
- 26 March 2018: unscrew drill string and recover 15.20 m of drill pipe. Rig down and demobilize from location.

Petrology from drill cuttings: Hole BA1C

The cuttings log for Hole BA1C indicates a dunite interval extending to 98 m underlain by a harzburgite interval at 98–400 m. The cuttings log indicates thinner dunite intervals at 102–104, 105–115, and 254–256 m depth. The drill cuttings log is available in Table **T14**. A lithologic section based on the log is in Figure **F82**.

Hydrothermal alteration/veins: Hole BA1C

There are no notes on alteration minerals in the cuttings log. Because there are no primary mantle minerals in most of the core from Hole BA1B, it is likely that all of the cuttings for Hole BA1C are dominated by serpentine ± brucite assemblages.

Geochemistry: Hole BA1C

XRF analyses of cuttings, at 10 m intervals, were made at Sultan Qaboos University (SQU). See discussion in **XRF analysis of drill cuttings at SQU** in the **Introduction to Science Theme 3** chapter.

Downhole measurements: Hole BA1C

No downhole logs were recorded because the hole collapsed at ~63 m shortly after drilling. Efforts to reopen the borehole failed.

Operations: Hole BA1D

Rotary Hole BA1D (drilled in early 2018) is located 108 meters from cored Hole BA1B (also drilled in early 2018). Drilling operations and core curation information are reported in Table **T3** in the **Methods** chapter.

Detailed petrological observations were made on core from Hole BA1B during summer 2018 onboard *Chikyu*. Here we summarize the onsite log of lithology Hole BA1D drill cuttings. The log is available in Table **T15**. A lithologic section based on the log is in Figure **F83**.

All times are reported as local time in Oman (UTC + 4 h).

Drilling summary

- Spud in: 24 Feb 2018, 11:10 h
- Surface casing (SW) installed: 26 Feb 2018, 16:30 h
- Surface casing type: MS; 9-5/8 inch
- Depth of surface casing: 0.30–26.0 mbgl
- Hole diameter: 8 inches at 26.9–50.0 mbgl; 6-1/8 inches at 50.00–400 mbgl
- TD of borehole: 400.00 mbgl
- Completion type: open hole
- Discharge by air lift: 0.44 L/s
- Static water level: 15.50 mgbl (12 March 2018)

Geology summary

Serpentinized dunite and harzburgite.

Technical issues

No drilling activities from 25 Feb 2018 due to waiting for surface casing delivery from Muscat and 28 Feb–08 March 2018 due to rig compressor breakdown and waiting for spare parts.

Operations summary

- 22 Feb 2018: prepare drill site, including removing top soil and installation of empty barrel at borehole location.
- 23 Feb 2018: mobilize drill rig, equipment, and drilling crew from Hole BA1C location.
- 24 Feb 2018: spud drill with 12-1/4 inch tricone bit using air foam to 24 mbgl.
- 25 Feb 2018: no drilling—waiting for casing supply from Muscat.
- 26 Feb 2018: resume spud drilling to 26.0 mbgl, install 9-5/8 inch MS casing, and grout cement.
- 27 Feb 2018: drill 8 inch diameter hole 26–50.0 mbgl using hammer drill bit type and air foam. Collect and describe drill cuttings every meter; collect subsamples for later analysis. Stop drilling at 50 mbgl to flush hole and POOH completely. Change bit to 6-1/8 inch tricone and continue drilling to 52.4 mbgl. Stop drilling due to rig compressor failure.

- 28 Feb–08 March 2018: drill rig under breakdown—waiting for spare parts from USA.
- 09–14 March 2018: resume drilling with 6-1/8 inch tricone bit 52.4–330 m. Collect and describe drill cuttings every meter; collect subsamples for later analysis.
- 15 March 2018: drill 6-1/8 inch hole 330–400 mbgl (TD). Wash and clean hole for 15 min, followed by well development test (air-lift test) for 75 min (see **Supplementary material** > **N_Drill site reports**). (Q = 0.44 L/s, EC = 865.00 µS/cm, pH = 9.67, T = 32.30°C). SWL = 15.50 mbgl.
- 16 March 2018: POOH, rig down, and mobilize rig to Hole BA1C location.

Petrology from drill cuttings: Hole BA1D

The shipboard core description of core from Hole BA1D revealed a dunite-rich interval extending to ~160 m depth underlain by a harzburgite-rich interval from ~160 to the bottom of the hole at ~400 m. Similarly, the cuttings log for Hole BA1D indicates a dunite interval extending to ~250 m underlain by a harzburgite interval at 250–400 m.

Hydrothermal alteration/veins: Hole BA1D

There are no notes on alteration minerals in the cuttings log. Because there are no primary mantle minerals in most of the core from Hole BA1B, it is likely that all of the cuttings for Hole BA1D are dominated by serpentine ± brucite assemblages.

Geochemistry: Hole BA1D

XRF analyses of cuttings, at 10 m intervals, were made at Sultan Qaboos University (SQU). See discussion in **XRF analysis of drill cuttings at SQU** in the **Introduction to Science Theme 3** chapter.

Downhole measurements: Hole BA1D

Wireline logs were recorded by the University of Montpellier group using a slimline logging system in March 2018 (Tables **T56**, **T57** in the **Methods** chapter). The full set of logs are available in **Supplementary material** > **L_Wireline logging**. The dual laterolog resistivity logs partially coincide with the cuttings log, indicating dominantly low-resistivity (<1000 Ω·m) dunite layers at 0–150 and 180–200 m. Higher resistivity harzburgite is dominant at 200–400 m. Preliminary optical and acoustic televiewer log analyses reveal mostly steep fractures with the majority striking northwest–southeast and decreasing fracture and vein frequency with increasing depth. Fluid column logs show increasing pH of 9.04–10.5 from 17.03 (water level) to 76 m, and a variable pH of 10–10.5 deeper than 76 m. Electrical conductivity increases from 665 (water level) to 2306 µS/cm at 400 m. The temperature log shows a steady increase of 34°–43°C at 400 m. The Eh log generally indicates a thin layer of oxidized water to 50 m below surface, followed by reduced water at 50–400 m (**Supplementary material** > **L_Wireline logging**). Cross-borehole multilevel hydraulic tests were conducted in Holes BA1A and BA1D in 2018 and 2019. Results of these tests are published in Lods et al. (2020).

References

Arason, P., and Levi, S., 2010. Maximum likelihood solution for inclination-only data in paleomagnetism. Geophysical Journal International, 182:753-771. https://doi.org/10.1111/j.1365-246X.2010.04671.x

Birch, F., 1961. The velocity of compressional waves in rocks to 10 kilobars, Part 2, J. Geophys. Res., 66:2199–2224.

Bruni, J., Canepa, M., Chiodini, G., Cioni, R., Cipolli, F., Longinelli, A., Marini, L., Ottonello, G., and Zuccolini, M.V., 2002. Irreversible water-rock mass transfer accompanying the generation of the neutral, Mg-HCO_3 and high-pH, Ca-OH spring waters of the Genova Province, Italy. Applied Geochem., 17:455-474.

Cardozo, N., and Allmendinger, R.W., 2013. Spherical projections with OSXStereonet. Computers and Geosciences, 51:193–205. https://doi.org/10.1016/j.cageo.2012.07.021

Dasgupta, R., and Hirschmann, M.M., 2010. The deep carbon cycle and melting in Earth's interior. Earth Planet. Sci. Lett., 298:1-13.

De Obeso, J.C., and Kelemen, P.B., 2020. Magnesium and iron mobility during serpentinization, oxidation and weathering of mantle peridotite at low temperatures: the case of Wadi Fins, Oman (invited). Phil. Trans. Roy. Soc. London A, 378:20180433.

Frost, B.R., 1985. On the stability of sulfides, oxides and native metals in serpentinite. J. Petrol., 26:31-63.

Godard, M., Jousselin, D., and Bodinier, J.L., 2000. Relationships between geochemistry and structure beneath a palaeo-spreading centre: a study of the mantle section in the Oman ophiolite. Earth and Planetary Science Letters, 180(1-2):133-148. https://doi.org/10.1016/S0012-821X(00)00149-7

Godard, M., Awaji, S., Hansen, H., Hellebrand, E., Brunelli, D., Johnson, K., Yamasaki, T., Maeda, J., Abratis, M., Christie, D., Kato, Y., Mariet, C., and Rosner, M., 2009. Geochemistry of a long in-situ section of intrusive slow-spread oceanic lithosphere: Results from IODP Site U1309 (Atlantis Massif, 30°N Mid-Atlantic-Ridge). Earth and Planetary Science Letters, 279:110-122. https://doi.org/10.1016/j.epsl.2008.12.034

Hanghøj, K., Kelemen, P.B., Hassler, D., and Godard, M., 2010. Composition and genesis of depleted mantle peridotites from the Wadi Tayin Massif, Oman Ophiolite; major and trace element geochemistry, and Os isotope and PGE systematics. Journal of Petrology, 51(1-2):201-227. https://doi.org/10.1093/petrology/egp077

Kelemen, P.B., Kikawa, E., Miller, D.J. et al., 2004. Proc. ODP, Init. Repts., 209: College Station, TX (Ocean Drilling Program). https://doi.org/10.2973/odp.proc.ir.209.2004

Kelemen, P.B., Matter, J., Streit, E.E., Rudge, J.F., Curry, W.B., and Blusztajn, J., 2011. Rates and Mechanisms of Mineral Carbonation in Peridotite: Natural Processes and Recipes for Enhanced, in situ CO_2 Capture and Storage. Annu. Rev. Earth Planet. Sci., 39:545–576.

Khedr, M.Z., Arai, S., Python, M., Tamura, A., 2014. Chemical variations of abyssal peridotites in the central Oman ophiolite: Evidence of oceanic mantle heterogeneity. Gondwana Research, 25(3):1242-1262. https://doi.org/10.1016/j.gr.2013.05.010

Lippard, S.J., Shelton, A.W., and Gass, I.G., 1986. The ophiolite of northern Oman. In Geological Society Memoirs, 11: Blackwell Sci.

Lods, G., Roubinet, D., Matter, J.M., Leprovost, R., Gouze, P., and Oman Drilling Project Science Team, 2020. Groundwater flow characterization of an ophiolitic hard-rock aquifer from cross-borehole multi-level hydraulic experiments. J. Hydrology, 589:125152. https://doi.org/10.1016/j.jhydrol.2020.125152

Lorand, J.P., 1987. A new occurrence of native iron in a serpentinized mantle peridotite—Maqsad, Sumail massif, Semail ophiolite (southern Oman). C.R. Acad. Sci. Ser. II, 304:703–706.

Mellini, M., and Zanazzi, P.F., 1987. Crystal structures of lizardite-1T and lizardite-2H1 from Coli, Italy. American Mineralogist, 72:943-948.

Monnier, C., Girardeau, J., Le Mée, L., and Polvé, M., 2006. Along-ridge petrological segmentation of the mantle in the Oman ophiolite. Geochem., Geophys., Geosys., 7(11). https://doi.org/10.1029/2006GC001320

Rospabé, M., Benoit, M., Ceulenner, G., Hodel, F., Kaczmarek, M.A., 2018. Extreme geochemical variability through the dunitic transition zone of the Oman ophiolite: Implications for melt/fluid-rock reactions at Moho level beneath oceanic spreading centers. Geochim. Cosmochim. Acta, 234:1-23. https://doi.org/10.1016/j.gca.2018.05.012

Takazawa, E., Okayasu, T., Satoh, K., 2003. Geochemistry and origin of the basal lherzolites from the northern Oman ophiolite (northern Fizh block). Geochemistry, Geophysics, Geosystems, 4(1021). https://doi.org/10.1029/2001GC000232

Figure F1. Lithostratigraphic column for cuttings, Hole BA1A.

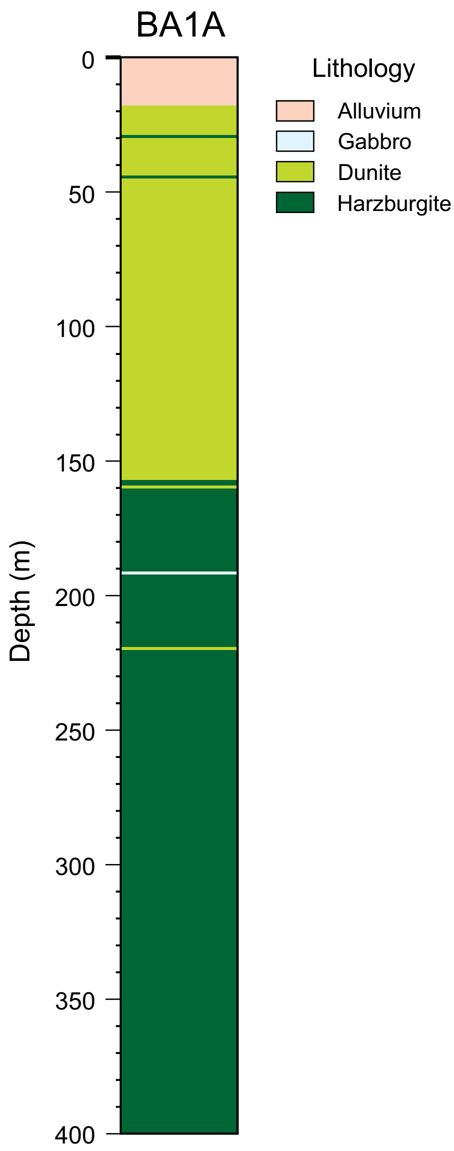

Figure F2. Transmitted light micrographs of drill cuttings, Hole BA1A. **A, B.** Opaque sulfide overprinting (50 m depth; plane-polarized light [PPL]) concentrated in (A) mesh cores and (B) mesh rims. **C, D.** Colorless fibrous texture fragment (50 m) in (C) PPL; (D) cross-polarized light (XPL). **E, F.** Mottled serpentine mesh, diopside, and fibrous texture (370 m) in (E) PPL; (F) XPL.

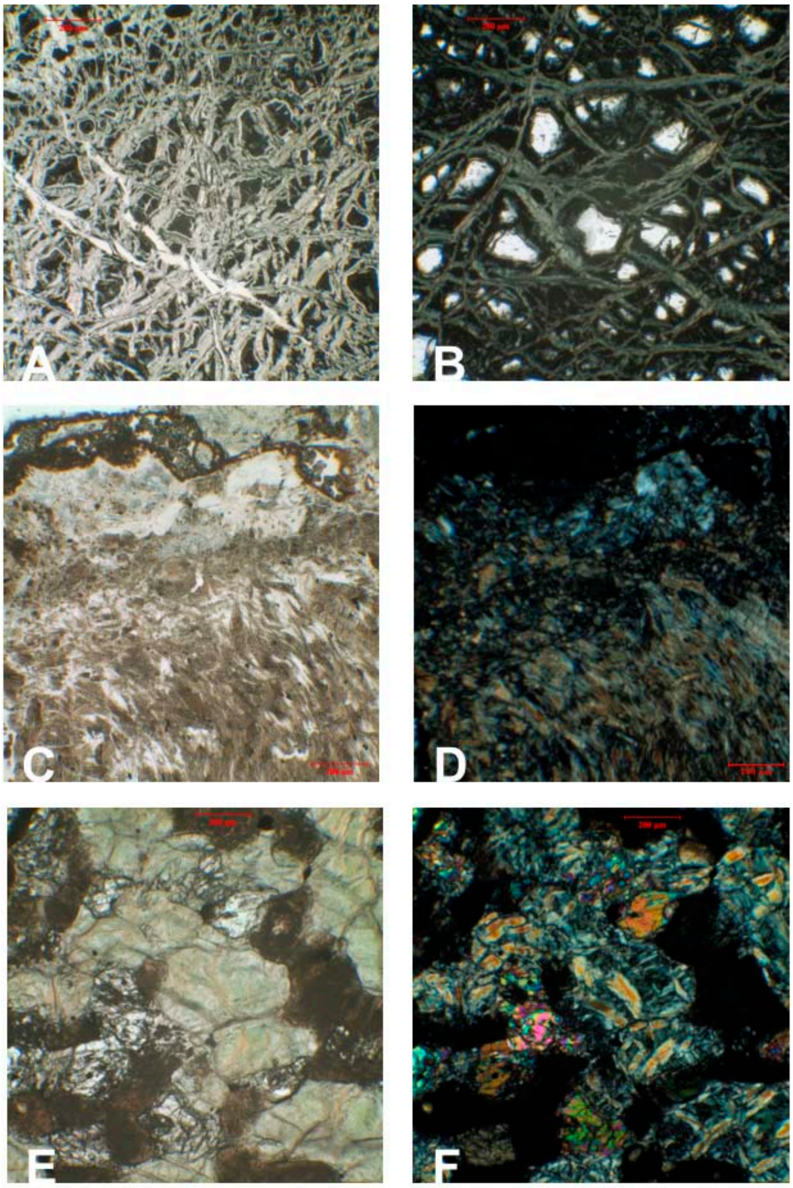

Figure F3. Lithostratigraphic column, sequences, and depth logs for mode (olivine, spinel, plagioclase, clinopyroxene, orthopyroxene) and grain size, Hole BA1B.

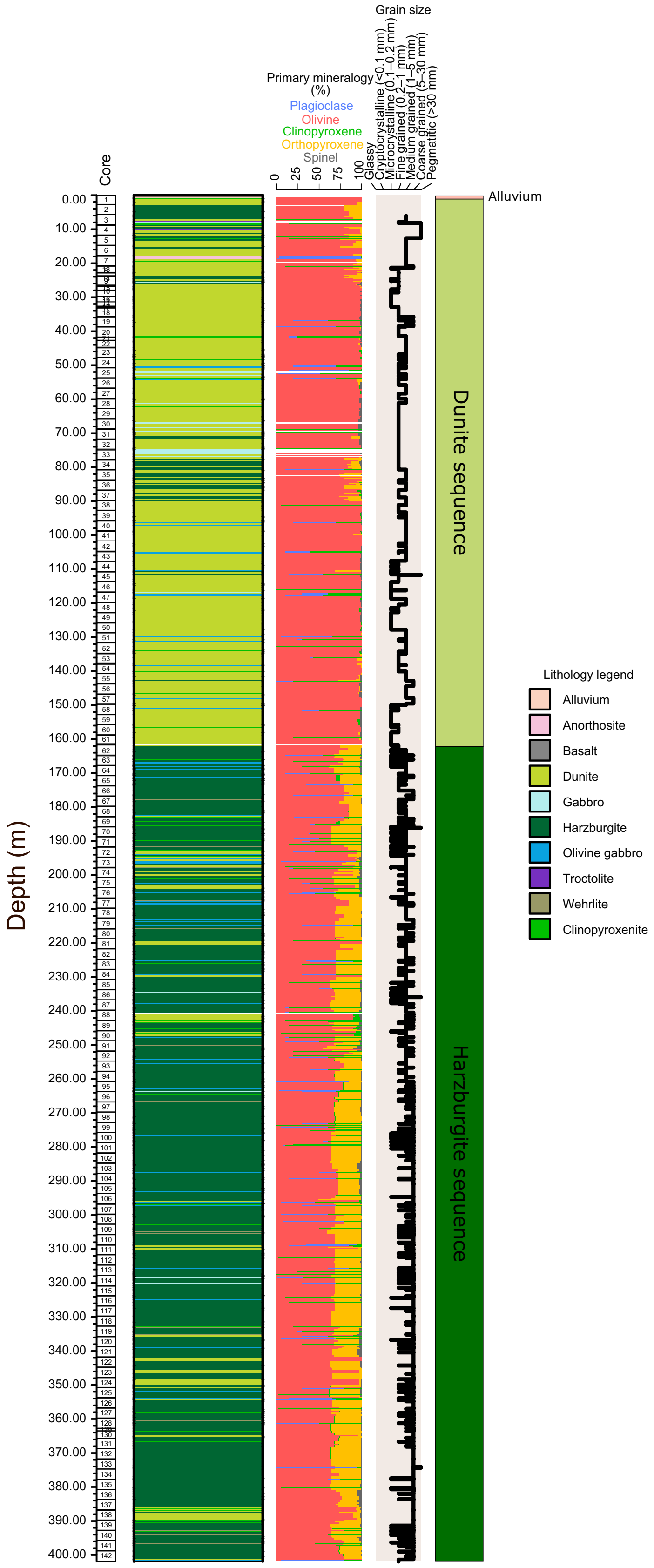

Figure F4. Pie charts showing the lithology thicknesses in percentages and unit counts, Hole BA1B.

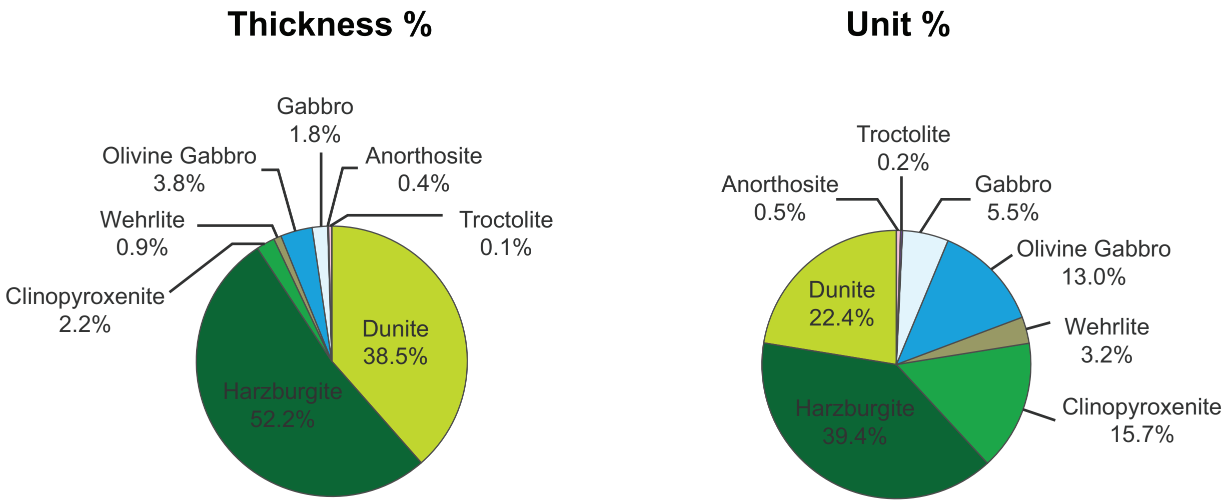

Figure F5. A, B. Dunite vs. harzburgite occurrence and corresponding mineral composition evolution with depth, Hole BA1B. Ol = olivine, Opx = orthopyroxene, Cpx = clinopyroxene, Sp = spinel.

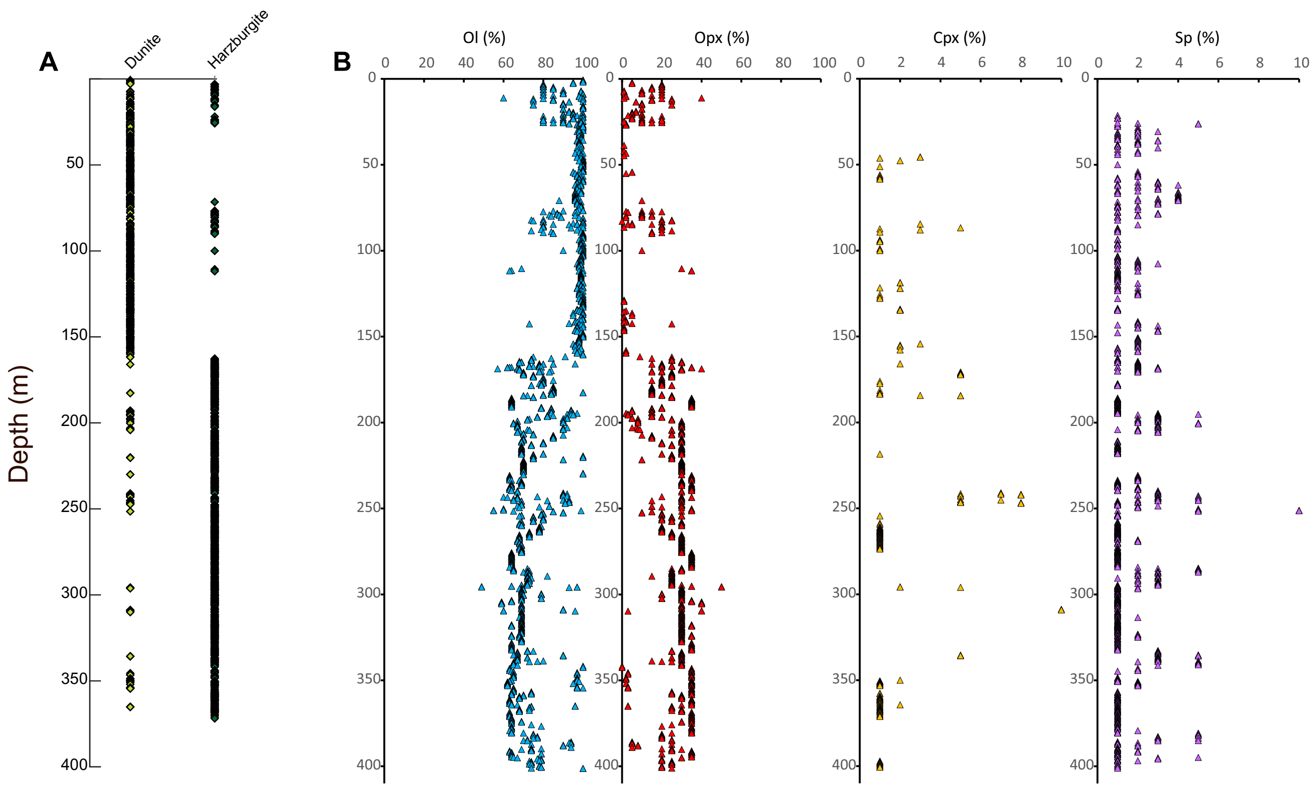

Figure F6. Frequency of dike types, occurrences, and mineralogy evolution, Hole BA1B. Ol = olivine, Pl = plagioclase, Cpx = clinopyroxene.

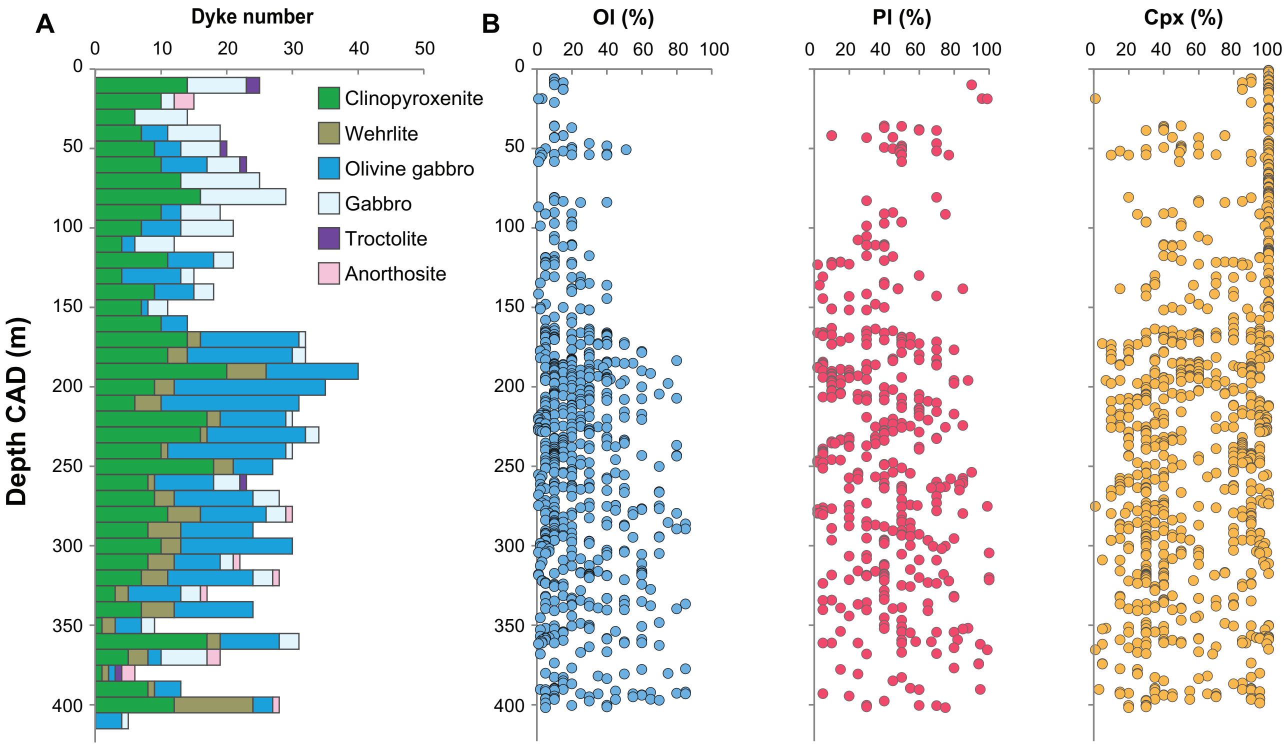

Figure F7. Pie charts showing unit and subunit counts and the corresponding cumulative thickness for the four different lithologic sequences defined in Hole BA1B: (**A**) Dunite with Gabbro Sequence; (**B**) Harzburgite with Gabbro Sequence.

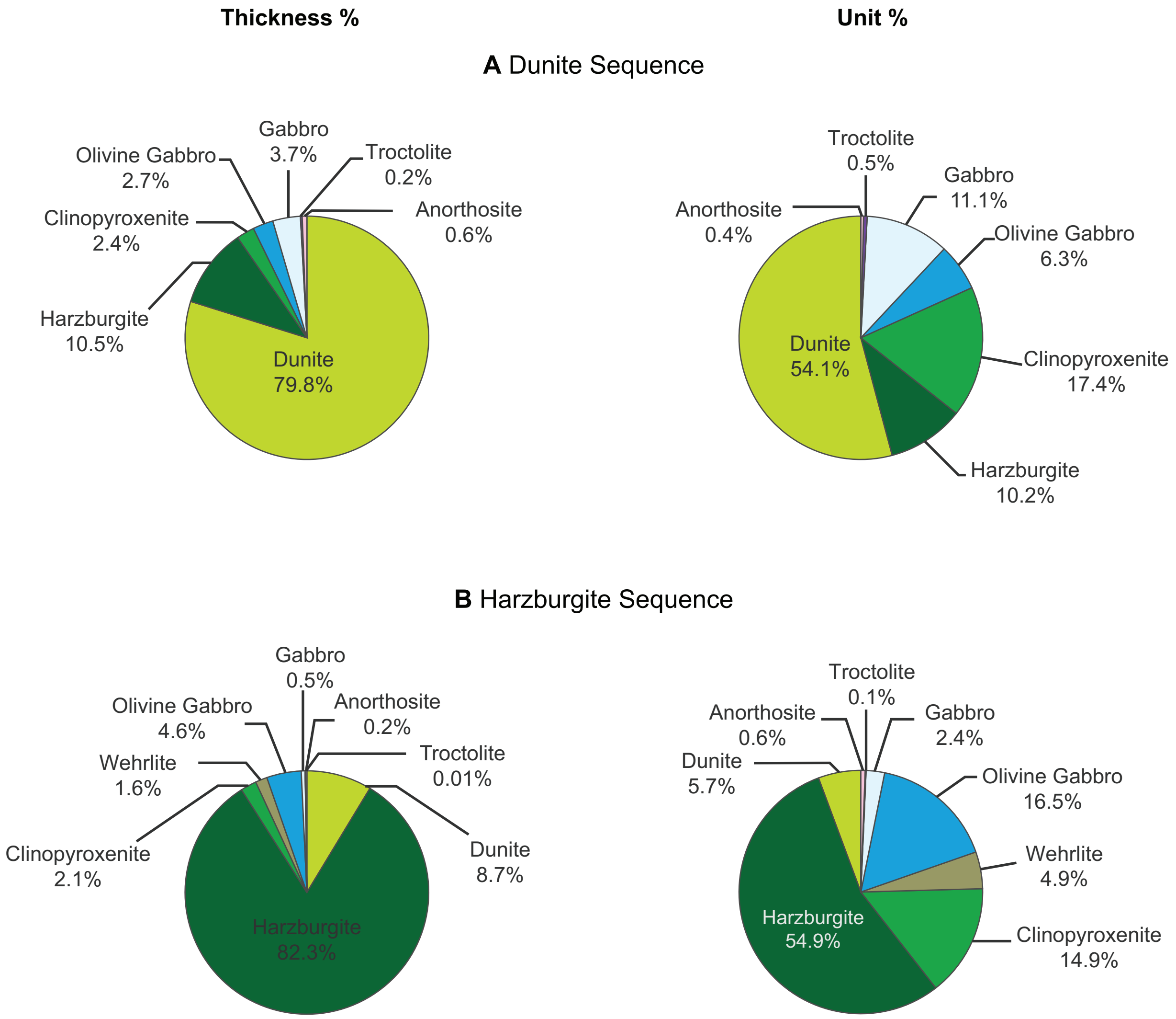

Figure F8. Principal rock types, Hole BA1B. **A.** Highly oxidized and altered dunite from Dunite with Gabbro Sequence (4Z-1, 20–45 cm). **B.** Dunite from Dunite with Gabbro Sequence (11Z-4, 35–60 cm). **C.** Harzburgite from Harzburgite with Gabbro Sequence (81Z-1, 25–65 cm). **D.** Layering of orthopyroxene-rich harzburgitic layers and orthopyroxene-free dunitic layers from Harzburgite with Gabbro Sequence (106Z-3, 40–70 cm).

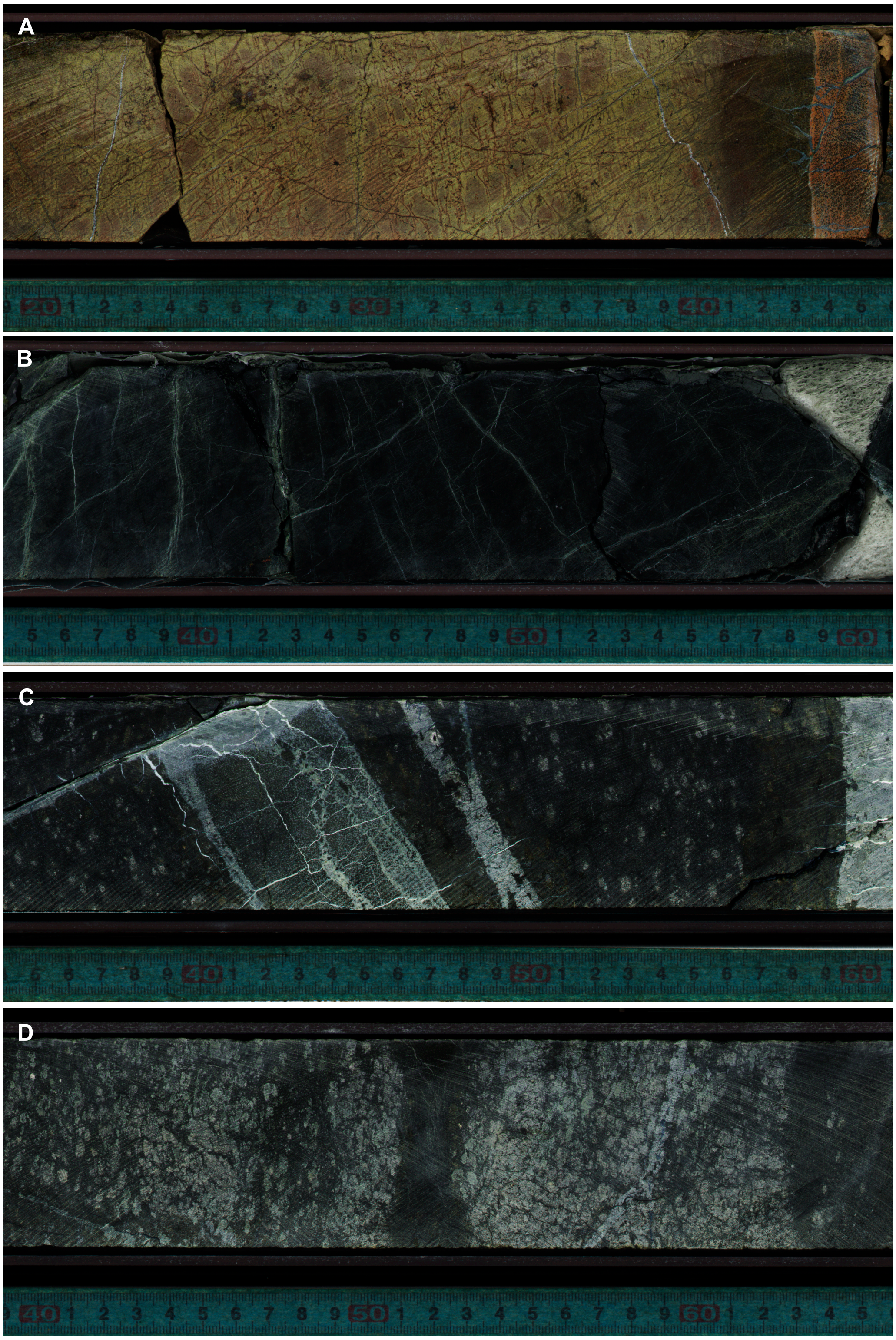

Figure F9. Harzburgites from Dunite with Gabbro Sequence, Hole BA1B. **A**. Olivine (ol) proximal to larger orthopyroxene (opx) grains (35Z-3, 11–14 cm; XPL). **B**. Olivine grain partially surrounded by orthopyroxene (35Z-3, 11–14 cm; XPL). **C**. Exsolution lamellae of clinopyroxene (cpx) inside orthopyroxene (34Z-4, 14–17 cm). **D**. Vermicular spinel (sp) associated with medium grains of clinopyroxene (35Z-3, 11–14 cm; PPL). **E**. Clinopyroxenite intruding harzburgite (55Z-3, 33–37 cm; XPL). serp = serpentine.

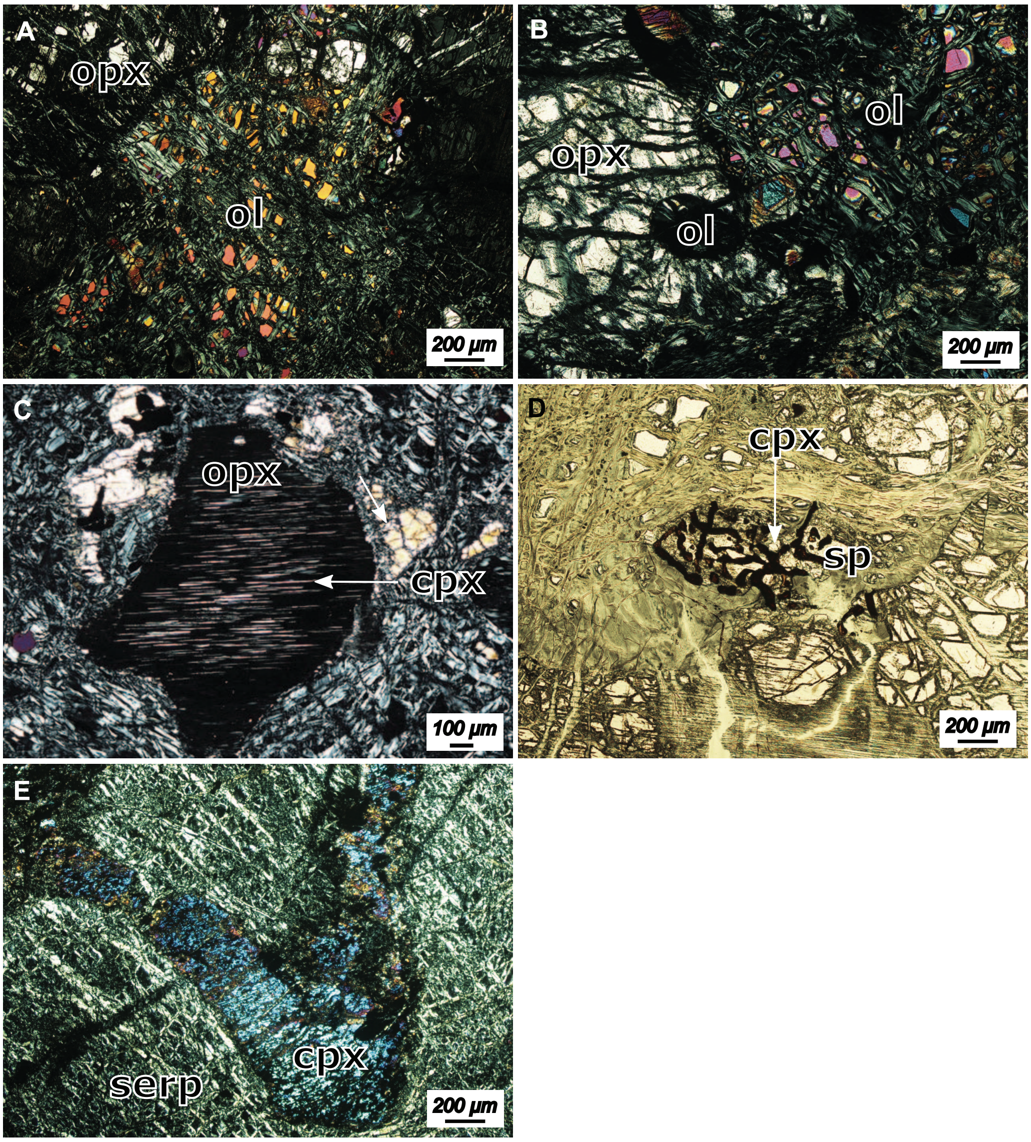

Figure F10. Harzburgites from Harzburgite with Gabbro Sequence, Hole BA1B. **A.** Partly serpentinized coarse olivine (ol) with protogranular texture (97Z-2, 43–45 cm). **B.** Coarse orthopyroxene (opx) and olivine in harzburgites (97Z-2, 43–45 cm; XPL). **C.** Exsolved clinopyroxenes (cpx) in orthopyroxene (87Z-2, 66–68 cm; XPL). **D.** Subhedral grains of clinopyroxene (64Z-1, 27–30 cm; PPL). **E.** Anhedral polygonal spinel (sp) (87Z-2, 66–68 cm; XPL). **F.** Clinopyroxene of clinopyroxenite intruding harzburgite (103Z-3, 69–71 cm; XPL).

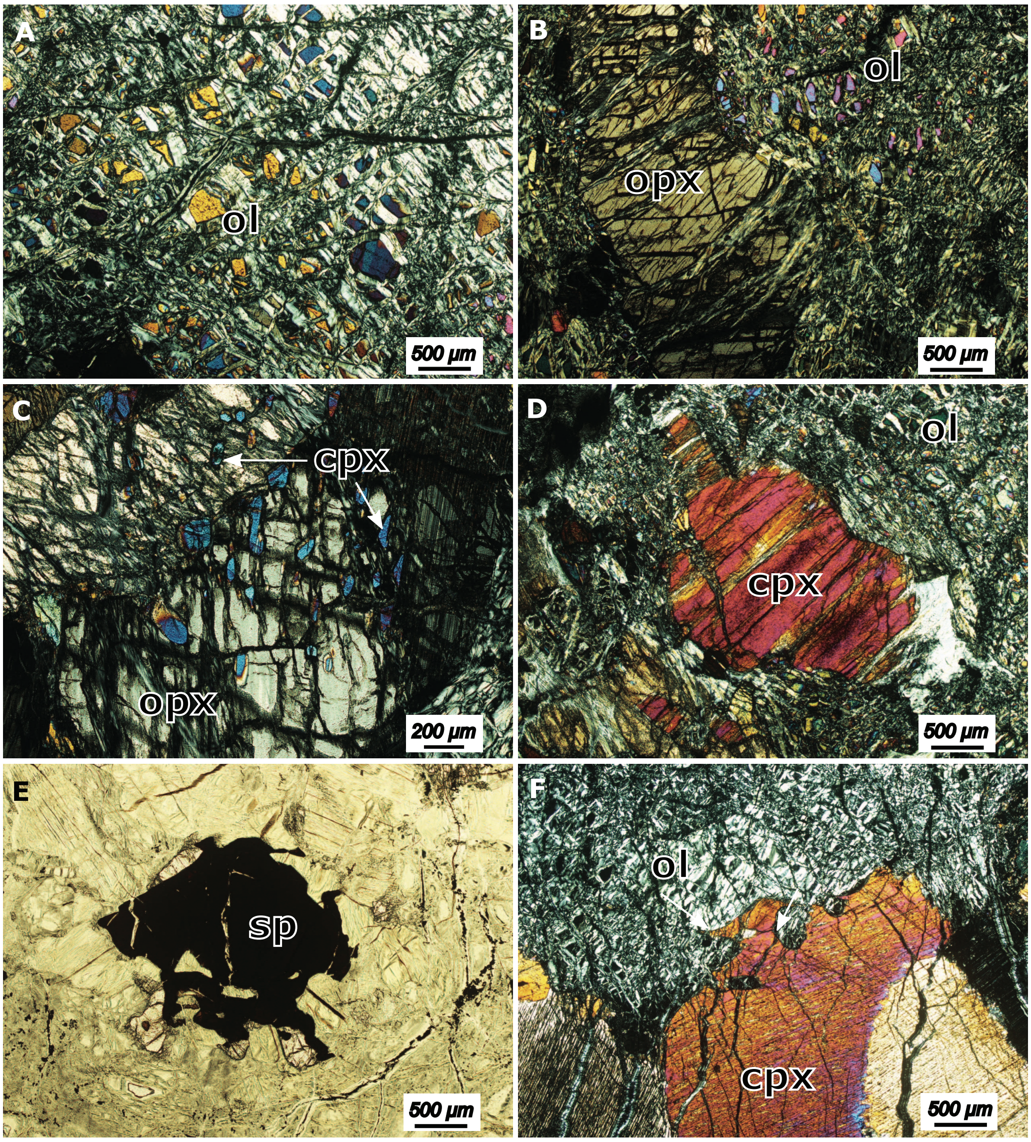

Figure F11. Dunite from Dunite with Gabbro Sequence, Hole BA1B. **A**. Typical complete serpentinized dunite with orange olivine cores (24Z-3, 14–19 cm; PPL). **B**. Typical complete serpentinized dunite with black olivine cores (57Z-4, 43–46; PPL). **C**, **D**. Fresh olivine (ol) relics in serpentinized dunite (57Z-2, 63–66 cm; [C] PPL, [D] XPL). **E**. Spinel (sp)-rich dunite with chromite as the major spinel phase (54Z-4, 1–6 cm; reflected light [RL]). **F**. Sulfides (sulf) replacing chromite (38Z-1, 1–6 cm; RL).

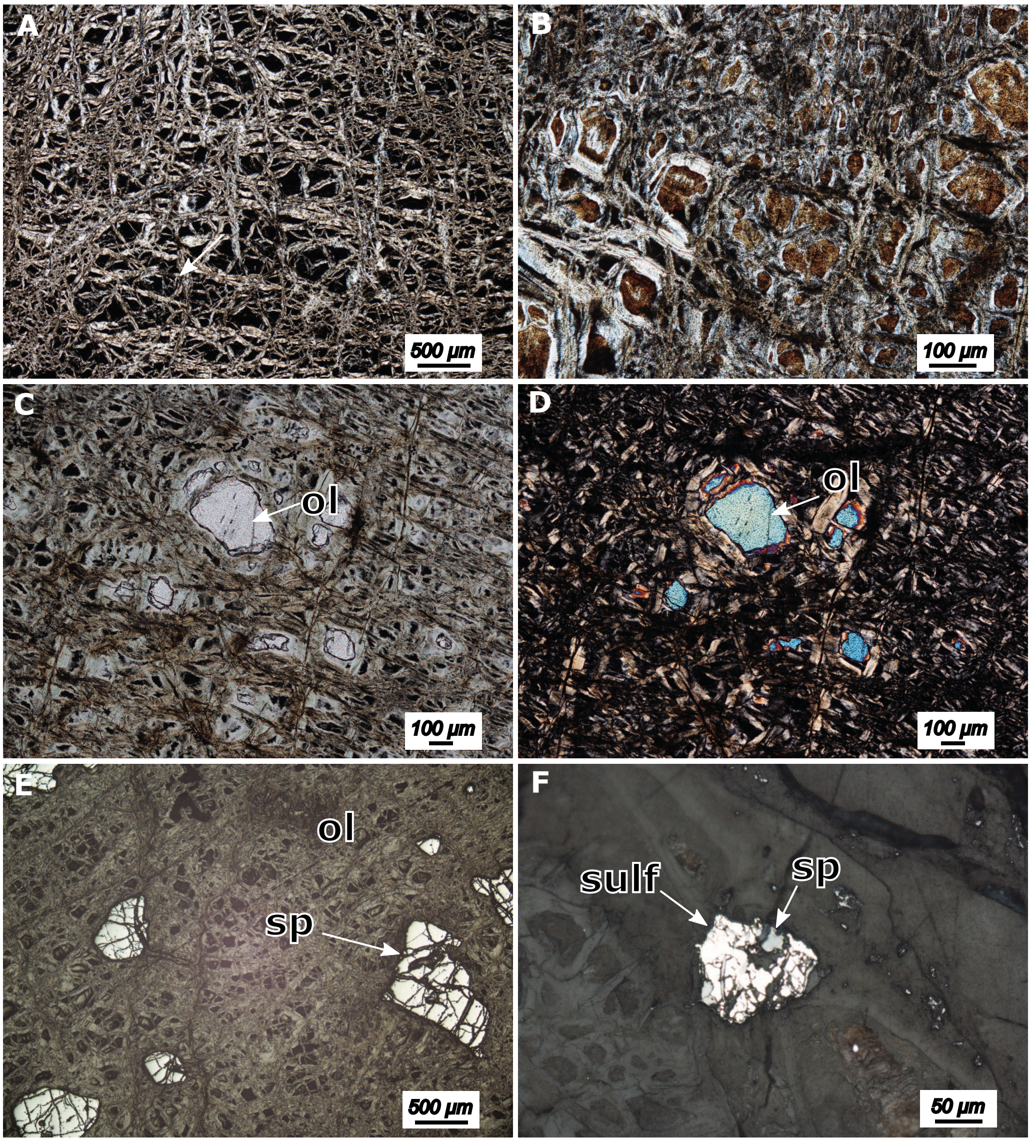

Figure F12. Dunite from Dunite with Gabbro Sequence, Hole BA1B. **A**, **B**. Two different types of chlorite (chl) precipitating at the contact between serpentinized dunite and gabbroic dike (58Z-2, 45–48 cm; [A] PPL, [B] XPL). ol = olivine.

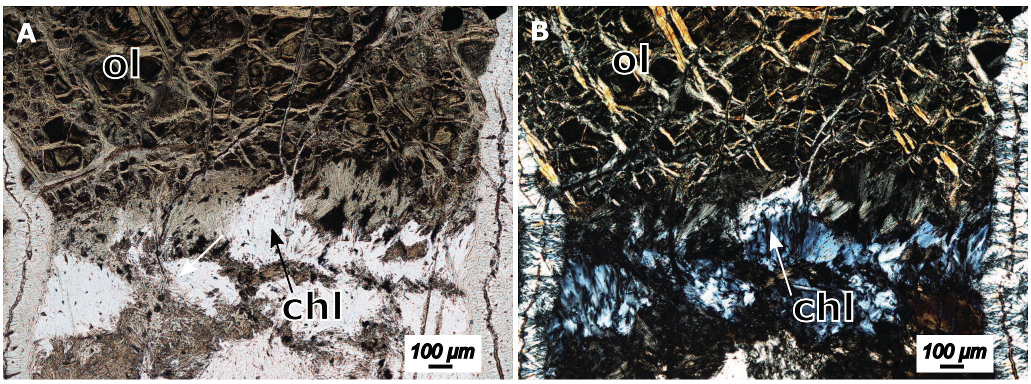

Figure F13. Dunite from Harzburgite with Gabbro Sequence, Hole BA1B. **A**, **B**. Serpentinized olivine (ol) with less altered clinopyroxene (cpx) and textural relics of orthopyroxene (opx) (106Z-3, 49–52 cm; [A] PPL, [B] XPL). **C**. Magnetite (mgt) replacing chromite (chr) in serpentinized olivine (124Z-3, 37–40 cm; RL). **D**. Contact between olivine gabbro and serpentinized dunite (red line) with gradual change from brown toward colorless serpentine (124Z-3, 37–40 cm; PPL). Black rectangle = location of E and F. **E**, **F**. Contact between olivine gabbro and serpentinized dunite with a fine layer of serpentine (serp) at the contact (124Z-3, 37–40 cm; [E] PPL, [F] XPL). grt = garnet.

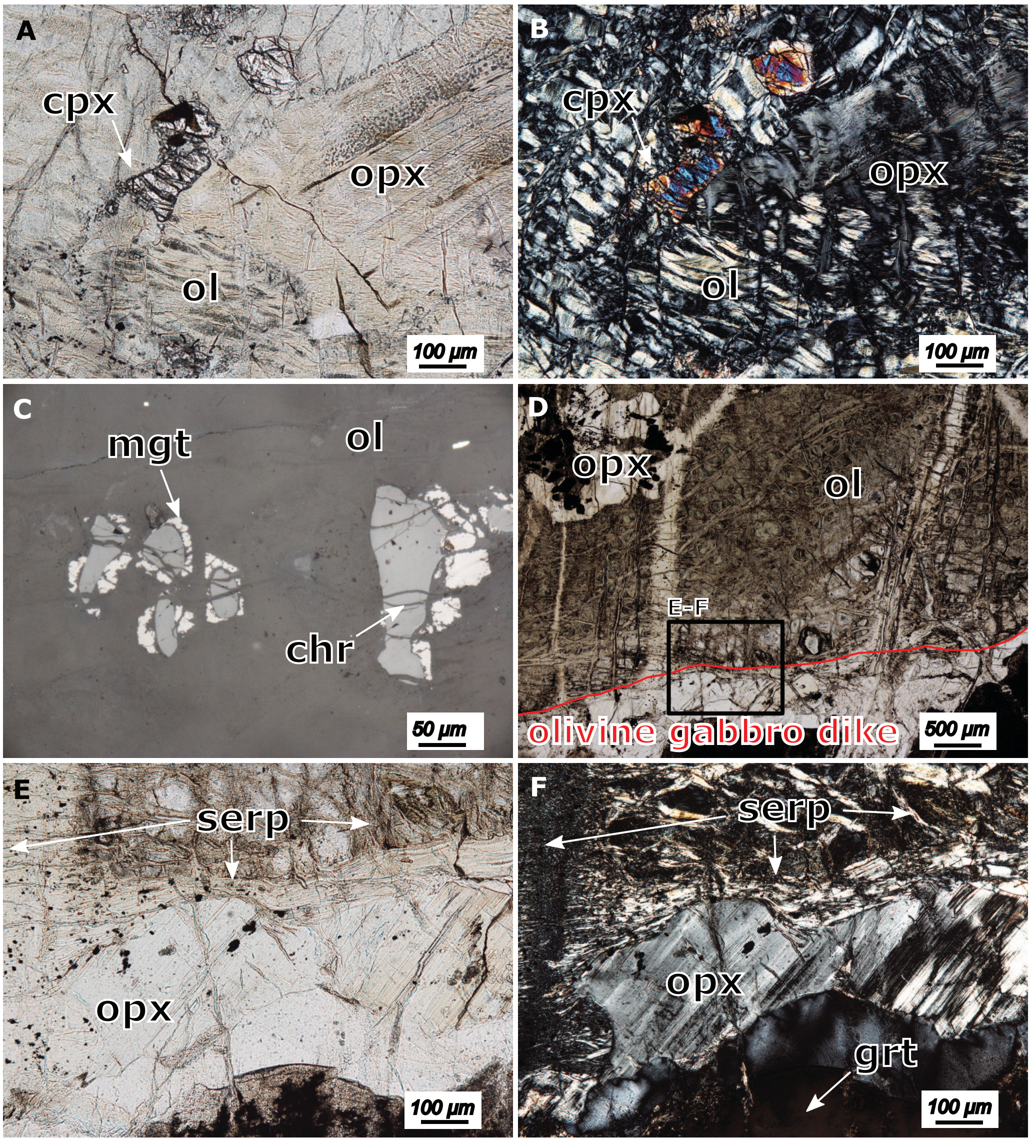

Figure F14. Plots of dike and halo apparent thicknesses in host rocks around dike vs. depth, Hole BA1B.

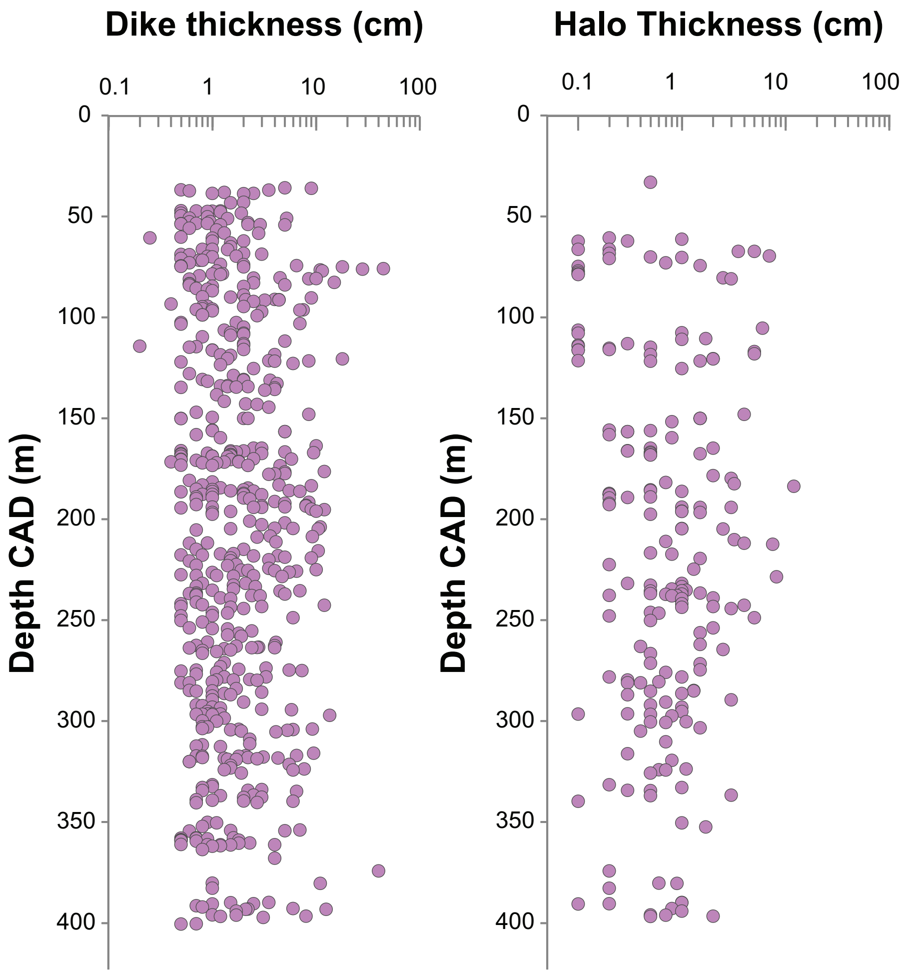

Figure F15. Dike types, Hole BA1B. **A**. Coarse-grained gabbro dike from Dunite with Gabbro Sequence (19Z-1, 0–12 cm). **B**. Microgabbro dike from Dunite with Gabbro Sequence (28Z-2, 45–65 cm). **C**. Medium-grained gabbro dikes from Harzburgite with Gabbro Sequence (64Z-2, 53–72 cm). **D**. Layered gabbro dike from Harzburgite with Gabbro Sequence (124Z-3, 22–50 cm).

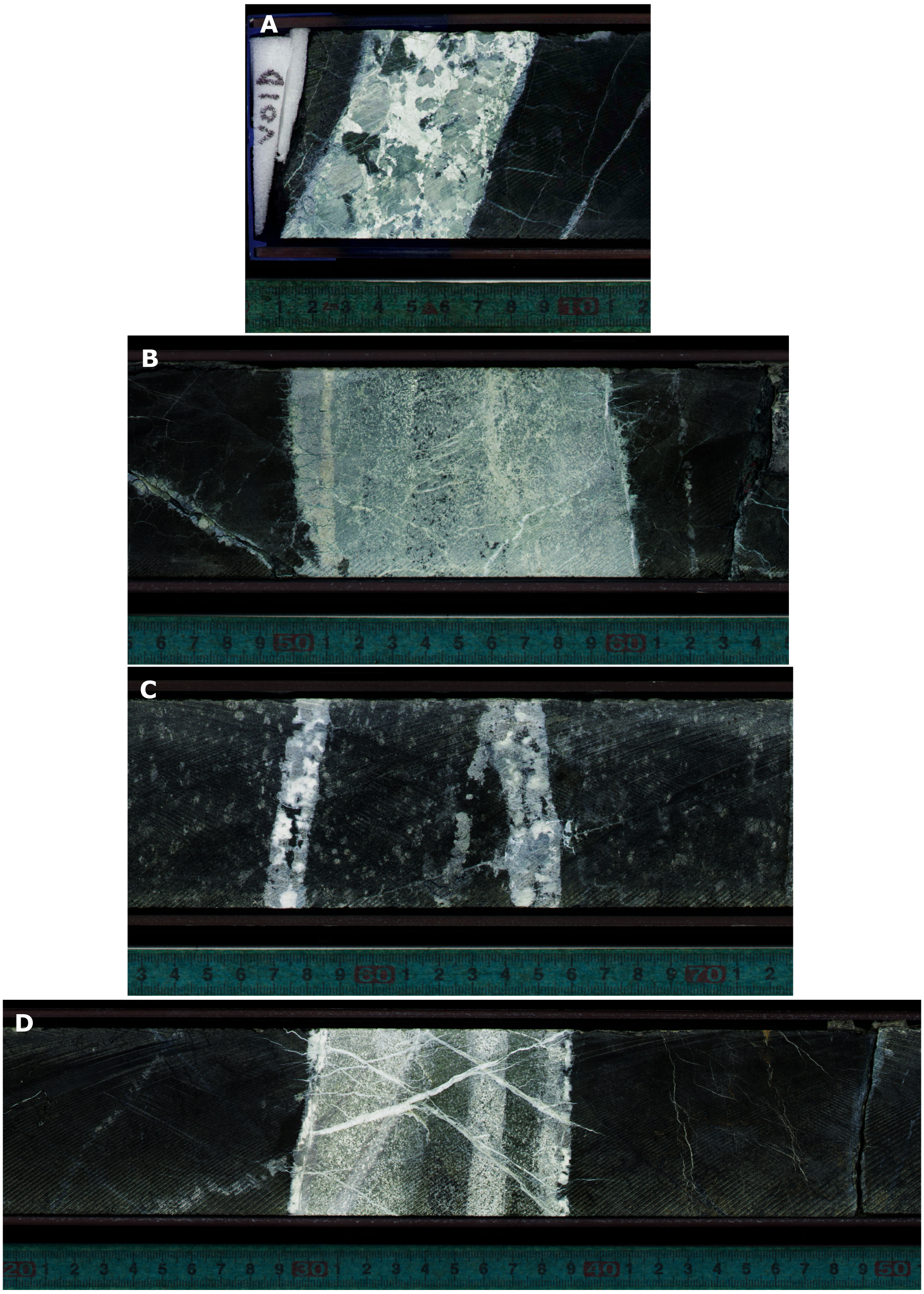

Figure F16. Dike alteration, Hole BA1B. **A.** Rodingitized patch from Dunite with Gabbro Sequence (2Z-1, 28–54 cm). **B.** Rodingitized gabbro from Harzburgite with Gabbro Sequence (82Z-4, 47–65 cm). **C.** Red clinopyroxenite from Harzburgite with Gabbro Sequence (87Z-2, 23–33 cm).

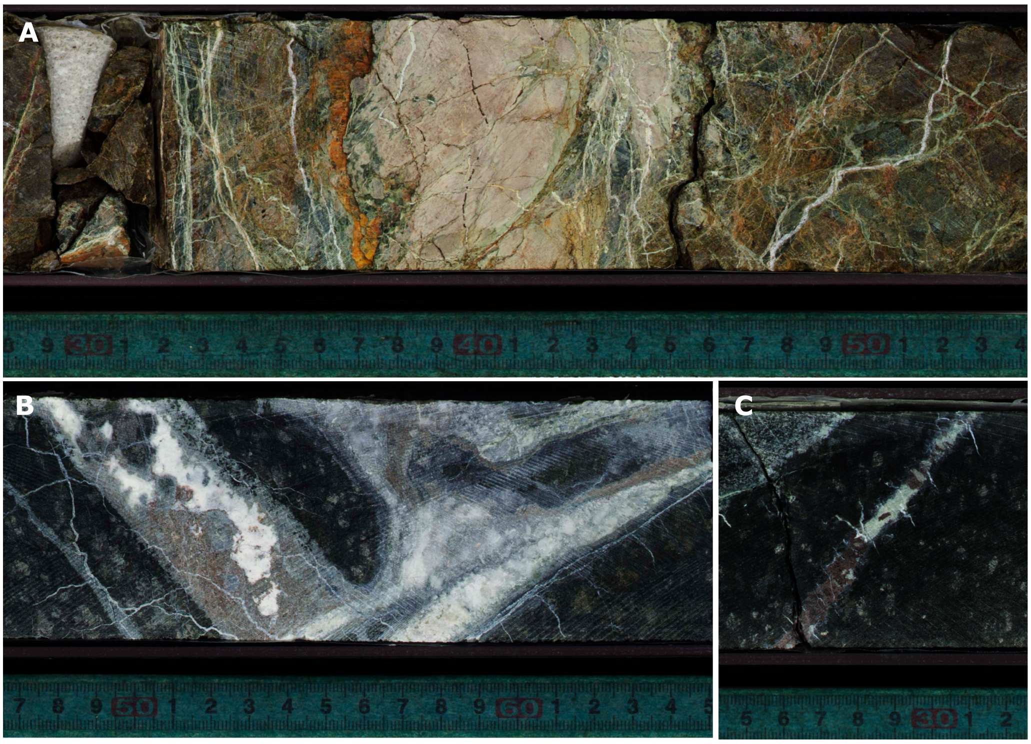

Figure F17. Gabbro dikes, Hole BA1B. **A.** Equant granular clinopyroxenes in gabbro dikes (33Z-1, 32–35 cm; XPL). opx = orthopyroxene. **B.** Serpentinized olivine (ol) partially surrounded by clinopyroxene (cpx) (30Z-2, 10–13 cm; XPL). **C.** Deformed clinopyroxene with undulose extinction (33Z-1, 32–35 cm; XPL). plag = plagioclase. **D.** Clinopyroxene intruding harzburgite (33Z-1, 32–35 cm; XPL).

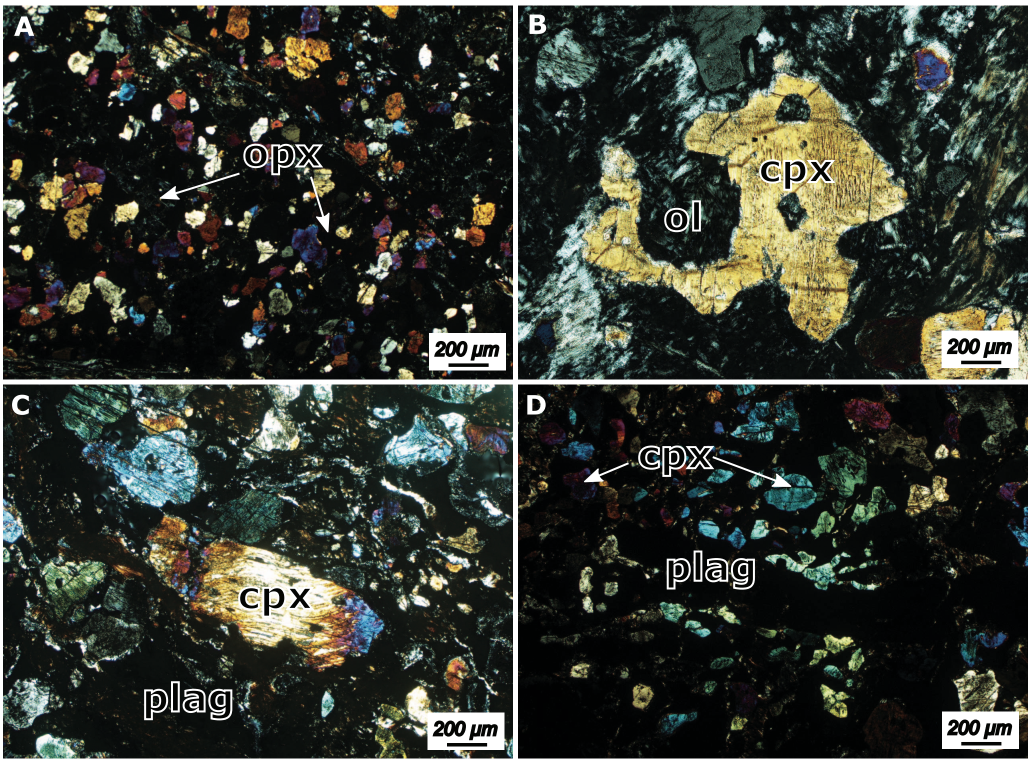

Figure F18. Gabbro dikes, Hole BA1B. **A.** Olivine (ol) proximal to larger orthopyroxene grains (35Z-3, 11–14 cm; XPL). cpx = clinopyroxene. **B.** Vermicular spinel associated with medium grains of clinopyroxene (35Z-3, 11–14 cm; XPL). **C.** Olivine grain partially surrounded by orthopyroxene (opx) (35Z-3, 11–14 cm; XPL). **D.** Interstitial plagioclase (plag) altered to clay minerals and cumulus phases clinopyroxene and olivine (55Z-3, 33–37 cm; XPL).

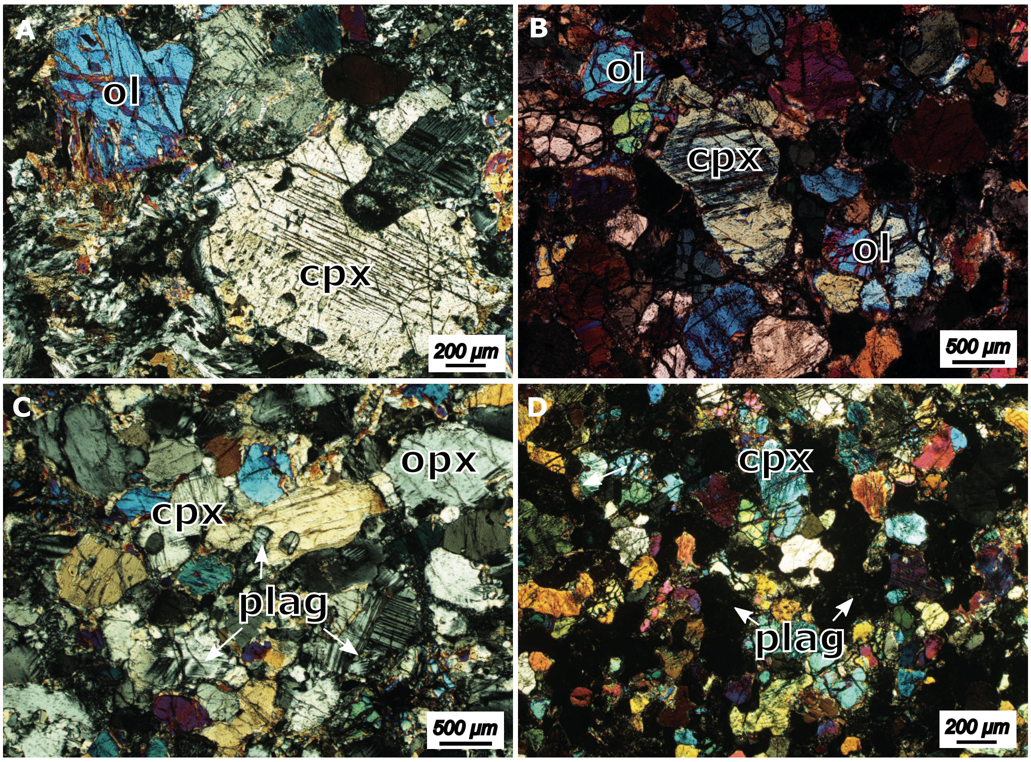

Figure F19. Dike types, Hole BA1B. **A.** Clinopyroxenite dike in Dunite with Gabbro Sequence (31Z-2, 26–40 cm). **B.** Clinopyroxenite dike in Harzburgite with Gabbro Sequence (93Z-1, 60–70 cm). **C.** Two olivine-rich clinopyroxenite dikes in Harzburgite with Gabbro Sequence (103Z-3, 47–74 cm).

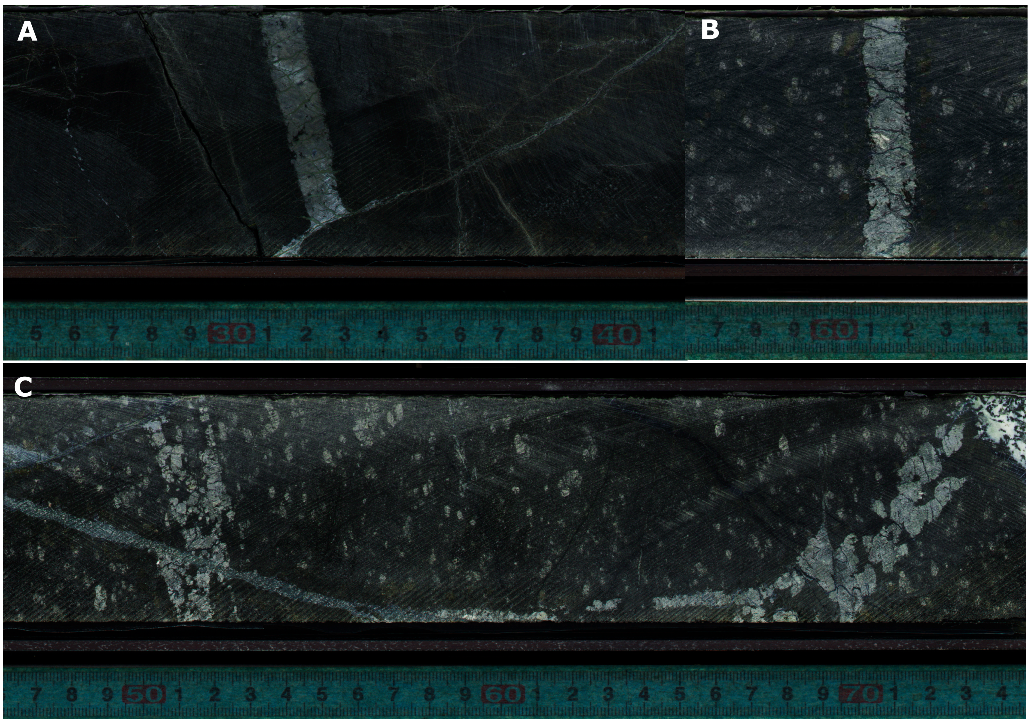

Figure F20. Clinopyroxenitic dikes in dunites from Dunite with Gabbro Sequence, Hole BA1B. **A**, **B**. Overview of a typical clinopyroxenitic dike with serpentinized olivine (ol) and altered clinopyroxene (cpx) (3Z-1, 39.5–42.5 cm; [A] PPL, [B] XPL). **C**. Talc (tlc) replacing clinopyroxene (20Z-4, 60.5–65.5 cm; XPL). **D**. Carbonate (carb) vein crosscutting olivine and clinopyroxene (20Z-4, 60.5–65.5; XPL).

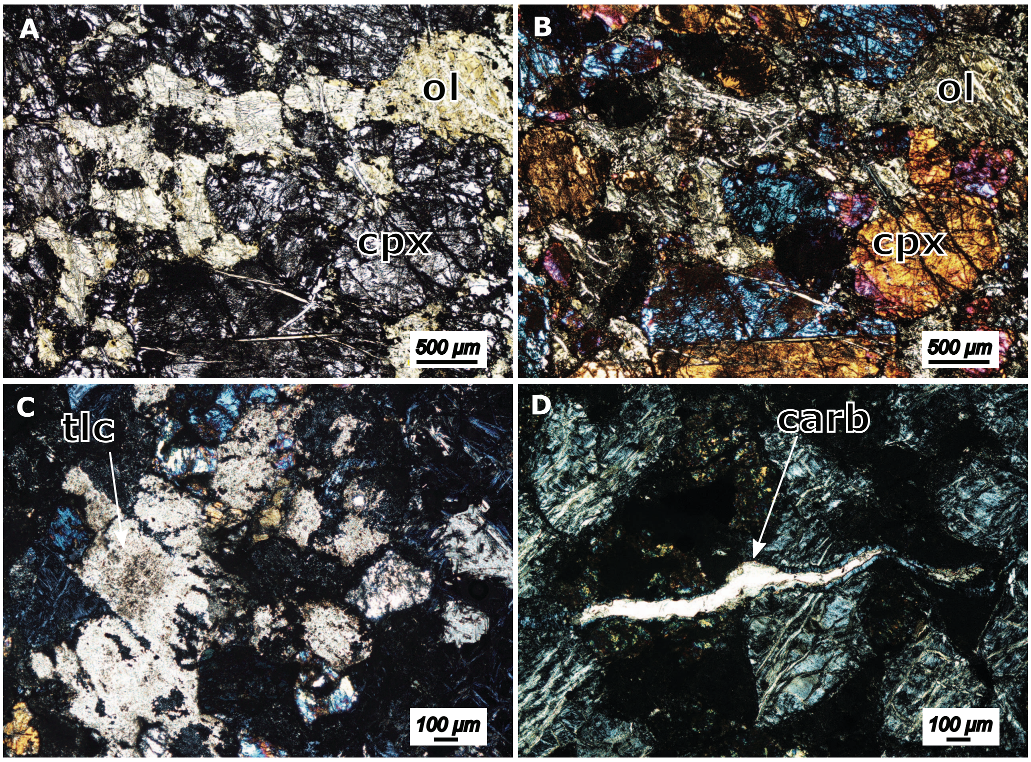

Figure F21. Clinopyroxenitic dikes in harzburgite from Harzburgite with Gabbro Sequence, Hole BA1B. **A.** Coarse-grained clinopyroxene (cpx) with orthopyroxene (opx) inclusion (98Z-2, 79–82 cm; XPL). **B.** Irregular contact between clinopyroxenitic dike and serpentinized dunite (98Z-2, 79–82 cm; XPL). **C**, **D.** Typical clinopyroxenite with serpentinized olivine (ol), clinopyroxene, and interstitial orthopyroxene (74Z-1, 36–41 cm; [C] XPL, [D] PPL). **E.** Phlogopite (phlog) formed in the contact between clinopyroxene and serpentinized harzburgite (98Z-2, 79–82 cm; PPL).

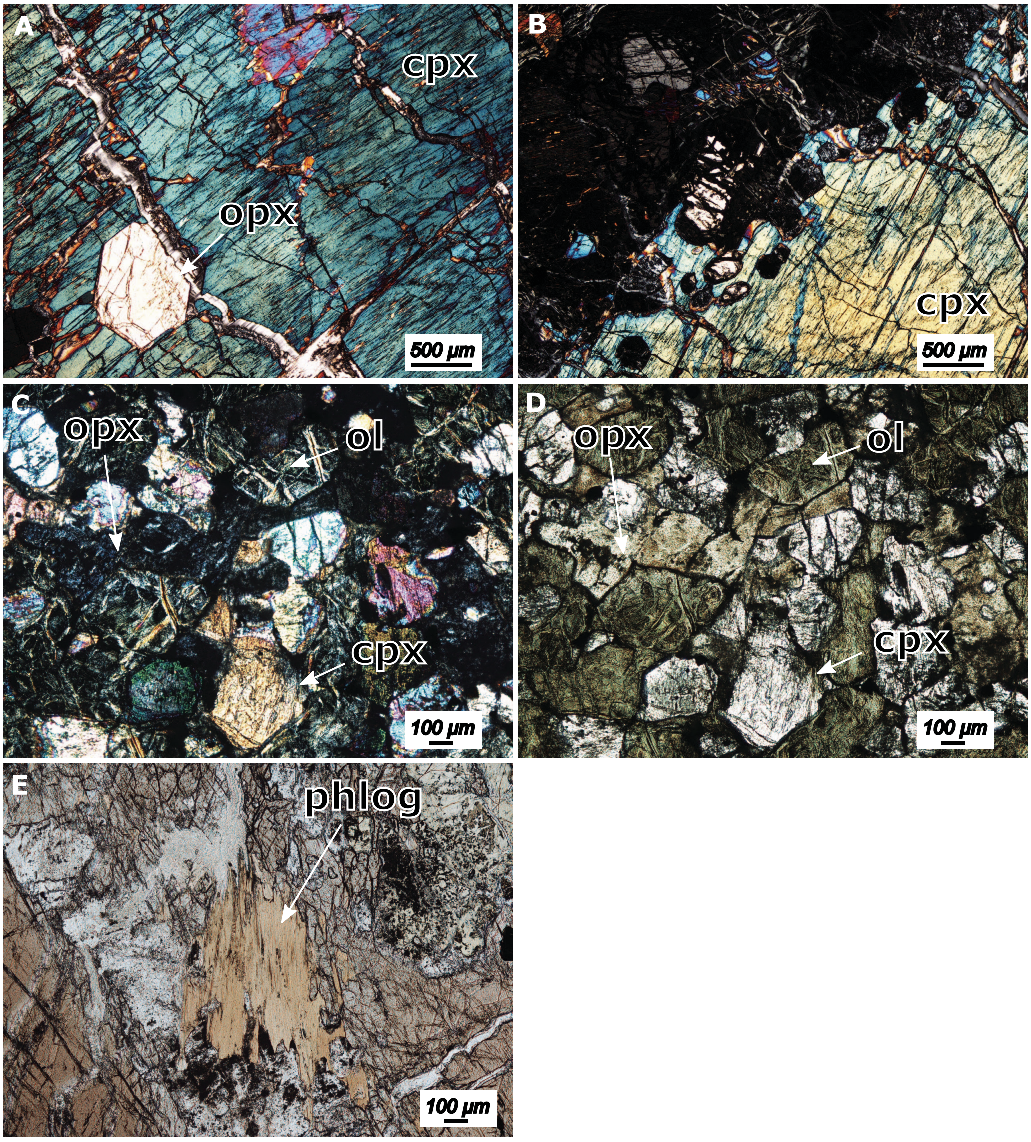

Figure F22. Dike types, Hole BA1B. **A**. Wehrlite dike accompanied by small gabbro seams in Harzburgite with Gabbro Sequence (77Z-1, 30–50 cm). **B**. Leucocratic intrusion described as anorthosite in macroscopic description in Harzburgite with Gabbro Sequence (45Z-3, 70–90 cm). **C**. Leucocratic intrusion described as troctolite in macroscopic description in Harzburgite with Gabbro Sequence (134Z-4, 5–25 cm).

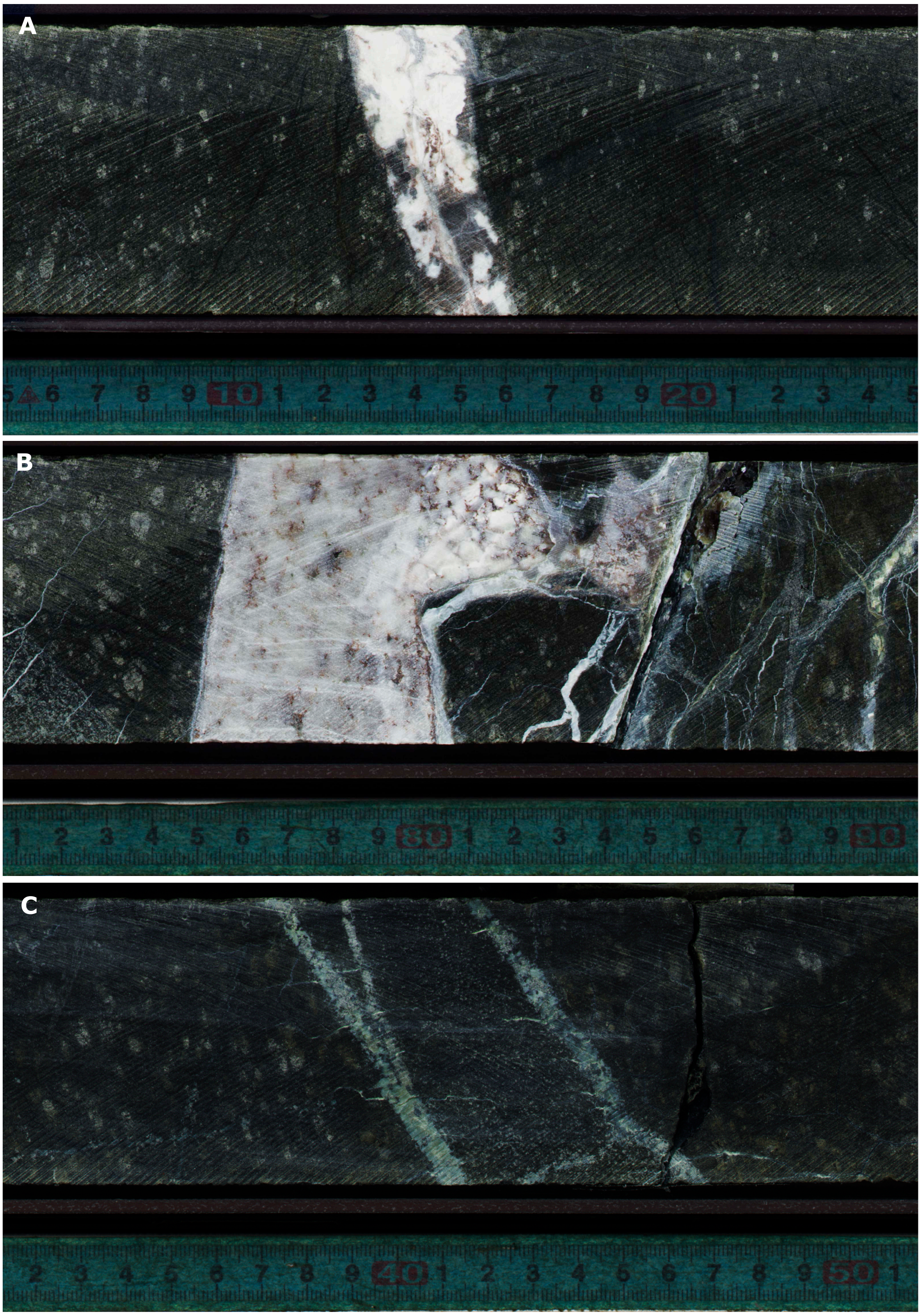

Figure F23. Wehrlite from Harzburgite with Gabbro Sequence (134Z-4, 69–71 cm). **A**, **B**. Typical overview of granular wehrlite with serpentinized olivine and orthopyroxene (opx) in (A) PPL and (B) XPL. **C**. Various sulfides (sulf) replacing chromite in RL. sp = spinel.

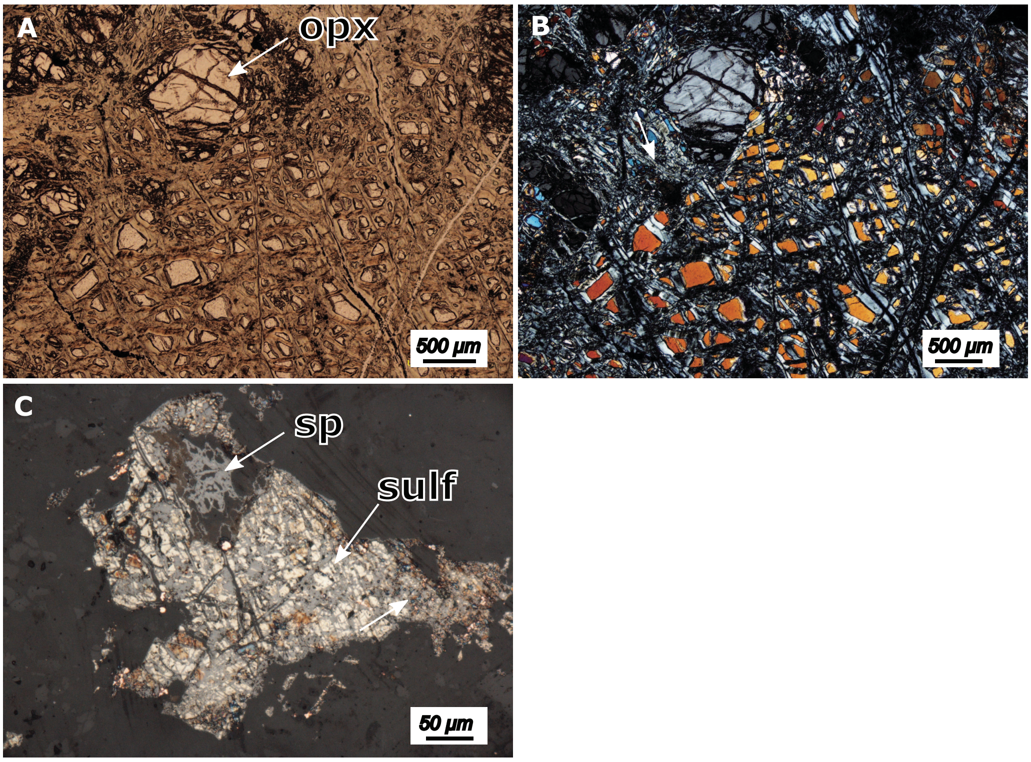

Figure F24. Leucocratic intrusion in Dunite with Gabbro Sequence, hydrogrossular replacing plagioclase (7Z-1, 48–53 cm; PPL). grt = garnet.

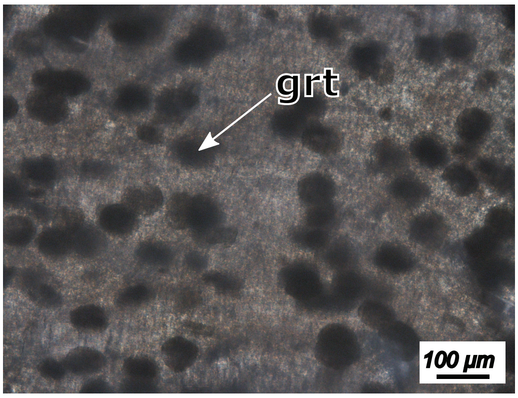

Figure F25. Lithostratigraphy summary log, Hole BA1B.

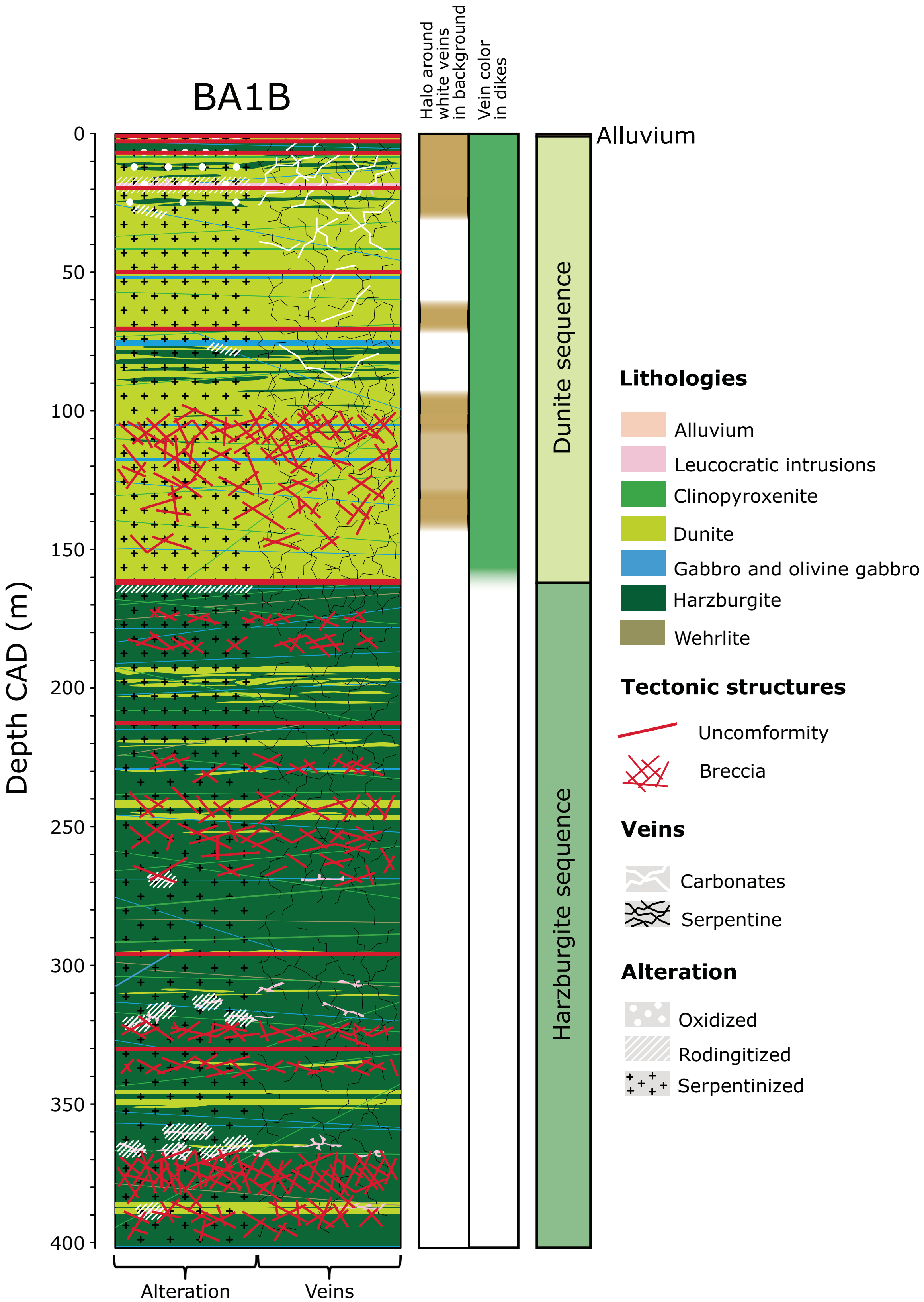

Figure F26. Crosscutting relationships of veins, Hole BA1B. Symbols indicate some of the most common younger vein types. For example, open symbols represent carbonate-bearing veins. Labeled points correspond to all of the vein types for which a significant number of relationships were observed. The horizontal axis indicates the number of instances in which one of the many vein type was observed to cut one of the common types, and the vertical axis represents instances in which one of the common types cuts them. For example, there are 3 observations of waxy green serpentine veins cutting carbonate-bearing veins, and ~40 observations of carbonate veins cutting waxy green veins.

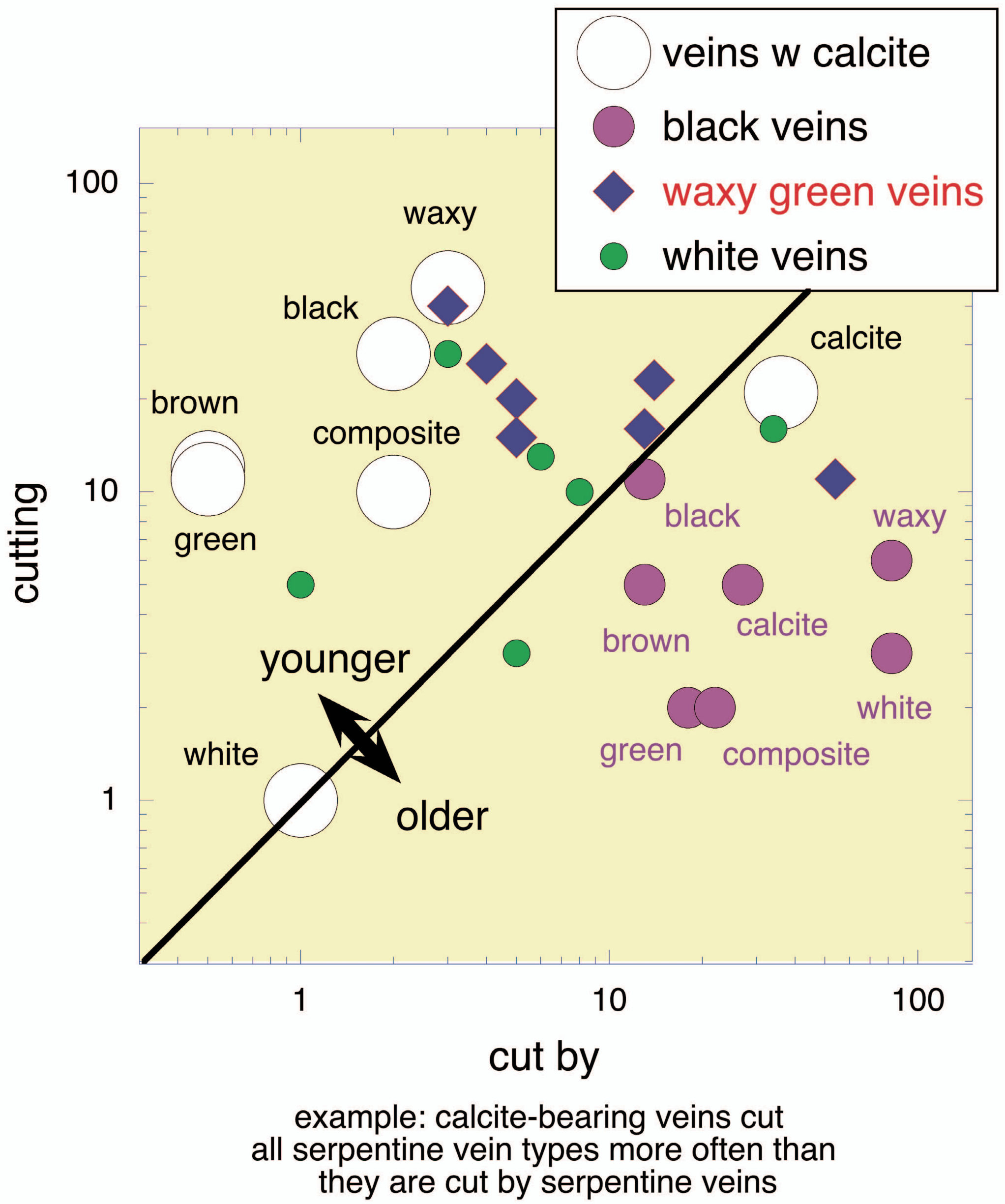

Figure F27. Composite photomicrograph of mesh veins and (dark) cores, demonstrating coarsening of serpentine mesh veins associated with a through-going oxide vein, Hole BA1B (PPL, 2.5×; field of view [FOV] = 4.2 mm) (TS 26Z-3, 42–45 cm).

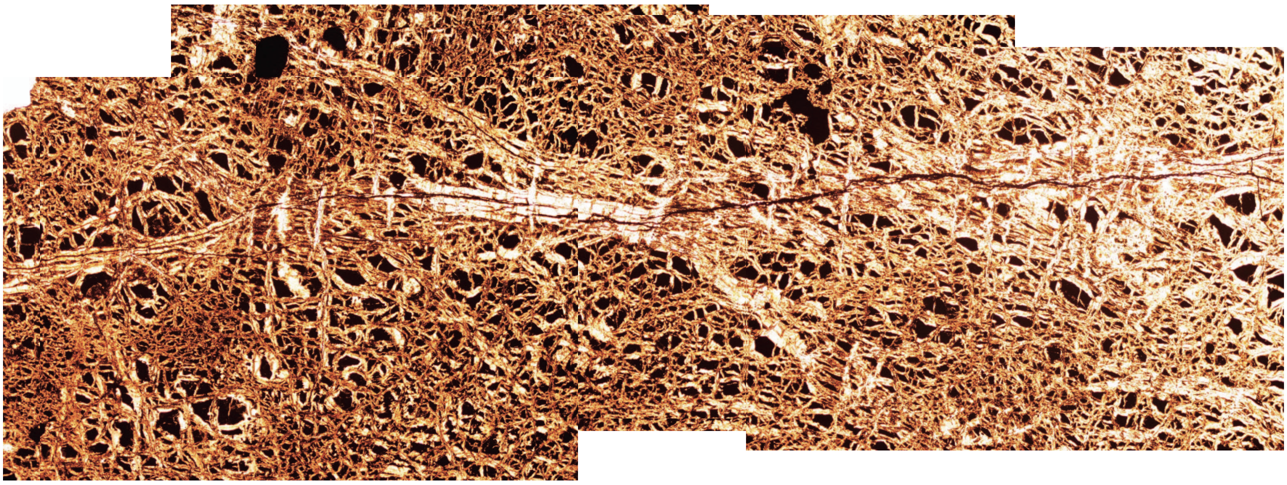

Figure F28. Variation of area% veins, Hole BA1B, excluding black serpentine veins (vein type Sa), and patchy alteration of deformed magmatic blocks (Sg). Areas were computed for each meter of core, based on vein width and vein density data. This procedure resulted in spuriously high values, sometimes > 100%, and was modified with the assumption that actual vein densities were 0.5, 1, 3, 3, and 3 per 10 cm for vein density levels 1–5, yielding results that correspond approximately to estimated vein areas determined by visual inspection of core, and quantify the relative variation of vein area downhole. However, the specific values remain—obviously—highly uncertain.

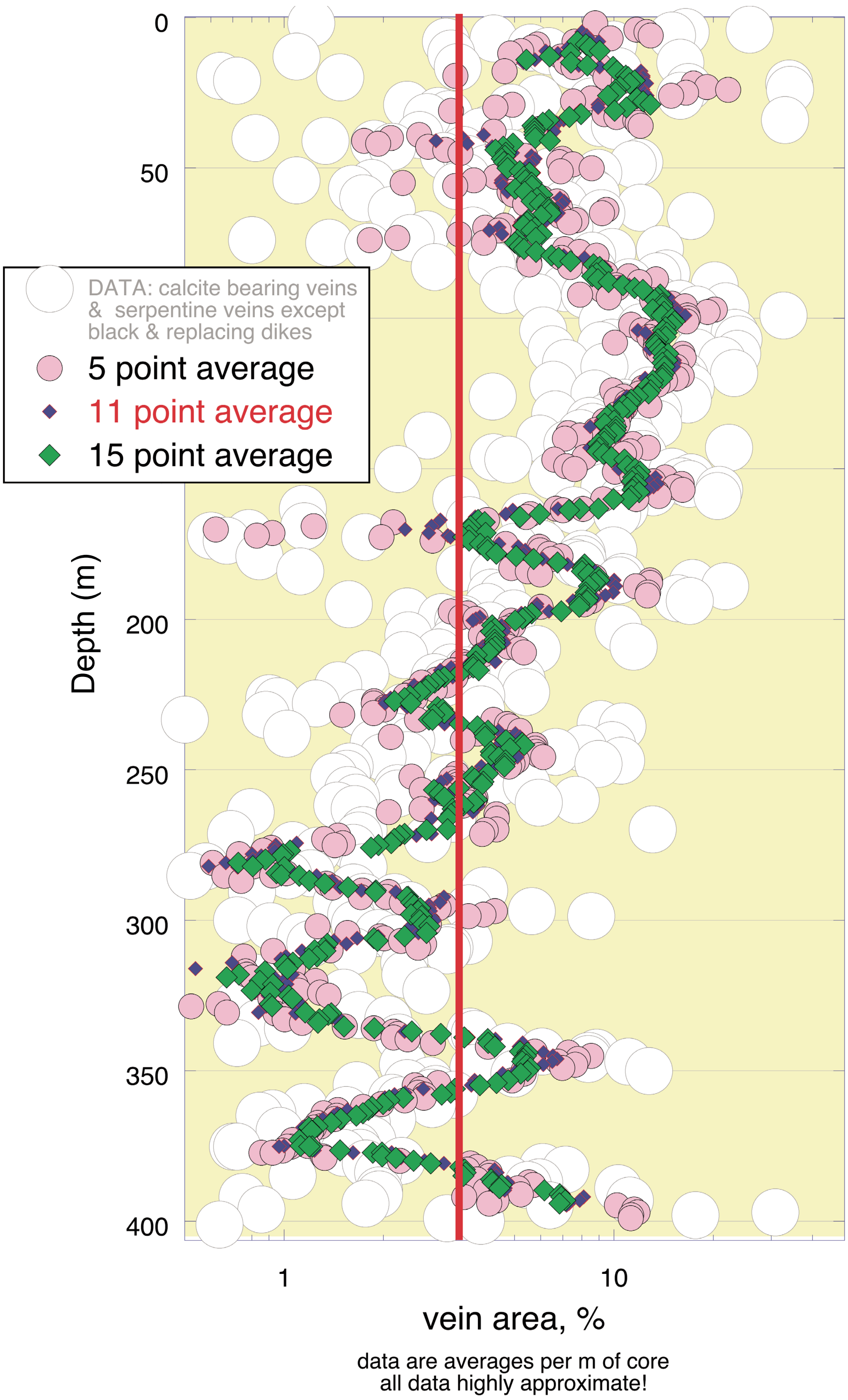

Figure F29. Observed vein types as a function of depth, Hole BA1B.

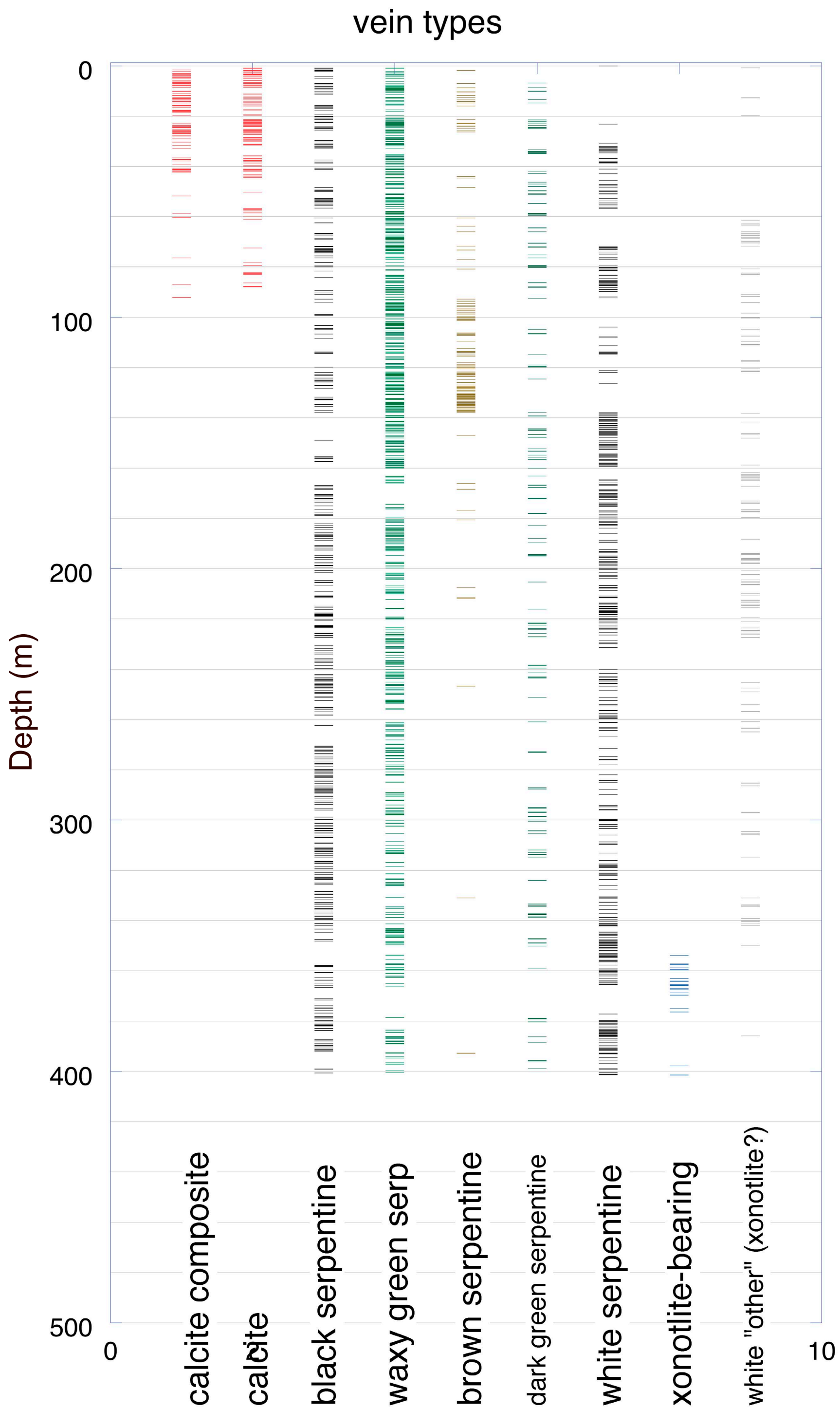

Figure F30. 25-m running average of specific vein type observations as a function of depth, Hole BA1B.

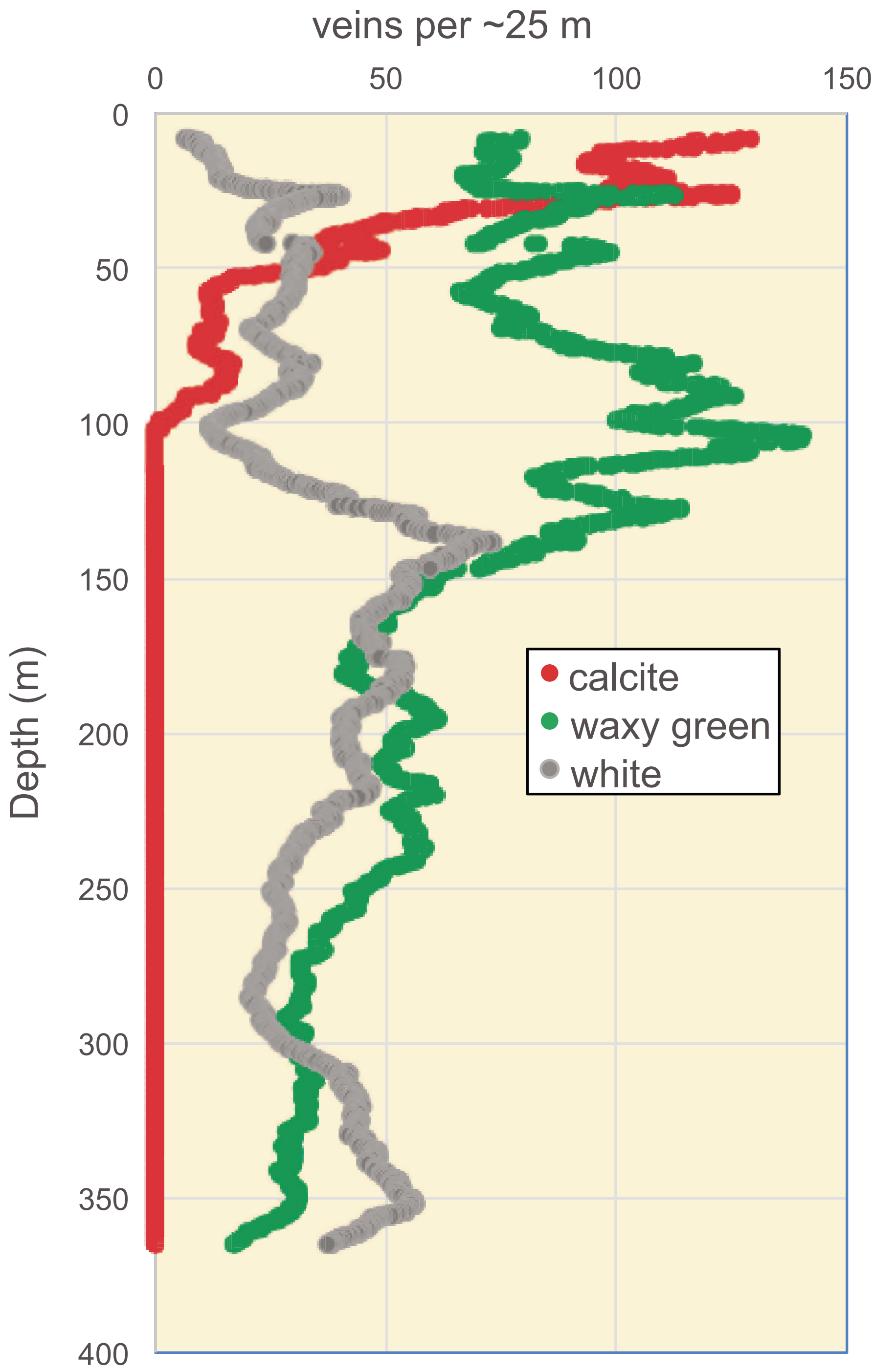

Figure F31. Exemplary images of vein types, Hole BA1B. **A.** Vein types described during this leg. **B.** Vein type Ca1 (17.76–17.79 m depth). **C.** Vein type Ca2 (4.51–4.53 m). **D.** Vein type Cb (0.75 m). **E.** Vein type Sa (1.96 m). **F.** Turtle-textured vein type Sb (202.2–202.3 m). **G.** Chaotic-textured vein type Sc (109.6 m). The Sc vein cuts the contact between a dike and host peridotite. **H.** Vein type Sd (131.8 m). The thicker Sd vein cuts a thinner Sd vein.

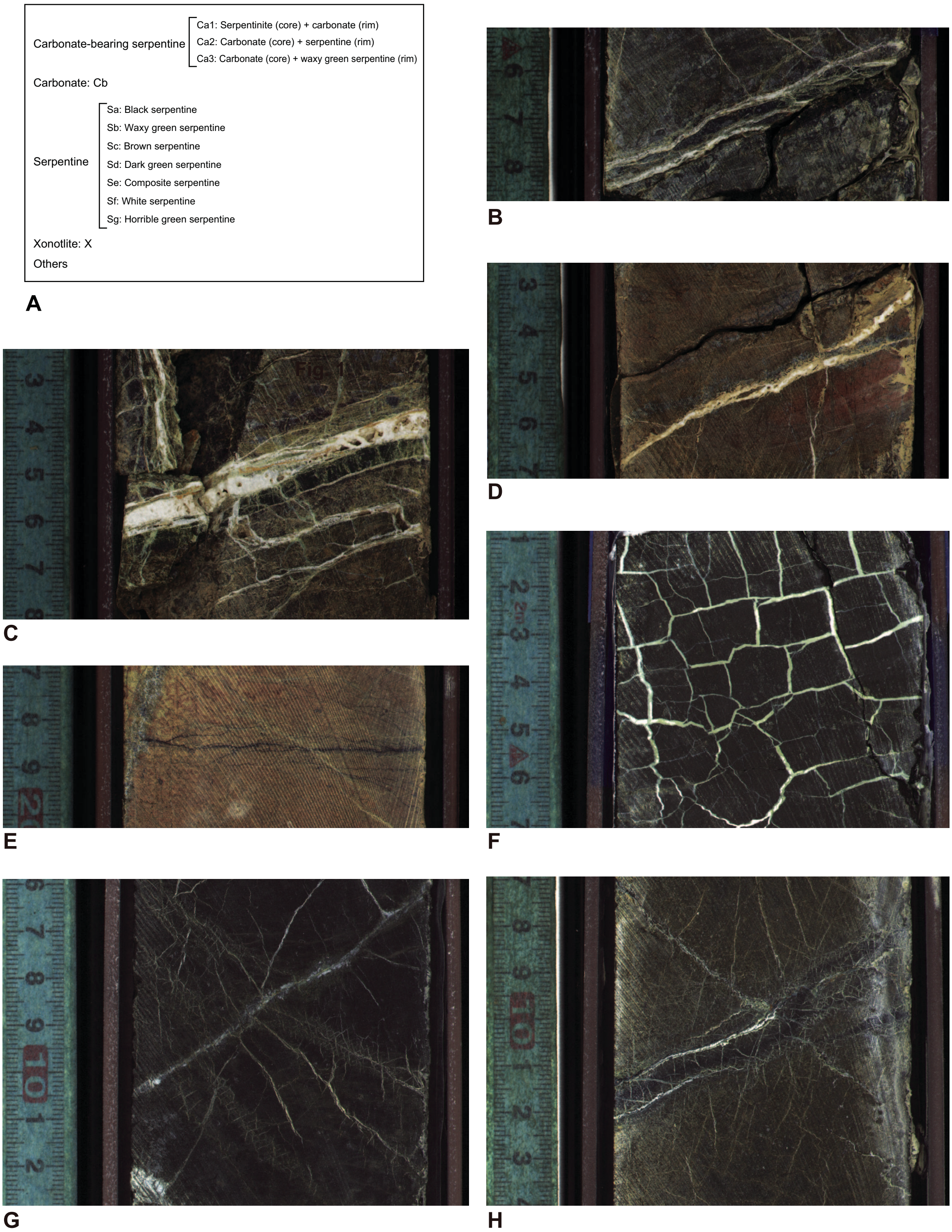

Figure F32. Exemplary images of vein types, Hole BA1B. **A.** Composite green and black vein type Se (132.6 m depth). **B.** Composite green and white vein type Se (135.9 m). **C.** Vein type Sf (12.5 m). **D.** Vein type Sg (105.6–105.8 m). **E.** White vein type X cutting a magmatic dike (202.3–202.5 m).

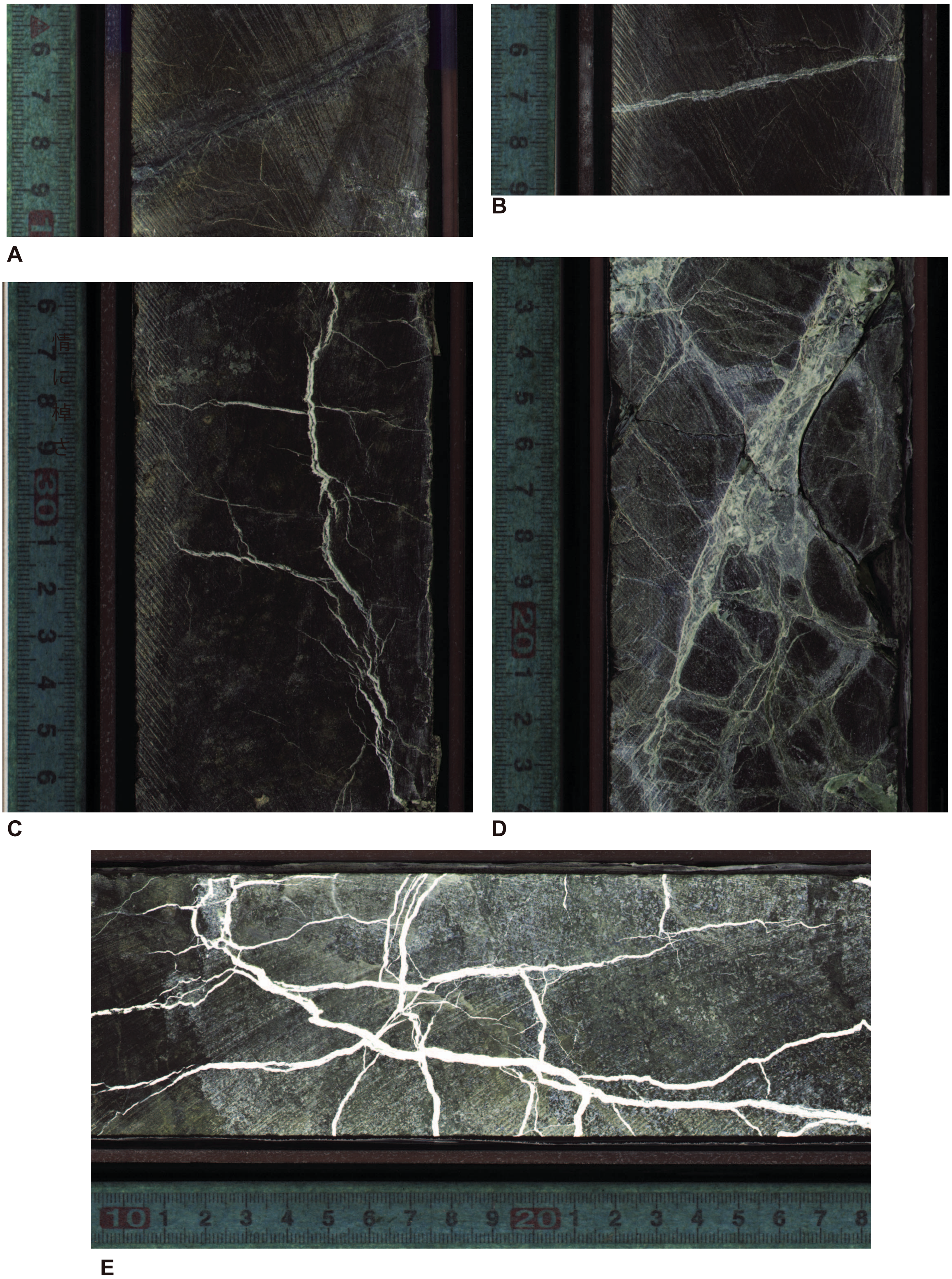

Figure F33. Typical veins in dunite and harzburgite lithologies, Hole BA1B. **A.** Pervasive mesh network in harzburgite composed of serpentine and magnetite). **B.** Subparallel serpentine veins "emerging" from the pervasive mesh texture. **C.** Long-range serpentine networks, logged as vein sets or networks of banded serpentine veins. **D.** Long-range composite serpentine veins in places cut by crosscutting "Frankenstein" type veins. **E.** Late calcite bands within banded or composite serpentine veins. **F.** Late calcite veins crosscutting earlier serpentine vein textures.

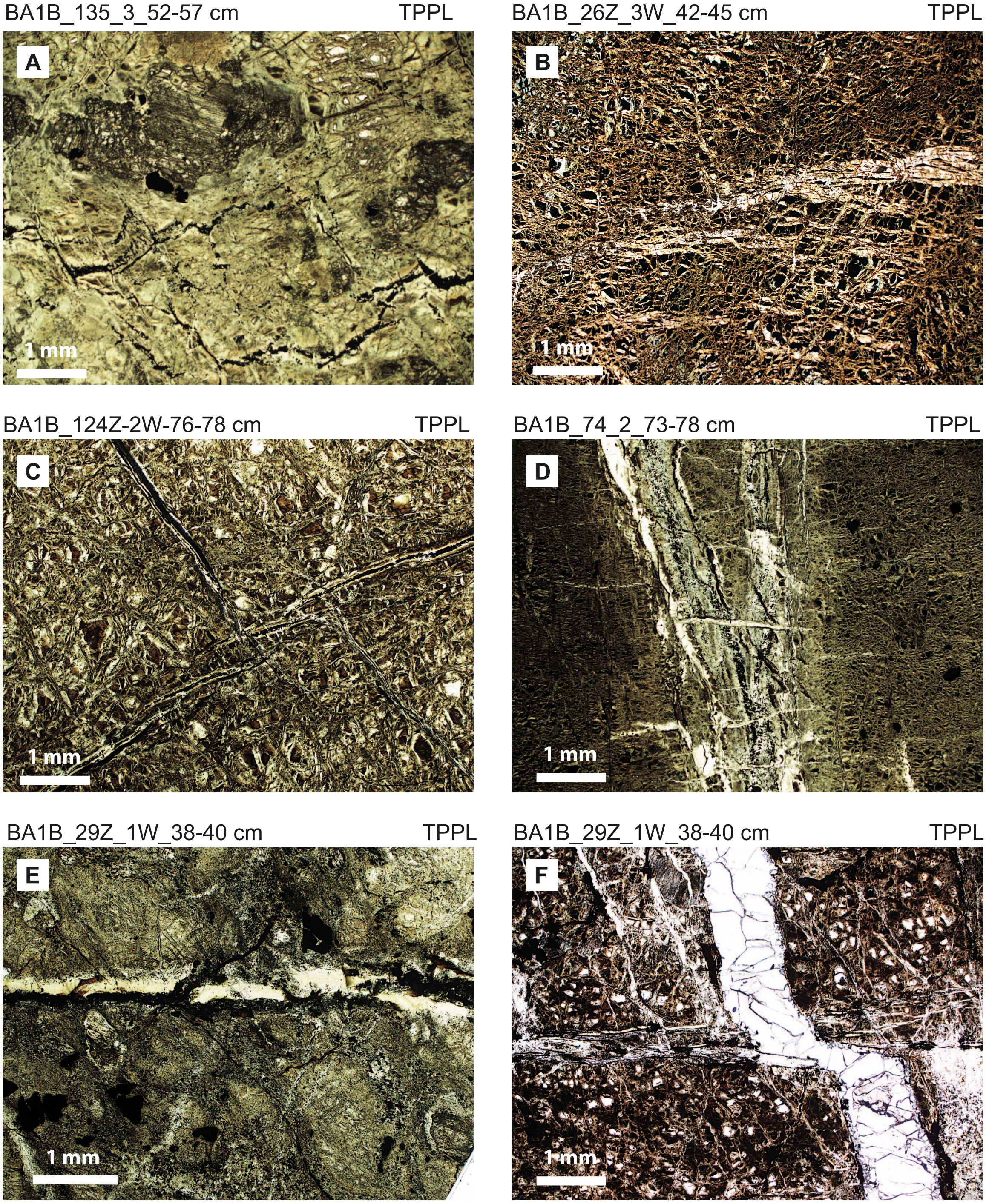

Figure F34. Typical veins in and near rodingitized gabbro and pyroxenite dikes, Hole BA1B. **A**, **B**, Microcrystalline/amorphous serpentine. **C**, **D**. Patch of "waxy green serpentine." **E**. Xonotlite. **F**. Prehnite.

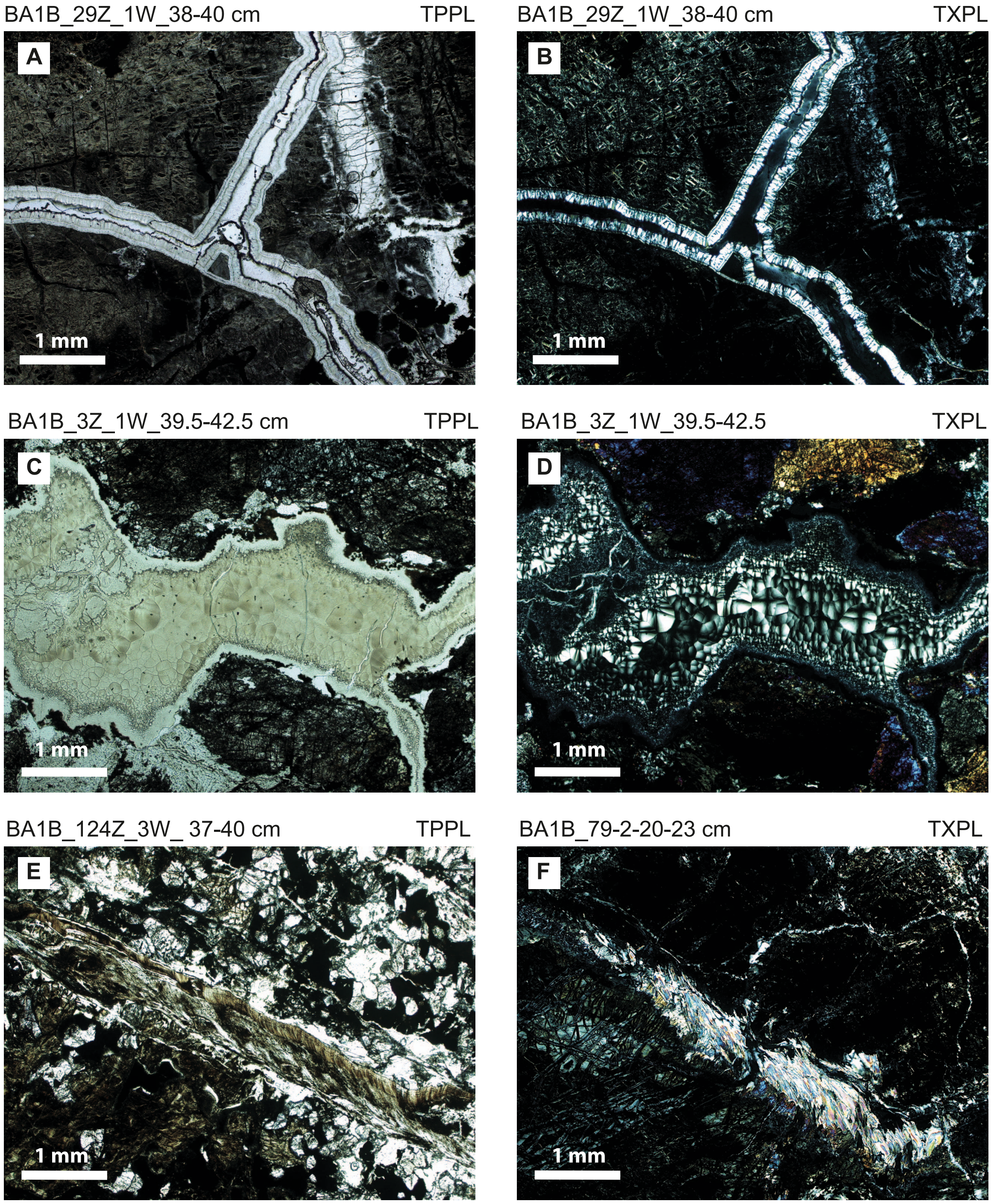

Figure F35. Reflected light microscopy of opaque minerals, Hole BA1B. **A.** Rare sulfides occur in the upper half of the hole. **B.** In rare cases, native copper and Ni-Fe alloy were recognized in serpentine veins of the mesh texture in the lower third of the hole.

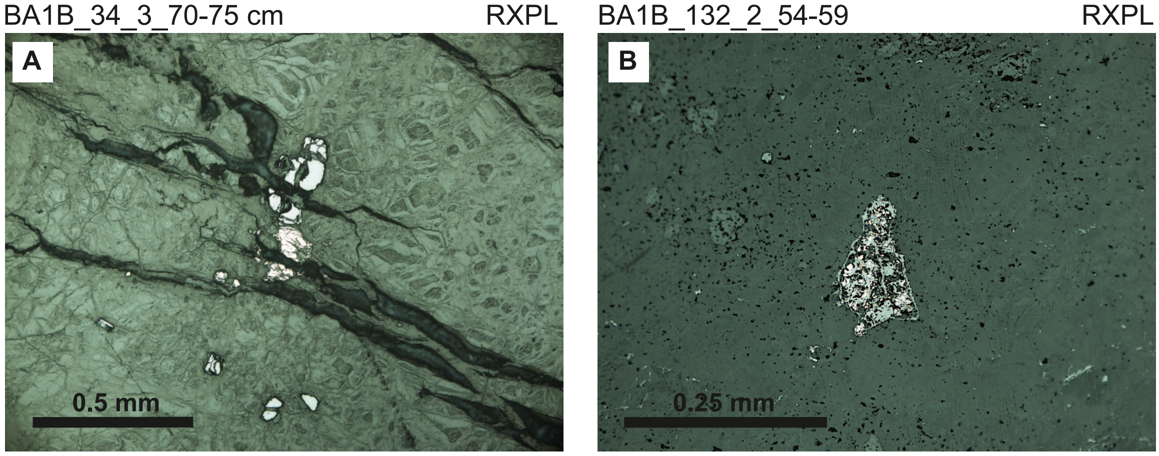

Figure F36. X-ray diffraction patterns of powder samples collected at the locations marked by red crosses on pictures of the core sections, Hole BA1B. **A, B.** White serpentine vein (Sf) mainly composed of serpentine (S) and magnetite (M) (56Z-1, 14–15 cm). **C, D.** White vein that crosscuts the magmatic dike, exclusively composed of xonotlite (30Z-2, 14–16 cm). All the main peaks are associated with xonotlite and were thus not indexed.

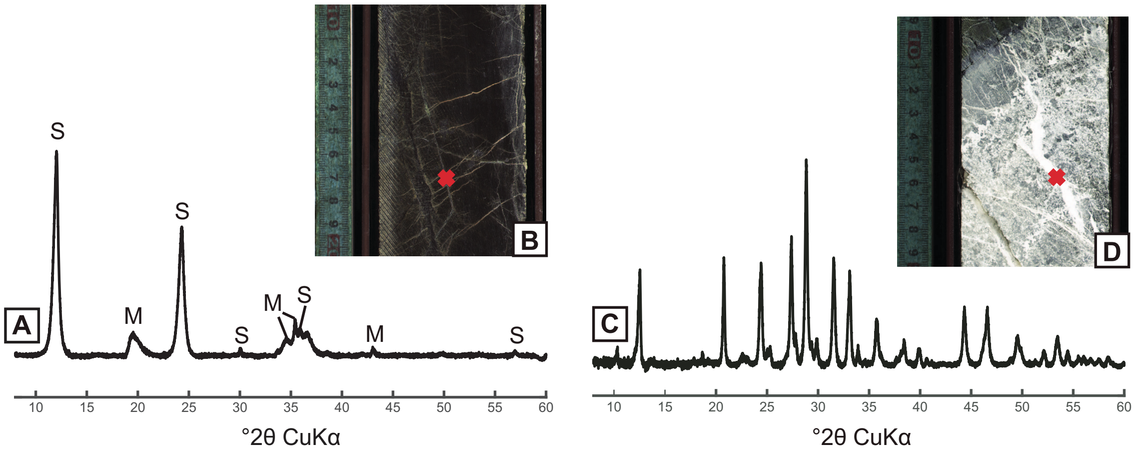

Figure F37. Photomicrographs and quantitative data from Hole BT1B constraining (A, B) oxygen fugacity in core, (C) downhole measurements of water composition, and (D) published geologic data from the mantle section of the Samail ophiolite. **A.** Hematite veins and disseminated veins in surrounding host rock in the upper part of the hole (onsite TS BT1B-4Z-2, 43–48 cm; PPL, 2.5×, FOV = 4.2 mm). **B.** Awaruite (bright silver) and native copper (copper colored!) armored in magnetite within a mesh serpentine vein (shipboard TS BT1B-132Z-3, 54–59 cm; RL, PPL). **C.** Downhole fO_2 in water, calculated from Eh and pH data collected during geophysical logging of Hole BT1B in March 2018 (Pezard et al., pers. comm.) (log fO_2 ~ 67.6 Eh + 4 pH –83.11). **D**. Observations of mineral phase equilibria (Lorand, 1987; de Obeso et al., 2020) in Samail peridotites, and water composition in water monitoring well NSHQ14 (Paukert et al., 2012), 10 m from Hole BA3A, a few kilometers south-southwest of Hole BA1B.

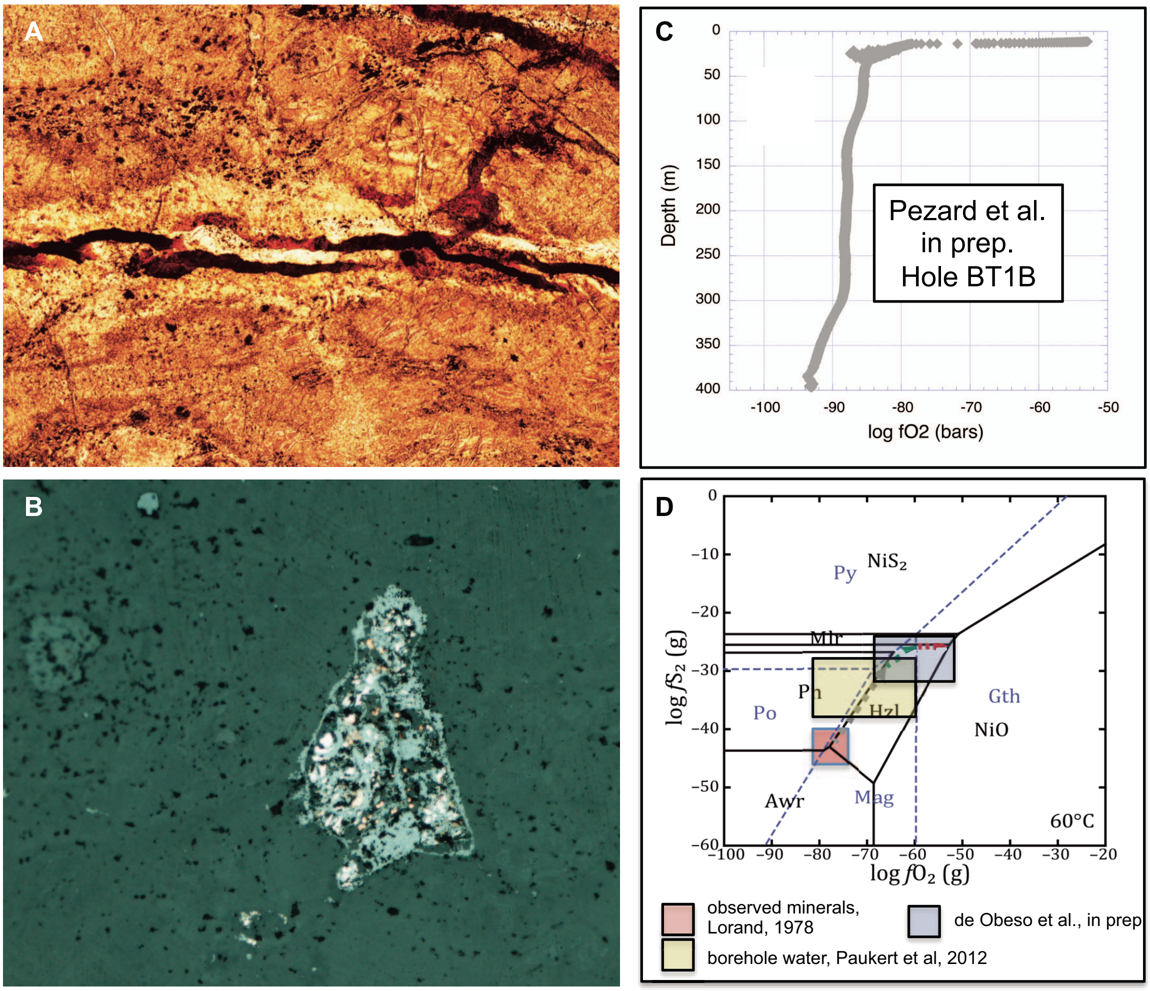

Figure F38. pH and temperature of water in Hole BT1B in March 2018, measured during geophysical logging (Pezard et al., pers. comm.).

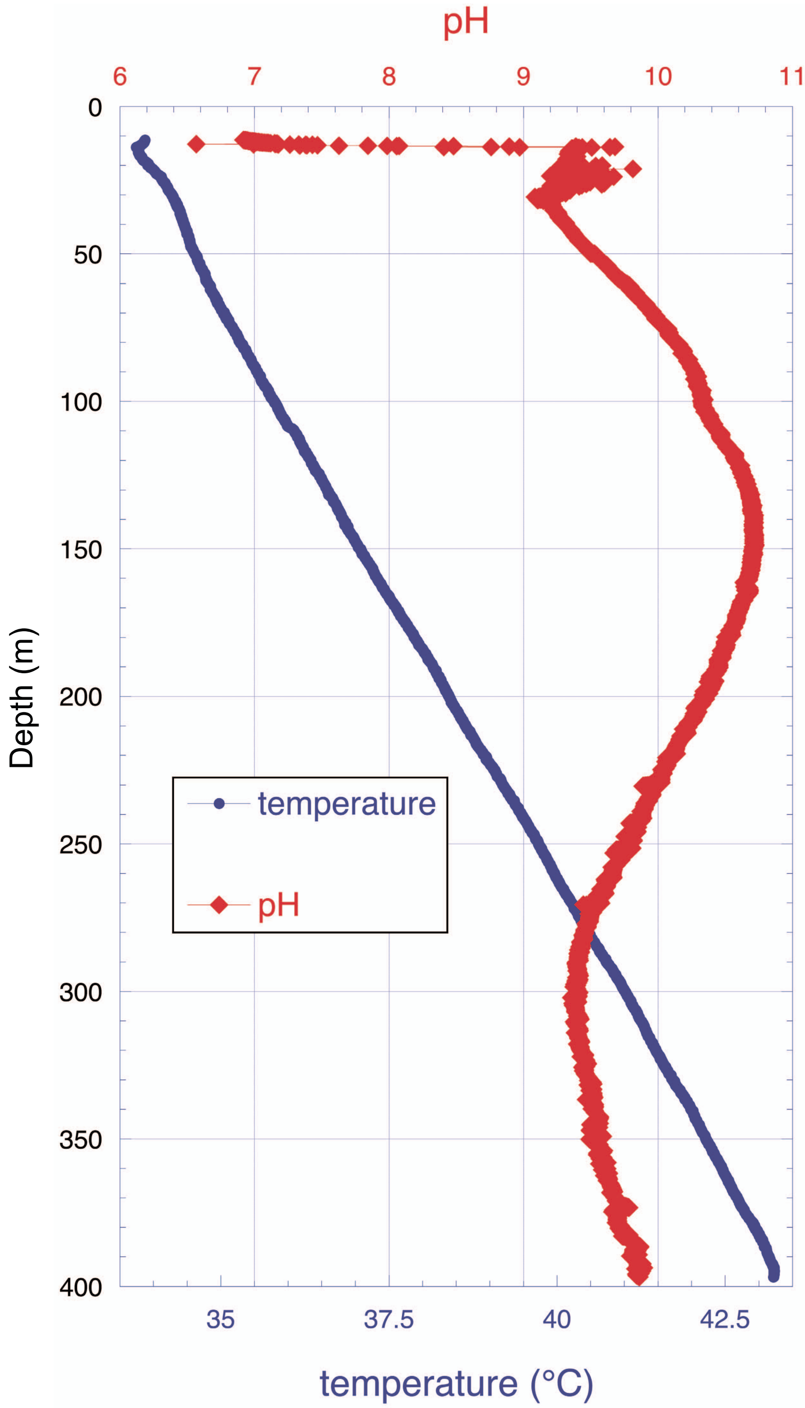

Figure F39. Negative correlation between frequency of calcite-bearing veins (data as in Fig. F30) and pH at the same depth, Hole BA1B.

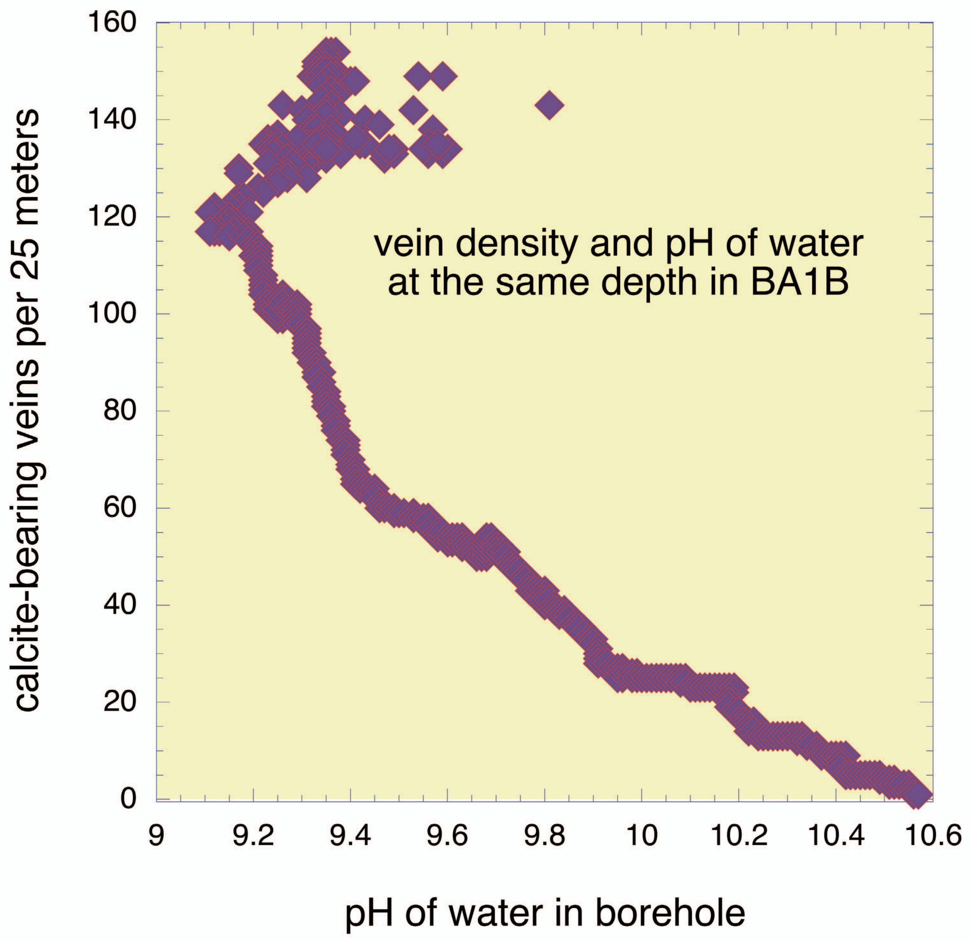

Figure F40. Intrusive textures, Hole BA1B. **A.** Two gabbroic dikes with sharp contacts but different grain sizes. **B.** Different dike types, from left: irregular pyroxenite, sharp gabbroic dike cut by a fault, two different crosscutting generations of gabbroic dikes, an irregular gabbroic dike, and a crosscutting relationship between a pyroxenite and a gabbro. **C.** Sharp contact. **D.** Irregular contact. **E.** Crosscutting dikes. **F.** Curved contact.

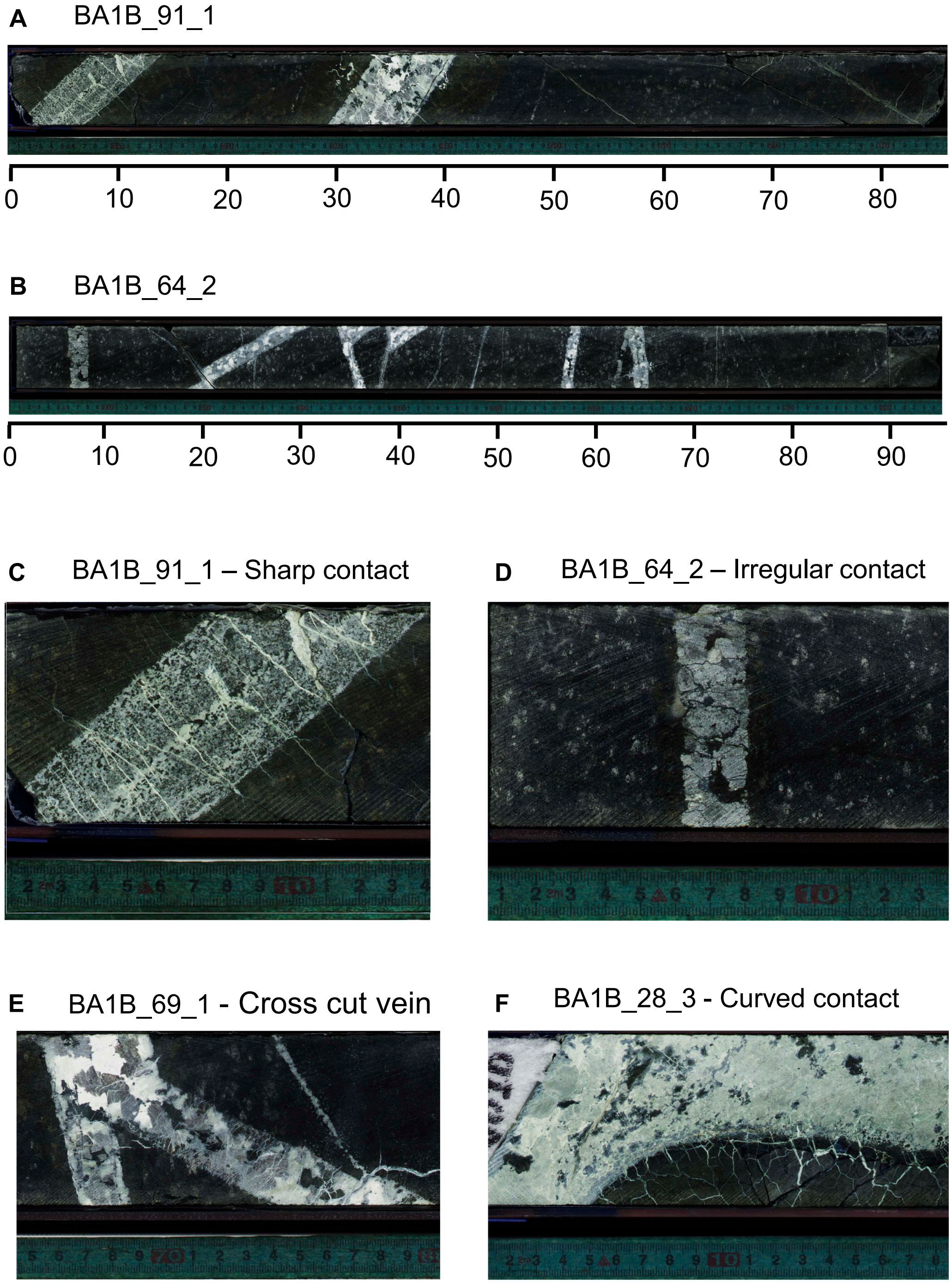

Figure F41. Locations and dips of magmatic contacts plotted alongside Hole BA1B lithology. Comparative graphic with apparent thickness vs. depth. Blue bars = gaps in the data corresponding to faults or cataclastic zones.

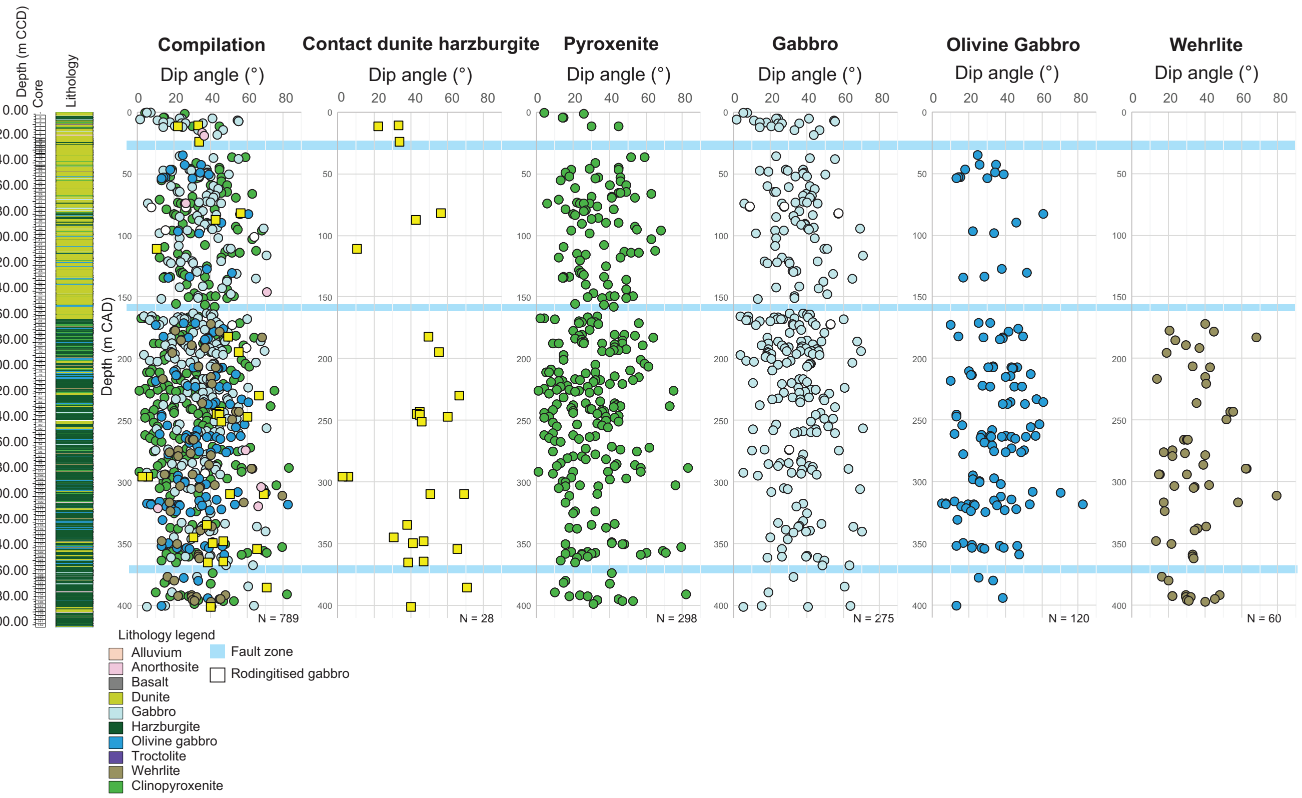

Figure F42. Rose diagram plots with statistics (using Stereonet 9.5, Cardozo and Allmendinger, 2013) of the dip angle for each type of contact, Hole BA1B.

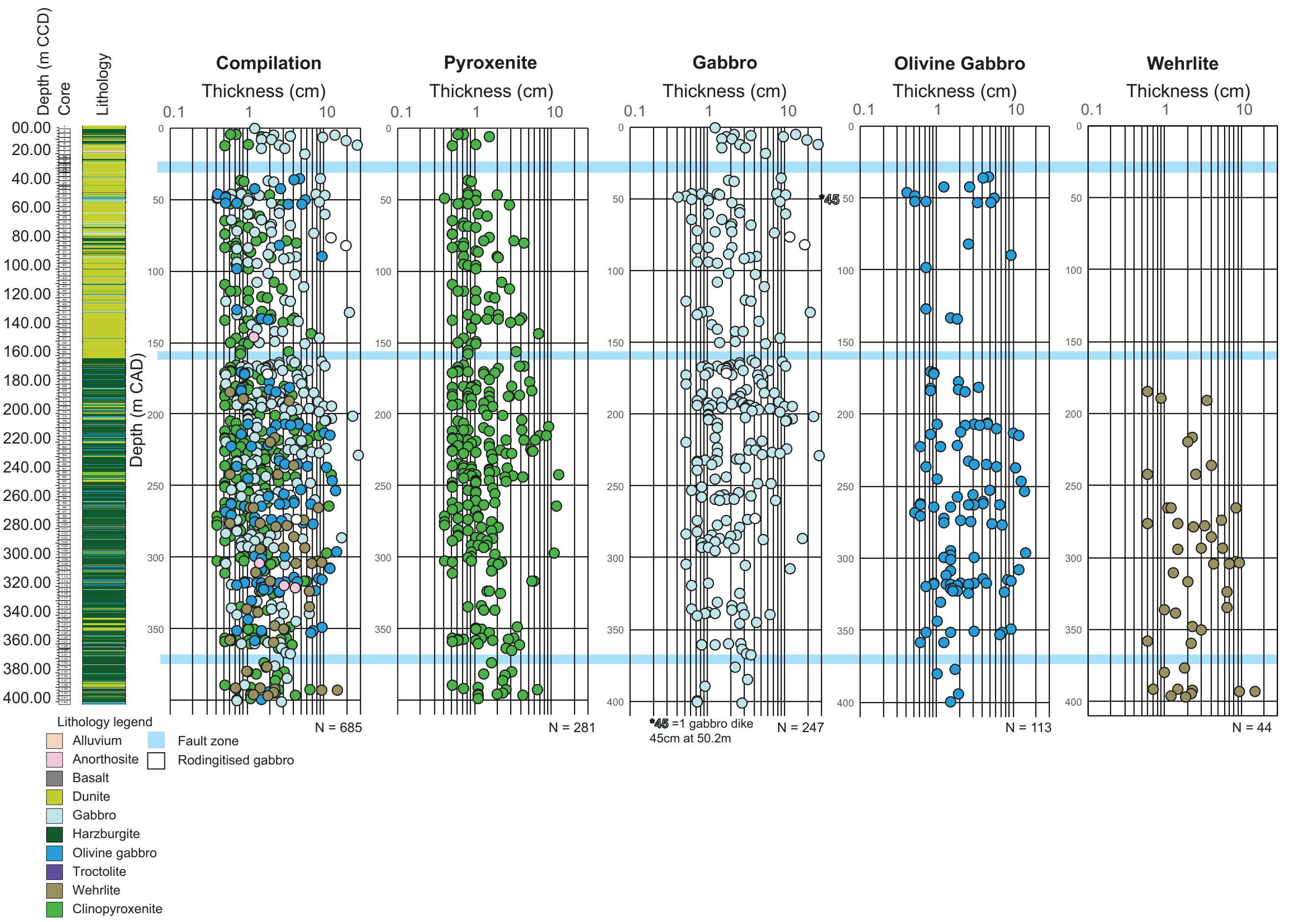

Figure F43. Locations and thicknesses of magmatic contacts plotted alongside Hole BA1B lithology. Comparative graphic with the dip angle calculated vs. depth. Blue bars = gaps in the data corresponding to faults or cataclastic zones.

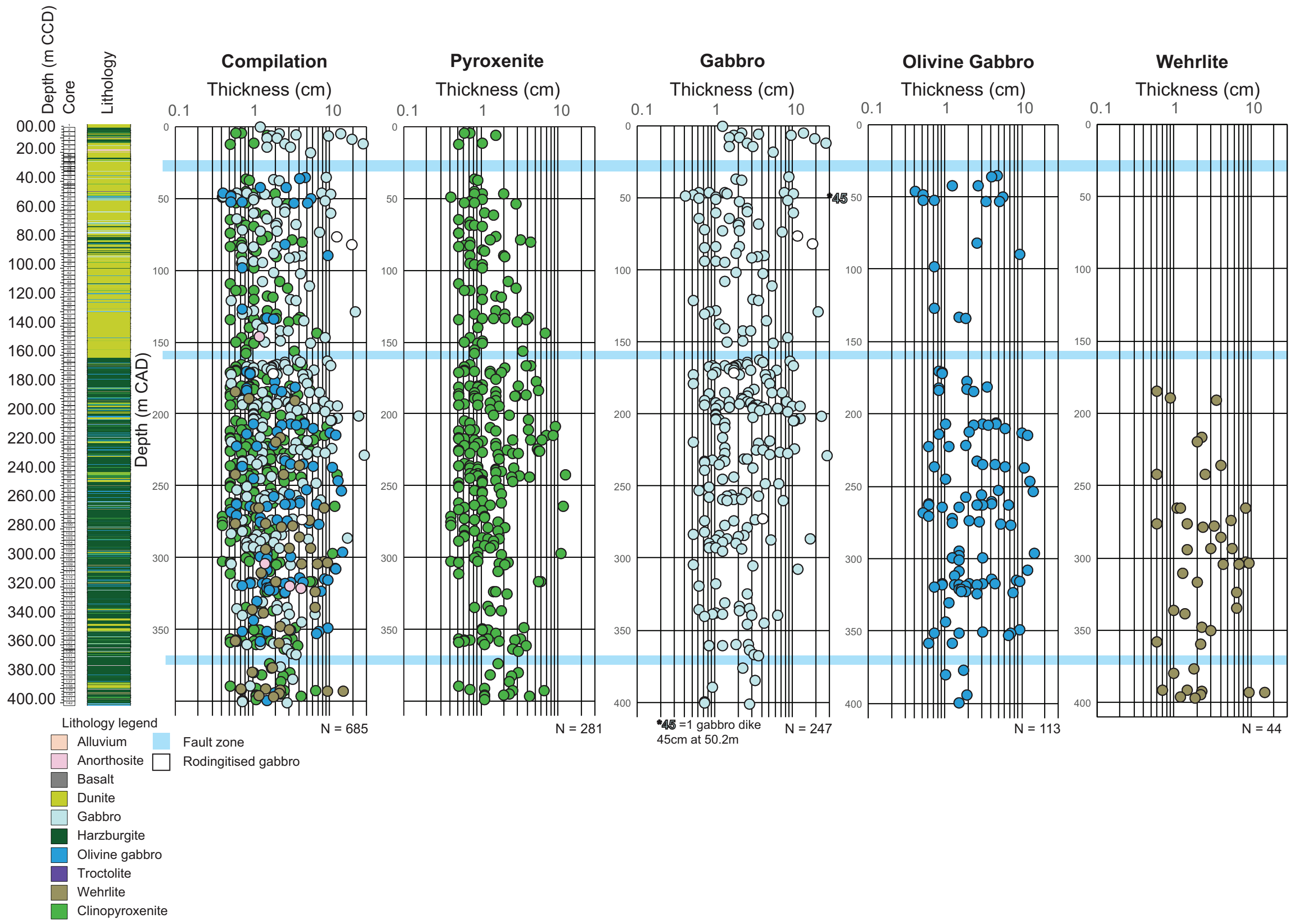

Figure F44. Types of peridotite fabric defined by geometry of pyroxene, Hole BA1B. **A.** Harzburgite shows porphyroclastic texture with slightly elongated pyroxene. **B.** Harzburgite shows protomylonitic foliation with strongly elongated pyroxene. **C.** XCT scan; slightly elongated pyroxenes are exhibited by brighter colors. **D**. XCT scan; strongly elongated pyroxenes are exhibited by brighter color. **E.** Left: slightly elongated pyroxenes form porphyroclastic texture; right: strongly elongated pyroxenes form protomylonitic texture. **F.** Folded pyroxenite dike. The protomylonitic foliation lines the axial plane of the fold and is parallel to it.

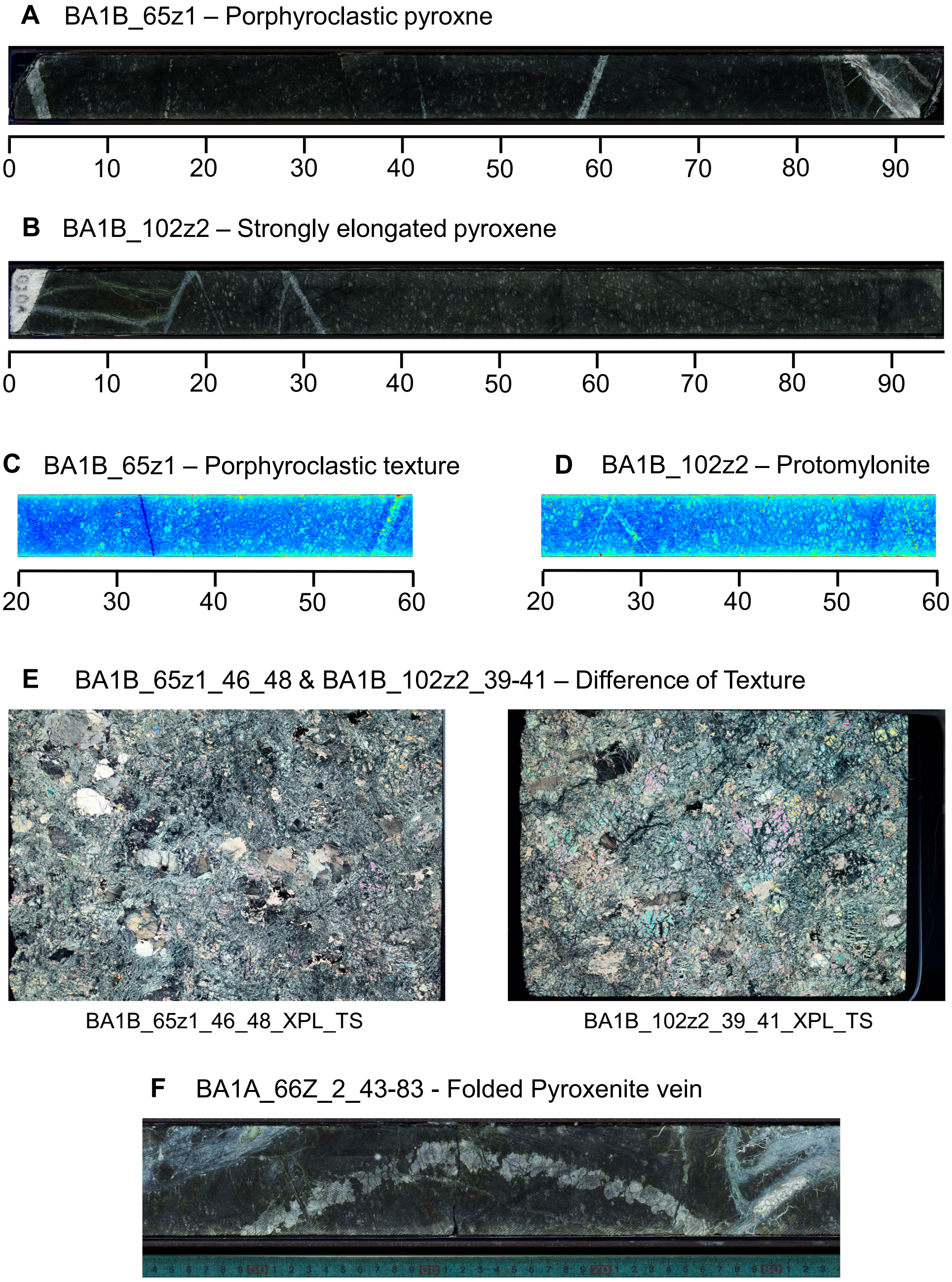

Figure F45. Downhole dip angle and crystal-plastic fabric intensity of foliation in dunites and harzburgites, Hole BA1B. **A.** Crystal-plastic intensity: 0 = undeformed–protogranular, 1 = weakly foliated (porphyroclastic), 2 = moderately foliated (porphyroclastic), 3 = protomylonite, 4 = mylonite, 5 = ultramylonite, 6 = pseudotachylite. **B.** Dip angle of the pyroxene impregnation foliation in dunite and harzburgite and harzburgite foliation. **C.** Rose diagram of dip angles of pyroxene foliation. Most dip angles are <30°.

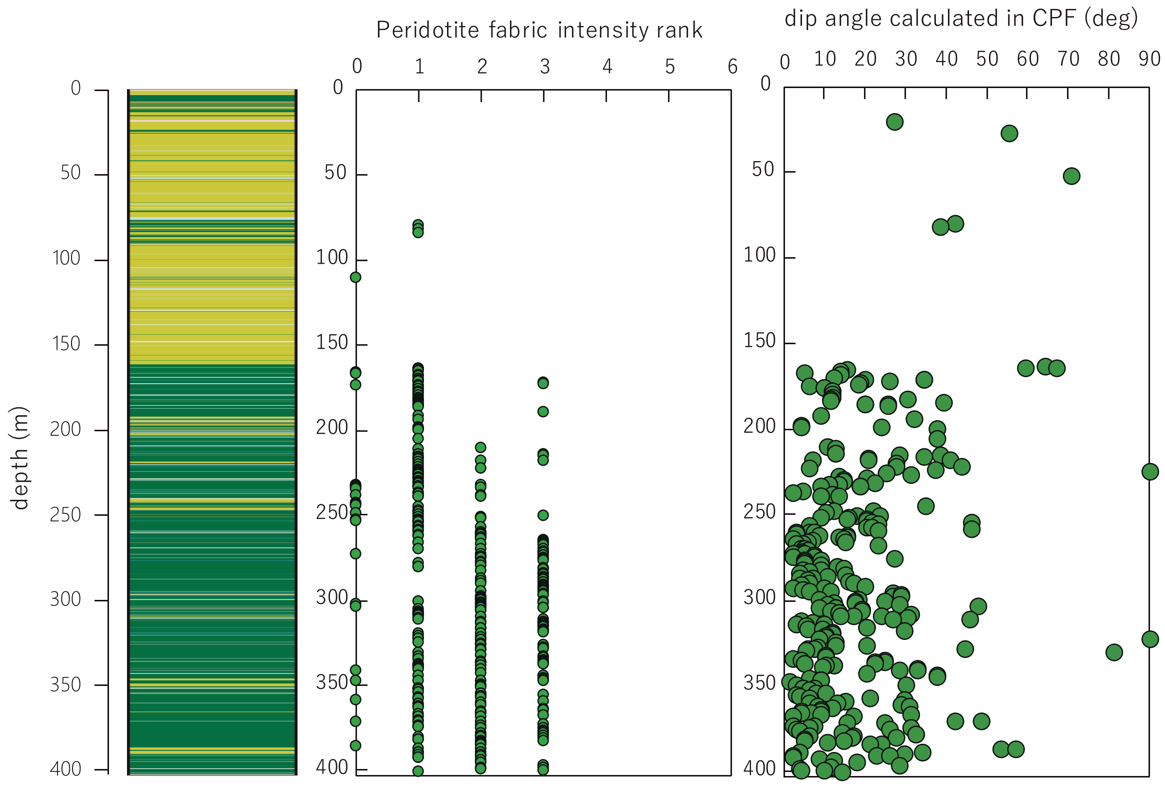

Figure F46. **A.** Core scan of a typical serpentinite vein network in the Harzburgite with Gabbro Sequence. **B.** TS image of the region highlighted in A with the main serpentinite vein visible down the center and a small microfracture in the country rock (red arrow). **C, D.** Photomicrographs focused on the microcrack highlighted in B. Brittle fracturing is evidently present at the microscale even in sections of core that appear to be strain free (C: PPL, D: XPL).

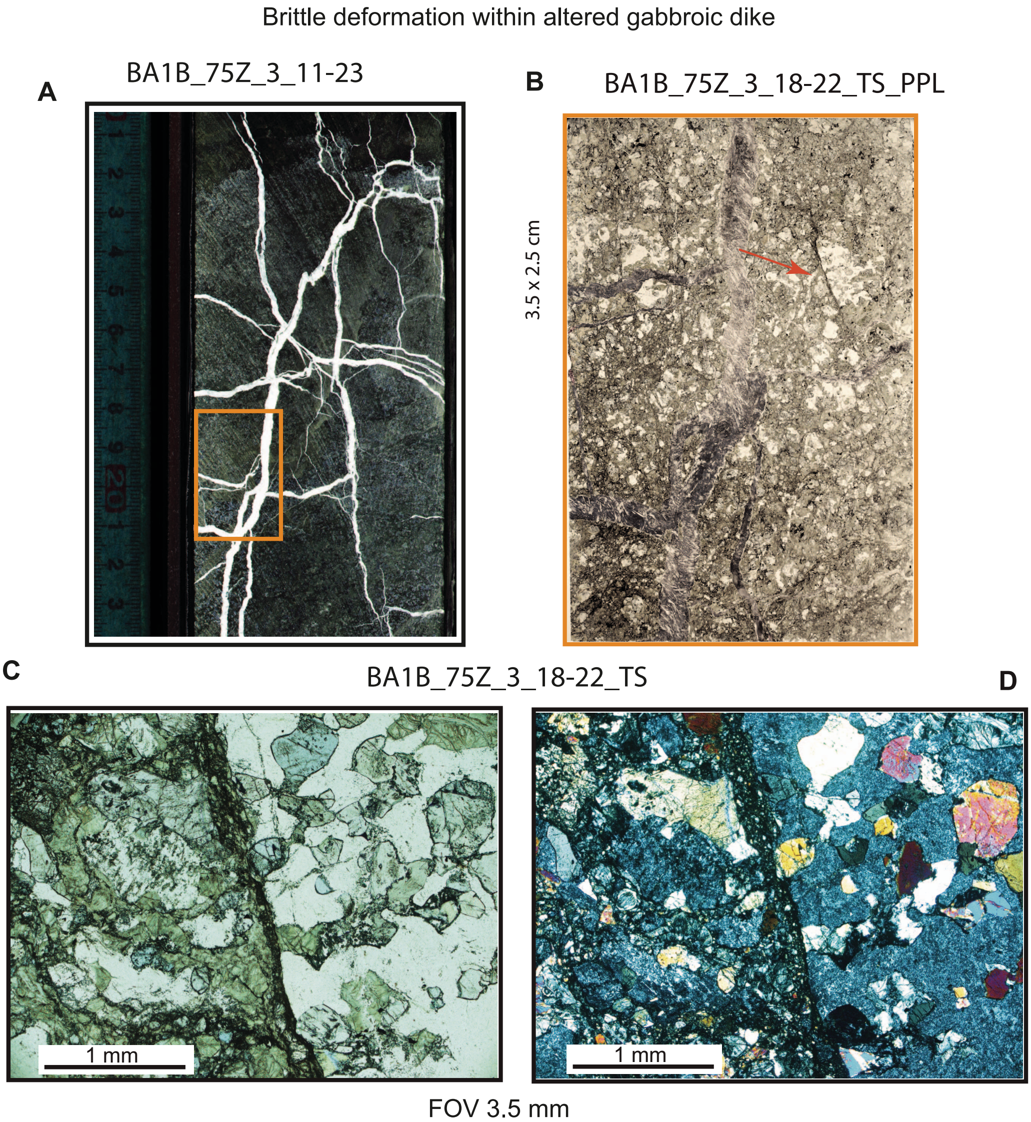

Figure F47. **A**. Core scan of high-strain brittle/ductile shear zone in a gabbroic dike. **B**. TS image of the region highlighted in A displaying three clearly different regions: (bottom left) serpentinized dunite country rock, (middle) low strain but still deformed edge of the dike, and (upper right) highly deformed apparently ultramylonitic center of the dike. **C**, **D**. Photomicrographs detailing the boundary between the highly strained center of the dike and the lower strain edge (C: PPL, D: XPL).

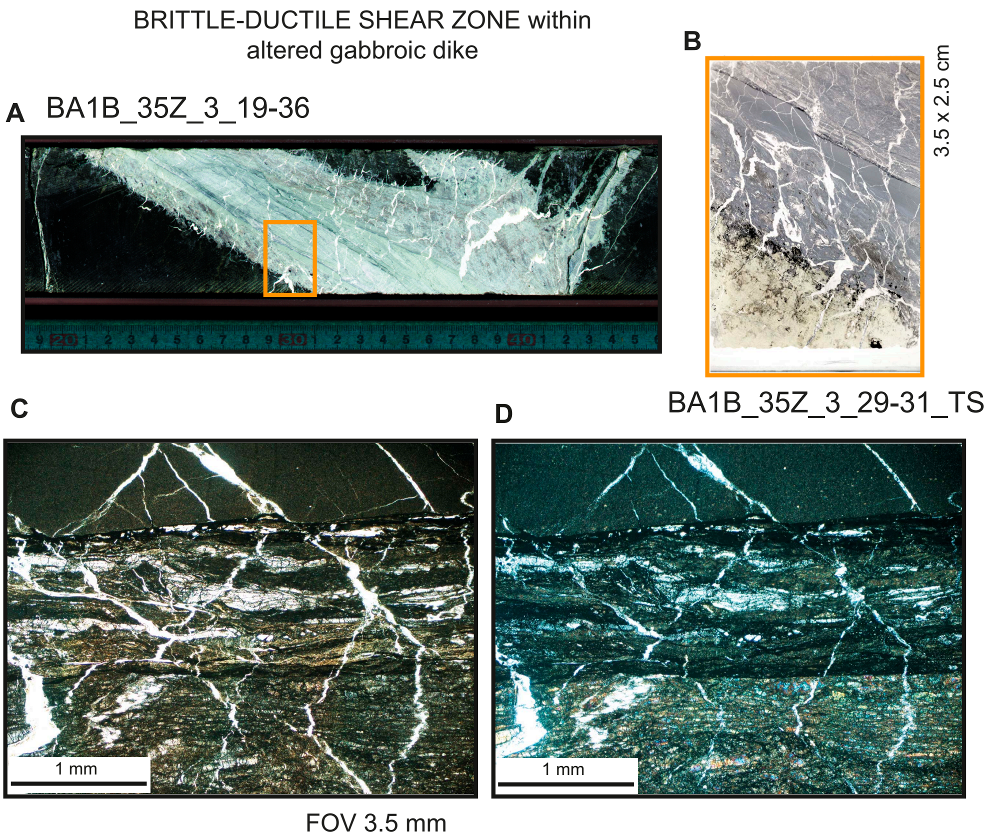

Figure F48. A. Core scan of the intersection of a vein and an altered gabbroic dike. Slight crystal-plastic fabric is visible in the gabbro at the mesoscale. **B.** TS image from the area highlighted in A revealing sheared fabric in the vein and bimodal grain size distribution in the minerals that make up the gabbro. **C–H.** Photomicrographs from various sites of gabbro showing coarse deformed grains with high internal strain mantled by fine, strain-free grains of the same phase. These textures are typical of dynamic recrystallization in mylonitic rocks and is clear evidence of crystal-plastic deformation mechanisms operating within the gabbroic dike (C, E, G: PPL, D, F, H: XPL). (E–H) Examples of mantled textures in plagioclase. Formation of new grains occurs along deformation bands in coincidence with formation of hydrous minerals: (C, D) amphibole, (E, F) phlogopite.

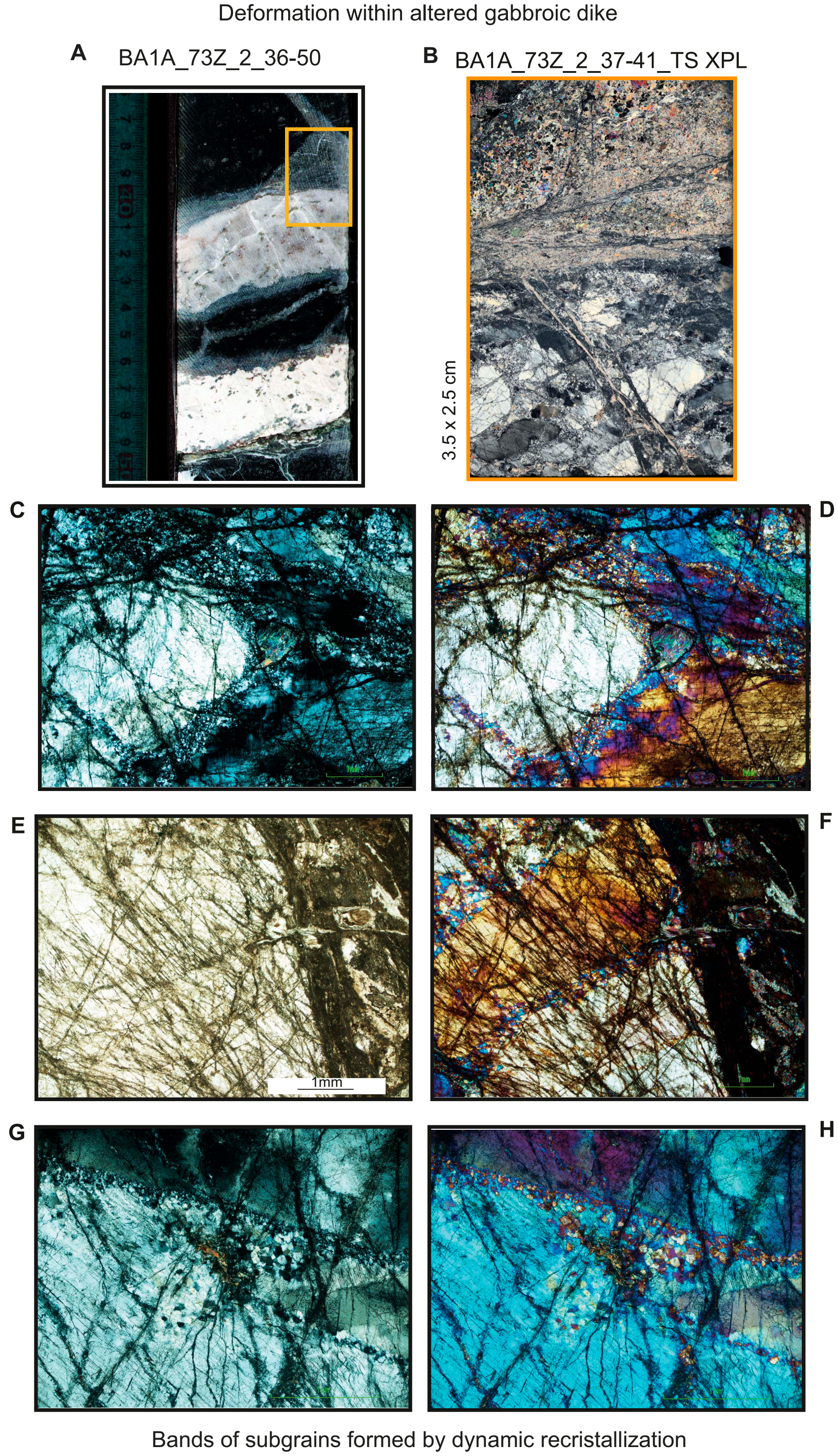

Figure F49. A. Core scan of an altered gabbroic dike with veins along the upper and lower contacts. **B.** TS scans of the area highlighted in A. **C–F.** Photomicrographs showing evidence of ductile and brittle/ductile deformation in the dike and different episodes of veining and alteration along its contacts (PPL).

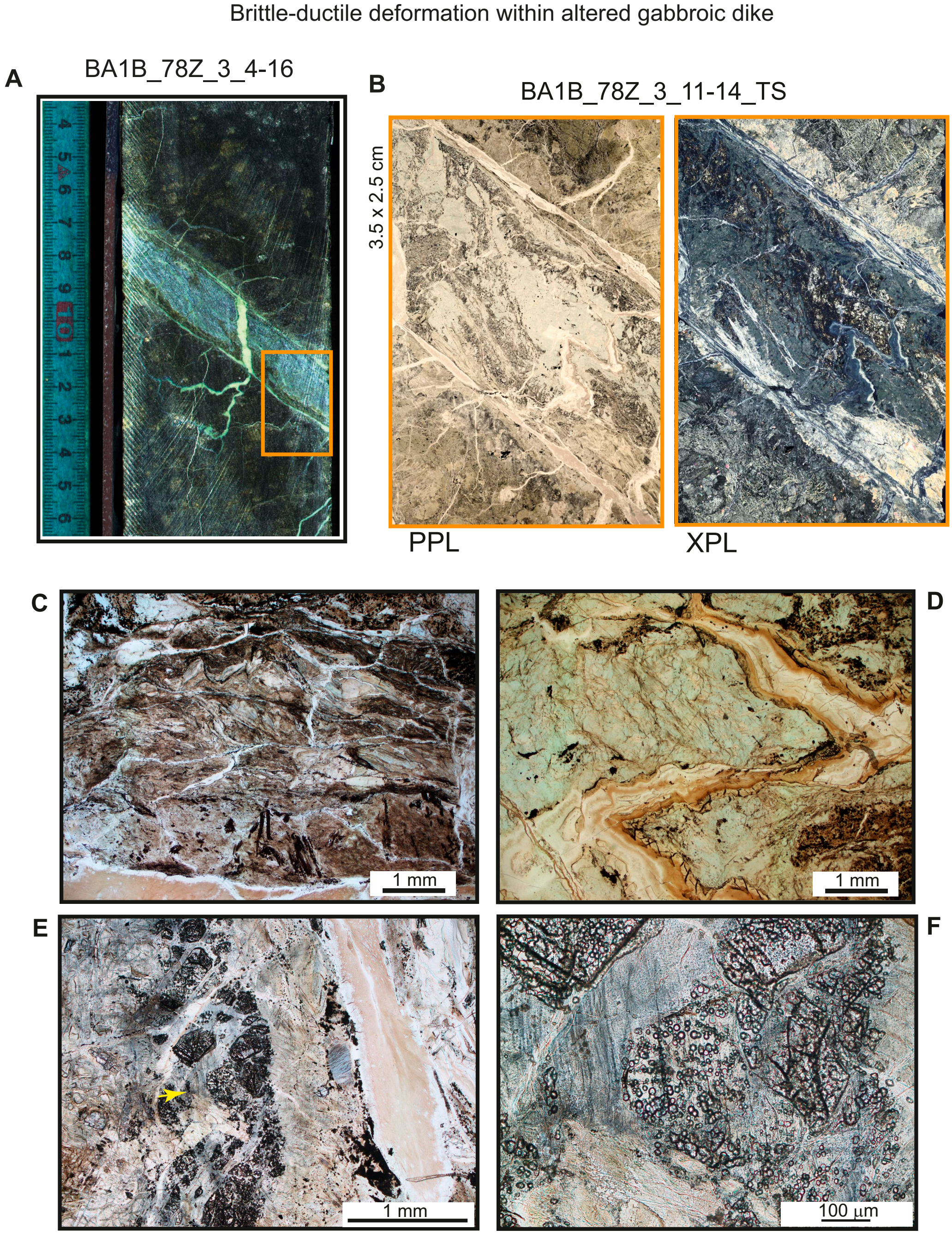

Figure F50. Different types of brittle features, Hole BA1B. **A**. Shear zone in a dike displaying crystal-plastic deformation. Most crystal-plastic or semibrittle shear zones in Hole BA1B were located within or at the margins of gabbroic dikes where rheological contrasts exist. **B**. Complex deformation zone contained between two small gabbroic dikes. The outer boundaries display crystal-plastic shear zones along the edges of the dikes. Between these shear zones is a brittle cataclastic zone. The structure has been extensively altered and exploited by veins either during or postdeformation. **C**. Altered cataclastic zone showing a complex network of alteration and veins. The origin of these features is unclear. **D**. Semicohesive cataclastic zone that has undergone extensive fracturing and grain size comminution. **E**. Several brittle fractures or shear veins displacing a gabbroic dike. Where a group of fractures or veins appeared to occur as a set in this way, they were logged as cataclastic zones.

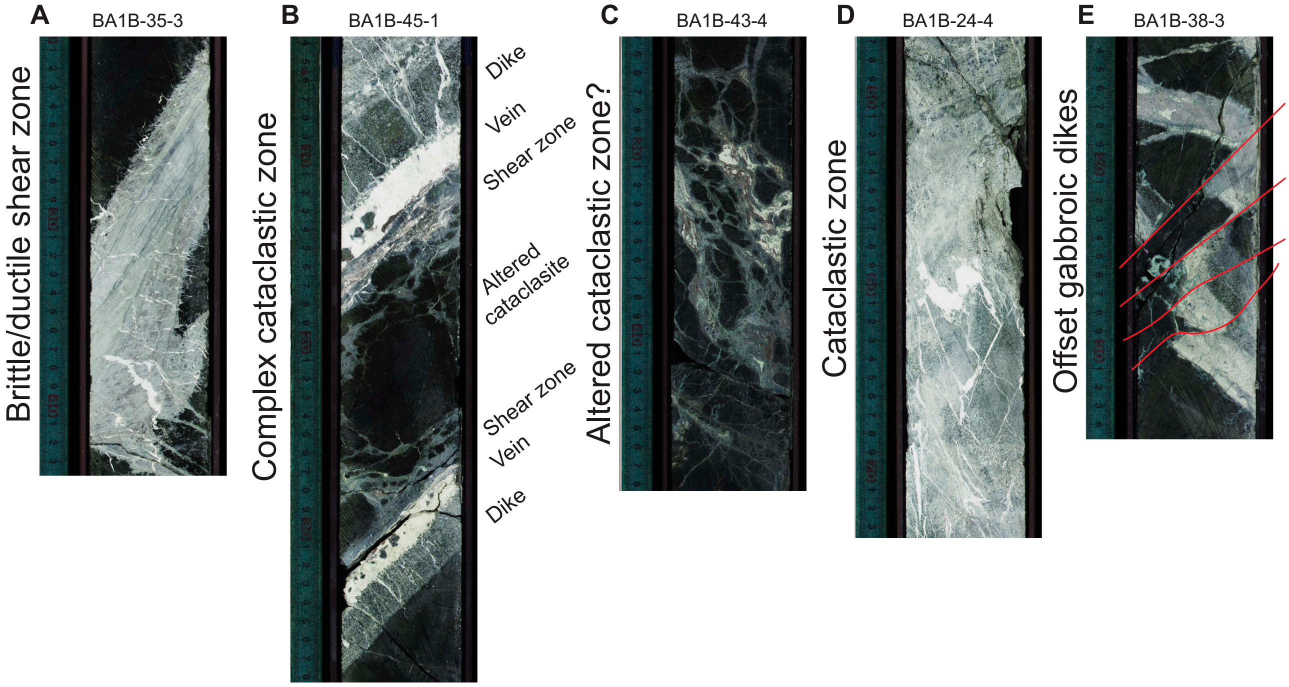

Figure F51. **A.** Locations and thicknesses of fault zones plotted with Hole BA1B lithology. **B**. Thicknesses of damage zones for each deformation feature. Note that where a feature crossed a discontinuous boundary between two sections of core, the two sides were logged as individual features, as the relation between the two sections was not observed. An example is the major fault zone at 160 m depth that was logged as 3 separate fault zones across three cores. In reality, these are likely to be part of a single fault zone ~3 m thick. **C.** Plot of deformation intensity rank ascribed to each feature. Intensity increases from 1 to 5; for full explanation of ranking procedure see **Structural geology** in the **Methods** chapter. **D**. Plot of damage zone thickness multiplied by deformation intensity rank. This is a semiquantitative plot that aims to highlight the importance of each logged feature by considering both the thickness and the intensity of deformation. **E.** Fracture and vein density rank. For full explanation of ranking procedure see **Structural geology** in the **Methods** chapter. Across these plots a clear correlation is present between the position of the major fault zone and the main boundary between dunite and harzburgite. There is also a switch from higher to lower fracture and vein density across this tectonic and lithologic discontinuity.

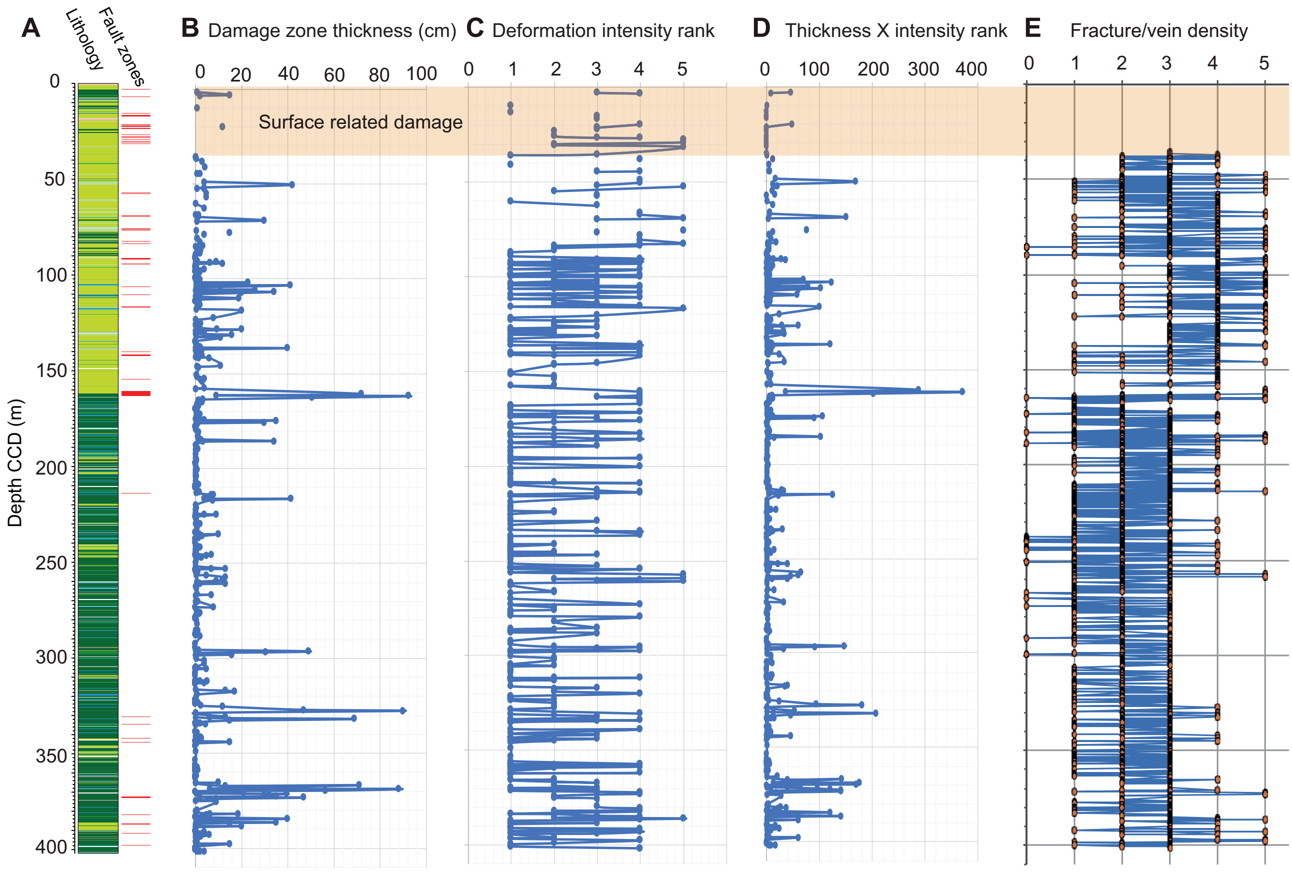

Figure F52. Plots of dip angle for each logged deformation feature in Hole BA1B; (**A**) all features, (**B**) shear veins and slickensides (features logged as slickensides were mineral lineations within shear veins), (**C**) cataclastic zones, (**D**) fault zones, (**E**) joints, (**F**) semibrittle or plastic shear zones. Note that features for which dip could not be accurately measured are not included in this plot.

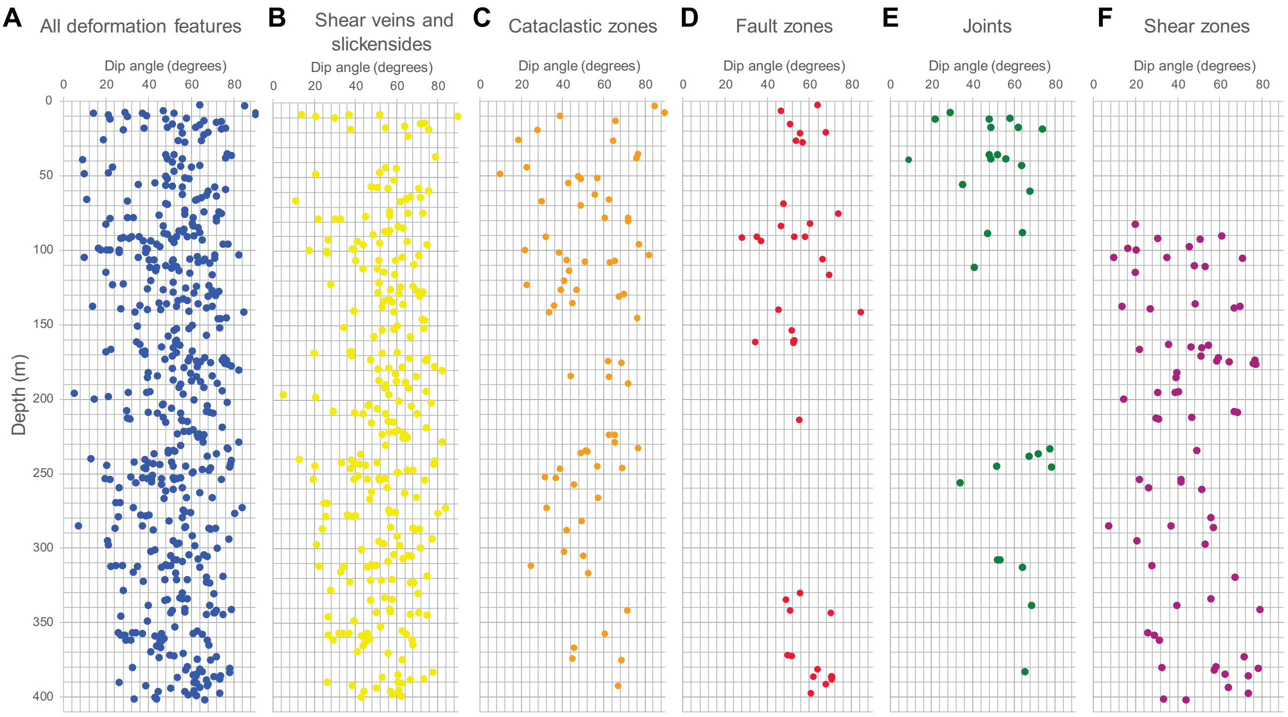

Figure F53. Rose diagrams of the dip angle of deformation structures sorted by type of feature, Hole BA1B. Fault zones, shear veins, and joints have generally steep dips, mostly 50° or greater, whereas shear zones and cataclastic zones are more moderately dipping with wider distributions.

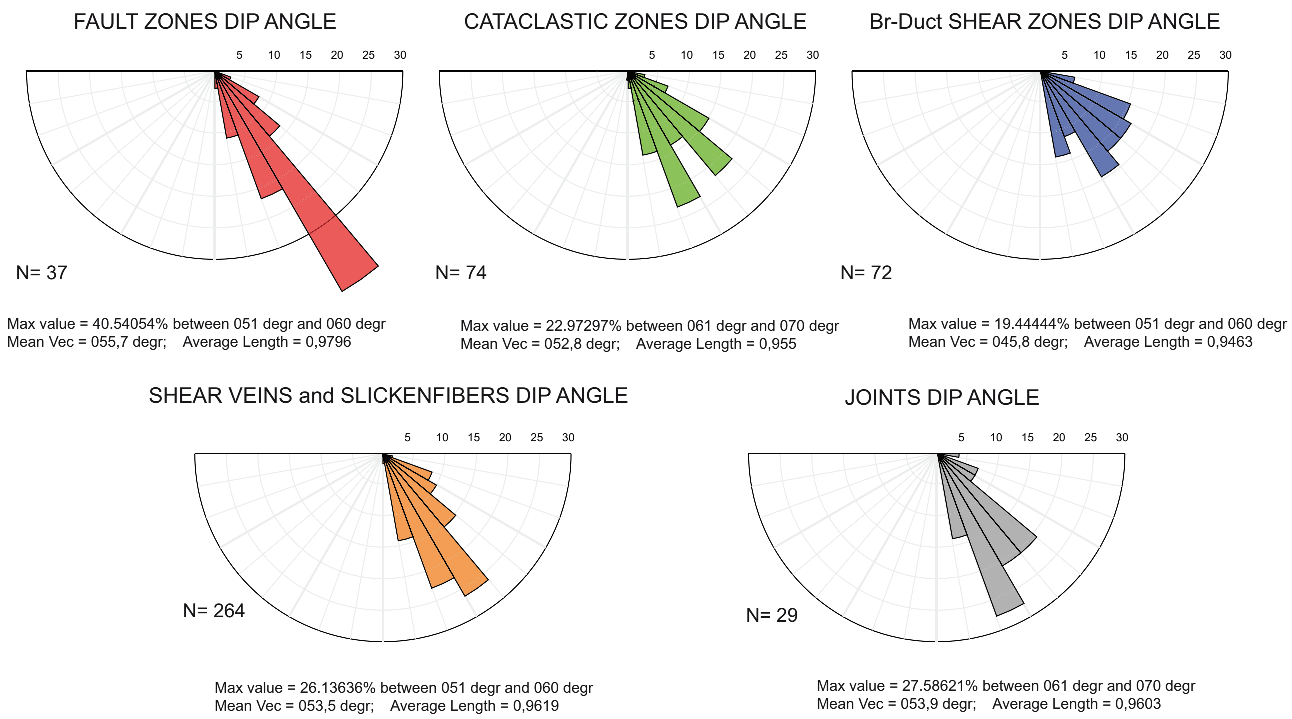

Figure F54. **A.** Locations and thicknesses of fault zones, BA1B. Key sections of the core where faulting is present are clearly observable, in particular the major fault zone at the boundary between the predominantly dunite unit and the predominantly harzburgite unit at 160 m depth. **B.** Typical fault zone from the fault cluster in the upper section of the hole, generally incohesive gouge or breccia units that could rarely be reliably oriented. **C.** Part of the upper section of the major fault zone at 160 m, semicohesive and composed primarily of heavily fractured dunite. **D.** Part of the middle to lower section of the major fault zone, cohesive, highly foliated, and displayed semibrittle or crystal-plastic character. **E.** Base of the major fault zone, defined by a narrow plastic shear zone within a gabbroic dike. **F.** Semibrittle fault zone of the type that is found in the lower part of the hole, which contains both folded and fractured material.

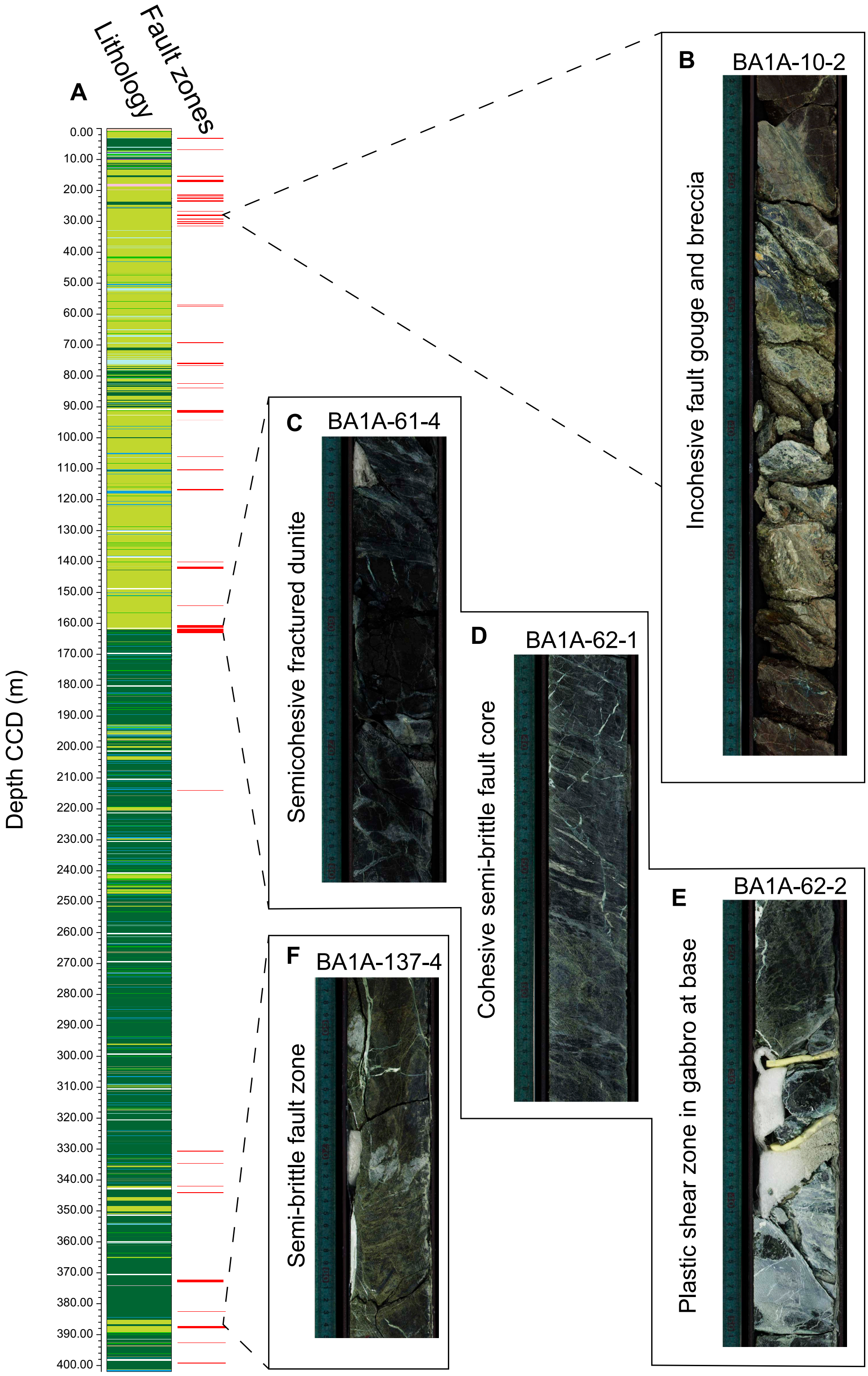

Figure F55. Different types of shear veins observed in Hole BA1B. **A**. Narrow, black, almost invisible vein identified as a shear vein through the offset of dikes along its length. **B**. Two straight, highly altered shear veins that cut intrusions and often contain mineral lineations or slickenfibers. **C**. Complex anastomosing shear vein that cuts the intrusion. Displacement could not be measured in this case, as the other part of the dike is not observed in the core.

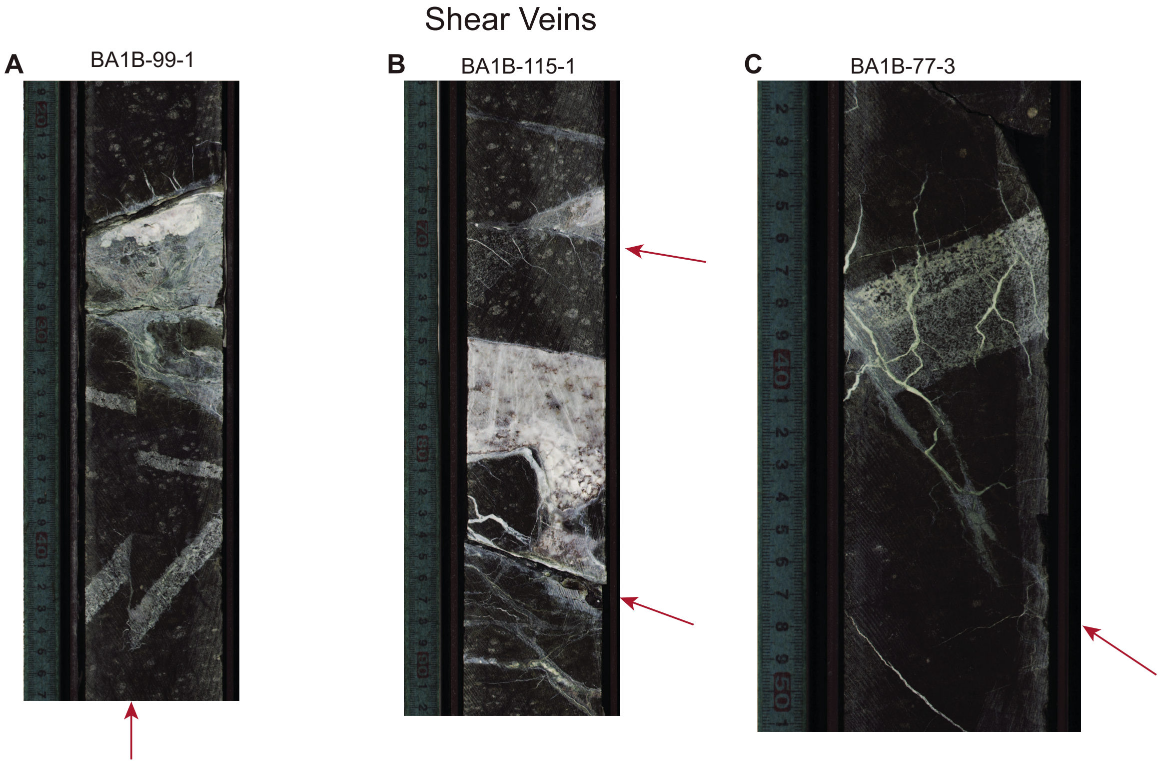

Figure F56. A. Plot of dip angle vs. depth of features that displayed an offset, sorted into apparent normal or reverse shear sense based on that offset, Hole BA1B. Large offsets could not be captured in the core, so this data set is biased toward features with smaller, observable displacement. The shear sense given is that which was apparent when viewing the feature on the cut surface of the core. Features with a normal apparent shear sense (extensional) appear in general to be slightly steeper dipping than those with a reverse apparent shear sense (compressional). **B**. Plot of lineation plunge angle vs. dip angle of the plane on which they were measured. Points along the diagonal line are dip-slip (plunge similar to dip), points along the *y*-axis are strike-slip (plunge << dip), and points in between are oblique-slip (plunge < dip). Points beyond the diagonal line are likely due to the wavy nature of some of the measured planes; however, these points can be assumed to relate to dip-slip features.

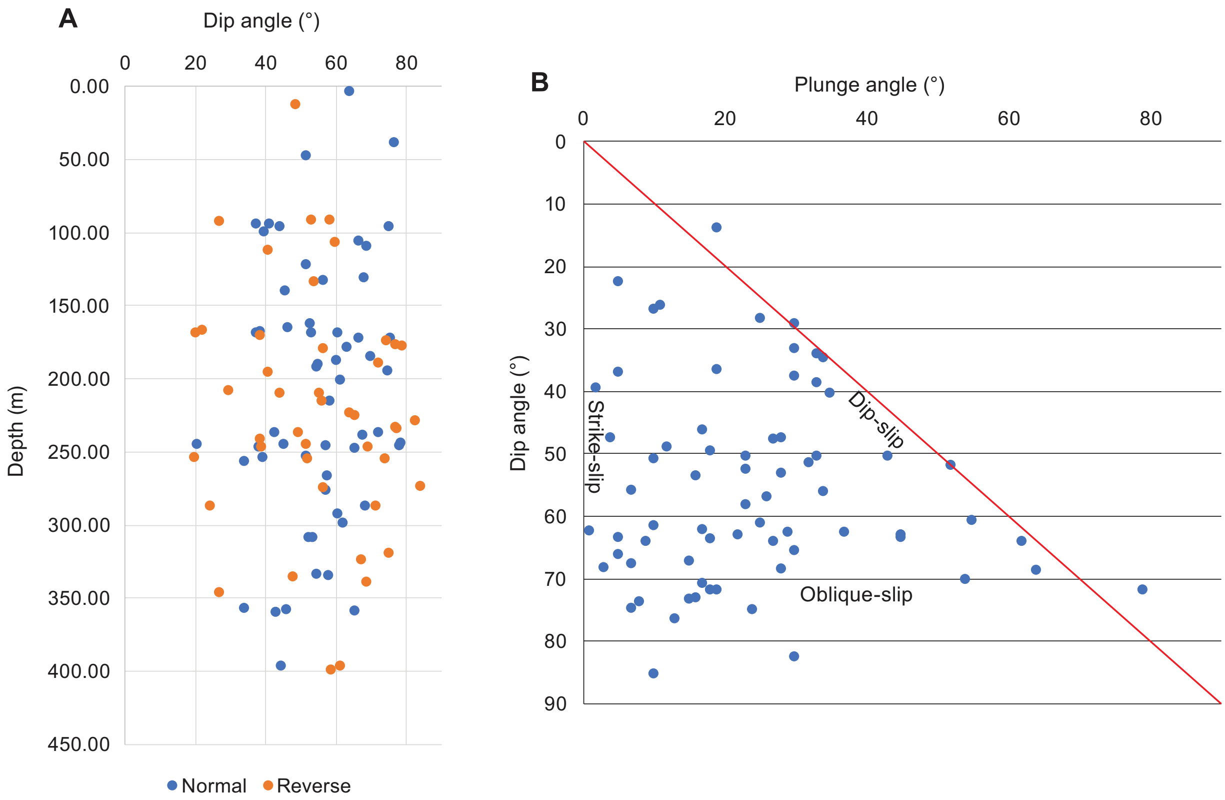

Figure F57. Variation of dip angles of different alteration vein types and key structures, Hole BA1B. **A.** Compilation of dips of all carbonate, carbonate-serpentine, and serpentine veins. Xonotlite veins (X) were only specified in the lower part where identified by XRD. **B.** Lightened core image of a section rich in carbonate veins in altered dunite showing variable apparent dip (white veins). **C.** Black serpentine veins with white Riedel shear veins (Sa/Sf) in harzburgite and white irregular veins associated with pyroxenite dike. Black background serpentine veins (Sa) partly form systematic branched sets. **D.** TS scan (PPL, 3 cm width) of serpentinized dunite showing white conjugate serpentine veins (Sf). **E.** TS scan of harzburgite in the lower part of the hole showing serpentine-magnetite vein sets (Sa) and a xonotlite or white serpentine vein set normal to a dikelet (X/Sf).

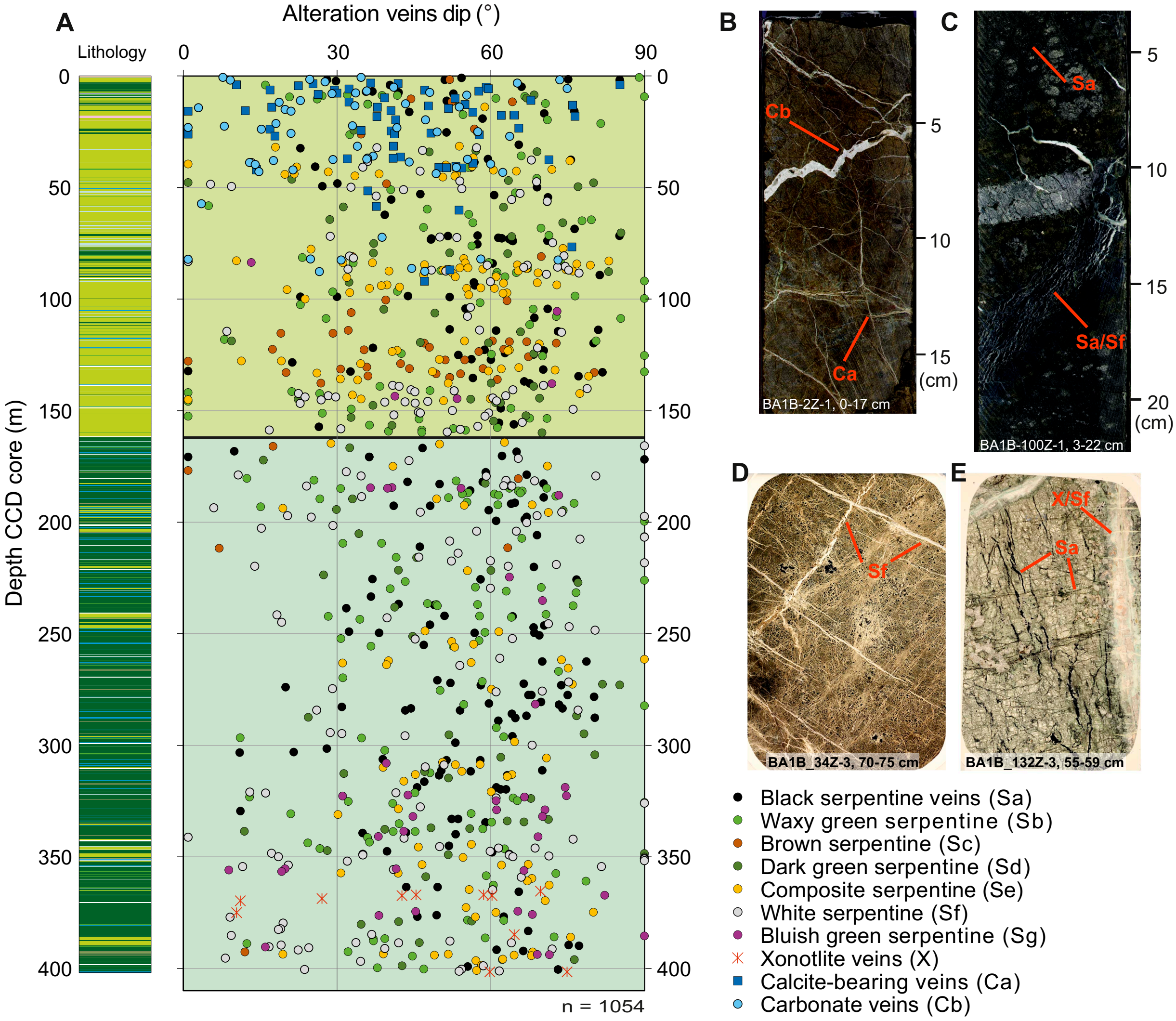

Figure F58. Rose diagrams of dips of veins in the upper (0–162 m) and lower (162–403 m) part of Hole BA1B showing the frequency distribution of dip angles of all serpentine veins, carbonate (-bearing) veins, and selected serpentine vein generations (binning angle for all = 10°). Rose diagrams of Sc and Sd veins are only shown in the parts of the core where enough measurements could be taken. Apart from the diagrams for all compiled serpentine veins (first row, marked with *), all rose diagrams were calculated using the vein density (values of 1–5 as defined by the vein alteration team) as a simple weighting factor. This was done in order to take into account that only one measurement was taken for systematic sets; however, high-density vein sets are still underrepresented.

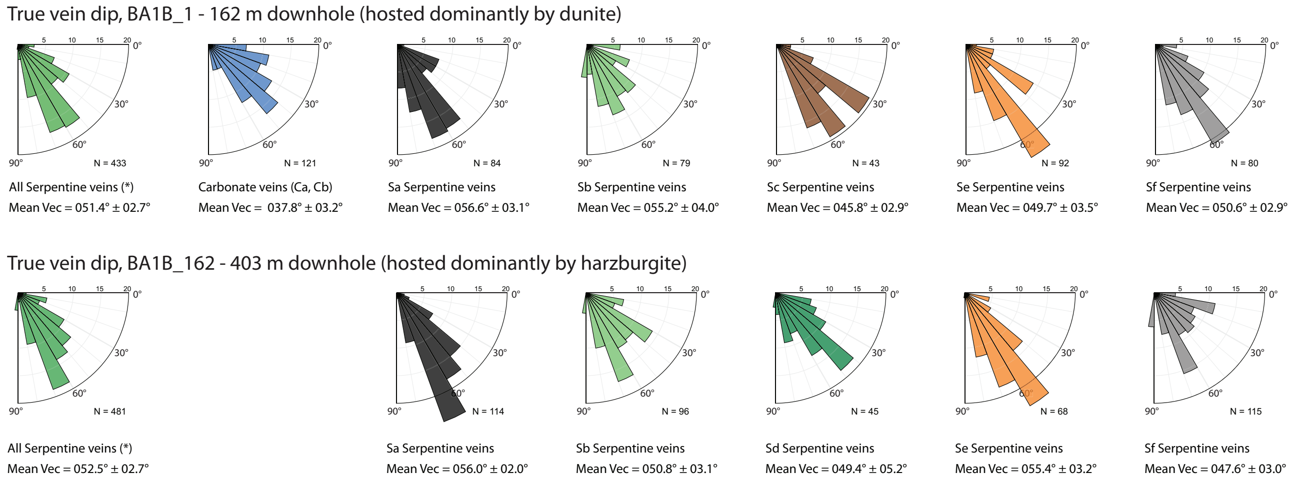

Figure F59. Downhole plots of LOI, CO_2, Mg# (cationic Mg/(Mg + Fe), calculated assuming all Fe as FeO), TiO_2, Ni, and Cr in whole-rock samples, Hole BA1B. Oman mantle data from Godard et al. (2000), Hanghøj et al. (2010), Khedr et al. (2014), Lippard et al. (1986), Monnier et al. (2006), Rospabé et al. (2018), and Takazawa et al. (2003).

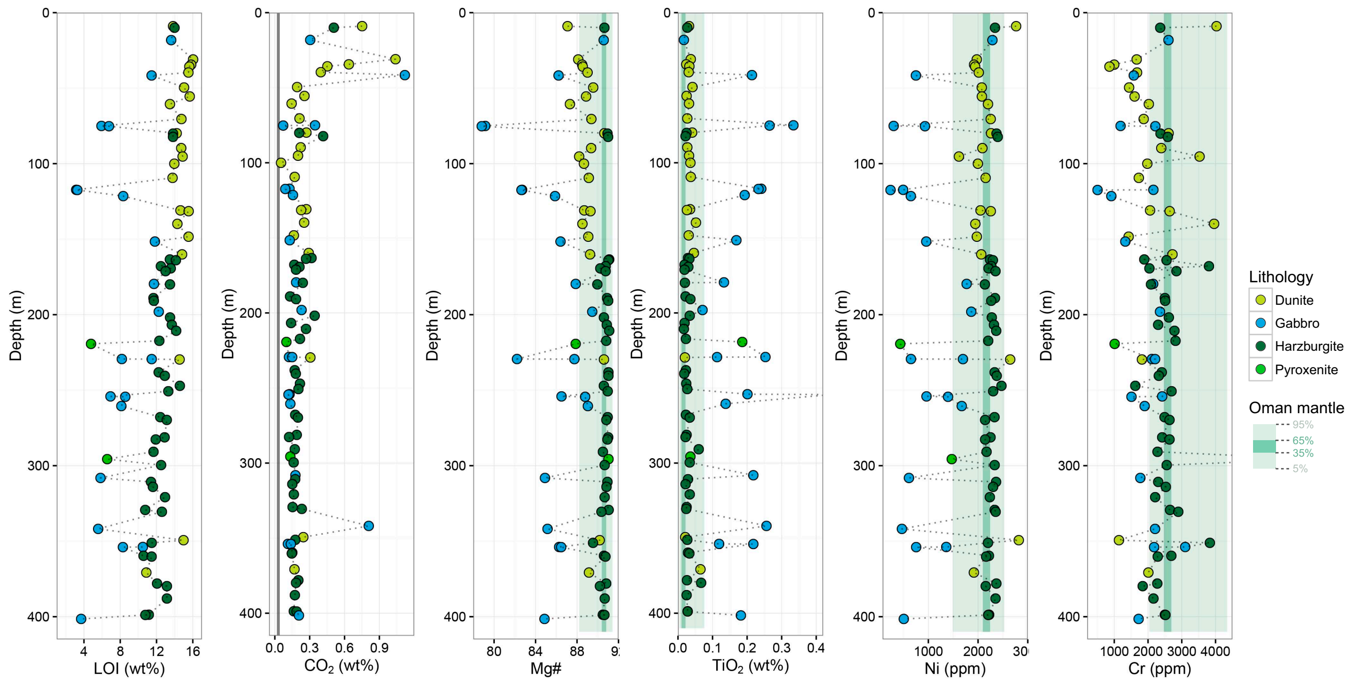

Figure F60. Relationships for volatile elements, LOI, and carbon, Hole BA1B: H_2O vs. LOI, CO_2 vs. LOI, H_2O + CO_2 vs. LOI + $Fe_{(III)}$, IC vs. TC (inorganic carbon vs. total carbon).

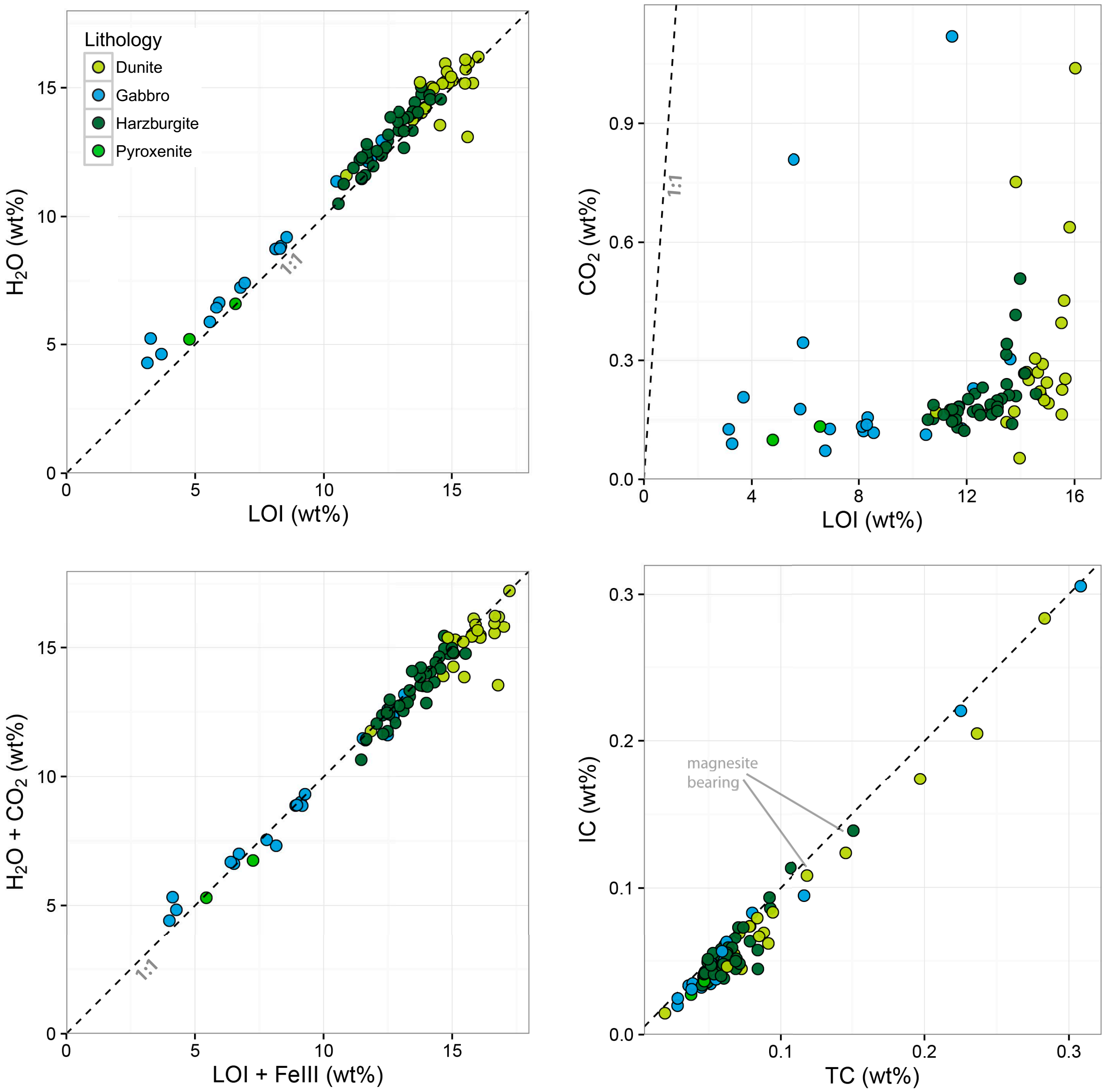

Figure F61. Correlation plots vs. Al_2O_3 in the dunites and harzburgites with the peridotites from Oman ophiolite: MgO, SiO_2, CaO, Fe_2O_3, Cr, and TiO_2. Oman mantle data from Godard et al. (2000), Hanghøj et al. (2010), Khedr et al. (2014), Lippard et al. (1986), Monnier et al. (2006), Rospabé et al. (2018), and Takazawa et al. (2003).

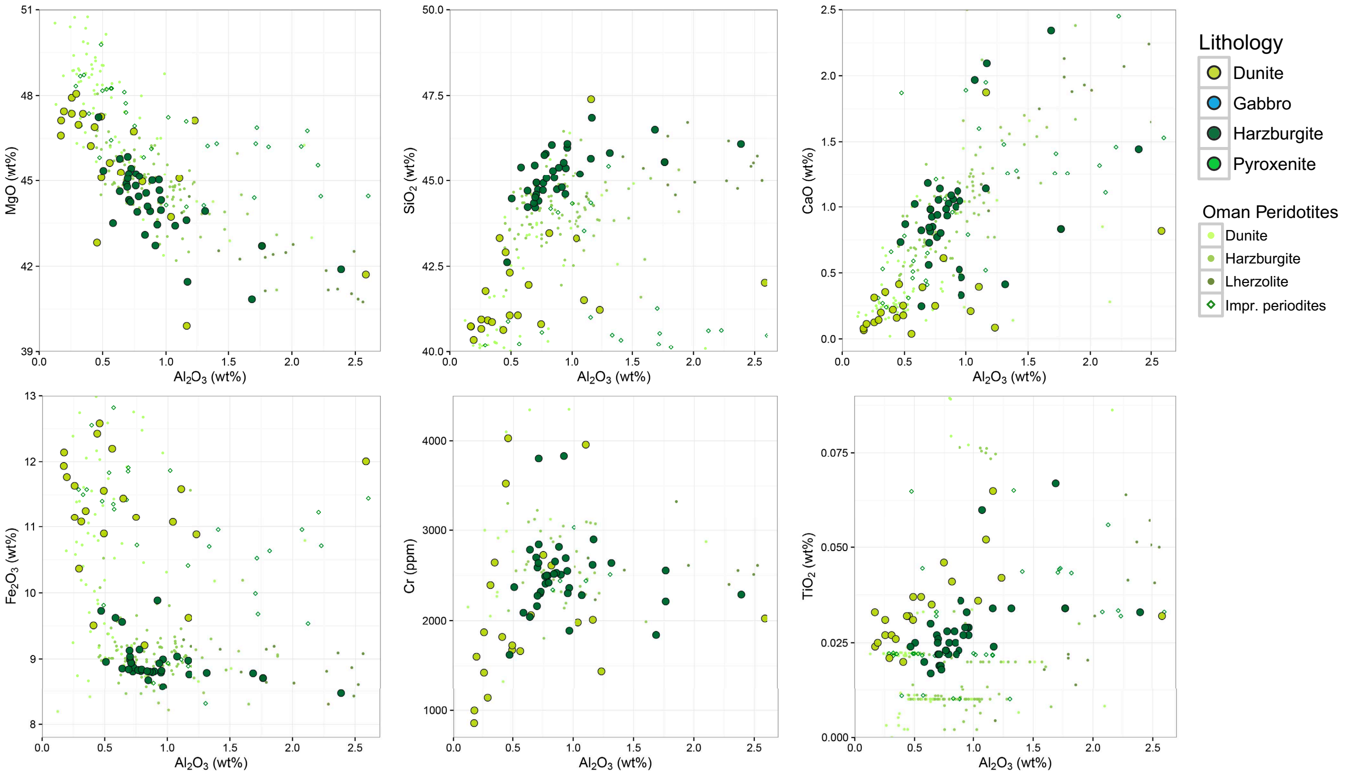

Figure F62. Correlation plots vs. SiO_2 of the BA1B rocks with peridotites from Oman ophiolite and samples from Holes GT1A and GT2A (Leg 1): Al_2O_3, MgO, Fe_2O_3, CaO, TiO_2. Oman mantle data from Godard et al. (2000), Hanghøj et al. (2010), Khedr et al. (2014), Lippard et al. (1986), Monnier et al. (2006), Rospabé et al. (2018), and Takazawa et al. (2003).

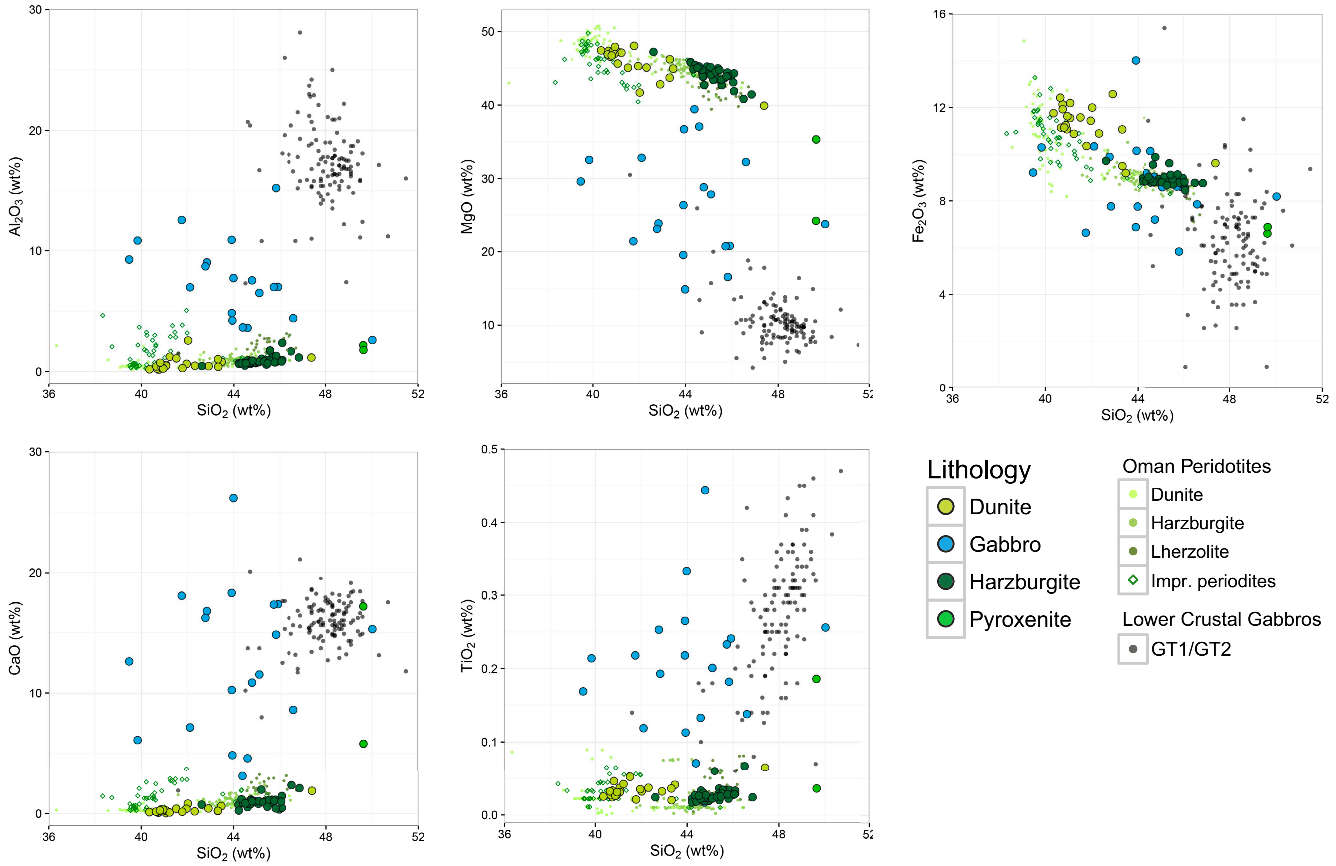

Figure F63. Dunites, harzburgites, and gabbros from Hole BA1B compared to literature data (Oman mantle data from Godard et al., 2000; Hanghøj et al., 2010; Khedr et al., 2014; Lippard et al., 1986; Monnier et al., 2006; Rospabé et al., 2018; Takazawa et al., 2003) and samples from Holes GT1A and GT2A: (A) Mg# vs. Ni; (B) Mg# vs. Ca#.

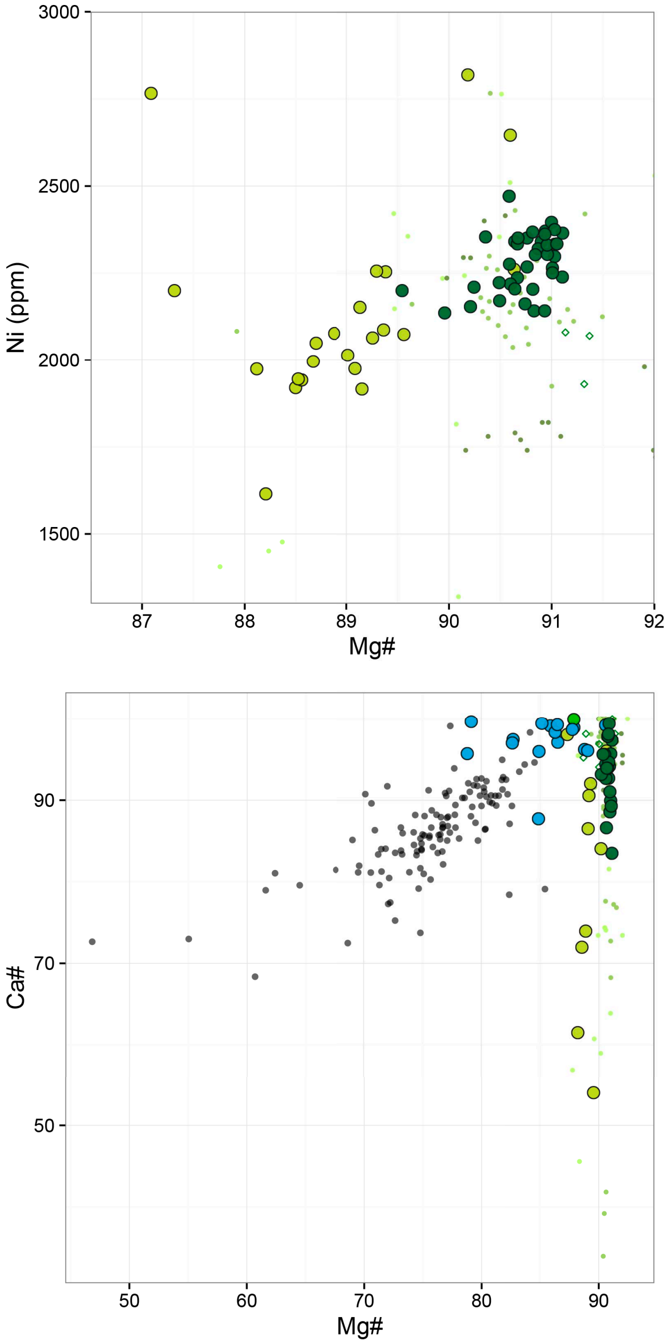

Figure F64. Correlation plot of FeO and MgO for samples from Hole BA1B compared to literature data (Oman mantle data from Godard et al., 2000; Hanghøj et al., 2010; Khedr et al., 2014; Lippard et al., 1986; Monnier et al., 2006; Rospabé et al., 2018; Takazawa et al., 2003) and samples from Holes GT1A and GT2A.

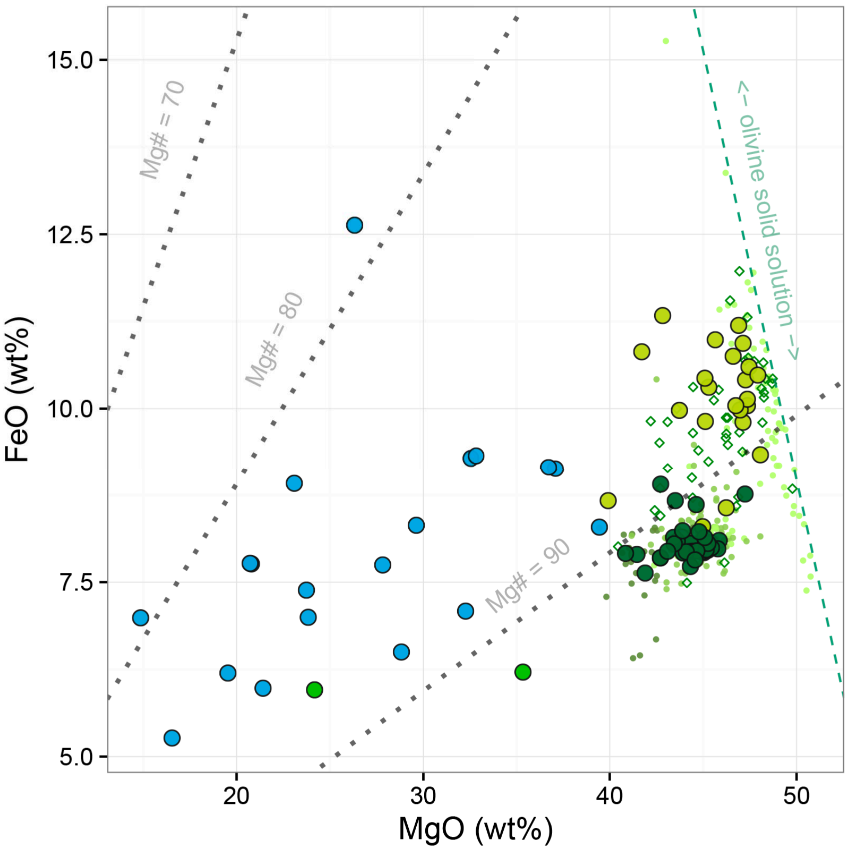

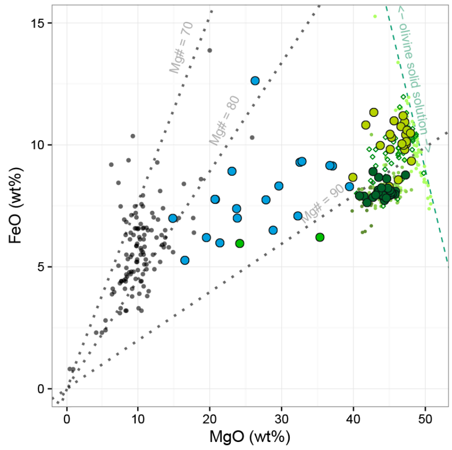

Figure F65. Plot showing TiO_2 vs. Mg# for samples from Hole BA1B compared to literature data (Oman mantle data from Godard et al., 2000; Hanghøj et al., 2010; Khedr et al., 2014; Lippard et al., 1986; Monnier et al., 2006; Rospabé et al., 2018; Takazawa et al., 2003) and samples from Holes GT1A and GT2A.

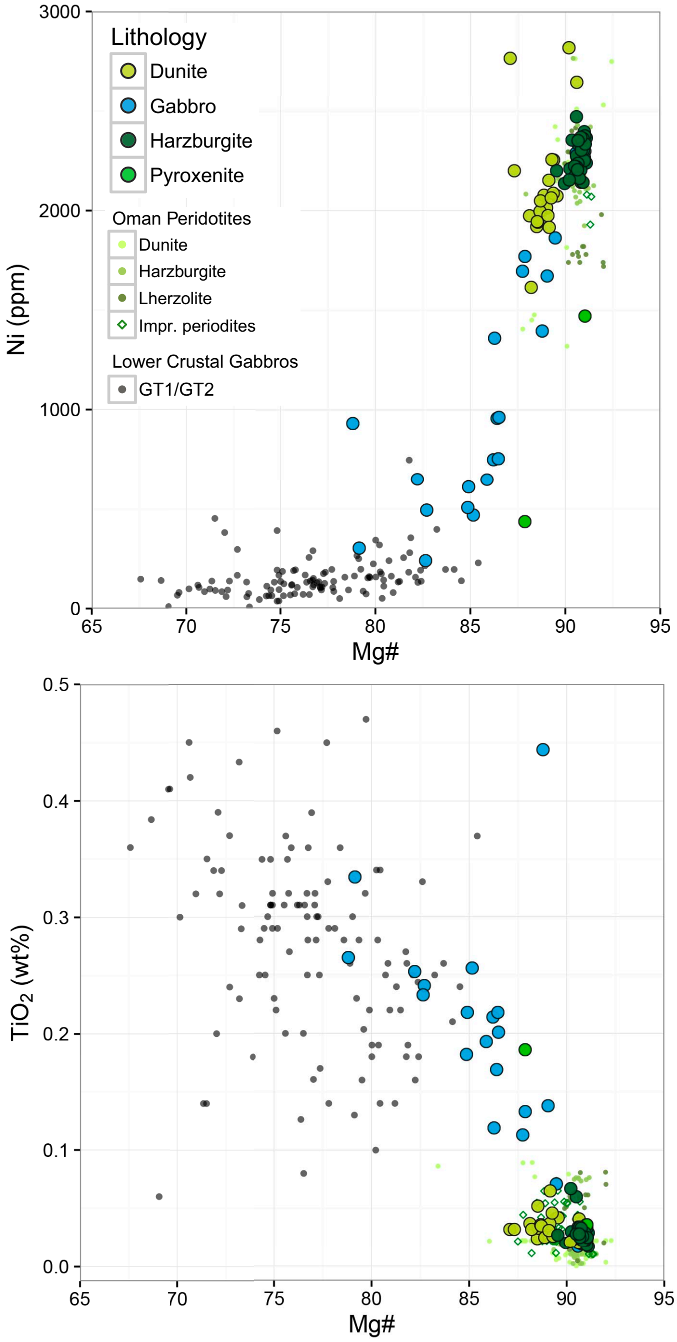

Figure F66. Downhole plots of NRM intensity, bulk magnetic susceptibility, and Koenigsberger ratios, Hole BA1B.

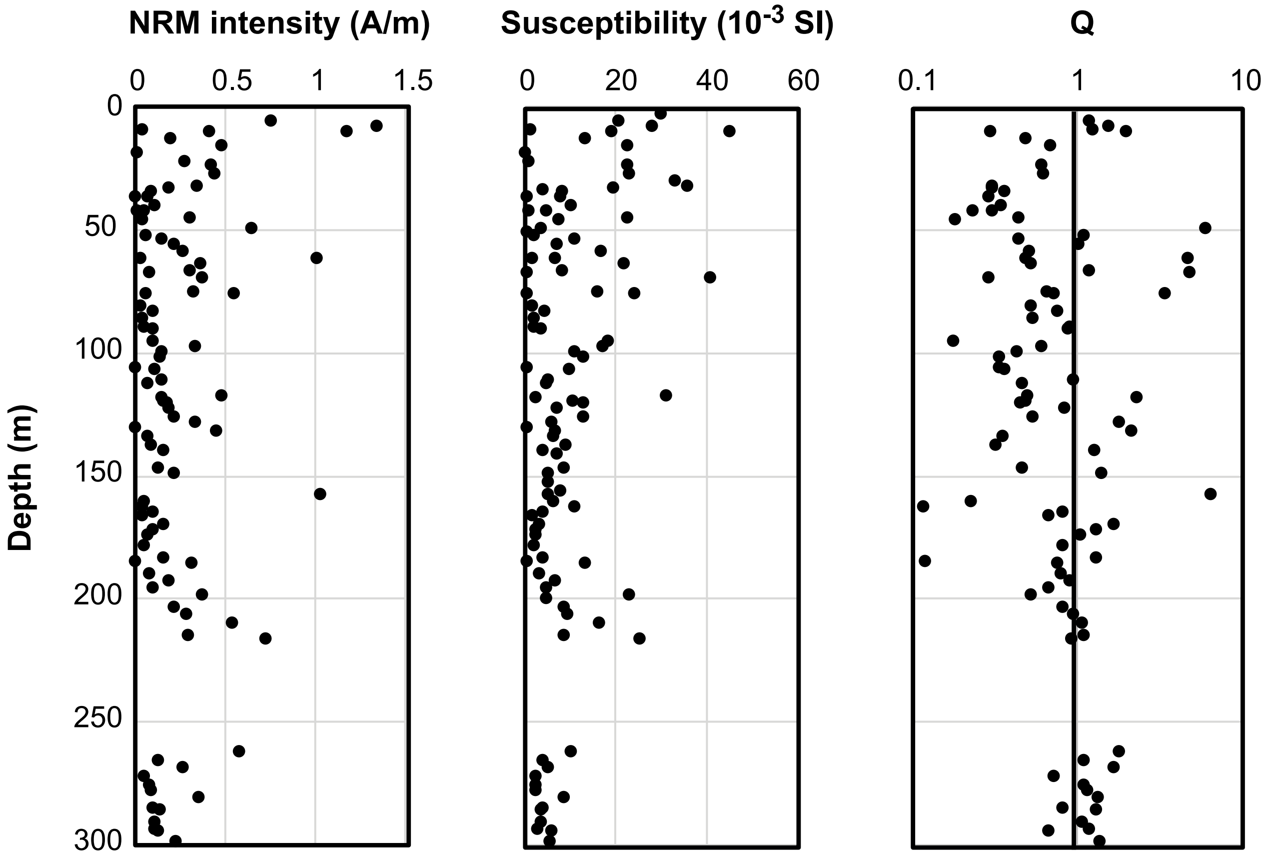

Figure F67. Downhole plots of NRM, ChRM, and soft component inclinations isolated from principal component analysis, Hole BA1B.

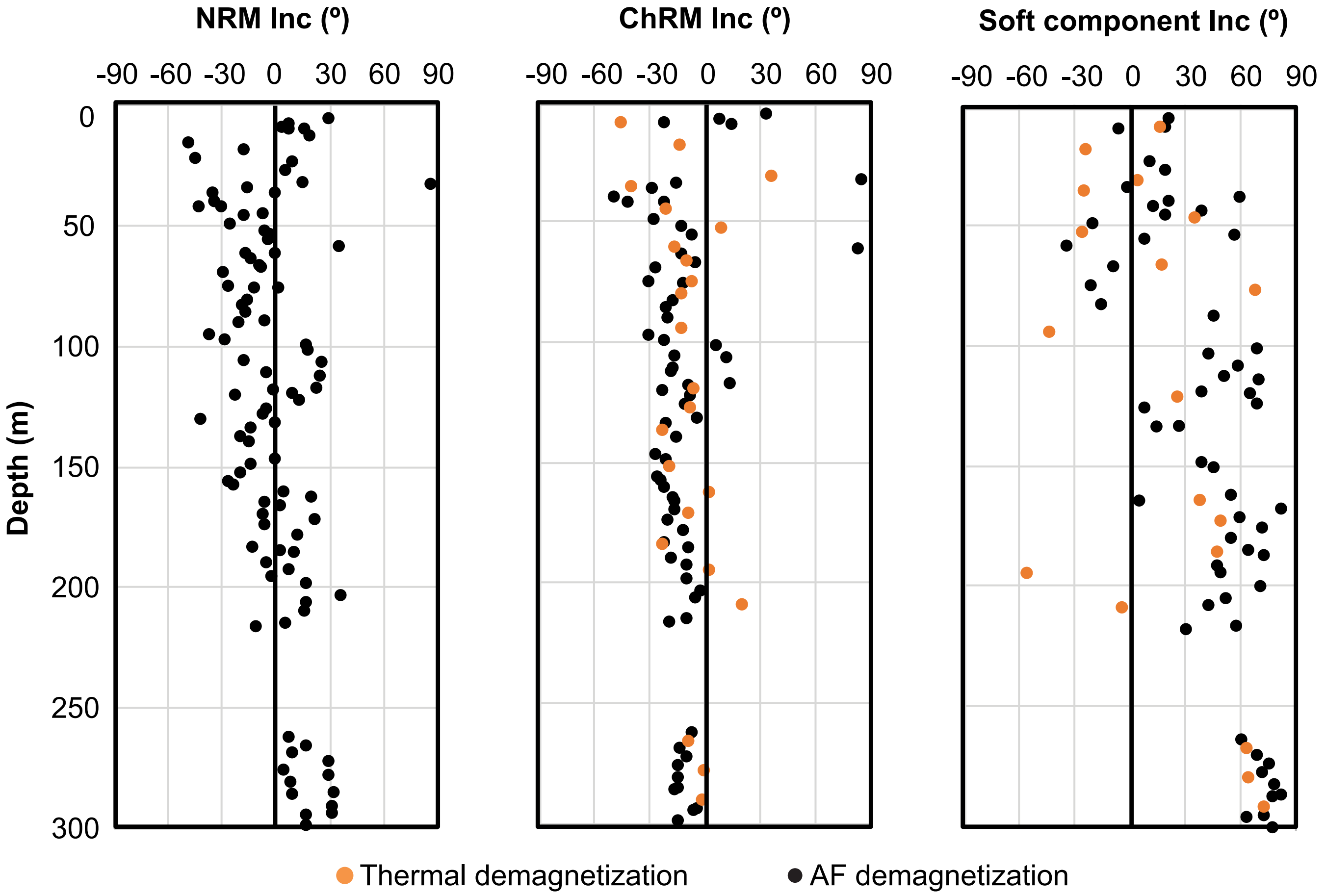

Figure F68. **A.** Representative orthogonal vector projections displaying behavior of magnetic remanence directions during progressive AF demagnetization of discrete samples, Hole BA1B. **B.** Curves of intensity as a function of field strength.

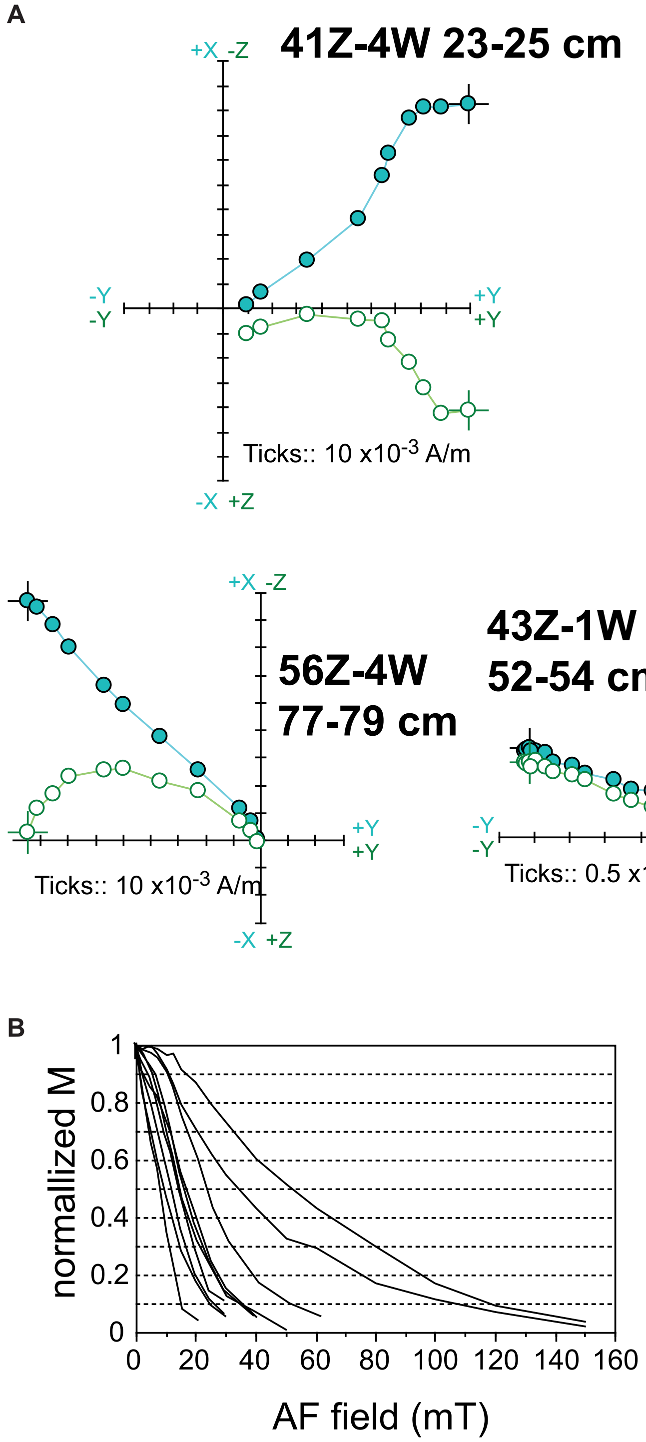

Figure F69. A. Representative orthogonal vector projections displaying behavior of magnetic remanence directions during progressive thermal demagnetization of discrete samples, Hole BA1B. **B.** Curves of intensity as a function of temperature.

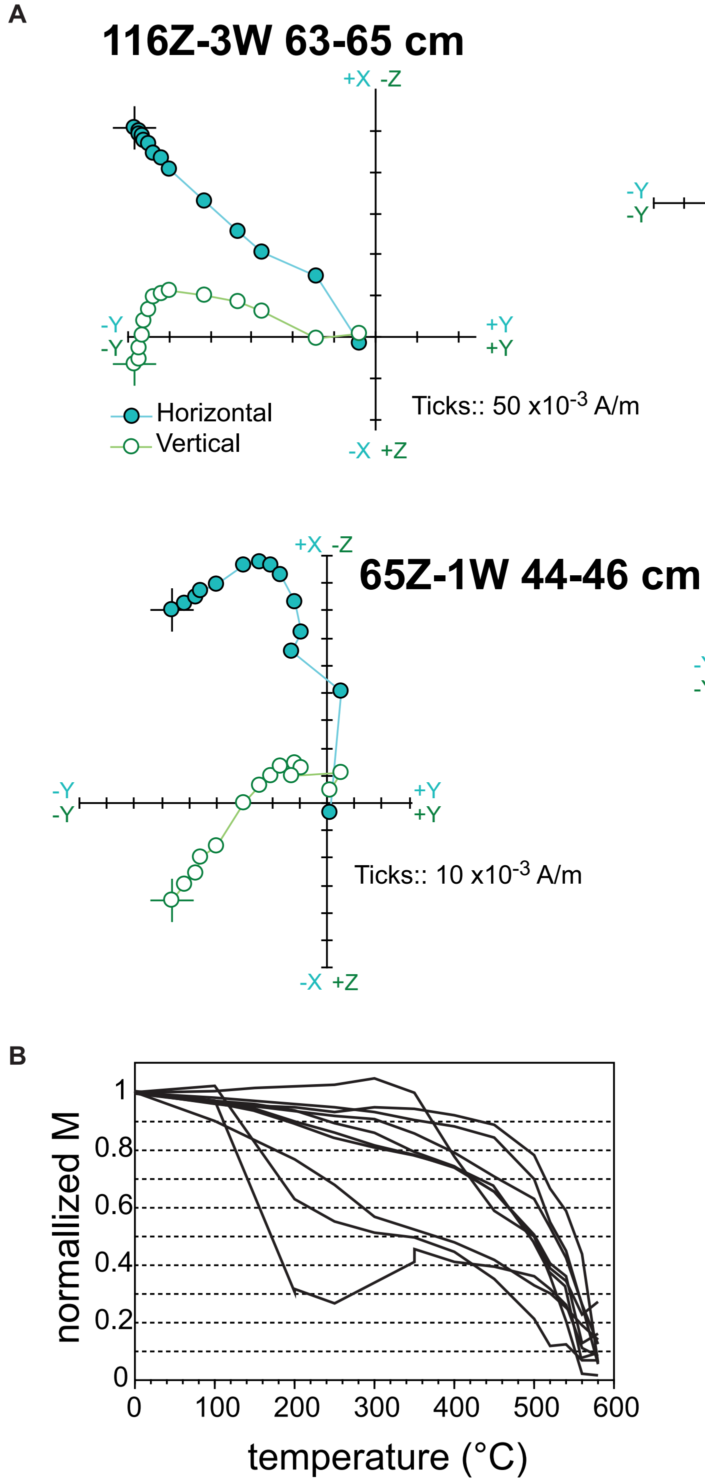

Figure F70. Downhole plots of median destructive field (MDF) and median destructive temperature (MDT) from demagnetization results, Hole BA1B.

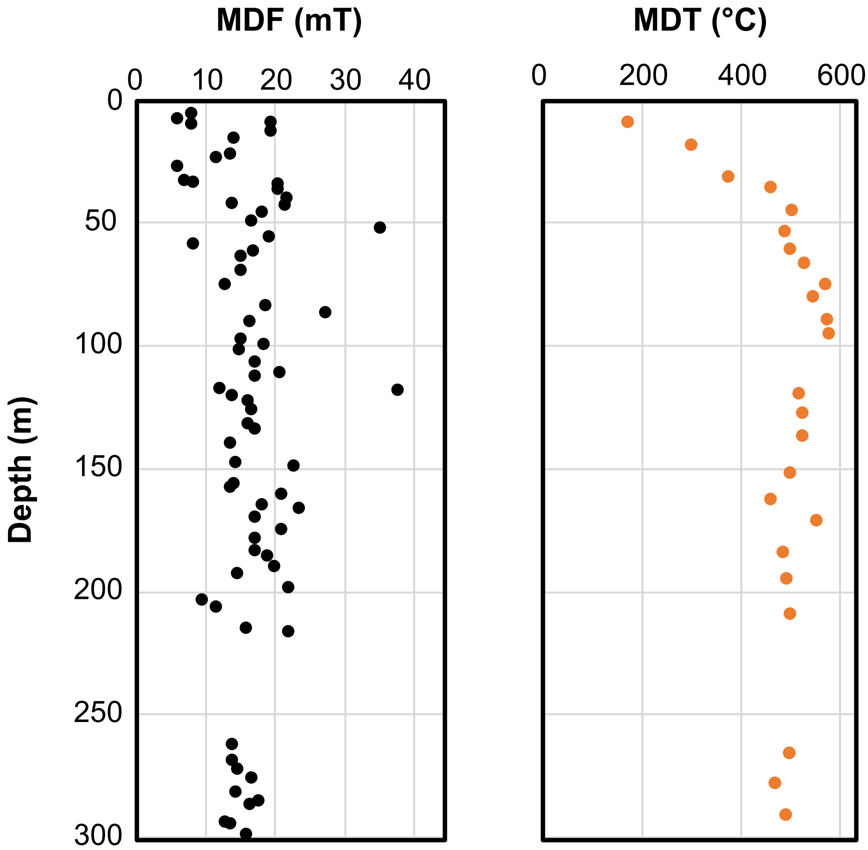

Figure F71. **A.** Downhole plots of magnetic anisotropy intensity, shape, and K_{min} orientation, Hole BA1B. **B.** Degree of anisotropy as a function of bulk susceptibility. **C.** Shape parameter vs. degree of anisotropy of magnetic susceptibility.

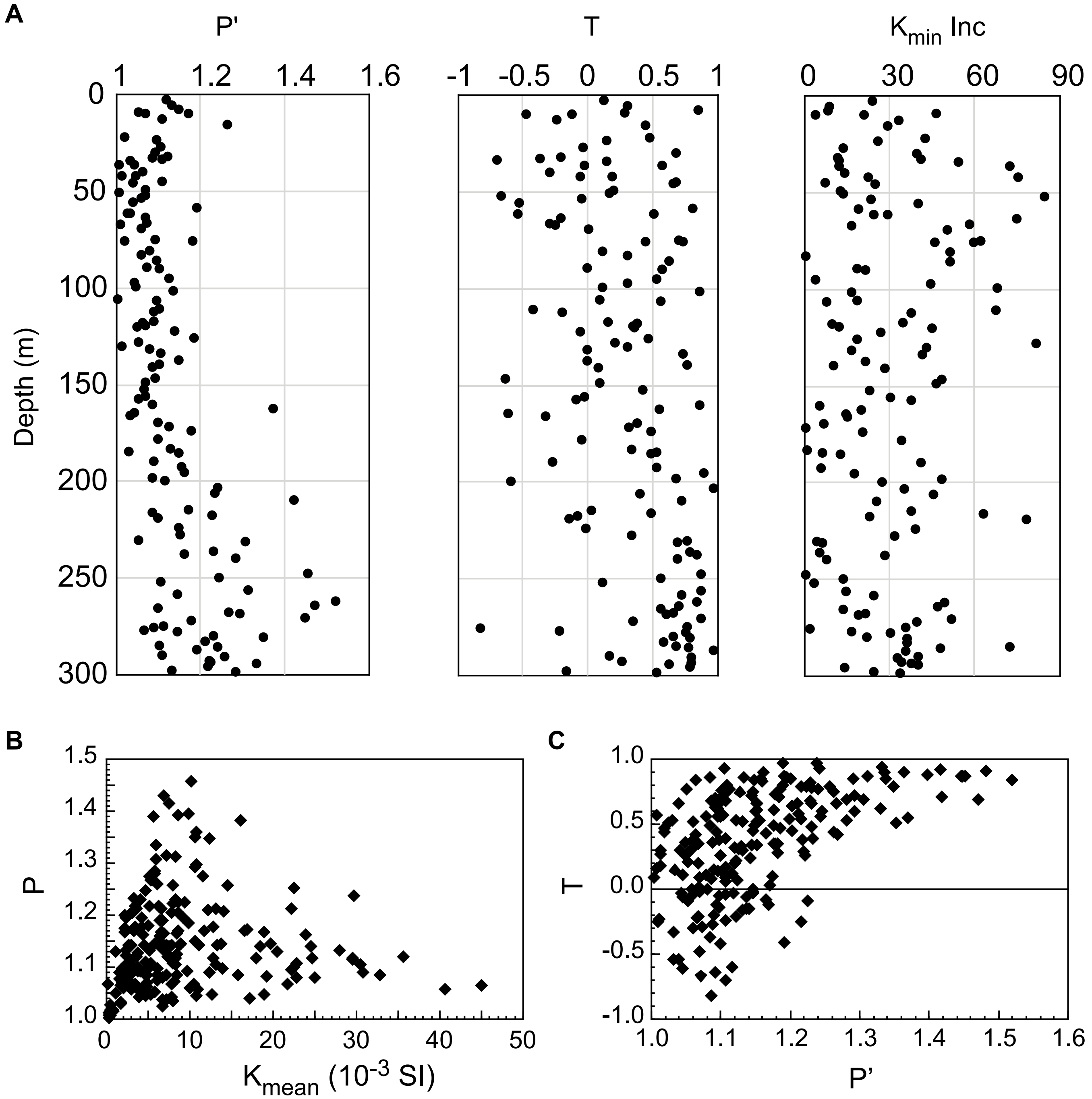

Figure F72. Contoured stereoplots of principal susceptibility axes from AMS analyses plotted on lower hemisphere equal-area projections in the core reference frame, Hole BA1B.

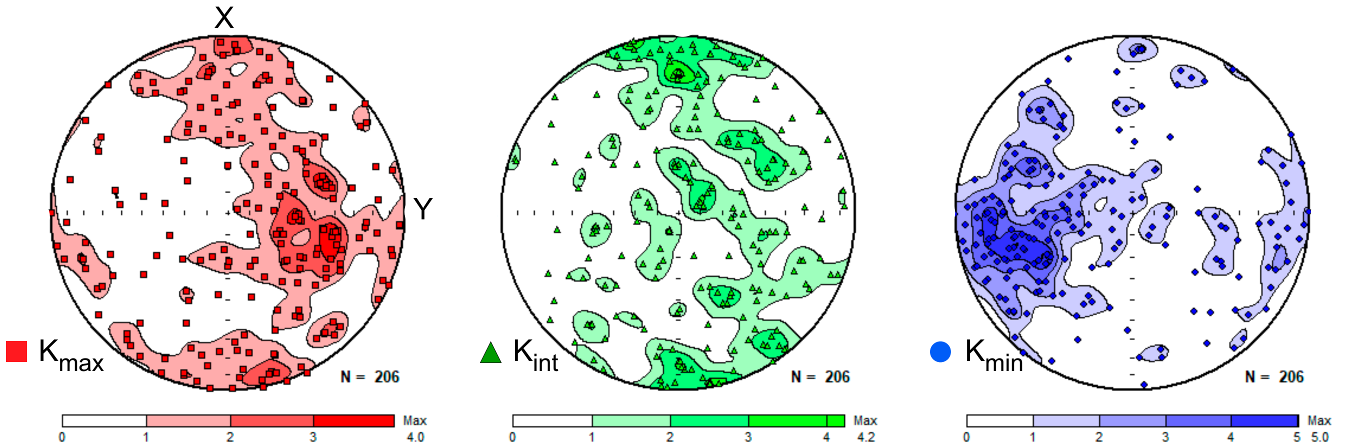

Figure F73. Downhole plot of (**A**) GRA density, (**B**, **C**) magnetic susceptibility, (**D**) electrical resistivity, (**E**) NGR, and (**F**) average and mode of CT values in each section, with Hole BA1B lithology.

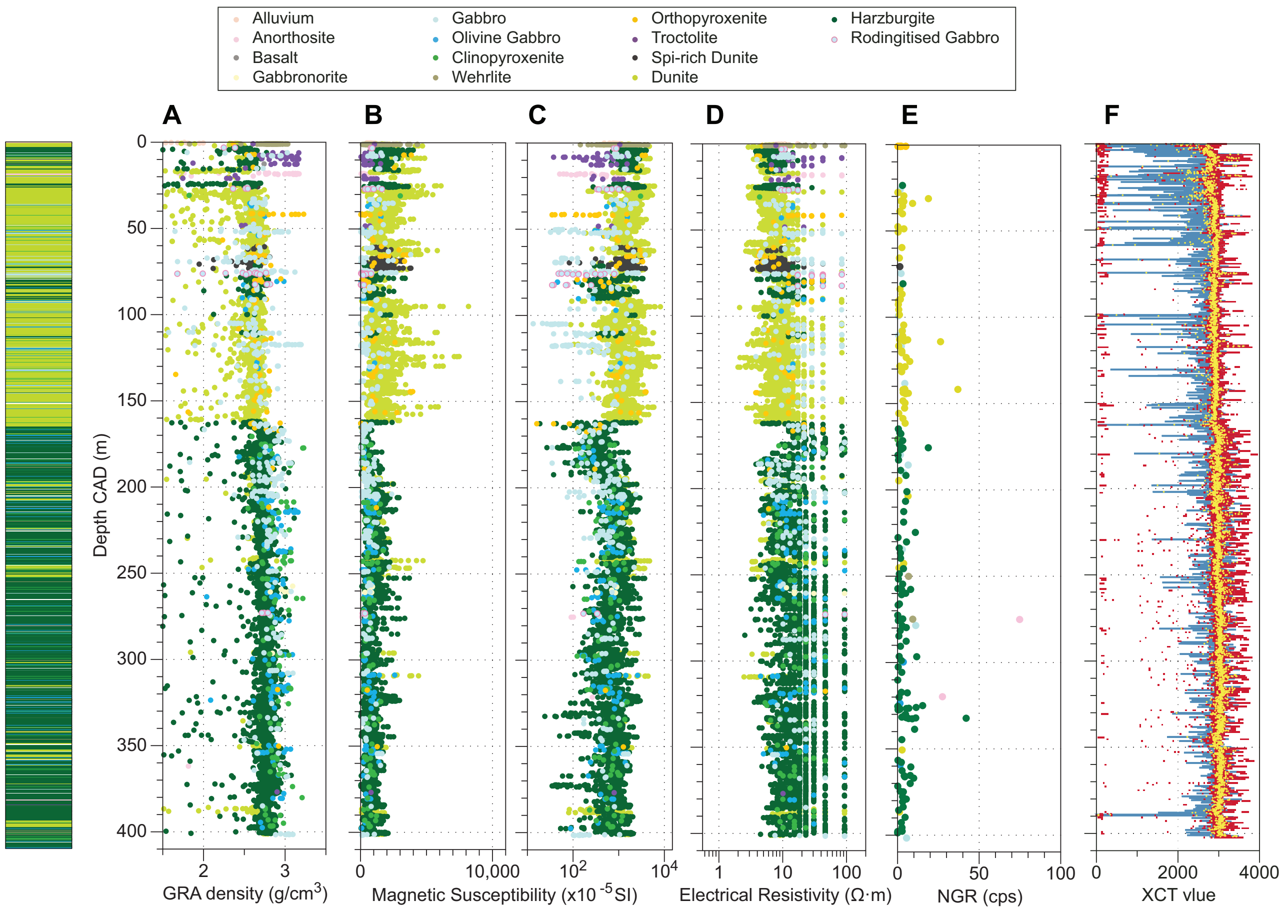

Figure F74. Examples of MSCL-I image, average and mode of CT values, and CT image, Hole BA1B. **A.** Dunite (18Z-1). **B.** Gabbroic layer in the Dunite with Gabbro Sequence (57Z-2). **C.** Harzburgite with veins and fractures (62Z-1). **D.** Harzburgite with vein (97Z-3). Images credit: Dr. Michibayashi.

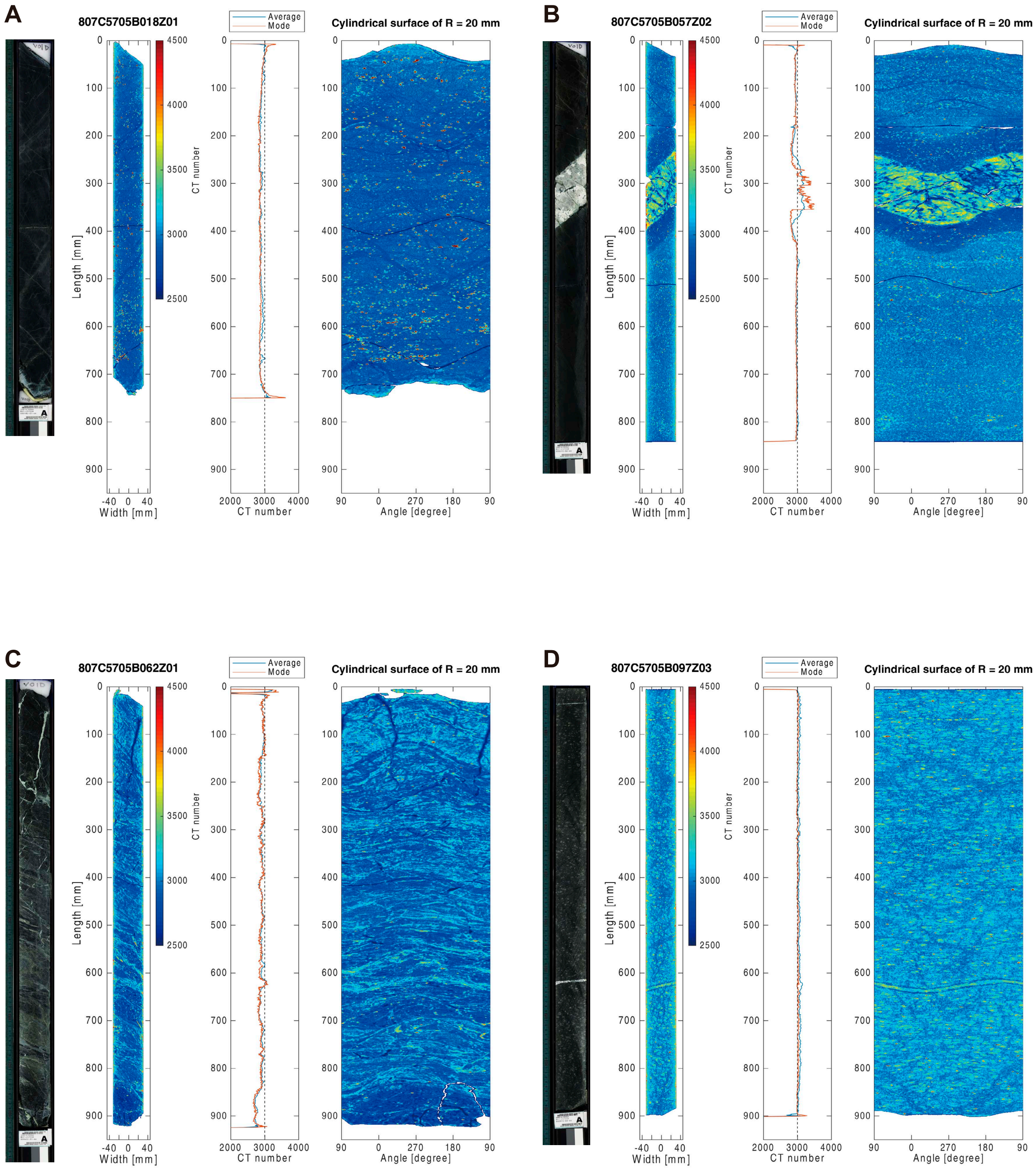

Figure F75. Correlation between (**A**) GRA density and XCT value and (**B**) whole-round resistivity (i.e., electrical conductivity) and magnetic susceptibility, Hole BA1B.

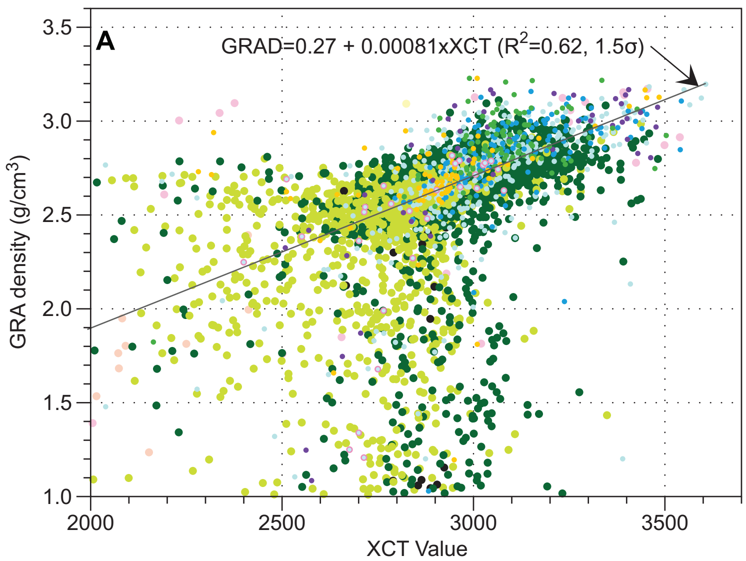

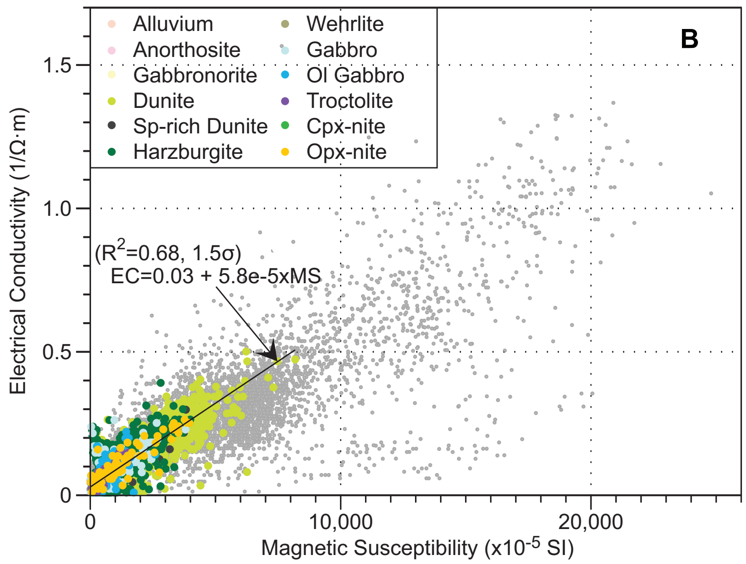

Figure F76. Downhole plots of discrete sample measurements of physical properties, Hole BA1B. (**A**) *P*-wave velocity (V_P), (**B**) bulk density, (**C**) grain density, (**D**, **E**) porosity, (**F**) electrical resistivity under dry and wet conditions, (**G**) bulk magnetic susceptibility (AMS), and (**H**) thermal conductivity.

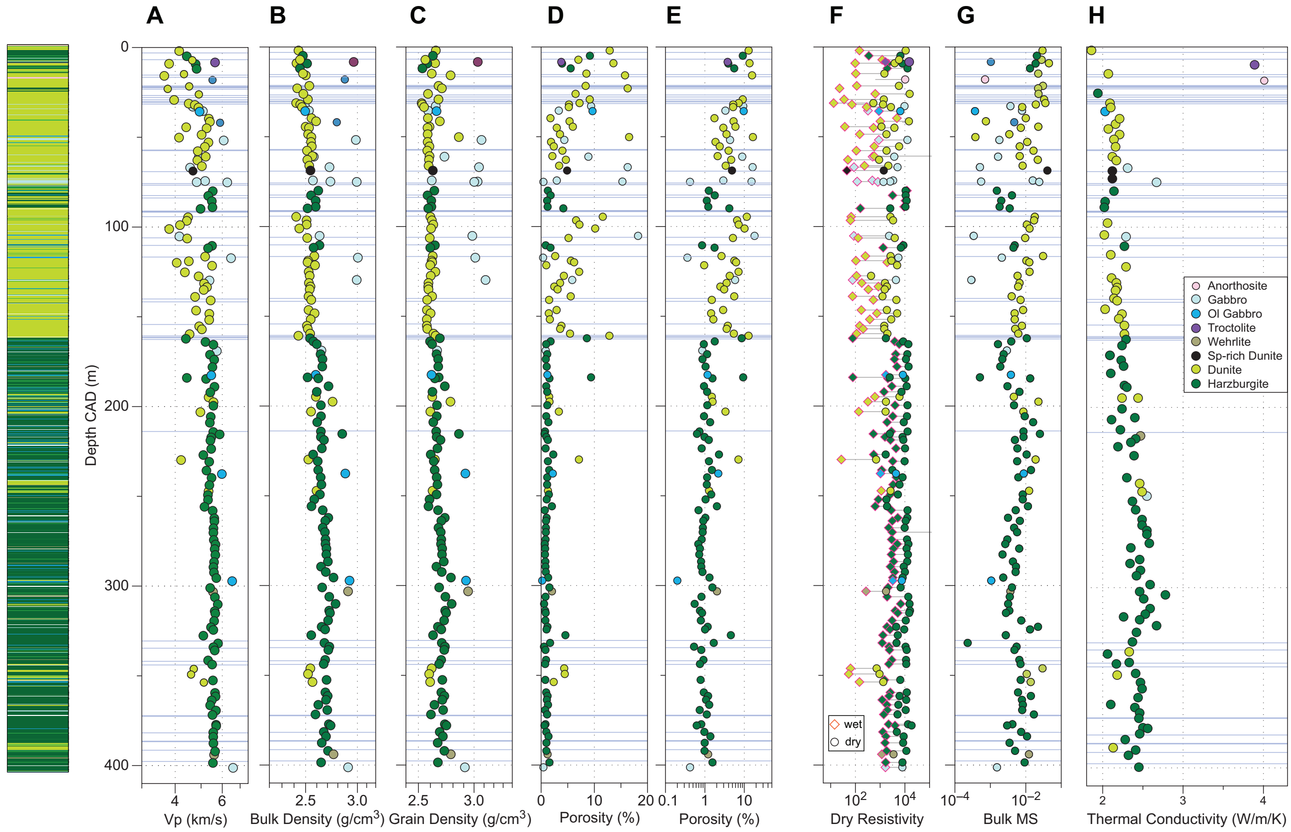

Figure F77. Downhole plots of (**A**) average *P*-wave velocity, (**B**) azimuthal anisotropy of *P*-wave velocity, and (**C**) perturbation of velocity in each orientation from the average (red = *x*-axis, orange = *y*-axis, blue = *z*-axis), Hole BA1B.

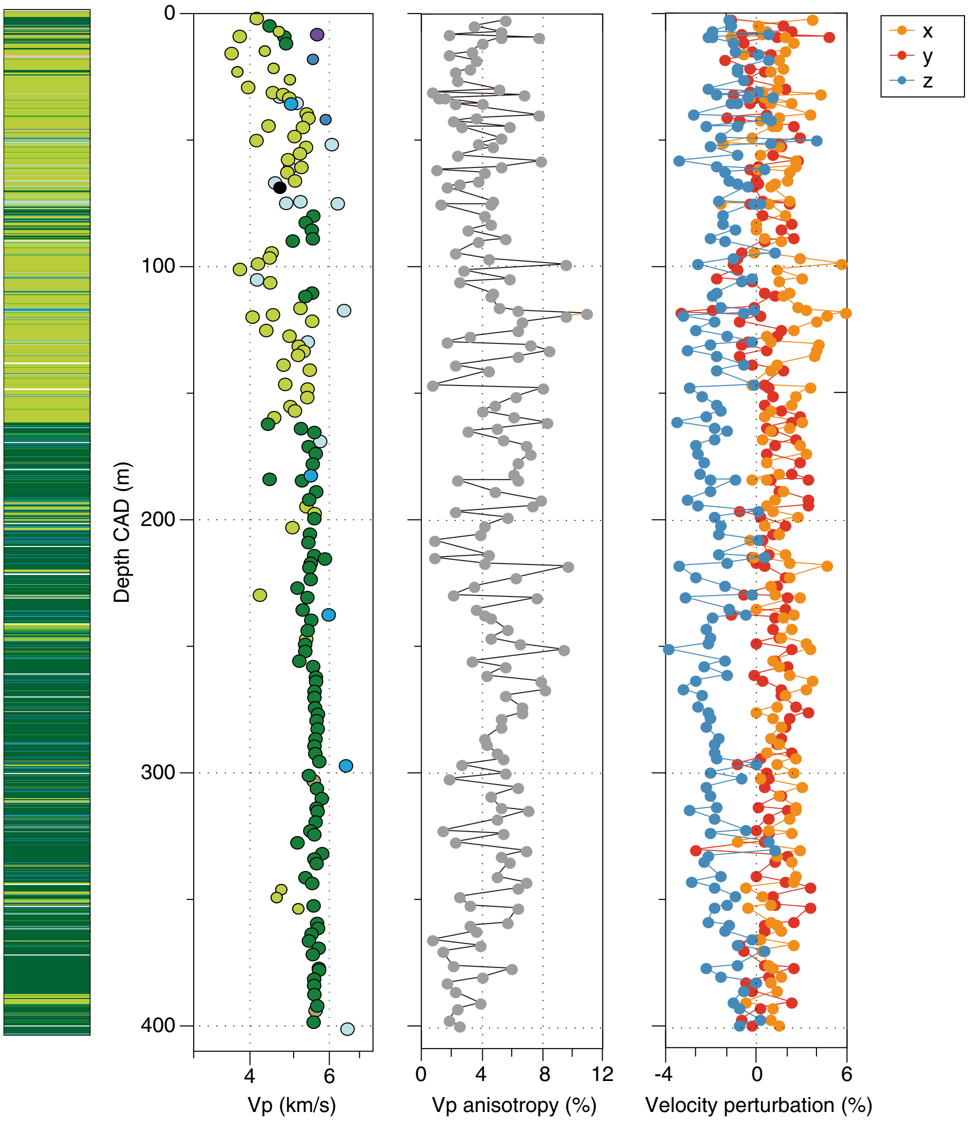

Figure F78. Relationships between *P*-wave velocity and porosity in minicube samples plotted on (**A**) linear scale and (**B**) logarithmic scale of the horizontal axis, Hole BA1B. Hole CM2B data are also plotted for comparison.

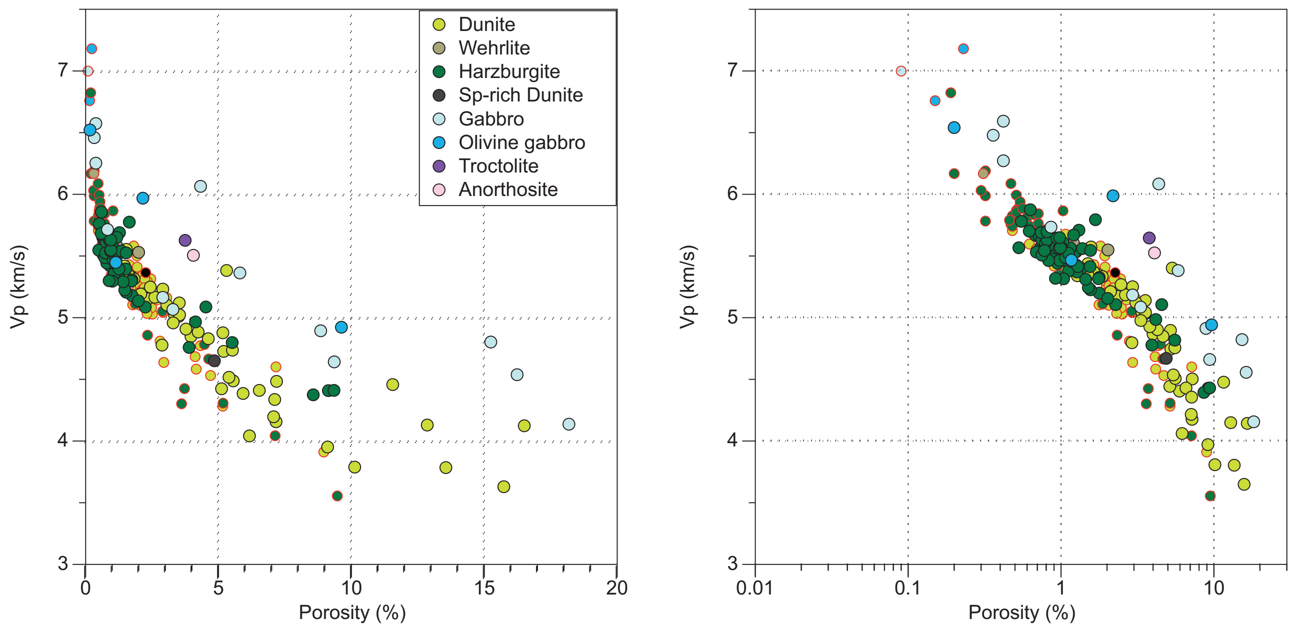

Figure F79. Relationship between *P*-wave velocity and (**A**) bulk density and (**B**) grain density, Hole BA1B. Hole CM2B data are also plotted for comparison.

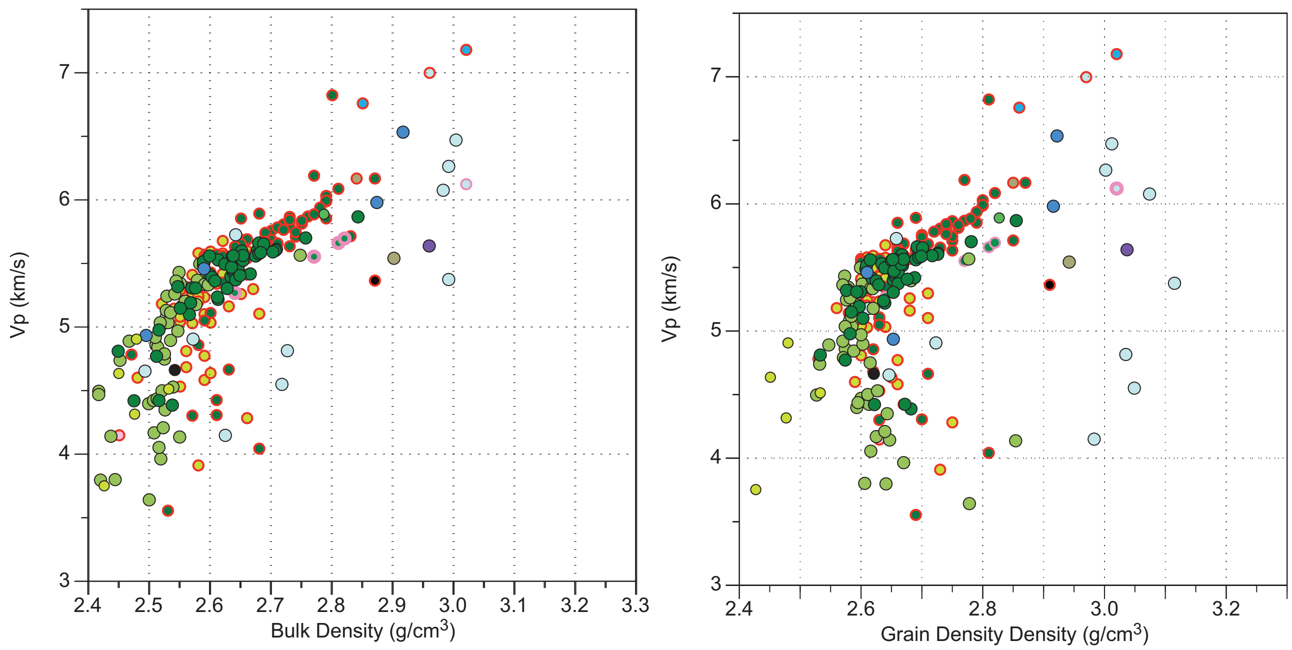

Figure F80. Correlation between bulk magnetic susceptibility and electrical resistivity of the minicube samples (dry and wet measurements), Hole BA1B.

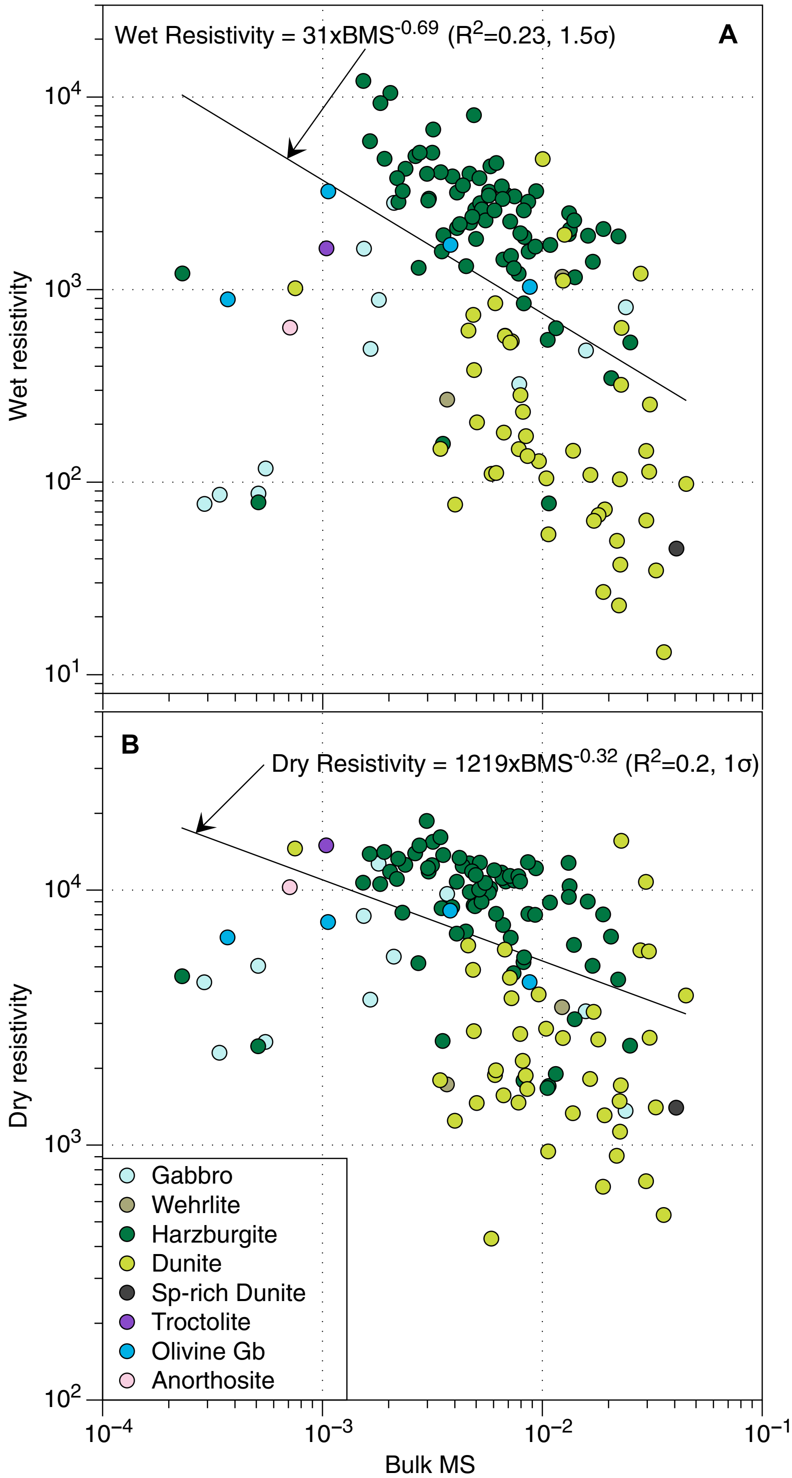

Figure F81. Thermal conductivity and *P*-wave velocity of the minicube samples plotted with XCT value, Hole BA1B. These physical properties are correlated to the XCT value, and fitting lines are shown in each figure.

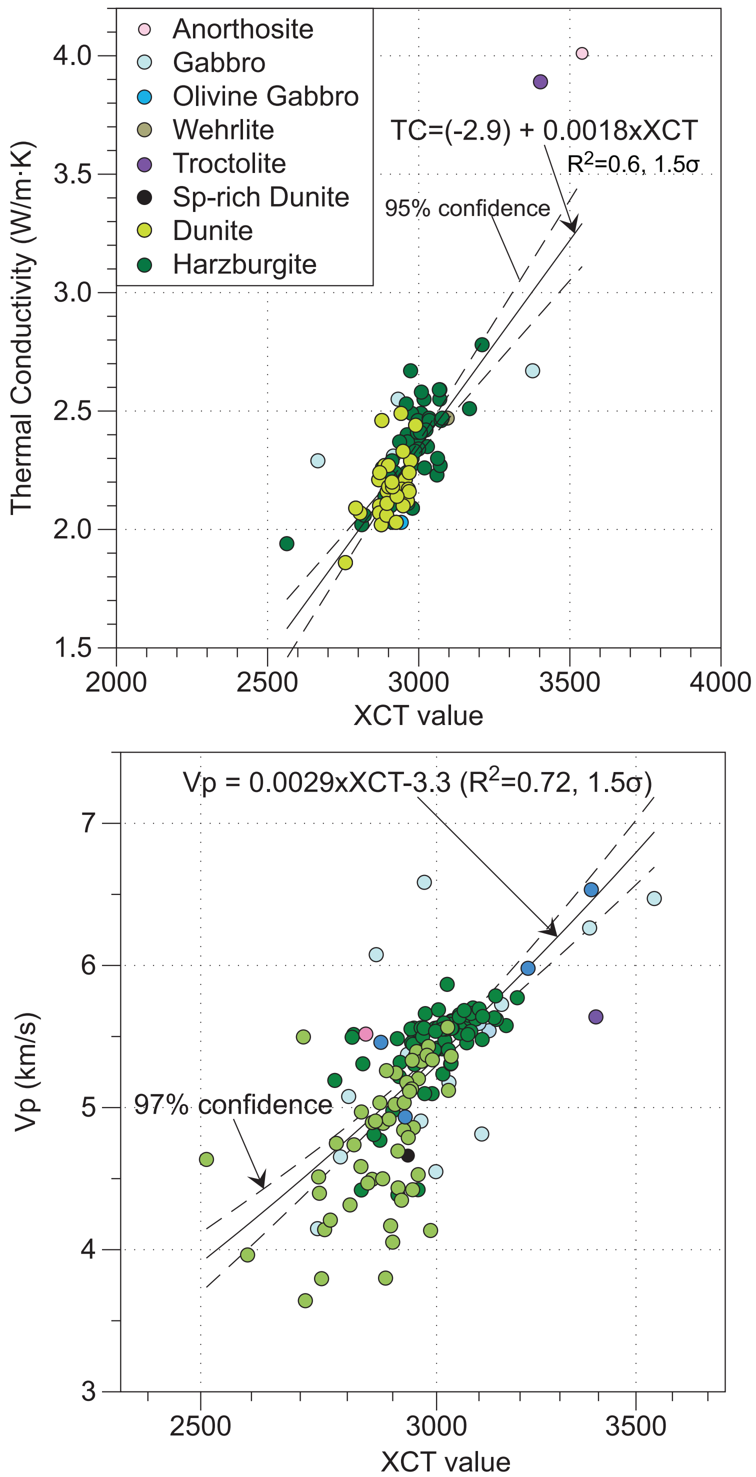

Figure F82. Lithostratigraphic column, Hole BA1C.

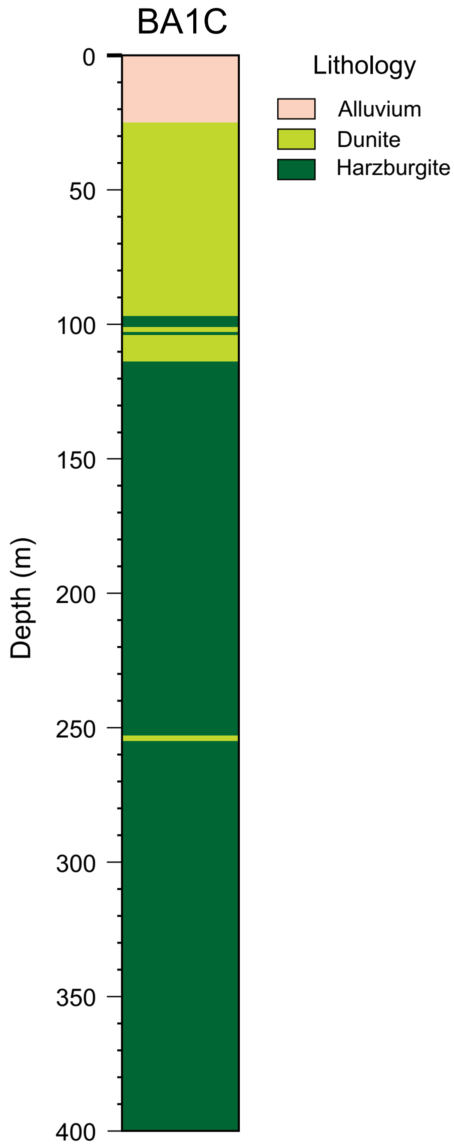

Figure F83. Lithostratigraphic column, Hole BA1D.

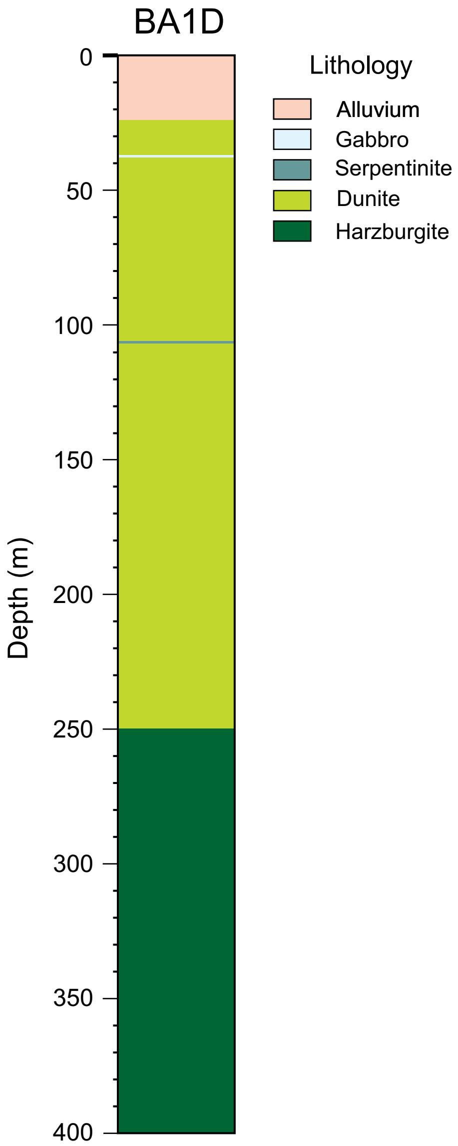

Tables

Table T1. Cuttings log, Hole BA1A. **This table is available in Microsoft Excel format.**

Table T2. Operations and coring summary, Hole BA1B. **This table is available in Microsoft Excel format.**

Table T3. Number and thickness of rock types occurring within the full core, Hole BA1B. **This table is available in Microsoft Excel format.**

Table T4. Number and thickness of rock types occurring within each principal lithologic sequence, Hole BA1B. **This table is available in Microsoft Excel format.**

Table T5. Details of the principal lithologic sequences, Hole BA1B. **This table is available in Microsoft Excel format.**

Table T6. Compilation of secondary minerals in veins identified by X-ray diffraction, Hole BA1B. **This table is available in Microsoft Excel format.**

Table T7. Whole-rock major elements, trace elements, and volatiles, Hole BA1B, with mineralogy by XRD. **This table is available in Microsoft Excel format.**

Table T8. All trace element data measured by LA-ICP-MS (corrected based on SiO_2 from XRF post-ship-shore calibration) including repeats, Hole BA1B. **This table is available in Microsoft Excel format.**

Table T9. Natural remanent magnetization values and principal component analysis results, Hole BA1B. **This table is available in Microsoft Excel format.**

Table T10. Magnetic susceptibility values and anisotropy parameters, Hole BA1B. **This table is available in Microsoft Excel format.**

Table T11. Summary of discrete physical properties measurements, Hole BA1B. **This table is available in Microsoft Excel format.**

Table T12. Velocity, density, porosity, electrical resistivity, and magnetic susceptibility, Hole BA1B. **This table is available in Microsoft Excel format.**

Table T13. Thermal conductivity, Hole BA1B. **This table is available in Microsoft Excel format.**

Table T14. Cuttings log, Hole BA1C. **This table is available in Microsoft Excel format.**

Table T15. Cuttings log, Hole BA1C. **This table is available in Microsoft Excel format.**

Supplemental tables

Table ST1. MSCL-W (GRA density, NGR, *P*-wave velocity, MS, NCR), Hole BA1B. **This table is available in Microsoft Excel format.**

Table ST2. MSCL-C (color spectrum and MSP), Hole BA1B. **This table is available in Microsoft Excel format.**